DESIGN AND DEVELOPMENT OF A NOVEL BALL-ON-CUP TRIBOMETER FOR THE CHARACTERIZATION OF AN INGENIOUS TOTAL HIP PROSTHETIC LINER MADE OF UHMWPE AND ITS COMPOSITE

A Thesis

For The Award of The Degree of

DOCTOR OF PHILOSOPHY

by

ASHIRBAD JANA

[Roll No. 146103028]

DEPARTMENT OF MECHANICAL ENGINEERING
INDIAN INSTITIUTE OF TECHNOLOGY GUWAHATI
GUWAHATI, ASSAM – 781039
INDIA
April 2023

Department of Mechanical Engineering
Indian Institute of Technology Guwahati
Guwahati, Assam - 781039
India

CERTIFICATE

It is certified that the work contained in the thesis entitled "**DESIGN, DEVELOPMENT AND CHARACTERIZATION OF INGENIOUS UHMWPE AND ITS COMPOSITE TOTAL HIP PROSTHETIC LINERS USING A NOVEL BALL-ON-CUP TRIBOMETER**" submitted by **Mr. ASHIRBAD JANA** [IITG Roll No. – 146103028] to the Indian Institute of Technology Guwahati, Guwahati, India for the award of the degree of Doctor of Philosophy has been carried out under our supervision in the Department of Mechanical Engineering, Indian Institute of Technology Guwahati. This work has not been submitted elsewhere for the award of any other degree or diploma.

Dr. S. KANAGARAJ
Professor
Department of Mechanical Engineering
Indian Institute of Technology Guwahati
Assam, India

Dr. S. SENTHILVELAN
Professor
Department of Mechanical Engineering
Indian Institute of Technology Guwahati
Assam, India

This Thesis Is Dedicated to

The Most Important Women in My Life

My Mother

Mrs. Sarbani Jana

and

My Wife

Mrs. Joyasree Mondal (Jana)

and

My Daughter

***Aashree** (Matu)*

ACKNOWLEDGEMENT

I would like to express my sincere gratitude to my thesis supervisors and my well-wishers, Prof. S. Kanagaraj and Prof. S. Senthilvelan for their valuable guidance and constant encouragement throughout my Ph.D. work. Their cognizance, enormous goodwill and unruffled patience made me work at ease and kept me highly motivated throughout my journey along with them. Their innovative ideas and consistent support by providing all the necessary facilities, were helpful in successful completion of my research work. I have been immensely benefited from each and every moment of my association with them.

I would like to express my gratitude towards my Doctoral committee members Prof. S. K. Dwivedi (chairman), Dr. N. Muthu and Dr. S. Senthilkumar for continually reviewing the progress of our research with valuable suggestions and constructive criticism to improve the quality of the thesis.

I am grateful to Prof. T.G. Sitharam, Director, IIT Guwahati and Prof. G. Biswas (former Director), Prof. K. S. R. Krishna Murthy, Head, Department of Mechanical Engineering, IIT Guwahati, Prof. A. K. Dass and Prof. P. Mahanta (former HODs) for providing the facilities during my research work.

Financial support provided by the SERB, Department of Science and Technology (DST), MOE, India and Northeast Centre for Biological Sciences and Healthcare Engineering (NECBH) by Department of Biotechnology is greatly acknowledged.

I would like to thank Department of Mechanical Engineering officers, Mr. Saifuddin Ahmed, Materials Science laboratory, Mr. Sanjib Sarma, Strength of Materials Laboratory, Mr. Jiten Basumatary, Advanced Manufacturing Laboratory and Mr. N. K. Das and his associates, Central workshop for their support during my experimentation, testing and fabrication throughout the research work and office staffs Mr. Nabajyoti Dutta and Mr. Raju Talukdar for helping me in the academic and administration works.

I, sincerely acknowledge Prof. Bikramjit Basu, Materials Research Center, IISc Bangalore and his team for providing *in vitro* cytocompatibility testing facilities.

I extend my heartfelt thanks to the project members Mr. Kishore Kumar Padi, Mr.Pritam Gagoi and Mr. Anirban Basumataray for their strong support during the experimental performance of the research. I am very much grateful to Biomedical Devices and Biomaterials laboratory colleagues Dr. Devarshi, Dr. Aparna, Mr. Vaibhav, Mrs. Nandani and Mr. Ragdeep for their valuable support at different phases of my research work.

It has been a pleasure to work with my colleagues Mr. Uttam, Mr. Sujit and Mr. Saptarshi and I am also thankful to all my department colleagues, who helped me directly and indirectly at various stages of my work.

My sincere thanks to Central Instruments Facility, IIT Guwahati, for giving permission to utilize the facilities throughout the thesis work.

I also thank my friends Mr. K. Durgaprasad, Mr. Amritava Sarkar, Mr. Ankan Mishra and Mr. Karthik Pandian, who supported me during my stay at IIT Guwahati.

I would like to sincerely thank my professors Dr. P. S. Robi, Dr. S. K. Kakoty, Dr. D. Chakraborty, Dr. V. Kulkarni, and Dr. S.N. Joshi for their lessons and guidance throughout my thesis work.

I express my gratitude to my friends Dr. R. Vignesh Babu and Dr. Swayamdipta Bhaduri, who always encouraged me at every stage of my research work.

I extend my hearty gratitude to my parents Mr. Asit Ranjan Jana and Mrs. Sarbani Jana for their unconditional love and moral strength throughout these years, who taught me the essence of hard work, patience, belief, and dedication of what I do.

I would like to sincerely thank my younger brother Mr. Anirban Jana and wife Mrs. Joyasree Mondal (Jana) for their moral support, love, and patience towards me.

I am thankful to the Supreme energy for all this raising step towards the successful life, opportunity, and good health to serve for the nation and earth.

(**Ashirbad Jana**)

Date: **IIT Guwahati**

ABSTRACT

Total hip replacement (THR), regarded as the orthopaedic operation of the 20th century, uses ultra-high molecular weight polyethylene (UHMWPE) as the acetabular liner since 1960s. However, the life of a metal-on-plastic THR is often limited to 15-20 years, primarily due to excessive wear debris generation during its operation, leading to osteolysis and aseptic loosening of the prosthetic joint leaving behind a painful revision surgery. Presently worldwide research is dedicated in improving the life of a metal-on-plastic THR by the improvement of tribological characteristics of an UHMWPE acetabular liner.

The objective of present work is to develop UHMWPE and UHMWPE-MWCNT composite based acetabular liners and their preclinical evaluation as per international guidelines to compare their wear performance. An ingenious technique is proposed for the manufacturing of the acetabular liner using medical grade UHMWPE-GUR1050 polymer powder by a cold isostatic compaction against a mirror finished metallic surface, and it is followed by shape-constrained sintering. UHMWPE powder is processed with experimentally obtained optimum value of compaction pressure, sintering temperature and sintering duration to get products having the properties at par with hot isostatic processed (HIPped) products, viz., relative density of ~ 97% and Vickers hardness of ~ 5.0. Moreover, the newly developed acetabular liners are found to possess inborn plateau finished bearing surface with R_a <100 nm and a negative skewness of 1.156, altogether making it an ideal choice for any bearing applications. UHMWPE-MWCNT nanocomposites with different concentrations of the filler are processed for enhancing the mechanical properties of virgin polymer to the maximum possible extent. Up to 0.25 wt.% of MWCNT is successfully dispersed and distributed homogeneously in UHMWPE by ultra-sonication and magnetic stirring to improve the hardness and compressive yield strength of UHMWPE by 77% and 43%, respectively, with 60% increase in tensile yield strength. After the confirmation of biocompatibility of UHMWPE-0.25MWCNT nanocomposites, it is used to manufacture acetabular liner with improved mechanical properties compared to the pure polymer.

A novel mechanism is designed as a modular attachment for a standard pin-on-disc machine to transform the same into a 'Ball-on-Cup' tribometer similar to an orbital bearing machine (OBM) hip simulator meeting the ISO-14242-3 recommendations. The novel 'Ball-on-Cup' tribometer is developed to study *in vitro* tribological characteristics of the newly developed UHMWPE and UHMWPE-0.25MWCNT acetabular liners against stainless steel (SS) femoral

heads with ISO-14242-3 recommended kinetics at an accelerated frequency of 5 Hz. A 1:2 volumetric solution of 2% w/v high molecular weight Sodium Alginate and 0.75% w/v Gellan gum is used as a lubricant during wear simulation of the developed prosthesis for its rheological similarity with the synovial fluid.

In vivo condition of human hip joint is simulated with significant success using the novel 'Ball-on-Cup' tribometer, where Sodium Alginate/Gellan gum is used as a lubricant, generating spherical and sub-spherical shaped wear debris from the tested prosthesis under the action of adhesive and fatigue wear. These wear debris are found to be morphologically similar in comparison to those retrieved from the human body while using THA. The stable wear rate of ~20 mm^3/MC observed for non-crosslinked UHMWPE acetabular liner against SS femoral head is found to be at par with that of reported values by most of the laboratories worldwide for cross-linked UHMWPE liners, which is reduced further by ~ 55% after 0.25 wt.% of MWCNT reinforcement. Hence, it is concluded that UHMWPE and UHMWPE-MWCNT composite processed with the proposed ingenious technique may be considered as potential aspirants for the next generation acetabular liner in metal-on-polymer THR in order to increase its longevity.

LIST OF CONTENT

CHAPTER 2: LITERATURE REVIEW

LIST OF FIGURES

LIST OF TABLES

NOMENCLATURES

P_C – Compaction pressure

T_S – Sintering temperature

t_S – Sintering duration

T_{VS} – Least viscous point

G' – Storage modulus

G" – Loss modulus

η^* – Complex viscosity

T_{MO} – Onset melting point

T_{ME} – Melting end point

T_{MP} –Peak melting point

T_{VO} – Onset temperature of viscous flow

T_D – Diffusion point

R_a – Average surface roughness

Φ – Diameter

X_C - Degree of crystallinity

ΔH - The heat of fusion

ΔH_{100} - Melting enthalpy at 100% crystallinity

X **-** Nose radius of polymer diffusion

R_{RMS} - Root mean square roughness

S_{ku} - Kurtosis value

CHAPTER 1

INTRODUCTION

1.1. Brief History of Total Hip Replacement

Total hip replacement (THR) is a surgical procedure generally conducted to relieve arthritis pain or some hip fractures in which the hip joint is replaced by a prosthetic implant consisting of both the acetabulum and the femoral head. It has been over 100 years of revolutionary operative history and is regarded as the most successful orthopaedic interventions of its generation. Figure 1.1(A) shows the photograph of German Professor Themistocles Glück who made the earliest recorded attempts at hip replacement surgery around 130 years ago, in 1891[1]. His inspiration was to help his patients suffering from tuberculosis that weakened the body and caused damage to their hip joints. Glück created an implantable femoral head prosthesis using ivory and fastened with nickel-plated screws. In 1925 Marius Smith-Petersen, the American surgeon, created the first '*mould arthroplasty'* out of glass in a hollow hemispherical shape providing a new smooth surface over the femoral head. But it failed to withstand the great forces going through the hip joint and shattered. Later, he along with Philip Wiles went on to try stainless steel to create the first total hip replacement which was fitted to bone with bolts and screws[2].

Remarkable success achieved in 1953 when English surgeon George McKee began to use cobalt-chrome socket as the new acetabulum and his first patient was able to walk painlessly with an artificial hip joint [3]. Figure 1.1(B) shows the photograph of Sir John Charnley, considered as the father of the modern THA, designed his '*low friction arthroplasty*' in the early 1960's consisting of three parts: a metal femoral stem, a polyethylene acetabular component and acrylic bone cement inspired by the work of dentists[4]. This cemented hip replacement became popular due to its toughness and ability to be used as grout to improve the fitness of the implant. Charnley design being a low friction solution improved patient movement post-surgery that solved the squeaking noise heard from other implant solutions at that time[5]. His design also included a smaller femoral head which reduced implant wear over time.

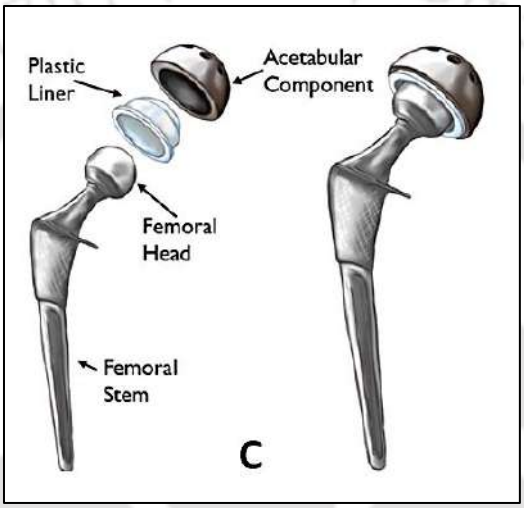

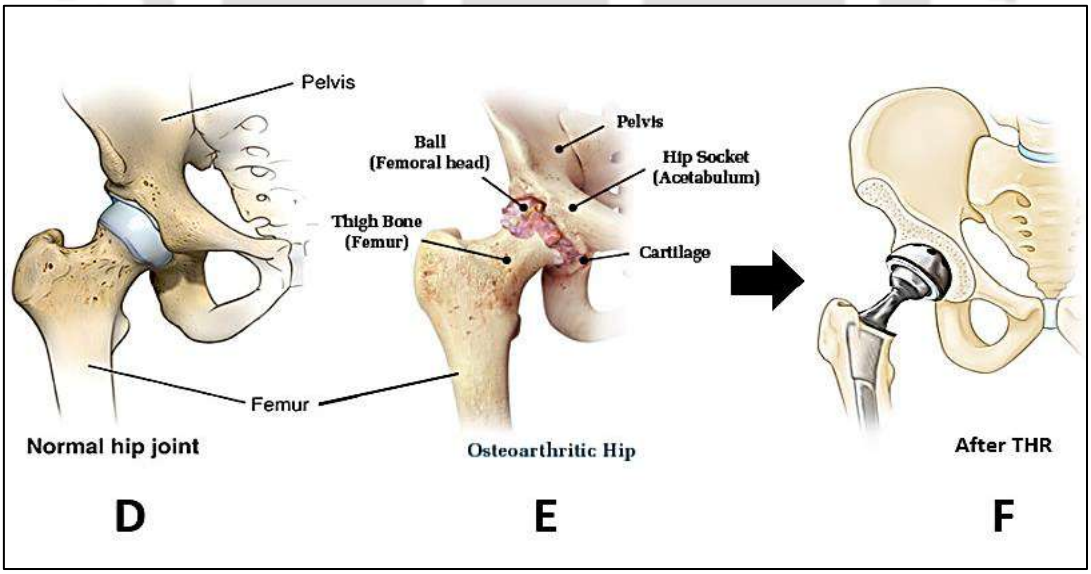

***Figure 1.1**. (A) Themistocles Glück was the first to present the use of ivory to replace femoral heads during the 1890s (B) Sir John Charnley is considered as the father of the modern Total Hip Arthroplasty (THA) (C) Components of a low friction THA (D) A Normal Human Hip joint (E) An Arthritic Hip joint with damaged cartilage (F) Hip joint after Total Hip Replacement [www.hipreplacement.com]*

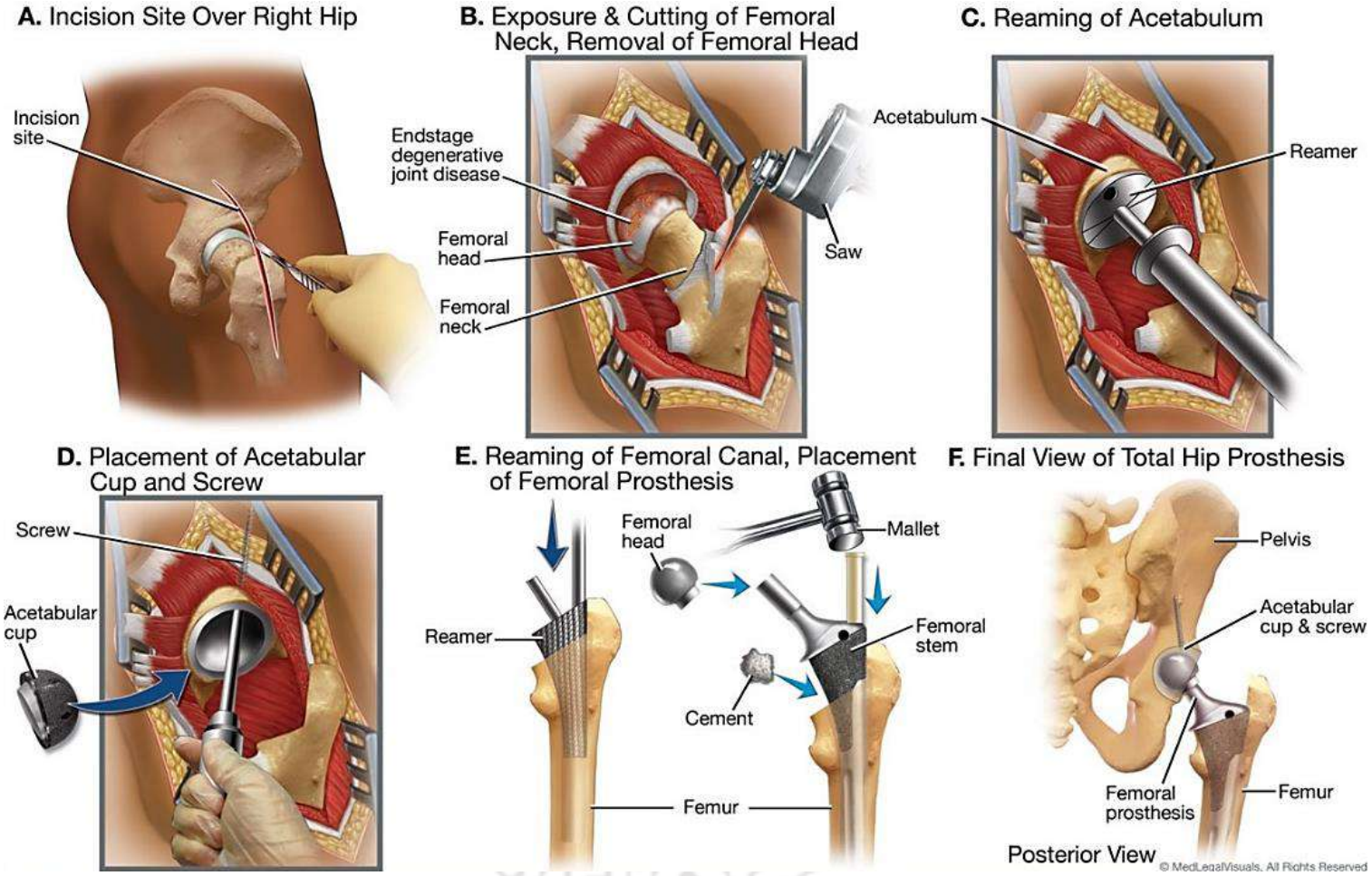

Figure 1.2. *Right total hip replacement procedure (A) Incision site over right hip (B) Removal of femoral head (C) Reaming of acetabulum (D) Acetabular liner fixation (E) Femoral stem fixation (F) Final view of total hip prosthesis* [©MedLegalVisuals]

He purposefully used a small femoral head which reduced wear due to its smaller surface area improving the life span and success of the surgery. Overall, Charnley contributions laid the groundwork for modern implant designs and surgical techniques[6]. The contemporary prostheses used to replace arthritic or damaged hip joints are still identical in basic principle with Charnley design, shown in Figure 1.1(C). Human hip joint is a ball and socket synovial joint, formed by an articulation between the head of the femur and the pelvic acetabulum as shown in Figure 1.1(D). Figure 1.1(E) shows a human hip joint after arthritic damage, and after been replaced by an artificial joint through THR procedure it finally looks like as shown in Figure 1.1(F).

Since the introduction of the modern hip replacement by Dr. Charnley, the implant designs have been improved to offer cementless fixation or press-fit fixation options, larger femoral head sizes to reduce the dislocation risk, and improvements in bearing surface materials notably the highly cross-linked polyethylene, which further reduced the wear rate. Computer-assisted surgery (CAS) has been around since the early 1990s. In a Computer Assisted Surgical procedure, the surgeon uses a combination of instruments and computer software to assist with implant position and orientation. Currently, in the 7th decade of modern THA, over six million joint replacements are performed every year in USA, [7]. In India, about 6 million people are affected and 1.5 million joint arthroplasty surgeries have been performed [8]. Techniques have been standardised as shown in Figure 1.2 and the average age of those receiving the hip replacements has reduced as the number of successful operations is increased. This magnified the problems of implant failure due to wear of bearing surfaces. A variety of combinations are attempted to find one with fewest complications and best long-term survival.

1.2. Evolution of bearing surfaces in total hip arthroplasty

Bearing surface for THA has been evolved significantly during past fifty years and it is briefly shown in Figure 1.3, starting with Glück's ivory femoral head and Charnley's low-friction arthroplasty followed by the present day's third generation ceramic-on-ceramic bearing surfaces and sequentially cross-linked polyethylene. To identify future scope of research in this field and achieve ultimate goal of improvement, a careful study of this evolutionary process along with the strength and weakness of all available options should be done very judiciously.

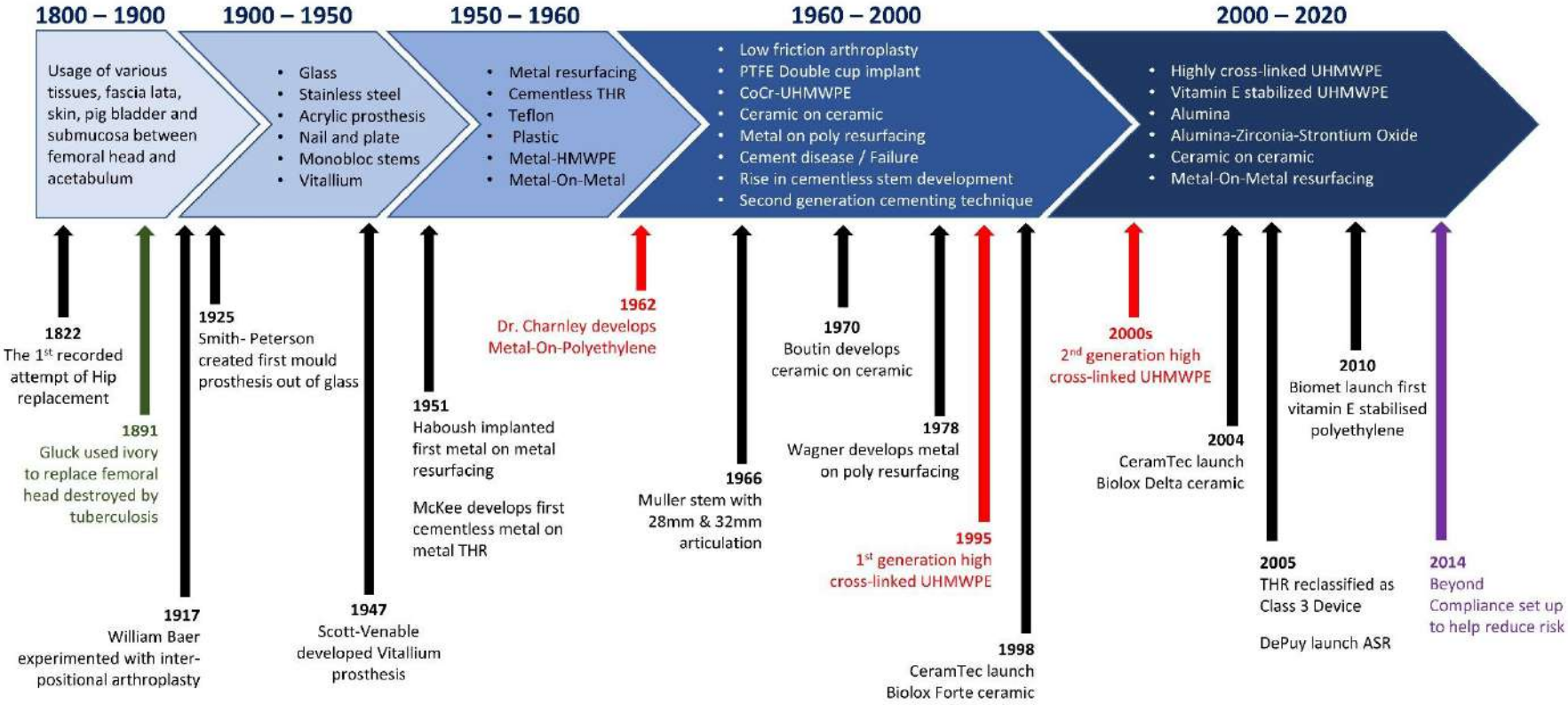

Figure 1.3. *A timeline depicting major advances in the evolution of bearing materials*

TABLE 1.1. *Comparison of different bearing surface combinations* [10]

Bearing combinations	Advantages/Indications	Disadvantages
Metal-on-Polyethylene	✓ Most forgiving combination in terms of component placement ✓ Least expensive ✓ Used for elderly patients with low functional demands	○ Highest wear among all three combinations ○ Smaller femoral heads with relative decrease in stability and range of motion compared to metal-on-metal ○ Boundary lubrication mechanism which increases wear with bigger femoral head ○ Backside wear
Ceramic-on-Polyethylene	✓ Increased hardness, scratch resistance and burst strength ✓ Increased wettability for improved lubrication ✓ Lower wear rates compared with metal-on-polyethylene ✓ Excellent clinical results	○ Risk of fracture of the ceramic ○ Higher wear rates than ceramic-on-ceramic
Metal-on-Metal	✓ Larger femoral heads available with increased stability, jump distance and range of motion ✓ Mixed fluid film lubrication mechanism which decreases wear with bigger femoral heads ✓ Self-polishing capacity ✓ Better wear resistance than metal-on-polyethylene (low volumetric wear) ✓ Used in young patients with high functional demands	○ Highest biological reactivity and cytotoxicity with highest number of wear particles ○ High levels of metal ions in blood, urine and remote organs ○ Not used in females in their reproductive years or patients with renal failure ○ Metal sensitivity (Delayed type hypersensitivity) ○ Possible carcinogenesis and genetic damage ○ Perfect component positioning is essential to prevent failure
Ceramic-on-Ceramic	✓ Lowest biologic reactivity ✓ Low friction and wettability ✓ Low surface roughness ✓ Highest wear resistance ✓ Reserved for young, high functional demand patients with metal sensitivity	○ Brittleness and possible component fractures ○ Small femoral heads with decreased range of motion ○ Stripe wear with possible squeaking ○ Less forgiving combination ○ Most expensive

The optimal performance of bearing surface is contributed mostly by the corrosion resistance, wear resistance, synoviaphilic surface, low friction and high fracture toughness characteristics of the material. Each bearing combination has its own evolution, advantages and limitations, which are summarized in Table 1.1. Total hip replacements are highly conforming to low-contact stresses. Polyethylene failure in total hip is mainly contributed by abrasion and adhesion wear mechanisms [9].

1.2.1. FDA-approved bearing surfaces

1.2.1.1. Metal-on-polyethylene

Metal-on-polyethylene, introduced by Sir John Charnley, is still the most common bearing combination worldwide and it is shown in Figure 1.4(A). However, a long-term follow-up on patients during 1990s revealed the problems associated with osteolysis and wear debris [11]. Then, the technique of cross-linking in the molecular structure of polyethylene by gamma irradiation is introduced to increase its wear resistance while generating undesired free radicals.

Figure 1.4*. FDA approved bearing combinations for total hip replacement (A) Metal-On-Polyethylene (B) Ceramic-On-Polyethylene (C) Metal-On-Metal (D) Ceramic-On-Ceramic [HipReplacement.com]*

The first generation of highly cross-linked polyethylene is emerged in the market in 1998. To resolve the problematic effect of the free radicals without affecting the wear resistance, several attempts like thermal treatment after irradiation, post-irradiation annealing or melting, sequentially cross-linking and vitamin E doping on polyethylene are made. Sequentially cross-linked PE (X3 HXPE) has shown better oxidative stability while

maintaining its mechanical properties. Additionally, the density, crystallinity and tensile properties of the X3 HXPE remained unchanged under oxidative environment, [12]. Due to its antioxidant characteristics, Vitamin E doped polyethylene has decreased free radicals and shown superior results in terms of longevity of the irradiated joint arthroplasties [7].

1.2.1.2. Ceramic-on-polyethylene

Reduction in polyethylene thickness to accommodate larger femoral heads for better stability and range of motion inspired further attempts to reduce polyethylene wear, leading to the introduction of a new bearing couple: ceramic femoral heads against acetabular polyethylene liners shown in Figure 1.4(B). It is expected that the low surface roughness of ceramics decreased polyethylene wear. The first ceramic femoral head is made of zirconia, which was introduced in 1985 and later it is recalled in 2001 [13]. Catastrophic failure in addition to thermal instability due to high frictional force led to generation of cracks and ultimately third body wear which made zirconia unpopular. The next generation ceramics such as zirconia toughened alumina have yielded lower wear debris, better scratch resistance, lower coefficient of friction and increased wettability compared with cobalt-chromium heads, when polyethylene liners were used, [14]. However, the evidence is limited and longer prospective studies can establish the real advantages and limitations of this bearing couple in THA.

1.2.1.3. Metal-on-metal

Metal bearings, as shown in Figure 1.4(C) have followed their own evolutionary pathway since the beginning of joint arthroplasty surgery. The first prototype developed by Philip Wiles in 1938 had inadequate implant quality and manufacturing problems. George Kenneth McKee came up with the first generation of metal-on-metal bearings used in THA in the 1950s, which was clinically introduced as cobalt-chromium- molybdenum alloy in 1966 [15]. Wear produced by metal-on-metal was very less as compared to the conventional metal-on-polyethylene as shown in Figure 1.5. Muller and Weber of Switzerland introduced the second generation of this bearing surface in 1988. By 1999, there were 1.5 million Metasul prostheses implanted worldwide [16], [17].

High concentration of metal ions is found in the hip joint and the high non-physiological serum levels of cobalt and chromium ions in the blood and organs of patients after metal-

on-metal hip arthroplasty are still a matter of concern [18], [19]. Number of metal wear particles is observed to be higher due to their smaller size despite having lower volumetric wear, and it may be associated with early osteolysis, inflammatory reactions followed by prosthetic loosening, [20]. Additionally, metal-on-metal bearing surfaces are less forgiving to third-body wear. Due to these limitations, metal-on-metal bearing prostheses are indicated for use in younger patients and certain patients with higher demands than the average population for its better wear characteristics.

1.2.1.4. Ceramic-on-ceramic

Ceramics are always an attractive option to use as a bearing surface not only for their high wear resistance, hardness, low friction and high wettability but also for biologic inertness, low-surface roughness and fluid film lubrication, [21]. In 1970, ceramics are first introduced in France by Pierre Boutin, [22]. Temporary abandonment of ceramics for improper manufacturing as well as brittleness leading to component fracture, pain and high wear rates ended with the introduction of zirconium dioxide (Zirconia) femoral heads in 1985. The first zirconia to receive FDA clearance was the magnesium partially stabilized zirconia (Mg-PSZ), which was later replaced by the Yttria stabilized tetragonal zirconia polycrystals (Y-TZP) and it is shown in Figure 1.4(D). Despite its high fracture toughness and burst strength, zirconia was withdrawn from the market in 2001 due to its thermal instability leading to phase transformation by frictional heating during operation, cracks and ultimately third-body wear [23]. Even though 2nd and 3rd generation ceramics are reintroduced in the market, including alumina and Delta ceramics, concerns remain with ceramic-on-ceramic bearing surfaces. Delta ceramic is extremely hard and of bigger size compared to the earlier ones which gives THA instant stability. However, component fracture, whether ball or acetabulum, is used to be a serious complication [24]-[26]. Consequently, with improvements in design, fracture rates have been decreased considerably. Audible squeaking of ceramic-on-ceramic hip prostheses has been a recent topic of interest.

1.3. Metal-on-UHMWPE THR: The modern gold standard

It is clear by recent research and American Joint Replacement Registry (AJRR) data that HXPE is the modern gold standard bearing material for THR being the most forgiving and least expensive among all, which means that the clinical and bio-tribological performance

of any other bearing material should be compared with it. However, life of a Metal-on-HXPE THA is limited to 15-20 years showing the highest volumetric wear rate compared to other bearing combinations as shown in Figure 1.5.

Figure 1.5. *Quantitative comparison of yearly wear loss among different THR bearing combinations [www.hipandkneesurgery.ie]*

1.3.1. UHMWPE liner Manufacturing techniques

Usually, the commercially available polymer liner component of an artificial hip joint prosthesis is manufactured by machining of UHMWPE bar, made of ram extrusion process. Figure 1.6(A)-(D) shows the stepwise technique for the manufacturing of UHMWPE acetabular liners (or acetabular cups). However, this technique leaves residual machining mark on the finished bearing surface, as shown in Figure 1.6 (E), leading to undesirable consequences like formation and detachment of platelet-like flakes from initial machining marks [27], [28] . Some researchers aimed to conduct a manufacturing process of UHMWPE liner using compression moulding process, converting the UHMWPE powder into a solid product [29], [30]. Both these techniques are based on uniaxial processing condition, leading to anisotropic material properties and inborn defects like micro-voids, weak bonding and fusion defects as shown in Figure 1.6 (F) and Figure 1.6(G) [28], [31].

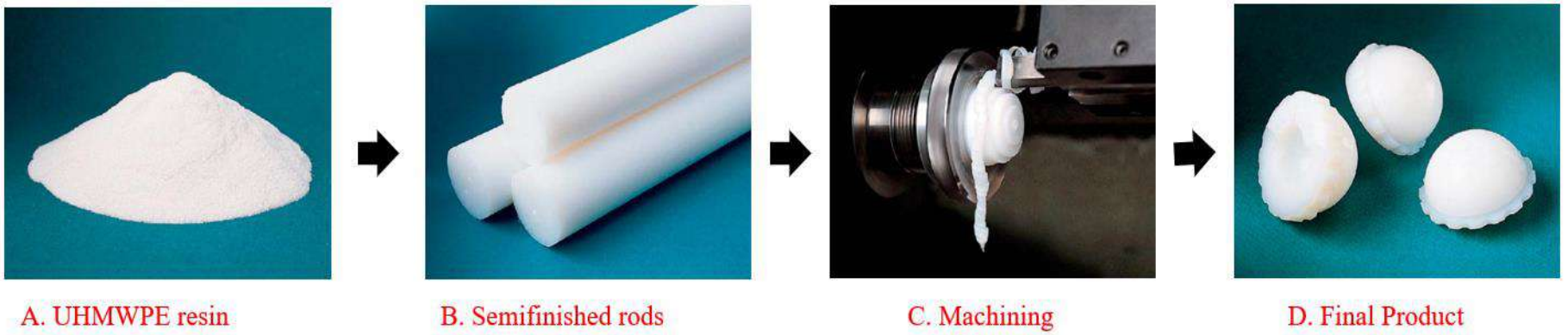

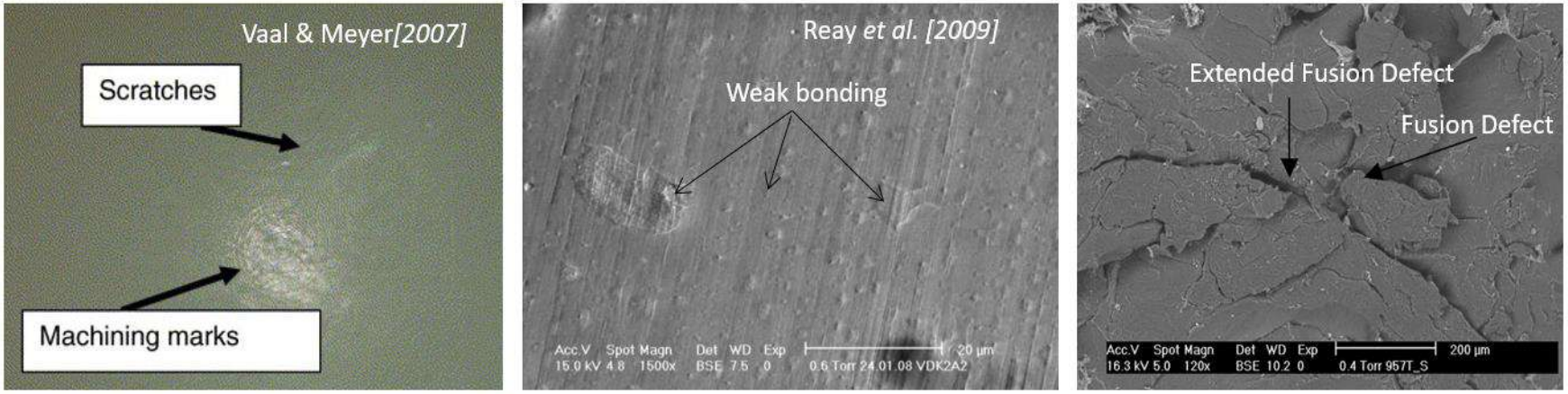

Figure 1.6*. Conventional manufacturing technique for UHMWPE acetabular liners for THR (A) UHMWPE resin powder (B) Ram extruded polymer blocks (C) Shaping into acetabular liner by machining of rods (D) Finished UHMWPE acetabular liners [40]*

Defect induced in UHMWPE products due to conventional manufacturing techniques (E) Residual Machining marks and scratches on bearing surface [28] (F) weak bonding (G) fusion defects [31]

1.3.2. Reasons of failure of UHMWPE liners

Though different combinations of materials are used in Total hip replacements (THR), the artificial hip prosthesis implantation is not once in a lifetime procedure, and the chances of revised surgery may vary depending on the lifestyle, activities and other post operative factors for a patient. THR may fail in various ways and the pie chart of major issues responsible for revision surgeries is shown in Figure 1.7.

The failure could be due to infection, aseptic loosening, dislocation, or a Periprosthetic fracture [28]. However, more than 65% of the implanted UHMWPE acetabular liners are found to fail due to lack of mechanical integrity or strength. Some of the retrieved liners are shown in Figure 1.8, indicating their modes of failure.

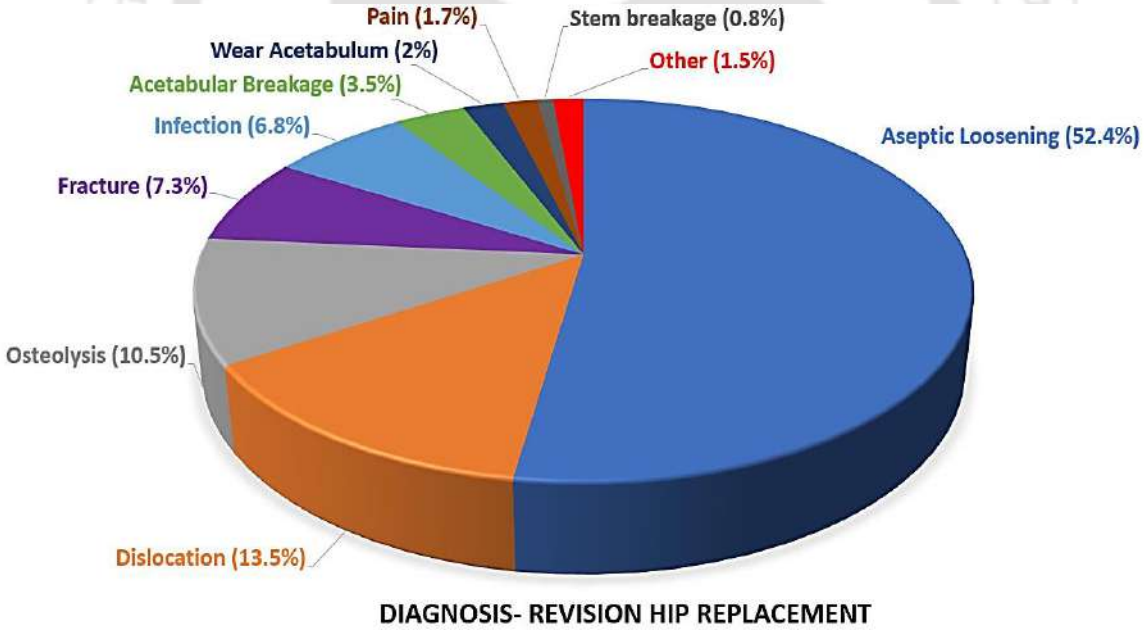

Figure 1.7. *Statistics of diagnosis resulting in revision surgery hip replacement [28]*

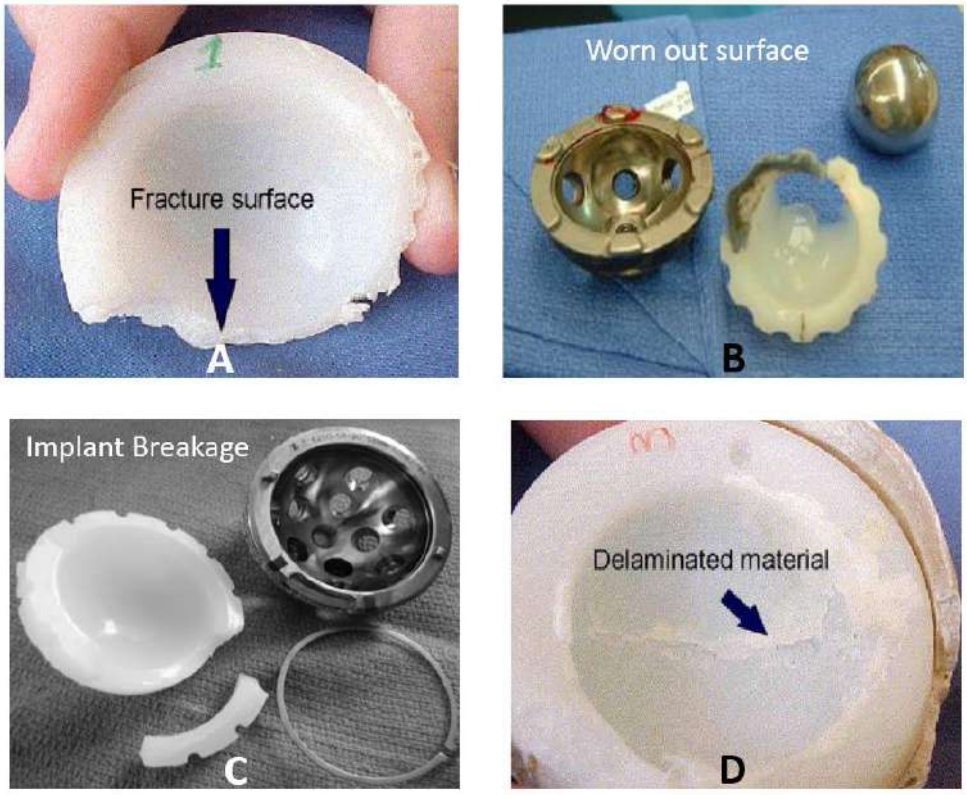

***Figure 1.8**. Different modes of failure of a polymer acetabular liners (A) Surface fracture [28](B) Worn-out surface [Bezwada et al. (2012)] (C) Implant Breakage [Stephen et al. (2010)] (D) Delamination of material [28]*

Since the early 1960s, UHMWPE has been used as a major bearing surface in total hip and total knee joint prostheses. UHMWPE possesses superior mechanical toughness and wear resistance over most other polymers and its rate of wear is approximately 0.1 mm/year against a 32 mm femoral head, when it is used as an acetabular component in total hip replacement. However, recent studies reported that wear debris produced from UHMWPE, though very small in quantity, causes adverse tissue biological response which results in gradual bone absorption known as osteolysis [11], [32], [33].

A clinical consequence of debris-induced osteolysis is loosening of the prosthesis and discomfort to the patient which eventually led to revision surgery. Therefore, to ensure the long-term success of the prosthesis, the quantity and the rate of UHMWPE wear debris generated under *in vivo* condition must be minimized. Wear results when surfaces produce local mechanical damage and unwanted loss of material resulting to the generation of wear particles. Conventional wear includes fatigue, and interfacial or bearing surface wear. Hence, a comprehensive investigation on wear in THR is essential for approaching any research work in this field.

1.3.3. Wear in UHMWPE

A wear is the microscopic material removal process from a surface. Wear mechanism can be classified according to its fundamental features and the morphology of the bearing surfaces. The prosthesis functioning condition and the surface damage during wear are characterized by the wear modes. Wear scheme can broadly be classified under two main categories, viz. single-phase and multiphase wear. Material removal from wearing surfaces due to movement of a solid, liquid or gas relative to a sliding surface is categorized as single-phase wear. In addition, there is a carrier for a second phase (particles, asperities, etc.) that actually produces the wear, it comes under multiphase wear. However, the wear mechanisms commonly found in an artificial hip joint are Adhesive, Abrasive, Fatigue, Fretting and Corrosive.

1.3.3.1. Abrasive wear

Abrasive wear, schematically shown in Figure 1.9(A1), is observed due to hard particles or hard protuberances that are forced to move against and along the solid surface. It is also defined as damage to the solid surface that generally involves progressive loss of material and is due to relative motion between that surface and a contacting substance or substances.

1.3.3.2. Adhesive wear

Adhesive wear is generated by the sliding of one solid surface along another surface. It occurs when the asperities on mutually opposing surfaces become fused together and are then subsequently ruptured because of their relative motion as schematically shown in Figure 1.9(B1).

1.3.3.3. Fatigue wear

Fatigue wear is the progressive and localized structural damage that occurs when a material is subjected to normal cyclic loading as schematically shown in Figure 1.9(C1). It exists in macroscopic and microscopic form. The macroscopic form can occur in non-conforming machine elements in the form of pitting or rolling contact fatigue. The main forms of this type of wear are so severe as to lead to failure. Fatigue wear on a microscopic scale is similar to that of the above described except that it is associated with individual asperity contacts rather than the single large region.

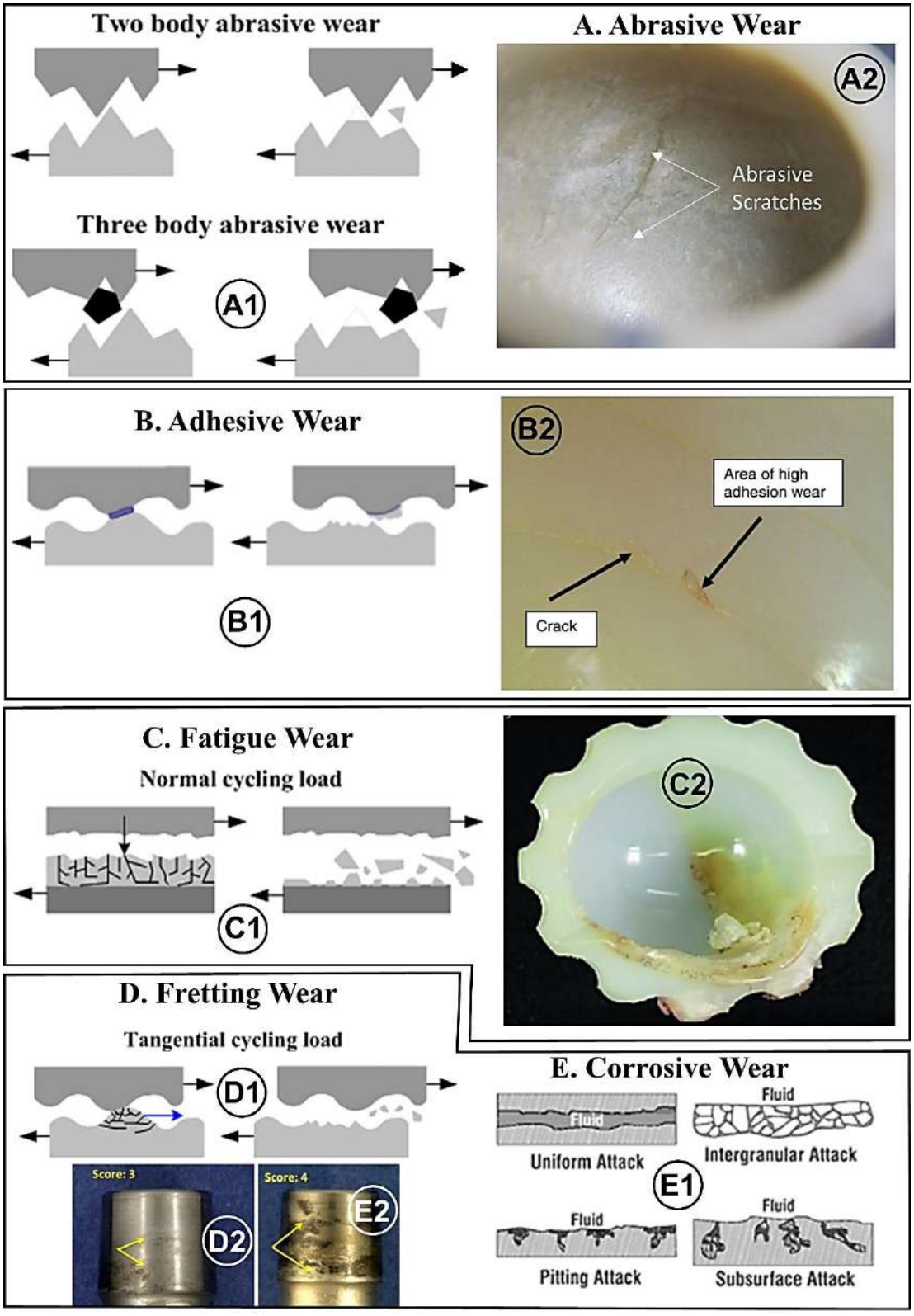

Figure 1.9. *Schematics of different wear mechanism found in THA (A1) Abrasive wear Mechanism (A2) Abrasive wear found in retrieved UHMWPE liner (B1) Adhesive wear Mechanism (B2) Adhesive wear found in retrieved UHMWPE liner (C1) Fatigue wear mechanism (C2) Fatigue wear found in retrieved UHMWPE liner (D1) Fretting wear Mechanism (D2) Fretting wear found in retrieved metallic stem neck (E1) Corrosive wear mechanism (E2) Corrosive wear found in retrieved metallic stem neck [www.substech.com],* [28]

1.3.3.4. Fretting wear

Fretting is the small amplitude oscillatory movement that may occur between contacting surfaces as shown in Figure 1.9(D1), which are usually at rest. The movement is the result of an external vibration, and it is a consequence of the cyclic stress to which one of the contact members is subjected causing another and usually more damaging aspect of fretting.

1.3.3.5. Corrosive wear

Corrosive wear occurs as a result of a chemical reaction on a wearing surface; the most common form of corrosion is oxidation; corrosion products, usually oxides, have shear strength different from those of the metal wearing surfaces from which they are derived. The oxides tend to flake away, resulting in the pitting of working surfaces as schematically shown in Figure 1.9(E1).

Though all kind of wear mechanisms mentioned above are observed in UHMWPE liners during its usage as shown in Figure 1.9 (A2-E2), majority of the retrieved liners are found to undergo primarily abrasive and adhesive wear mechanism, [34]. Some of the components showed indication of micro-contact fatigue damage, as evidenced by micro-pitting, [35]. In addition to different modes of wear, the implant materials are also expected to suffer fretting wear under cyclic working load for considerably long duration of usage and degrade in different ways in the very corrosive environment of the human body fluids [36], [37].

1.4. Preclinical wear test of the bearing material

After the success of THR, it has been applied to younger and more active patients. The need of solving or reducing wear problems is of primary importance as the wear products of hip implants can cause adverse tissue reactions leading to massive bone loss around the implant and consequently loosening of the fixation, hence reduce the life of the joint. Tribology research leads to greater implant efficiency, better performance, fewer breakdowns, and significant savings. Undoubtedly the biomaterials play an important role, and consequently *in vitro* tests for such materials give greater confidence. The objective of wear evaluation is to determine the dependence of wear rate on the test conditions (i.e.,

load, range of motion, lubricant and temperature). To obtain realistic results, a wear test can be performed to reproduce *in vivo* working conditions. The degree of reliability of these tests depends on how accurately the conditions of a prosthetic implant in the human body are recreated.

1.4.1. Wear testing devices

Wear resistance of surfaces not being an intrinsic property of the parent material, depends strongly on system variables such as environment, operating condition, type of counter face etc. Bearing materials developed for THR should ideally be characterized based on the wear characteristics of a device, which can simulate the tribological condition encountered by human hip joint, where the undesirable variation in material properties affecting the wear process could be identified and eliminated. A wide variety of machines are developed to characterize these materials [38].

A tribometer provides simulation of friction and wear under controlled conditions. Wear and friction are very sensitive to variables like load, temperature or humidity. Therefore, it is important to provide an apparatus where all these factors can carefully be controlled and monitored. Wear screening devices shown in Figure 1.10(A) are capable to evaluate exclusively the intrinsic properties of a material. Pin-on-disc and ball-on-disc are possibly the most widely used rotary tribometers, where a pin or a ball is pressed against a rotating disc on its flat surface making a plane or point contact, respectively. These kind of tribometers are commonly used to evaluate friction, abrasive wear and adhesion of any rotating test setup. When the pin is pressed against the perimeter of a rotating disc, it is called a block-on-ring device, generally used to assess fatigue wear in linear contact. Ball-on-plate and block-on-plate are linear sliding tribometers with a point or plane contact, respectively, and are typically used to quantity friction, wear, and adhesion of any reciprocating test setup. Vee block tribometer can be utilized to measure extreme pressure properties fluid lubricants in addition with sliding friction in linear contact. Tribometers can produce quick results using simplified specimens rather than actual prosthetic joints, hence, incapable to look into their distinguishing morphological aspects. So, influence of geometry on the lubrication or contact stress is required to be tested.

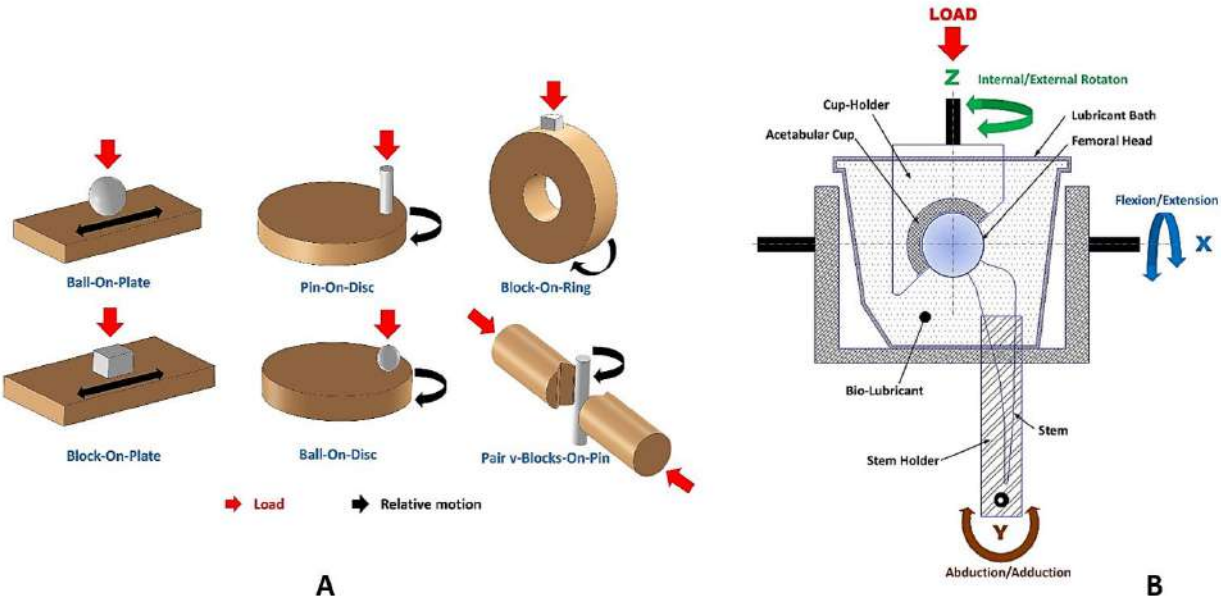

Figure 1.10. *(A)Some of the most popular wear screening devices [www.face-kyowa.co.jp] (B) Schematic Diagram of a Hip Joint wear Simulator [39]*

Hip joint wear simulator, as schematically shown in Figure 1.10(B), is a device where the appropriate test conditions cause the prosthesis to wear in a manner substantially equivalent to that of experienced by a patient. In order to accomplish the same, the wear simulator will typically apply a set of motions and loads under the lubrication condition, which create tribological conditions comparable to those occurring under *in vivo* state. The introduction of the engineering approach towards the TJR showed significant progress at the end of the 20th century. The joint simulators have been developed to replicate the biomechanics of human joints in controlled conditions in order to measure the rate of wear of the proposed material and its coefficient of friction. A hip joint simulator can be classified according to the DOF they reproduce. A *Single-axis* hip simulator mimics only flexion/extension movement while a *Two-axis* simulator reproduces flexion/extension movement and abduction/adduction motion or flexion/extension and inward/outward rotation. *Three-axis* simulator attempts to include full performance criteria such as flexion/extension, abduction/adduction movements and inward/outward rotation.

1.4.2. Inevitability of a hip joint simulator

Discovery of the importance of multi-directional motion in the process of wear was a major breakthrough for understanding the wear mechanisms of UHMWPE. Wear rate of UHMWPE produced by the pin-on-disc by generating linear-tracking motion was found to

be extremely small, typically two-three orders less in magnitude when compared with clinical results. Wear rates produced by the multi-directional motion hip joint simulators are found to be comparable with the average results reported in the literature in case of TJR. Thus, the mechanistic and morphological origins of microscopic wear debris generated from UHMWPE articular surfaces in total joint replacement prostheses cannot be investigated without a hip joint simulator due to its very complex multi-axial motion/loading nature at the articular surfaces in total joint replacements.

1.5. Motivation of the present work

The most common form of arthritis, known as degenerative arthritis or osteoarthritis, usually affects hip, knee and spine as they are heavy load-bearing joints. More than 250000 total hip arthroplasty (THA) and 500000 total knee arthroplasty (TKA) surgeries were performed annually in USA alone [40], [41] and the number of total joint replacements will increase exponentially in next twenty years as postulated in Figure 1.11(A) with the percentage distribution of arthroplasty procedures in Figure 1.11(B). Though the total hip replacement registry is not maintained properly in India, we can get an idea about the exponential growth in the number of THR procedures during 2006-2018 from Figure 1.11(C) published by Indian society of hip & knee surgeons (ISHKS) in 2019. During this period, a total 17124 number of THR procedures are registered in India starting with less than 100 surgeries in 2006, which are exponentially grown to 2500 surgeries in 2016.

THA was originally intended for older patients, but its remarkable success made it popular for young and much more active patients and the current age distribution of hip arthroplasty procedures is shown in Figure 1.12(A). Consequently, the expectation from a THA in terms of life as well as performance has significantly increased not only for pain relief but also physically demanding lifestyle without the need for a revision. Revision surgeries resulting from the wear of acetabular liner itself crossed 10000 per year [42].

Though different combinations of materials are used in THR, the artificial hip prosthesis implantation is not once in a lifetime procedure, and the chances of revised surgery may vary depending on the activities, lifestyle and other post-operative factors of a patient. Recent studies reported that wear debris produced from UHMWPE, though very small in quantity, causes adverse tissue biological response, which results in osteolysis due to gradual bone absorption [11], [32], [33].

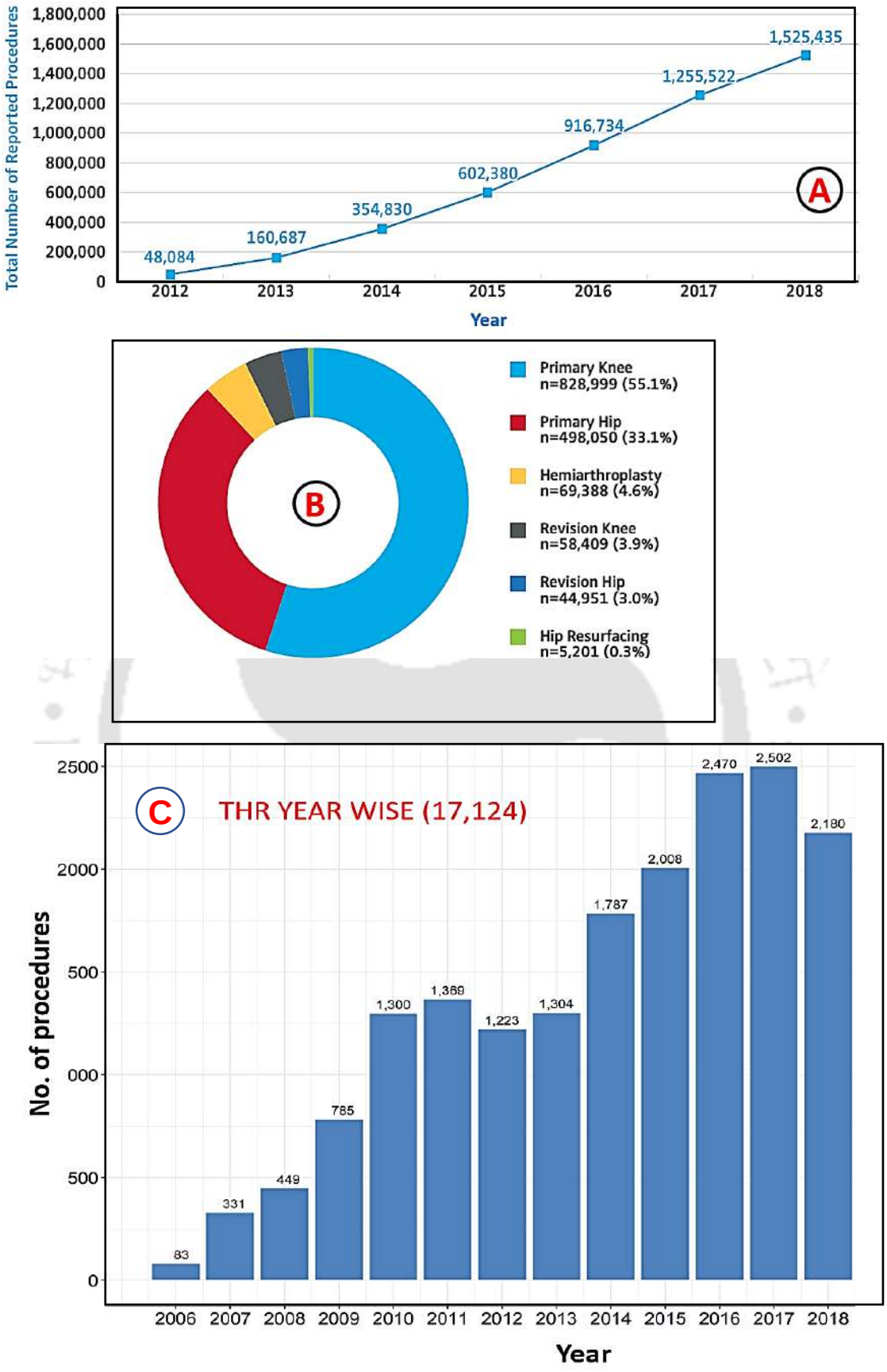

Figure 1.11*.(A)Cumulative THR procedural volume 2012-18 in USA (B) Distribution of Arthroplasty Procedures 2012-18 in USA* [43] *(C) Year wise THR procedures in India during 2006-2018 [ISHKS 2019]*

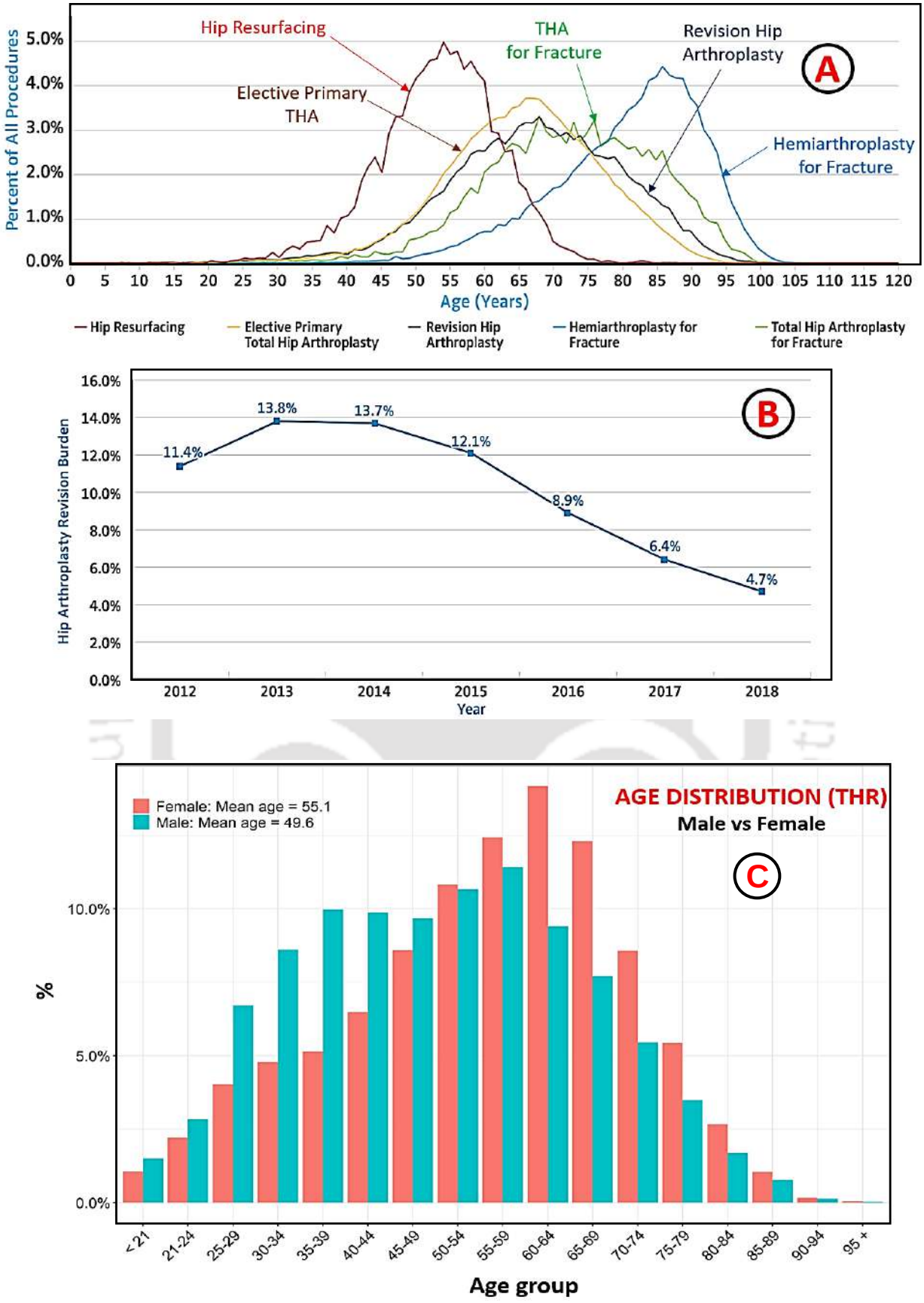

Figure 1.12. *(A)Age distribution of Hip arthroplasty procedures 2012-2018 (B) Revision burden of THA 2012-2018 [43] (C) Age distribution of Indian patients undergone THR surgery during 2006-2018 [ISHKS 2019]*

Aseptic loosening of the prosthesis due to debris-induced osteolysis causes discomfort to the patient and eventually lead to revision surgery. Hence, the number and the rate of UHMWPE wear debris generated under *in vivo* environment must be minimized to ensure the success of the prosthesis in long-term basis. Revision burden is the number of revision surgeries performed in a year divided by the total number of primary and revision surgeries performed in that same year, as defined by American joint replacement registry (AJRR), and it is perceived as the crude measure of arthroplasty success in a joint registry. According to AJRR, between 2012 and 2018, there were 44,951 hip revision surgeries out of a total of 498,050 primary metal-on-polyethylene (MoP) total hip arthroplasty procedures, leading to an overall revision burden of 9% [43]. During this interval, 12,586 'Linked patients' were registered and 70% of them went through revision surgeries in less than one year of their primary surgery even after the performance of MoP THR has been further enhanced by cross linking the polyethylene and stabilizing the same using suitable antioxidants, however, it is not reflected in the revision burden published in Figure 1.12(B).

Though the total hip replacement registry is not maintained properly in India, we can get an idea about the age distribution of the patients undergone THR procedure during 2006-2018 from Figure 1.12(C) published by ISHKS in 2019. The average age of Indian male patients is reported to be 49.6 years whereas, that of Indian female patients is found to be 55.1 years with maximum number of patients in the age group of 55-65 years. It is also reported that the number of primary and revision surgeries to be performed during 2005 and 2030 are expected to increase by 673% in USA and the revision surgeries in THA would reach by 90,000 in 2030 corresponding to an increase of 123% in comparison to that of 2005 [41].

This alarming statistical data clearly indicate the severity associated with the problem and thus a high-end engineering solution is needed to address the failure-related issues to ensure the longevity of the implant [28], [44]. In order to eliminate the failure issues associated with the polymeric acetabular liner, the requirement for advanced materials continues and the UHMWPE-based composite materials have been drawn the prime interest in this case. The researchers are still in search of the next generation bearing material for the purpose and facing lots of challenges in the authentic pre-clinical evaluation of the prosthetics as per international guidelines which motivated the present work.

1.6. Organization of Thesis

This thesis contains **7** chapters.

Chapter 1: INTRODUCTION discusses about the requirement of novel bearing materials for total hip arthroplasty (THA) based on the present scenario in total joint replacement (TJR) industries, different types of FDA approved bearing combinations in THA with their history of evolution. The advantages and limitations of all the commercially available bearing combinations are also highlighted including the current gold standard metal-on-UHMWPE. Later, the motivation behind the present work and the need of UHMWPE based composite materials in place of pure polymer as the bearing liner in TJR are also highlighted. The importance of using a hip joint simulator for the pre-clinical evaluation of THA *in vitro* is also discussed, based on whose performance the clinical life of a newly developed prosthesis is predicted.

Chapter 2: LITERATURE REVIEW deals with the earlier research done on UHMWPE and its composites intended for TJR using different bio-compatible fillers including MWCNT based on the published literature, which gives adequate information on synthesis of UHMWPE composites, experimental details, processing techniques, characterization of synthesized composite samples. This chapter also discusses about the techniques and international guidelines for pre-clinical evaluation of a material to be proposed for TJR. Based on these studies, it reports on the different technical gaps noticed from the available literature and accordingly, the objectives of the proposed thesis work are framed.

Chapter 3: PROCESSING OF UHMWPE-BASED SAMPLES AND THEIR CHARACTERIZATION gives the detailed description of raw materials used in the present study, chemical treatment of MWCNT, techniques used for mixing UHMWPE and MWCNT powder in different weight ratio. Thereafter a novel technique based on isostatic compaction followed by sintering of UHMWPE and UHMWPE-MWCNT powder for processing pure polymer and composite samples is explained with different characterization techniques involved with the outcome and discussion on UHMWPE-MWCNT composites

characterized through qualitative and quantitative analysis. The mechanical strength of the composites and the influence of MWCNT concentration on the polymer are reported in detail. The improvement of hardness, compressive properties, tensile properties and tribological characteristics of the composites over virgin polymer is explained in detail. The influence of MWCNT and its concentration on the properties of composites are explained with the help of physical and structural properties. In addition, the influence of different processing parameters on sintering kinetics and mechanical properties of UHMWPE are studied and the trends noticed on the characteristics of the polymer are discussed in detail. The superior characteristics in terms of hardness, mechanical integrity and tribology of the composites obtained from the present study are compared in order to understand the influence of compaction pressure, sintering parameters and MWCNT concentration for their optimization.

Chapter 4: DEVELOPMENT OF ACETABULAR LINERS explained an ingenious machining free manufacturing technique for the development of UHMWPE and UHMWPE-MWCNT composite based acetabular liners and techniques used for the evaluation of their inborn characteristics. The procedure followed in the present study at different stages is explained with the help of schematic flowcharts and pictorial representations, wherever it is required.

Chapter 5: ESTABLISHMENT OF SIMULATED *IN VIVO* **CONDITION** elucidates an orbital bearing machine (OBM) simulator to apply the tribological parameters to a THA as per international guidelines having the simplicity of a wear screening device. This chapter explains design of a modular mechanism based on an analytical model which can be attached to a conventional *Pin-On-Disc* tribometer to transform it into a *Ball-On-Cup* tribometer for testing the actual prosthetic joints as per **ISO 14242-3** guidelines. In addition, this chapter also explains the processing and experimental validation of a rheological analogue of synovial fluid (SFA) along with the raw material used. This SFA is meant to be used as the lubricant in *Ball-On-Cup* tribometer for testing of total hip arthroplasties (THA) for the fulfilment of recreating the simulated *in vivo* condition to imitate the realistic contact stresses and wear mechanism in them under *in vitro* state.

Chapter 6: WEAR TESTING describes how a Pin-On-Disc tribometer is used to evaluate the tribological characteristics of UHMWPE and UHMWPE-MWCNT for a rapid comparative study on their frictional coefficient and linear wear rate against a SS 316L disc under different lubricating conditions. The 'Ball-On-Cup' tribometer, on the other hand, is used to conduct accelerated protocols for testing the newly developed acetabular liners against SS 316L femoral heads under conditions approximating those occurring in the human body with SFA lubrication for a quantitative wear measurement. Morphology and size distribution of wear debris produced during the tribology tests are evaluated using SEM to elucidate the wear mechanism involved in each case to compare them with that of *in vivo* condition. Finally, this chapter reported the improvement in the wear resistance of UHMWPE acetabular liners against stainless-stell (SS) femoral head after the usage of MWCNT as filler with optimum concentration.

Chapter 7: CONCLUSIONS summarizes the overall work done and important findings of the present thesis work. Major conclusions and future scope of the work are reported in this chapter.

भारतीय प्रौद्योगिकी संस्थान गुवाहाटी
Indian Institute of Technology Guwahati

CHAPTER 2

LITERATURE REVIEW

2.1. Introduction

Adverse reaction of wear debris generated with surrounding tissues often lessens the prescribed lifespan of UHMWPE joints. Many attempts were made to find an alternative bearing material having improved wear resistance and performance in the past decades. The literature review section discussed about several such efforts made by many researchers to enhance the mechanical properties and wear resistance of UHMWPE, including gamma irradiation for promoting the cross-linked structure to improve wear resistance, vitamin E blending to protect the UHMWPE from the oxidation, bio-compatible filler reinforcement for improving mechanical performance, and surface texturing to improve lubrication. At the same time, international guidelines for testing the newly developed materials and the worldwide major breakthroughs in the development of hip joint simulators are also discussed along with different lubricating conditions used for *in vitro* characterization of THA.

2.2. Improvements on the wear resistance of UHMWPE

Following section discusses different studies on the modification of UHMWPE, like crystallinity, cross-linking and reinforcement, which are aimed to enhance the mechanical properties, and surface engineering to improve its wear resistance and bearing characteristics.

2.2.1. Crystallinity of UHMWPE

The mechanical properties of UHMWPE are greatly influenced by its crystallinity, which is directly related to the molecular arrangement. Thus, the wear performance of UHMWPE can be improved by altering its structure and the degree of crystallinity.

The degree of crystallinity in UHMWPE can be calculated by various methods, such as volumetric analysis, thermal analysis using DSC, X-ray diffraction, infrared, Raman spectra.

However, each of these approaches does not yield identical outcomes, as they measure different morphological structures and physical parameters [45].

Differential Scanning Calorimetry (DSC) is utilized to calculate the degree of crystallinity ($\boldsymbol{X}_C$) of UHMWPE as per the Equation 2.1.

$$X_C(\%) = \left(\frac{\Delta H}{\Delta H_{100}}\right) \times 100 \quad \text{... (2.1)}$$

where ΔH is the heat of fusion and ΔH_{100} = 293 J/g is the melting enthalpy of polyethylene at 100% crystallinity [46]. X-ray diffraction is also a widely used method to evaluate the $\boldsymbol{X}_C$ in UHMWPE. The diffraction profile is separated into two parts. The sharp peaks represent the diffraction of crystallites, and the broad peaks represent the scattering of amorphous phase. The measured intensity of the scattering can be used to calculate the X_C in UHMWPE using Equation 2.2. [47].

$$X_C(\%) = \frac{I_C}{I_C + I_A} \times 100 \quad \text{... (2.2)}$$

where, I_C and I_A are the scattered intensities for the crystalline and the amorphous phases of the polymer, respectively.

Parasnis and Ramani [48] experimentally showed that for obtaining maximum stiffness and $\boldsymbol{X}_c$ in compression moulded UHMWPE, the processing pressure must be within a narrow range. An elevation in the applied pressure at the melt temperature of UHMWPE (140°C) from 7.8 MPa to 15.6 MPa triggered the $\boldsymbol{X}_c$ to increase from 54% to 61%. However, further increase in the applied pressure at the melt state to 23 MPa caused the crystallinity to fall at 49%. Edidin *et al.* [49] estimated the degree of crystallinity of UHMWPE, which was found to be in the range of 39% and 75% and showed the lack of full crystallization imposes a limitation on its mechanical properties enhancement. Karuppiah *et al.* [50] kept UHMWPE samples at 110 °C, the recrystallization temperature of the polymer, for 48 h in order to allow the chains of UHMWPE to fold and form crystalline lamellae. As a result, surface crystallinity of UHMWPE was found to improve resulting in an increase of scratch and wear resistance, which is attributed to an increase in hardness and elastic modulus. Maksimkin *et al.* [51] proposed a new technique to get UHMWPE oriented films with high drawability and small concentration of a solvent as compared with conventional

methods. Increase of X_c in UHMWPE became noticeable with a film draw ratio (DR) beyond 18 as per DSC analysis. Very high X_c ~ 94% and well defined fibrillar structure were achieved for the films fabricated with DR 26 and DR 35. Khalil *et al.* [52] reported that X_C of polymers depends on its thermal history and identified many factors significantly affect the mechanical properties of laser sintered UHMWPE, such as powder bed temperature and laser energy, influencing the X_C in UHMWPE**.** They studied the influence of heating on the crystallisation of the UHMWPE and the degree of crystallinity of UHMWPE was observed to be increased with super-cooling. Dong *et al.* [53] prepared UHMWPE samples by sintering assisted with isothermal crystallization and studied the effect of sintering temperature in the range of 170°C-220°C on its crystallinity. A wide range of X_c and T_m for UHMWPE are generated by adjusting a number of factors, such as the nascent entanglement degree, sintering temperature, crystallization time and molecular weight of UHMWPE resin to survey the association between mechanical property and crystalline structure judiciously. In conclusion, a linear correlation between X_c and tensile yield strength was manifested validly and reliably.

2.2.2. Cross-linked UHMWPE using gamma irradiation

High dose of Gamma irradiation results in crosslinking the UHMWPE molecular structure, which helps to improve the hardness and wear resistance. Electron beam can also be used as a radiation source. The ionising radiation generates free radicals on polymers, some of them recombine to form the crosslinking between the molecular chain and reduce the chain stretch of the material. As a result, the plastic deformation of the material is found to be reduced significantly. Green *et al.* [54] reported that the particles released from an irradiated UHMWPE, though much smaller in size compared to those from a non-irradiated one, can be biologically more active and increases the probability of osteolysis. Muratoglu *et al.* [55] presented a novel method of increasing the cross-link density of UHMWPE which is irradiated in air at an elevated temperature with a high-dose-rate electron beam and subsequently is melt-annealed. This treatment improved the wear resistance of the polymer, as tested in a hip simulator, while maintaining its mechanical properties. This method led to the absence of detectable free radicals in the polymer, and it led to excellent resistance to oxidation of the polymer. Sreekanth and Kanagaraj [56] prepared UHMWPE sheets by compression moulding which were irradiated in air by Co^{60} γ-ray source and observed an increasing trend in hardness of UHMWPE with irradiation dosage. They reported 20% increase in Vickers hardness and 31% reduction in wear volume of virgin

UHMWPE with an irradiation dosage of 100 kGy. However, a high radiation dose on polymer accelerates the oxidation, and it increased the probability of material failure as a result of migration of excessive free radicals to the interface (crystalline/amorphous) and reaction with diffused oxygen. It is expected to cause oxidation and brittleness in the polymer, which influenced to increase the wear rate and wear debris generation. Oral *et al.* [57] concluded that irradiated, vitamin E–doped, and terminally γ-sterilized highly cross-linked UHMWPE exhibited high wear resistance with improved mechanical properties and fatigue toughness compared to first-generation highly cross-linked UHMWPE (irradiated and melted). If the material is heated below its melting point, it was found to preserve the crystallinity and mechanical properties, but excess free radicals are not eliminated completely. Oral and Muratoglu [58] incorporated vitamin E into irradiated UHMWPE in a two-step diffusion process to obtain a second-generation crosslinked bearing surface. This technique improved the mechanical and fatigue strength without sacrificing wear resistance and oxidative stability against accelerated and real time ageing *in vitro*.

Various alternatives to quench the free radicals and avoid oxidation include thermal treatment after irradiation. Heating the polymer to above its melting point eliminates the crystalline regions and the free radicals have good mobility. This combined effect improves the oxidative stability of the irradiated UHMWPE but reducing its crystallinity.

2.2.3 Vitamin-E-stabilised UHMWPE

As stated earlier, the free radicals induced by the irradiation process in the crystalline phase make the material susceptible to oxidation and consequently reduces the mechanical properties of UHMWPE. Vitamin E, being an antioxidant, found to improve the oxidative resistance and the mechanical and fatigue strength of cross-linked UHMWPE by stabilising the radiation-induced free radicals.

2.2.3.1. Methods of Vitamin E Blending

There are two standard methods for incorporating vitamin E in UHMWPE. The first method is diffusing vitamin E into irradiated UHMWPE using a two-step process viz., post radiation doping with vitamin E and homogenization into inert atmosphere. Oral *et al.* [59] made highly crosslinked UHMWPE blended with the lipophilic antioxidant α-tocopherol and found similar oxidation and wear resistance with contemporary first-generation UHMWPE for ~100-kGy irradiated α -T-doped sample after 5 weeks of accelerated aging in 80°C in

air but higher fatigue resistance. Brad *et al.* [60] analyzed the diffusion behaviour of vitamin E through UHMWPE and developed an alternative oxidation and wear resistant bearing surface in the form of vitamin E-doped 100-kGy irradiated UHMWPE, homogenized in argon gas at 120°C to ensure full vitamin E penetration. Accelerated aging decreased the UTS and fatigue crack propagation resistance of conventional UHMWPE by 32% and 51%, respectively. However, the changes in fatigue crack propagation resistance and UTS in vitamin E– doped UHMWPE were not significant after accelerated aging.

The second method is blending a liquid antioxidant into the UHMWPE powder before the mixture consolidates into a near-implant form and radiation crosslinking is performed. Lerf *et al.* [61] tested cross-linked UHMWPE with five different concentrations of vitamin E (nil to 1.0%) following ageing protocol under pressurized oxygen at 70 °C, as defined in the ASTM F 2003 standard with a prolonged period of 60 days and showed a vitamin E concentration as low as 0.05% is effective to protect irradiated highly cross-linked UHMWPE against oxidation when it was directly exposed to oxygen. This method is easier and takes shorter time to obtain uniform vitamin E concentration throughout the implant compared with the first method. However, the presence of vitamin E during the irradiation process reduces the efficiency of UHMWPE crosslinking, because vitamin E itself can act as a free radical scavenger.

Therefore, the concentration of vitamin E and the radiation dose must be optimized to achieve a good wear and oxidation resistance. More recently, some studies showed that the mechanical strength and fatigue resistance of vitamin E-stabilised UHMWPE can be further improved by some additional treatments. Oral *et al.* [62] achieved further improvement in the wear resistance of vitamin E-stabilised irradiated UHMWPE by spatially manipulating the vitamin E concentration throughout the implant and limiting cross-linking to the surface. Fu *et al.* [63] showed improved tensile strength, impact toughness, wear resistance and oxidation resistance by high temperature melting after the introduction of vitamin E into UHMWPE.

2.2.3.2. Effect of Vit. E on Tribological and Mechanical characteristics of UHMWPE

Vitamin E-stabilised UHMWPE has the ability to provide improved tribological characteristics compared with conventional UHWMPE [60], [62], [63]. Wear test results indicated that the wear rate of vitamin E-stabilised UHMWPE in clean serum and serum with third-body particles had a 4-fold to 10-fold decrease from that of conventional

UHMWPE [59], [61]. Teramura *et al.* [64] compared the wear behaviour between vitamin E-stabilised UHMWPE and conventional UHMWPE using a knee joint simulator. The results indicated that 0.3 wt.% vitamin E-stabilised UHMWPE had ~ 34% lower wear volume than that of the untreated material. It was believed that vitamin E addition could prevent delamination caused by oxidation and fatigue, and therefore, it influenced the lifespan of the UHMWPE component significantly. The mechanical properties of vitamin E-stabilised UHMWPE are affected by its concentration. When vitamin E concentration is in a range of 0.01–0.05 wt.%, it has a negligible effect on the mechanical properties of unsterilized and gamma sterilized UHMWPE. Wolf and Lederer [65] observed that the elastic modulus and tensile strength of 0.8 wt.% vitamin E stabilised material were 20% lower than that of the virgin and gamma sterilized UHMWPE, while the elongation and impact strength of it remained unchanged.

2.2.4. Surface modification of UHMWPE

Surface modification of UHMWPE was found to improve the function and lifetime of the artificial joints. This section reviews the commonly used surface modification method such as surface texturing technique for the improvement of the mechanical properties and wear resistance of UHMWPE.

2.2.4.1. Surface Coating

Surface coating techniques involve depositing a thin film on the base material. Due to presence of coating, range of features like osteoinduction, hydrophilicity, mechanical and biological properties, surface properties and bio-tribological characteristics are observed to be improved [65]-[70]. Chu *et al.* [66] followed the plasma spraying implantation or deposition techniques to modify the surface in order to enhance the surface properties such as wear resistance, and hardness. In the process, a thin layer of a hard metallic material is coated on the bulk material to improve its properties. Balani *et al.* [67] have addressed issues like successfully distributing multiwalled CNT reinforcement in HA coating using plasma spraying to improve the fracture toughness and crystallinity by 56% and 27%, respectively. The culturing of human cells onto CNT reinforced HA coating to elicit its biocompatibility with living cells. Unrestricted growth of human cells has been observed near CNT regions claiming assistance by CNT surfaces to promote cell growth and proliferation. Firouzi *et al.* [68] reported nylon coating on UHMWPE to achieve lower

cytotoxicity, less wear debris-induced osteolysis, and superior mechanical properties compared to neat UHMWPE.

Based on the preliminary results of biocompatibility and mechanical tests, nylon coated UHMWPE was proposed as a novel material in clinical applications. Calderon *et al.* [69] used Zirconium carbon nitride (ZrC_xN_{1-x}) coating with embedded silver nanoparticles as a surface modification option for multifunctional purposes including antimicrobial effect, corrosion resistance and maintaining or even improving their mechanical and tribological performance. Puértolas *et al.* [70] tested hydrogenated diamond like carbon (DLCH) coating on UHMWPE with a good performance on the wear resistance, hardness and biocompatibility. Their study reported a wear rate reduction of approximately 30%, when the samples were surface coated with a thin layer (<20 nm) of DLCH. Ruan and Bao [71] developed a way to improve the compressive and bending strength of UHMWPE fibers. Carbon nanotubes (CNT) and vapor-grown carbon fibers (VGCF) were used to coat the surface of UHMWPE fibers by pyrrole vapor deposition technique.

2.2.4.2. Ion Beam Surface Modification

The ion-beam texturing process is extremely controllable and reproducible to generate either a square or a round pattern using an electron formed screen mesh mask to the surface. This technique avoids the risk of delamination. Hardening and stiffening effects as well as improvement of tribological behaviour and mechanical properties of polymeric materials were reported on UHMWPE by using nitrogen ion implantation. It can also increase the wettability of the surface. Dong and Bell [72] reported a wear rate reduction from 1×10^{-8} mm^3/Nm for the untreated samples to $0.1 \times 10^{-8} mm^3/Nm$ for the Plasma Immersion Ion Implantation (PI^3) treated ones. Traditional ion implantation technique involves line-of-sight processing and thus it is not suitable for the treatment of bone implants with a complex shape and curved surface. To overcome the limitation, PI^3 is used for improvement of mechanical properties of the surface, biocompatibility, bioactivity, antibacterial activity and the wear performance of biomaterials. Powles *et al.* [73] treated the surface of poly-ether-ether-ketone (PEEK) with plasma immersion ion implantation using hydrogen ions. They reported that the modified surface was harder and denser in addition to the greater elastic recovery than the unmodified material. Shi *et al.* [74] explored the surface modification of UHMWPE using the non-line-of-slight PI^3 technique with nitrogen. The tribological behaviour of PI^3 treated UHMWPE against AISI 316L

stainless steel counter face was evaluated using a pin-on-disc tribometer under water lubricated conditions, where the hardness and elastic modulus of UHMWPE were observed to be improved.

2.2.4.3. Laser Surface Texturing

Texturing or surface engineering was accepted as an effective and feasible technique for friction reduction and improvement of wear resistance [74]-[76]. Commonly used surface texturing techniques for UHMWPE are electrical discharge etching and laser surface engineering.

Ito *et al.* [75] formed concave dimples on the surface of the metal femoral head by electrical discharge etching. In a hip joint simulator study, the total amount of polyethylene wear was 7.2 mg in the concave-patterned condition and 23.1 mg in the non-patterned condition. Using experimental and/or simulation methods, many researchers investigated the effects of dimple size, depth and area density on the friction and wear properties of UHMWPE and its counterpart. One common outcome is that the micro-texture increases the load-carrying capacity and the thickness of the joint lubricant film, resulting the reduction of friction and wear. Lopez *et al.* [76] studied load effects when dimple diameter was around 40–50 μm. It was found that under a light load, surface textures on either UHMWPE or its steel counterpart reduced friction. At high load, it was reported that only the textures on the UHMWPE surface could effectively reduce the friction. Wang *et al.* [77] reported that an area ratio in the range of 20–40% was ideal to maximise the total hydrodynamic pressure between the two moving surfaces. When dimples were fabricated on the surface of steel, the area density of 5–15% was effective for friction reduction at a lighter load. If the dimples were textured on the UHMWPE surface, the area density of 30% improved both friction and wear resistance under a water lubricated condition and at a relative high load. It is believed that by applying surface textures on either UHMWPE or steel surface, abrasive wear is reduced by improving the lubrication condition through storing wear particles and lubricant in dimples and by reduction of frictional heating of the sliding surfaces.

2.2.5. Fillers

A wide range of fillers are used to enhance the mechanical and lubrication properties of UHMWPE. An overview of the commonly used filler materials and their effects on the mechanical properties and the wear performance are presented below in detail.

2.2.5.1. Carbon Nanofibers (CNFs)

Owing to the intrinsic properties and cytocompatibility of carbon nanofibers (CNF), incorporation of the same to improve the mechanical properties and wear resistance of UHMWPE received increased attention. Studies on the mechanical properties of CNF reinforced polyethylene revealed that the yield stress, tensile modulus and hardness of the composites are increased by the addition of a certain amount of CNF. Based on hip simulator studies, Wang *et al.* [78] reported that pitch-based carbon fibre reinforced PEEK composite acetabular insert in articulation with a zirconia ceramic head was the excellent bearing combination, where 20% filler content resulted in a 100-fold reduction in the wear rate of the bearing couple compared to that of conventional UHMWPE/metal or UHMWPE/ceramic couple. Galetz *et al.* [79] reported that incorporation of 5 wt.% CNF as a reinforcement in UHMWPE resulted in an approximately 25% increase in the tensile modulus and nearly 30% improved wear resistance compared to the pure UHMWPE, but not so much improvement found at a higher CNF concentration (10 wt.%). The addition of carbon nanofibers resulted in an approximately linear increase in hardness of polyethylene. It was also reported that the mechanical properties of CNF reinforced polyethylene are sensitive to the CNF concentration.

Dangsheng [80] examined the hardness of carbon fibers (CF) reinforced UHMWPE composites and reported that the wear resistance of the composites was increased with CF content under both dry and distilled water lubricating conditions. The friction coefficient of the CF reinforced UHMWPE composites is found to be higher and more stable than that of the pure UHMWPE under dry sliding, whereas an opposite trend was observed under distilled water lubrication conditions. The abrasive wear and drawing out of CF in the wear surface of the composites are dominant in the wear mechanism. Sui *et al.* [81] tried 0.5 wt.%, 1.0 wt.%, and 3.0 wt.% CNF addition into UHMWPE. The tensile strength and tensile modulus of the UHMWPE had highest gain of 16% and 20% respectively at 1.0 wt.% of CNF, whereas a reverse trend was noted at 3 wt.% content. The presence of dispersed carbon nanofibers also led to a significant improvement of wear performance of UHMWPE

material. Borruto [82] proposed an alternative bearing surface made of polyether-ether-ketone (PEEK)/CNF in the field of total hip replacements. The wear tests as per ASTM 99G were performed with a pin on disc tribometer in an air environment under the following conditions: dry condition, demineralised water and human serum as a lubricant. The results observed from the composites demonstrated the high wear resistance of them and thus there was an extremely low quantity of debris generation irrespective of the lubricant used.

Utzschneider *et al.* [83] found that the wear debris of carbon fiber-reinforced (CFR)–PEEK was comparable with UHMWPE in its biological activity. Therefore, CFR-PEEK represented an alternative bearing material because of its superior mechanical and chemical behaviour without any increased biological activity of the wear particles. Wood *et al.* [84] prepared carbon nanofiber (CNF)–UHMWPE composites by paraffin-assisted melt-mixing resulting the improved distribution and dispersion of fillers. By using optimal 35 vol. % UHMWPE to paraffin oil, a final composite having much enhanced wear characteristics was found. With the addition of 0.5–3 wt.% CNF, the wear rate of UHMWPE was decreased by about 57%. However, the presence of agglomeration of reinforcement was reported to decrease the wear resistance. Xu *et al.* [85] reported that HDPE / CNF nanocomposite with 0.5 wt.% of reinforcement and coated with thicker silane coating (46 nm) showed the highest wear resistance with a wear rate reduction of nearly 68% compared to the neat HDPE, while a higher-level CNF addition (3 wt.%) resulted in a higher wear rate. Panin *et al.* [86] prepared UHMWPE/CNF (0.5%) composite by mixing UHMWPE GUR 2122 powder with CNF using ball milling followed by hot pressing. With the CNF loading, ~50% reduction in friction coefficient and ~ 200% increase in wear resistance of neat UHMWPE were observed due to solid lubricant effect of CNF.

2.2.5.2. Graphene

The outstanding mechanical and physical properties of graphene influenced to be used with UHMWPE to prepare a composite component proposed for artificial hip joint. Lee *et al.* [87] reported the Young's modulus, tensile strength, thermal conductivity and electrical conductivity of graphene to be 0.5-1 TPA, 130 GPa, 4840 W/mK and 7600 S/m, respectively. Chen *et al.* [88] prepared graphene oxide (GO)/UHMWPE composites by liquid-phase ultrasonication dispersion followed by hot-pressing with up to 1.0 wt.% of

GO. Yield strength of composite was reported to be increased by 20% with a GO concentration of 0.5 wt.%. Lahiri *et al.* [89] evaluated the wear resistance of the graphene nanoplatelet (GNP) reinforced UHMWPE composite at different concentrations (0.1, 0.5, and 1.0 wt.%) of GNP at three different loads (100, 200 and 300 μN) by scratch test. It was reported that the wear resistance of the material was improved by 4.5 times with 1 wt.% GNP composite in comparison with the pure UHMWPE. The coefficient of friction (COF) was not found to be increased with higher GNP content, and it may be associated to the released graphene during the scratch test, which is expected to lubricate the pathway. Ren et al. [90] studied graphene nanosheet (GNS)/UHMWPE composites prepared by ethanol-assisted dispersion, hydrazine reduction, and hot pressing of up to 2 wt.% GNS. The optimal concentration for the tensile modulus appeared at 0.5 wt.% with an enhancement of 12.8%, while the best result of tensile strength was increased by 23.9% at 0.25 wt.%.

2.2.5.3. Hard Particles

In addition to CNF and CNT, the particle reinforcement using other hard particles was reported to be a very promising method to improve the wear performance of UHMWPE. Xie *et al.* [91] studied the behaviour of compression moulded UHMWPE/quartz composites in the presence of organosiloxane before they are hydrolyzed. The results showed that the organosiloxane acts as a cross-linking agent for UHMWPE and a coupling aid for the quartz particles and the UHMWPE matrix. At low content of organosiloxane, the melting point and crystallinity of the UHMWPE/quartz composite was observed to be increased due to the molecular cross-linking of UHMWPE matrix. At about 0.5 phr organosiloxane while the degree of crystallinity of the composite is at the peak value of 57%, the mechanical properties and the wear resistance of UHMWPE/quartz composites reach their maximum. Wang *et al.* [92] prepared UHMWPE reinforced with Ti powder using the hot-pressing formation method. Hip joint wear simulator studies reported that the said composites against 316L stainless steel in simulated body fluid lubrication at 35 ± 1°C revealed the maximum reduction of 50% in wear rate for the UHMWPE/Ti composite liners at 20 wt.% content of titanium particles, where the abrasive wear and fatigue wear were found to be the failure mechanisms of the test material.

Plumlee *et al.* [93] investigated the wear behaviour and impact toughness of compression-moulded UHMWPE composites having 10 wt. % and 20 wt. % of micron-sized zirconium particles by dual axis wear simulator and Impact Tester. These composites showed

reduction in wear volume up to 36% compared to unfilled polymer retaining its impact toughness. Liu *et al.* [94] studied the UHMWPE filled with the bovine bone hydroxyapatite (BHA), which was prepared by the method of compression moulding. A ball-on-disc wear test was carried out with a Universal Micro-Tribometer to investigate the friction and wear behaviour of the UHMWPE/BHA composites cross-sliding against a Si_3N_4 ceramic ball with human plasma lubrication. For the UHMWPE/ 20%BHA composite, the micro-surface hardness and modulus of elasticity were found to be about 15% and 50% higher, respectively, than that of pure UHMWPE. The ploughing and fatigue fracture were found to be the main wear mechanism for the failure of an implant.

Ge *et al.* [95] conducted a hip joint wear simulator study to investigate the wear behaviour of UHMWPE/natural coral (NC) composites against CoCrMo balls at 25% bovine serum solution lubrication. The micro-hardness of UHMWPE composites containing 30 wt.% natural coral particles is increased up to 18.8 MPa compared to 10.2 MPa of neat UHMWPE, while the wear loss is reduced to 70%. The dominating wear mechanism was noted to be adhesive.

These hard particles can effectively take bearing load to protect the polymer matrix and thus improve the wear resistance of UHMWPE. However, the wear debris generated during the wear test is expected to accelerate the rate of wear.

2.3. Carbon nanotubes (CNT) as filler

Carbon nanotubes (CNT) are becoming a popular choice among researchers for developing a new generation of advanced implant material for its high strength, high aspect ratio, excellent thermal and electrical conductivity, and self-lubricating characteristics [93]-[98]. They are expected to enhance the mechanical properties and wear resistance of UHMWPE significantly, also found to promote bone growth and act as an antioxidant.

2.3.1. Enhancement of mechanical properties

Ruan *et al.* [96] reported an improvement in the UHMWPE toughness with the addition of 1 wt.% MWCNT. For an anisotropic UHMWPE/MWCNT composite films with high draw ratio, an up to 150% increase in strain energy density has been observed together with a simultaneous increase of tensile strength of ~25% and an increase of ductility up to 140%. Zoo *et al.* [97] prepared UHMWPE/MWCNT nanocomposites having different

concentrations of MWCNT (0.1, 02, 0.3, 0.4 and 0.5 wt.%). Monotonous increments in hardness and wear resistance with increasing filler concentration were reported without significant change in crystallinity of UHMWPE. Addition of 0.5 wt.% MWCNT increased its hardness and wear resistance by 12% and 80%, respectively. Kanagaraj *et al.* [98] found good enhancement of mechanical properties with an increase of CNT concentration in high density polyethylene (HDPE)-Carbon nanotubes (CNT) composites. By adding 0.44 vol% of CNT, the Young's modulus and toughness were reported to be increased by 22% and 32%, respectively. Crystallinity of composites also increased without affecting melting point and oxidation temperature of HDPE/ CNT composites. Kanagaraj *et al.* [99] studied the tribological characterization of a compression moulded composite sheet as a function of sliding distance in a ball on plate Tribometer, which produced a linear relation and confirmed significant decrease in wear volume and wear coefficient with an addition of CNT in the polymer.

Amoli *et al.* [100] prepared UHMWPE/MWCNT nanocomposites via in situ polymerization with Ziegler–Natta catalytic system for improved dispersion and distribution of CNT throughout the polymer matrix. Yield stress of sample with 1.5 wt.% MWCNT was reported to be about 1.5 times higher than that of pure PE, which was decreased slightly with further increment of MWCNT concentration. Tensile strength achieved its peak at 0.5 wt.% of MWCNT addition with an increment of 75% compared to PE. Maksimkin *et al.* [51] reported that the addition of 0.1–5 wt.% CNT increased the tensile strength and Young's modulus of UHMWPE by 8%–38% and 5%–100%, respectively. In addition to the improved mechanical properties, CNT-reinforced UHMWPE composite gained intensive interest because of their good wear resistance. By the incorporation of 0.1–4 wt.% CNT, the wear rate of UHMWPE was decreased by 26%–86%.

Sreekanth and Kanagaraj [56] studied influence of MWCNT concentration and irradiation dose on the wear resistance of UHMWPE/MWCNT composites. The wear volume of unirradiated UHMWPE was found to be reduced by 31%, 54% and 73% upon 2 wt.% MWCNT reinforcement, 100 kGy irradiation and combination of both, respectively. However, the wear performance of CNT-reinforced UHMWPE was noted to be sensitive to CNT concentration and its type. Liu and Sinha [101] blended 0.45 wt.% MWCNT, 0.1 wt.% granular form of carbon nanotubes and 0.5 wt.% single-walled carbon nanotubes into UHMWPE. The wear rates of these three types of CNT reinforced UHMWPE were slightly higher than that of pure UHMWPE material. Martínez *et al.* [102] reported that UHMWPE

/MWCNT composites were prepared with less than 3 wt.% of filler by ball milling and thermo-compression. They showed oxidative resistance after gamma irradiation at 90 kGy in air. ESR analysis carried out a week after the gamma irradiation pointed out that the MWCNT behaved as a radical scavenger. Ruan *et al.* [103] used MWCNT to reinforce and toughen gel-spun UHMWPE fibers and demonstrated that adding MWCNT can lead to super strong and ductile UHMWPE composite fibers. The 5 wt.% MWCNT composite fibers showed a significant increase in ductility, tensile strength and energy to fracture by ~34%, 18.8% and 64%, respectively in comparison with the pristine UHMWPE fibers. Sobajima *et al.* [104] reported the equivalence of compression moulded UHMWPE/MWCNT composites to cross-linked in terms of wear resistance and to non-crosslinked UHMWPE in terms of impact resistance with an optimum filler concentration of 2 wt.% MWCNT.

2.3.2. Influence in composites as an antioxidant

Iijima *et al.* [105] reported the various defects and impurities found in the as-grown CNT. Endo *et al.* [106] observed different point defects in the CNT walls and tips like vacancy and interstitial defects. These defective regions were found to be more reactive compared to defect less sites of CNT by Zhou and Shi [107] and Chakrapani *et al.* [108] due to their high electron affinities. Smith *et al.* [109] found these defects in CNT to be created only if the incident particles are energetic enough to displace Carbon atom. Cooper *et al.* [110] reported that defects formed on CNT due to irradiation were expected to increase the CNT-polymer bonding and thus significantly improved the mechanical properties of the composites. Hu *et al.* [111] reported similar results and found covalent bonds between CNT as a result of irradiation. Watts *et al.* [112] reported that CNT acted as polymer antioxidants due to high electron affinity. They concluded that addition of CNT helped to stabilize the polymer composites in presence of Oxygen due to their ability to take up Oxygen and prevent the oxidation of polymer. Krasheninnikov and Nordlund [113] reported that subjecting CNT into irradiation either displace the surface atoms or the incident atoms get absorbed on the surface forming the interstitial atom. Along with simple defects, a number of more complex defects associated with a rotation of a bond in the CNT atom network and other topological defects were formed in the graphitic network. They concluded that the irradiation induced defects forms bonds with the substrates and increased the CNT-substrate adhesion.

Schultz *et al.* [114] reported about the antioxidant property of single walled CNT. By conducting a comparative study on the free-radical scavenging activity of pristine, functionalized and ultra-short SWCNT with derivatives of the phenolic antioxidant, they revealed that all types of SWCNT are extremely effective antioxidants. Wallace *et al.* [115] confirmed improved mechanical properties of nanotubes bundles by mechanical testing of the irradiated CNT bundles. It was resulted due to irradiation-induced inter-tube links, which provided load transfer and enhanced the torsional stiffness in the bundle. Sammalkorpi *et al.* [116] studied the mechanical properties of CNT having point defects. Their results indicated that the Young's modulus of nanotubes having defects was essentially the same unless the vacancy concentration was extremely high. However, the tensile strength was reported to be influenced by the defects. Ritter *et al.* [117] studied the radiation damage on MWCNT and their Raman vibration modes. It was concluded that the number of defects in the CNT increased with irradiation dose leading to accumulation of vacancies causing weakening of the inter carbon bonds. They also reported that the growth of the concentration of non-equilibrium vacancies resulted mutual recombination with interstitial carbon atoms.

Zeynalov *et al.* [118] proved the antioxidant capability of MWCNT by examining their anti-oxidative effect on platelet structure by means of the model reaction of cumene initiated oxidation. The purified CNT was reported to have shown more profound inhibition of oxidation in comparison with un-purified ones. It was also reported by Galano [119] that the antioxidant activity of functionalized CNT was increased significantly compared to that of un-functionalized CNT. Martínez *et al.* [102] and Sreekanth *et al.* [120] in their studies found the antioxidant characteristics of MWCNT due to its high electron affinities, and thus acting as radical scavengers in polymers.

2.3.3. Biocompatibility of MWCNT

Biocompatibility is the first condition to be fulfilled by any material intended to be used under *in vivo* medical applications. As discussed earlier, the failure of TJR was influenced by the wear debris generated from the polymer implant. The local inflammation due to the wear debris depends on its particle size, total volume of the debris, aspect ratio, and its chemical reactivity. MWCNT reinforced composites found very promising for orthopaedic load bearing applications like TJR but the toxicity of CNT is still a debatable issue. While several research groups pointing to their similarity to asbestos fibers, Poland *et al.* [121],

others confirm their nontoxicity. CNT toxicity in both *in vivo* and *in vitro* studies found dependent on several factors, such as length, type of functionalization, concentration, and even the dispersant used to solubilise the nanotubes. They showed that the nontoxic length of CNT was asserted to be ~10 μm in later studies. Longevity of UHMWPE as an articulating surface material in TJRs can be enhanced by reinforcing MWCNT. However, the success of the UHMWPE/MWCNT composites depends on their biocompatibility. As the present study is intended to use MWCNT, literature relevant to its potential effects on biological system is very important.

It is generally believed that the functionalized CNT could be much less toxic due to more biocompatible functional groups attached on their surface, Bicano and Prato [122]. Lam *et al.* [123] instilled 0.1 and 0.5 mg of untreated carbon nanotubes intratracheally in mice. It was reported that it could cause serious toxic effects if the untreated CNT reached the lungs. They concluded that CNT with their impurities can cause potential health hazards. Koyama *et al.* [124] confirmed that the implanted CNT with impurities in mice induced immunological toxicity, whereas the CNT without any impurity showed good biocompatibility.

Yang *et al.* [125] injected SWCNT in male mice, reported that SWCNT accumulation in bone, but exhibited very good biocompatibility. Cherukuri *et al.* [126] tested the systemic toxicity effect of pristine SWCNT in a rabbit by intravenous injection at a dose rate of 7.5 ml of 20 μg/kg body mass and did not find any toxic effect. Sato *et al.* [127] reported that shorter CNT (~0.22 μm in length) were found to be better integrated into macrophages and phagocytes than the longer (~0.8 μm) one. Nel *et al.* [128] reported that length and shape of the CNT also influenced and determined the resulting immunologic response of macrophages. Schultz *et al.* [114] carried out cytotoxicity assays, which showed that concentration of both non-functionalized and derivatized SWCNT had little or no deleterious effects on cell viability. Studies done by Reis *et al.* [129] on UHMWPE/MWCNT composites and Ormbsy *et al.* [130] on PMMA/MWCNT composites also confirmed the cytocompatibility of wear debris generated from the nanocomposites with osteoblast like MG63 cells had grown on CNT, thus they appeared to have no toxic effect, potentially giving rise to applications such as coating for prosthetics. Based on the above literature, it can be assumed that the toxicity of CNT is not an intrinsic property, but it rather depends on

aspect ratio, length and the type of functionalization. The impurities, and not CNT themselves, were responsible for the reported toxicity, Lacreda *et al.* [131].

MWCNT were injected into rat knees in a recent study by Sobajima *et al.* [104] and monitored for 26 weeks without any migration of them. As MWCNT did not exhibit carcinogenicity when injected into the knees of mice genetically modified to spontaneously develop cancer, MWCNT/UHMWPE composite was proposed as a new biomaterial expected to be safe for clinical applications in both TKR and THR as the bearing material.

2.4. Hip Joint Wear Simulator Test

McKellop and Clarke [132] used a ten-station hip joint simulator to examine the wear rate of polyethylene acetabular liners against titanium alloy femoral heads under physiological loading with bovine serum lubricant and compared with stainless steel and cobalt chrome alloy heads. The average wear rate of polyethylene liners against titanium alloy head was found to be 34% and 26% more than that of stainless-steel (SS) head and cobalt chrome alloy head, respectively. Correlation with prostheses removed from patients recommended that the dissimilarities in wear rates would be even less *in vivo.* Saikko [133] studied frictional characteristics of 22 different femoral head-acetabular liner combinations on a micro-computer controlled servo-hydraulic hip joint wear simulator at different flexion-extension angle and superior-inferior load set waveforms with distilled water at 37 ± 1°C as a lubricant. But none of the joint designs emerged out as distinctly superior. Alumina/UHMWPE was proved to be the most favourable one in terms of the frictional behaviour with minimum frictional coefficient (μ_{min}) of 0.02, while titanium alloy Ti-6Al-4V against UHMWPE was extraordinarily poor μ_{max} of 0.15. Saikko [134] designed and developed a three-axial single-station hip joint simulator HUT-3 for wear and friction studies on THA under all three motion components, i.e., abduction-adduction, flexion-extension, and internal-external rotation in continuous level walking. Co-Cr-Mo femoral heads were tested against UHMWPE acetabular liners under distilled water at room temperature and the results were compared with those obtained from uniaxial HUT-2. UHMWPE debris from HUT-3 was obtained in the form of flakes compared to long streams in HUT-2. But the average wear rate and wear factors in both the simulators were found fairly similar. Mejia and Brierley [135] evaluated artificial hip joints in an 8-station bi-axial

hip simulator, designed by them, which mimicked the motions and loads observed in a hip joint while performing a typical walking cycle. The test was performed with a biaxial rocking motion of ± 23° at 1 Hz synchronized with 4500 N load in a calf serum environment at an equilibrium temperature of 33°C and the steady-state wear rate for UHMWPE/CoCr bearing surface was observed after 2 million cycles.

Saikko [136] carried out a study in a novel 12-station hip joint simulator 'HUT 4' with an anatomic position of the CoCr–polyethylene prosthesis under calf serum lubrication. The wear particles were found to be in the range of 0.1–1.0 μm with a mean wear factor of 5.7×10^{-7} mm^3/Nm for the polyethylene liners. These results were in good agreement with clinical observation. Essner *et al.* [137] performed a test to compare the hip joint simulator wear performance of ceramic-on-crosslinked polyethylene (C-o-XPE), metal-on-metal (M-o-M) and alumina-on-alumina ceramic (C-o-C) bearings against each other on a 12-station hip joint simulator (MTS, Eden Prairie, MN). The test was carried out at 1 Hz under a maximum load of 2450 N with 50% diluted alpha-calf serum as a lubricant and the C-o-XPE joints showed a linear relationship between wear and test duration. Affatato *et al.* [138] carried out a study for characterizing the wear behaviour of a new hybrid ceramic-on-metal bearing combination for THA, and compared the results with the gold standard of artificial hip joints in terms of lowest possible wear rate, viz., ceramic-on-ceramic. They employed a 12-station hip joint simulator manufactured by Shore Western in USA for performing the wear test with 25% sterile bovine calf serum as lubricant balanced with deionized water and 0.2% Sodium Azide for the postponement of bacterial degradation. They found that the wear in their proposed ceramic-on-metal bearings compared to ceramic-on-ceramic was significantly greater. They concluded that the geometrical conformity could lead to clinical failure due to a poor dynamic behaviour.

Hongtaoa *et al.* [9] performed a comparative study of ultra-high molecular weight polyethylene (UHMWPE) wear debris generated from the hip joint simulator and the implanted artificial joint on their size distribution, shape, 3-D feature, and thickness. Figure 2.1(I) shows that the wear debris obtained from joint simulator had various shapes and sizes such as block, strip, plate, and spherical etc. The volume distribution of the wear debris generated is shown in Figure 2.1(II) which had mean diameter of 7.54 μm, and medium diameter of 6.89 μm.

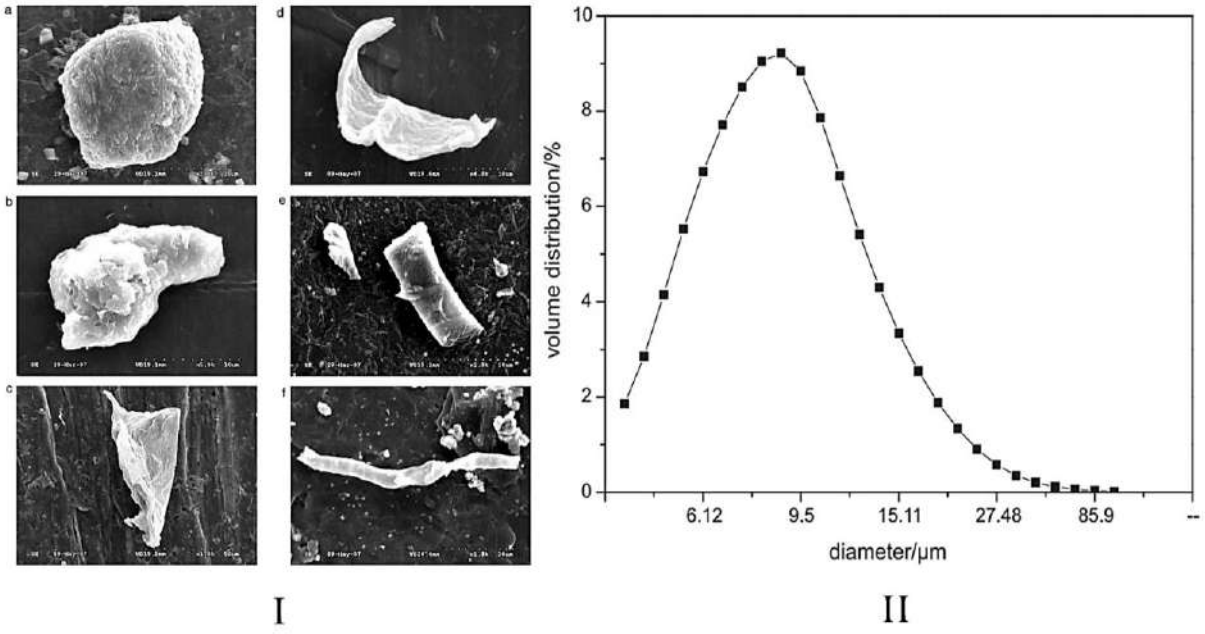

Figure 2.1. *(I) Different size and shapes of wear debris generated at simulator testing (II) Volume distribution of UHMWPE wear debris from the joint simulating test [9](permission sought)*

It is noticed that most of the wear debris from retrieved artificial joints were spherical or sub-spheroidal in shape as shown in Figure 2.2(I). The mean diameter and medium diameter of their volume distribution, shown in Figure 2.2(II), were about 18% and 43% of the wear debris obtained from the joint simulator, respectively. The results provided both theoretical and experimental foundation for refining the joint wear simulator with optimized assessment standards for the artificial joint.

Shahemi *et al.* [139] performed failure analysis of a retrieved polyethylene acetabular component failed due to aseptic loosening, as shown in Figure 2.(A), after 23 years of primary life**.** This degradation was majorly contributed by oxidation and polishing wear feature.

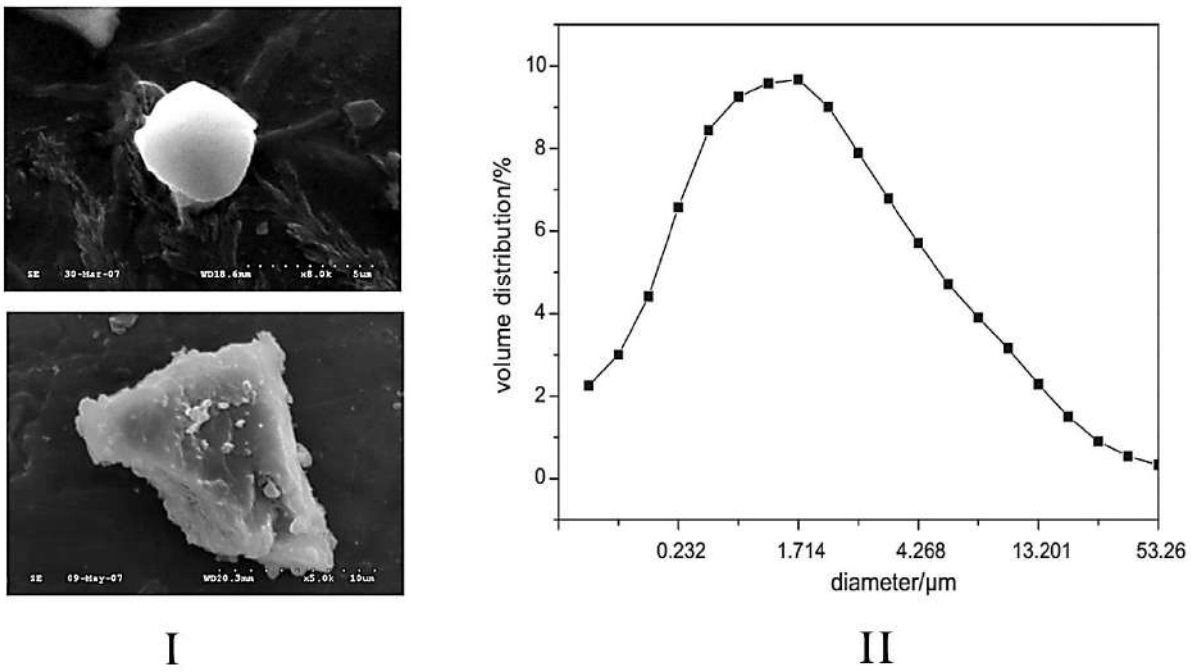

Figure 2.2. *(I) Different size and shapes of wear debris from the implanted artificial joint (II) Volume distribution of UHMWPE wear debris from the implanted artificial joint [9](permission sought)*

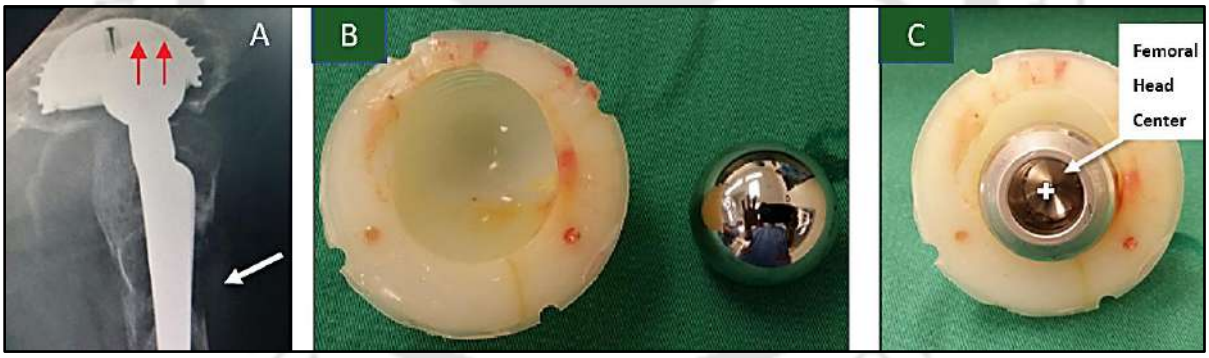

Figure 2.3. *(A) Radiographs of Orientation of femoral ball in patient's body after 23 years implantation (B) Retrieved UHMWPE acetabular liner and Co-Cr-Mo femoral head (C) Non-conform central hole of acetabular liner for femoral head fitting [139](permission sought)*

The delamination, ripple, cracks and craters were considered to be the symptoms for extensive usage of UHMWPE as an acetabular liner beyond recommended life span. They found a sharp difference in thickness between two regions resulting from acentric loading concentration, as evident in Figure 2.(B-C). For thin region, the linear wear rate was found to be 0.33 mm/year compared to 0.05 mm/year at the thicker side. Reduction of molecular weight was observed to be 42.5 % of its original value, and a low ratio of hardness to elastic

modulus of 3.59 × 10^{-3} was indicated as the major mechanical property degradation suffered by UHMWPE acetabular liner.

2.4.1. Simulator developed worldwide

Hip joint simulator plays the most important role in pre-clinical validation of newly developed materials. Currently used simulators basically differ in parameters like number of stations, loading cycle, ball-cup relative position, degree of freedom, lubricant chamber etc. Table 2.1 summarises the available hip joint simulators worldwide based on an extensive international literature survey. Multiple stations devices certainly provide greater flexibility, capacity, and the ability to perform multivariate analyses with greater confidence within a single test, but a single station control is still a commonly applied design solution as it could enable single specimen removal without test interruption.

***TABLE 2.1**. Modern hip joint simulator description*

Simulator name	DOF	Load Pattern	Lubricant	Features
HUT-I Custom-Made machine Finland Affatato [38]	FE: ±30◦	Type: hydraulic Profile: double peak L_{max}: 5000N Frequency: 0.4–2.2 Hz	Distilled water	Single channels in inverted position Temperature control (37±1 ◦ C)
HUT-II Custom-Made machine Finland Saikko [134]	FE: ±30◦	Type: pneumatic Profile: on/off L_{max}: 3500N Frequency: 1.08 Hz	Distilled water, Bovine serum	Five channels Inverted position Temperature control (37±1 ◦ C)
HUT-III Custom-Made machine Finland Saikko [140]	AA: range 12◦ FE: range 46◦ IO: range 12◦	Type: pneumatic Profile: on/off L_{max}: 3500N Frequency: 1.18 Hz	Distilled water, Bovine serum	Single channel Inverted position Temperature control (37±1 ◦ C)
MTS-BIONIX Commercial machine USA Pare [141]	BRM: ±22.5◦	Type: hydraulic Profile: physiologic L_{max}: 2450N L_{min}: 50N Frequency: 1Hz	Balanced alpha-calf serum	12 channels Non-inverted position Temperature control

Shore Western Commercial machine USA Affatato [142]	BRM: ±22.5°	Type: hydraulic Profile: sinusoidal L_{max}: 2450N L_{min}: 150N Frequency: 1.1 Hz	Calf serum Bovine serum	12 channels Inverted position
Shore Western Commercial machine USA Clarke [143]	BRM: ±22.5°	Type: hydraulic Profile: Paul L_{max}: 2450N L_{min}: 150N Frequency: 1Hz	Calf serum Bovine serum	9 channels Non-inverted position
AMTI Commercial machine USA Bragdon [144]	AA: ±8.5° FE: ±23° IO: ±10°	Type: hydraulic Profile: Paul L_{max}: 2450N L_{min}: 150N Frequency: 2Hz	Bovine serum	12 channels Non-inverted position Temperature monitoring
BRM Custom-Made machine Finland Saikko [145]	BRM: ±22.5°	Type: spring Profile: static L_{max}: 1000N Frequency: 1Hz	Calf serum	Three channels Non-inverted position Temperature monitoring
HUT-4 Custom-Made machine Finland Saikko [146]	AA: ±6° FE: ±23°	Type: pneumatic Profile: double peak L_{max}: 2000N L_{min}: 400N Frequency: 1Hz	Calf serum	12 channels Anatomical position
MARK I Custom-Made machine UK Affatato [38]	FE: ±25° IO: +8° to −20°	Type: pneumatic Profile: Paul L_{max}: 2000N Frequency: 1Hz	Calf serum	5 channels Non-inverted position
MARK II Custom-Made machine UK Smith [147]	FE: +30° to −15° IO: +8° to −20°	Type: pneumatic Profile: square wave L_{max}: 2000N Frequency: NS	Calf serum	5 channels Non-inverted position
PA II Custom-Made machine UK Galanis [148]	FE: +30° to −15° IO: ±10°	Type: NS Profile: Paul L_{max}: 3000N Frequency: 1Hz	Calf serum	Six channels Non-inverted position

PROSIM Commercial machine UK Barbour [149]	FE: +30° to −15° IO: ±10°	Type: pneumatic Profile: Paul L_{max}: 2780 N Frequency: 1Hz	Calf serum	10 channels Non-inverted position
MATCO-EW08 MMED Custom-Made machine USA Medley [150]	BRM: ±22.5°	Type: hydraulic Profile: Paul L_{max}: 2100N Frequency: 1.13 Hz	Calf serum Bovine serum	16 channels Inverted position
ENDOLAB Commercial machine Germany Caddick [151]	AA: +7° to −4° FE: +25° to −18° IO: +2° to −11°	Type: hydraulics Profile: Paul L_{max}: 3000N Frequency: 1Hz	Bovine serum	Six channels Non-inverted position
FIME II Custom-Made machine Mexico Vera [152]	AA: ±23° FE: ±23° IO: ±7.5°	Dynamic load system Different load patterns reproducible Frequency: 1.4 Hz	Bovine serum	NS channels Non-inverted position

2.4.2. International Guideline

The continuous research in enhancement of wear resistance of the bearing materials for hip prostheses became the need of a common protocol for wear testing of THR prosthesis. In 1989, International Organizations for Standardization (ISO) drafted a guideline to produce comparable results at laboratories worldwide [153]. " The standard guide for gravimetric wear assessment of prosthetic Hip-Designs in Simulator Devices" was introduced by the American Society for Testing and Materials (ASTM) in 1996 [154]. Since 2000, the ISO recommended specific methods for wear assessment and prescribed the kinematics to be applied in order to conduct a reliable wear test.

2.4.2.1. The Load profile

The force control system of a hip simulator mainly appointed to replicate a simplified gait cycle with a double peak profile axial load having a peak intensity of 3 kN as suggested by the ISO 14242-1 and ISO 14242-3 to perform a hip wear test, which is shown in Figure 2.4.

But many researchers have taken into account other requirements to assess the wear of articulating surfaces, since wear is also related to other parameters like velocity, acceleration, sliding distance etc. [155]. Substantial differences in final results are observed applying different load profiles. Initially sinusoidal load profiles with variable peak loads were popular for simulator characterization [156]. A number of studies are also focused on the effects induced on the wear by the application of an average static load. However, it is still debatable whether simplistic load profiles can reproduce physiological wear patterns and weight loss.

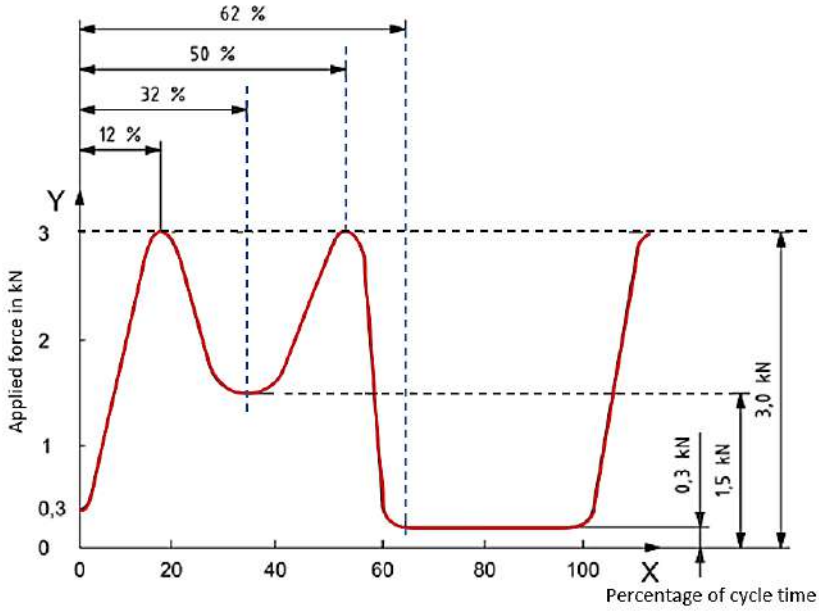

Time (% cycle) ± 3%	Applied Force (kN) ± 90N
0	0.3
12	3.0
32	1.5
50	3.0
62	0.3
100	0.3

Figure 2.4. *Variation of the force to be applied along the loading axis with time as per the ISO 14242 [157], [158]*

2.4.2.2. The Motion Profile

Human hip joint is a ball and socket joint with three degrees of rotational freedom as explained with nomenclature in Figure 2.5. As per the guidelines of ISO 14242-1 for a tri-axial hip simulator, the flexion/extension angular movement is a simple sinusoid between 25° and –18°, while the abduction/adduction is a sinusoid between 7° and –4°, and the inward/outward rotation work in a range between 2° and –10° as shown in Figure 2.6(A).

ISO 14242-3 prescribes the motion profile to be simulated by a bi-axial hip simulator with both the flexion/extension and abduction/adduction angular movements of ± 23° in sinusoidal manner having a temporal phase difference of 0.25 s as shown in Figure 2.6(B).

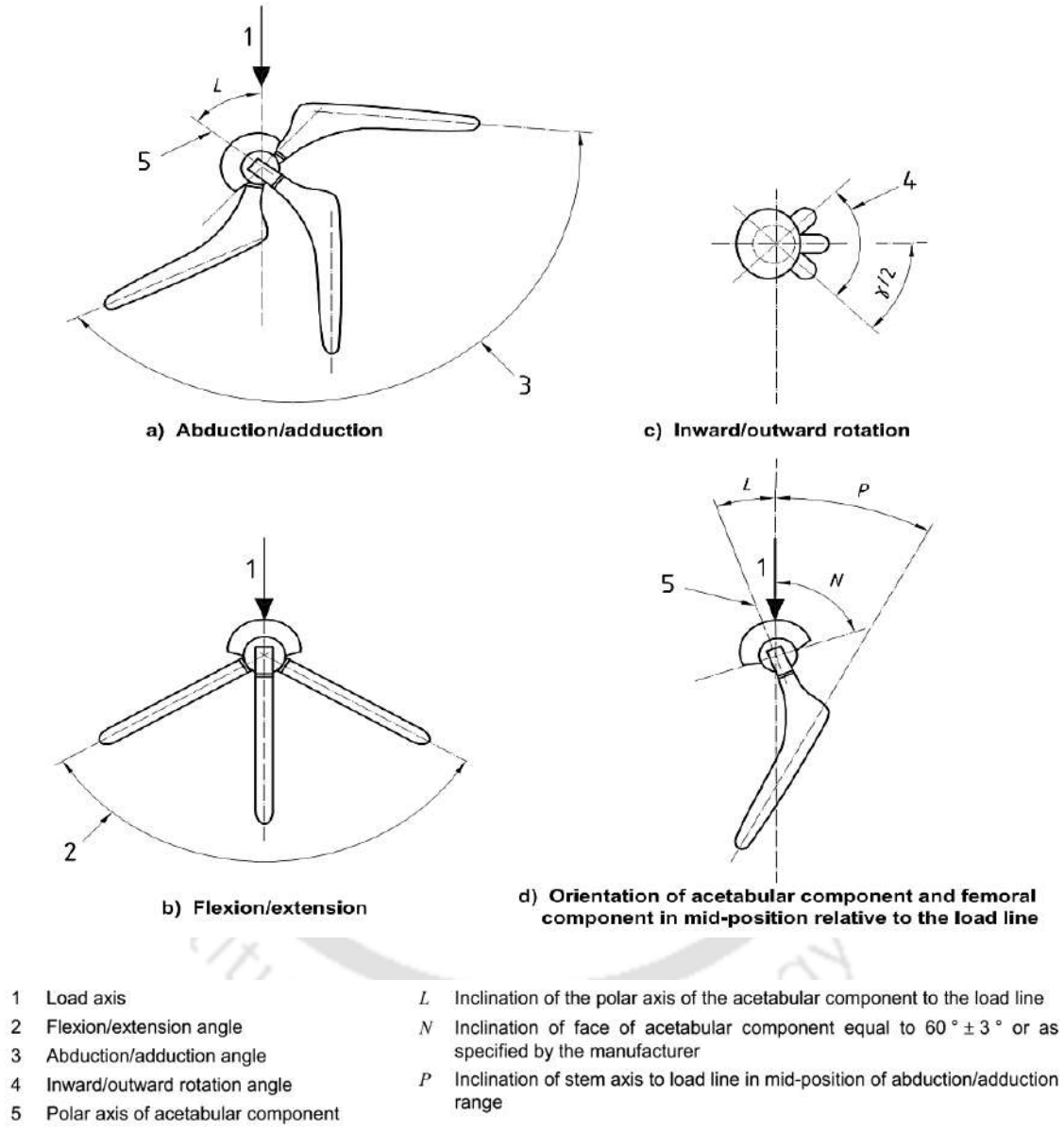

***Figure 2.5**. Angular movement of femoral component and orientation of components relative to the load line as per the ISO 14242 [158]*

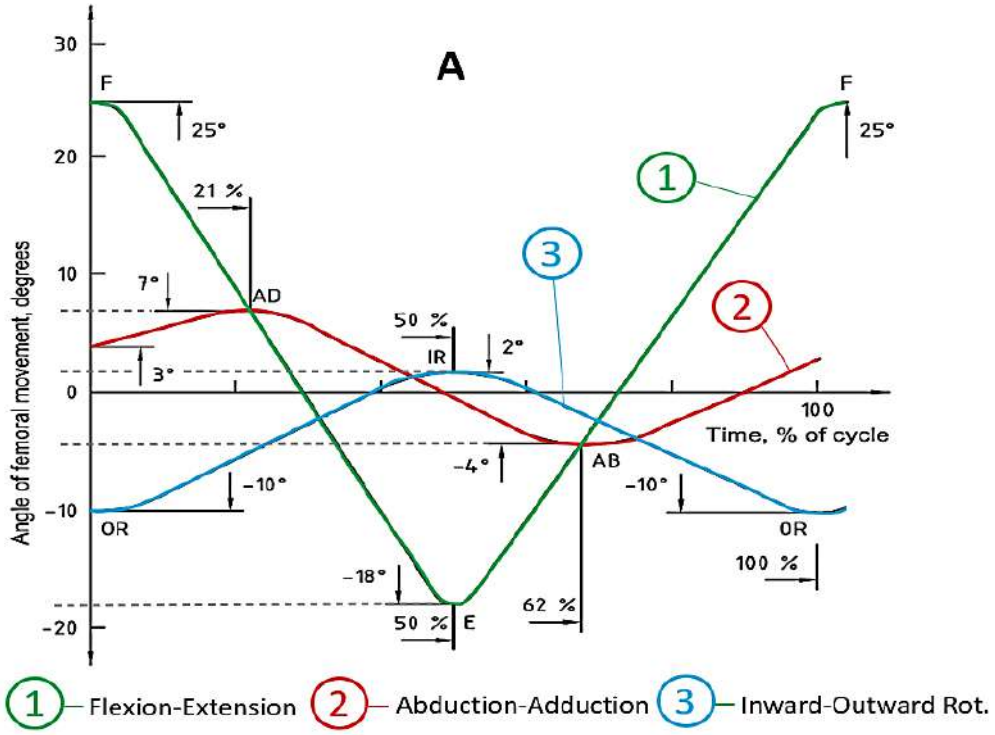

Time (% cycle) ± 1%	0	21	50	62	100
Angle of Flexion (+)/Extension (-) ± 3°	+25°		-18°		25°
Angle of Adduction (+)/Abduction (-) ± 3°	+3°	+7°		-4°	3°
Angle of Inward (+)/Outward (-) Rotation ± 3°	-10°		+2°		-10°

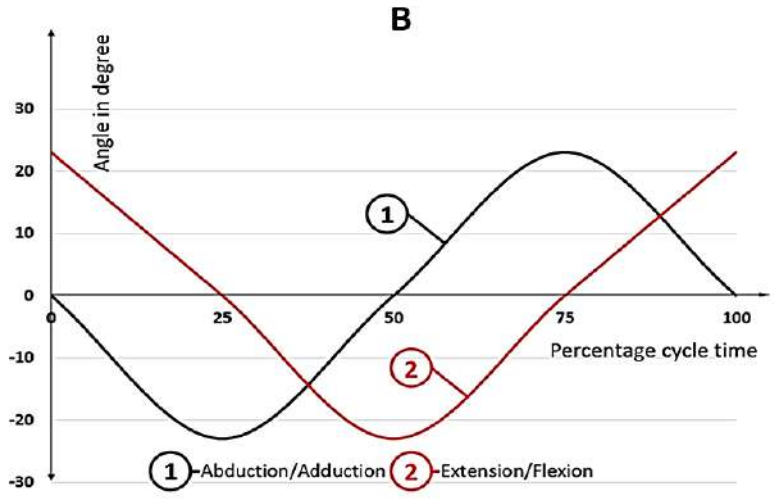

Time (% cycle) ± 1%	0	25	50	75	100
Angle of Flexion (+)/Extension (-) ± 3°	+23°	0°	-23°	0°	+23°
Angle of Adduction (+)/Abduction (-) ± 3°	0°	-23°	0°	+23°	0°

Figure 2.6. *Variation of angular movement to be applied to the femoral test specimen with time as per the (A) ISO 14242-1 [157](B) ISO 14242-3 [158]*

2.4.2.3. Lubricant and applications

One of the important features of a hip simulator is to maintain the required lubrication at the contact surface by a suitable fluid. Researchers used different test fluids like bovine serum, saline and water, enclosed in a flexible plastic bag in order to minimise fluid evaporation and changes due to air contamination of the lubricant or other components as per international standard and they are listed in Table 2.1 [37], [133], [139]-[151]. Moreover, temperature control system should be a part of an ideal simulator to maintain the temperature of the fluid test medium at 37° ± 2° C. Brown *et al.* [159] reviewed the ongoing discussion within researchers about the possibility of using different lubricants such as bovine serum, distilled water or synthetic ones, though providing the same wear behaviour. Saikko *et al.* [160] discussed about the main problem with lubricating conditions i.e., an increase in precipitated proteins and, as a consequence, lubrication regime while studying UHMWPE against a CoCr counter face. The gradual increase in proteins, related to temperature augmentation, would cause a gradual drop in wear rate because of an un-physiological protection effect against wear.

Generally, water, saline, gelatine solutions or other similar fluids do not produce relevant clinical wear rates or wear debris as protein degradation masks true wear rates. Hence, care should be taken with regard to protein concentration and ratio, temperature and volume of the lubrication serum. Idealistically simulation should be run at room temperature with a large, open lubricant chamber ensuring sufficient soluble protein and evaporation to prevent overheating. Smith *et al.* [161] used rheological approach to understand Synovial Fluid (SF) flow properties to provide an insight into the mechanical behaviour expected of an artificial SF analogue. Rheological properties of SF were found to be similar to that of a 50:50 mix of 0.75% w/v Gellan gum with 2% w/v high molecular weight Sodium alginate and it was proposed as a lubricant suitable for *in vitro* wear tests of orthopaedic implants.

2.4.3. Comparison across hip joint simulators

Results from simulator testing confirm the performance of material for a given morphology under various operating conditions. Different simulators differ in the wear results they provide for the same bearing combinations as shown in Figure 2.7, [162]. As a consequence,

Figure 2.7 emphasizes that it is impossible to compare the outcomes from different rigs even when the same prostheses are tested.

At the moment, in fact, not everyone follows ISO standards and the ones who do, introduce slight variations to them according to internal protocols which results in high data dispersion. On the other hand, the comparison presented in Figure 2.7 may not be comprehensive due to the presence of high number of uncontrolled variables in the form of mechanical simulation factors, the materials tested and bearing dimensions. Thus, it was not possible to compare, in the same picture, the *in vitro* vs *in vivo* mean wear rates.

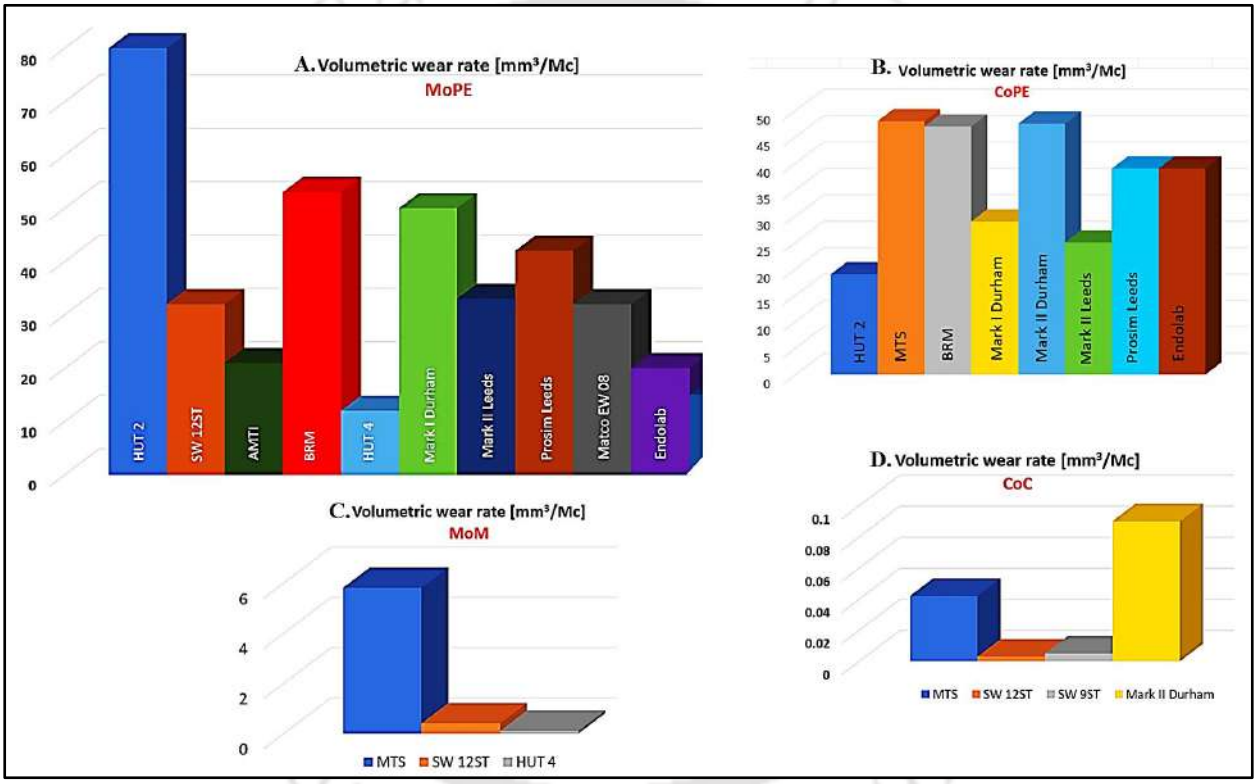

Figure 2.7. *Volumetric wear data, plotted for different bearings tested at hip joint wear simulators (A) M-o-PE (B) C-o-PE (C) M-o-M (D) C-o-C with testing parameters listed in Table 2.1.* [162]

2.5. TECHNICAL GAPS

- Due to semi-crystalline nature of UHMWPE, its mechanical properties are limited, which are also influenced by the operating parameters including compaction pressure, sintering temperature and sintering duration of the products

- A few attempts are made to improve the wear resistance of UHMWPE using nanofillers. However, the agglomeration and non-uniform dispersion of them limit their application in commercial scale of implants. In addition, these agglomerations act as stress concentration zones, which generate a greater number of wear debris during the usage of UHMWPE

- Due to high melt flow index of UHMWPE, incorporation of nanofillers further increases its viscosity, which limits the processability of the polymer without any defects including micropores and others

- The wear debris could act as a third body between the interfaces and accelerate the rate of wear and the material degradation. So, optimization of the mechanical properties of filler reinforced UHMWPE, such as hardness, size and concentration, is essential for the wear performance of particle-reinforced UHMWPE

- Carefully designed parametric studies are required to examine the systematic influence of contact surfaces, lubricant, load, articulating surface speed, relative position, surface roughness, temperature and motion directions on the behaviour of a material and their resulting wear phenomena

- An in-house developed hip joint wear simulator as per the international guidelines is a priority for developing a new bearing material, which could be explored as an acetabular liner. It will allow the researchers to play with the processing parameters and fine tune them with utmost ease. Moreover, the comparative studies between existing and newly developed materials, being done on the same platform, will increase the confidence level to propose the new material for TJR

- *In vitro* simulator testing of implants is generally performed using diluted solutions of calf or bovine serum as a lubricant as per the current ISO recommendations. But there are issues regarding the use of bovine serum as a test lubricant including batch to batch variation, degradation, precipitation and its animal origin. Moreover,

cholesterol and triglycerides present in bovine serum make it rheologically different from the synovial fluid consisting of phospholipids and hyaluronan.

- To qualify a material for TJR, the actual wear mechanisms in an artificial hip joint under a variety of operating conditions must be elucidated. It is still a grey area for the researchers. Several known and unknown factors affect the *in vivo* wear, while laboratory testing conditions are restrictive and controlled. Hence, a correlation between *in vitro* vs *in vivo* data remains a challenge

- It is also important to study the interaction of wear debris generated from the particle reinforced UHMWPE with surrounding tissues to evaluate and eliminate possible inflammatory reactions, which may cause osteolysis

2.6. OBJECTIVE OF PRESENT WORK

The objective of the present work is to design and develop medical-grade UHMWPE and UHMWPE-MWCNT composite based acetabular liners to be used in total hip replacements by an ingenious manufacturing technique and to perform their *in vitro* evaluation as per international guidelines using a novel hip joint simulator with a synovial fluid analogue as the lubricant.

In order to achieve the same, the following sub-objectives are to be carried out.

- To maximize the mechanical properties and integrity of UHMWPE test samples and acetabular liners by opting apposite processing parameters
- To synthesize UHMWPE-MWCNT nanocomposites with homogeneous dispersion and distribution of the filler having optimum concentration of reinforcement based on their mechanical properties and obtain samples and acetabular liners for their characterization
- To optimize the concentration of filler based on the mechanical properties and wear resistance of the samples
- To confirm the biocompatibility of UHMWPE and UHMWPE-MWCNT nanocomposite

- To develop rheological analogue of human synovial fluid for recreating the *in vivo* environment of an implanted THA
- To perform the wear screening test of UHMWPE and UHMWPE-MWCNT samples using a pin-on-disc tribometer
- To develop of a single station hip joint simulator following the ISO 14242-3 guidelines and perform *in vitro* simulator wear test on the newly developed acetabular liners

भारतीय प्रौद्योगिकी संस्थान गुवाहाटी
Indian Institute of Technology Guwahati

CHAPTER 3

PROCESSING AND CHARACTERIZATION OF UHMWPE-BASED SAMPLES

3.1. Introduction

More than 60% of the retrieved-failed UHMWPE acetabular components are found to have different types of mechanical failure, namely, aseptic loosening, fracture, and wear, which led to reduce the average life of total hip arthroplasty (THA) to 10–15 years [28], [44]. Thus, the present-day challenge is to process UHMWPE having desired mechanical integrity and toughness as an acetabular liner with improved bearing characteristics. The conventional way of processing the polymer is not possible in case of UHMWPE due to its very high molecular weight in the range of 3.5×10^6 to 7.5×10^6 g/mol and the melt viscosity of ~ 2.9×10^5 to 3.4×10^8 Pa.s [163], [164]. Moreover, homogeneous dispersion and distribution of fillers in such a viscous matrix are the major challenges during the processing of UHMWPE based composites. Compression moulding and bulk extrusion have been used for making UHMWPE-based products and these techniques rely on diffusion of polymer particles under simultaneous application of heat and uniaxial pressure without any bulk flow of the material leading to anisotropic characteristics with numerous flaws, such as fusion defect and weak bonding [28], [31]. Imperfect boundary diffusion leads to crack initiation and its propagation in the product.

The objective of the present chapter is to process UHMWPE and UHMWPE-MWCNT composite samples by cold isostatic compaction followed by sintering of polymeric powder with optimum processing parameters ensuring homogeneous distribution and dispersion of the filler in the highly viscous UHMWPE matrix to obtain desired enhancement of mechanical properties for their applications as biomaterials. Novelty of the present study is to focus on the bulk sintering of medical grade UHMWPE GUR1050 to identify the influence of compaction pressure and sintering temperature on sintering kinetics of UHMWPE for realizing their optimum values along with an apposite sintering duration.

3.2. Materials

UHMWPE powder with trade name of GUR 1050, having the molecular weight of 5.5-6 ×10^6 g/mol with the particle size of 140 ± 20 µm and the density of 0.942 g/cm^3 was kindly supplied by M/s Ticona Germany, Germany. Multi-walled carbon nanotubes (MWCNT) of 20-40 nm diameter and 5-20 µm length, which are used to synthesize UHMWPE-MWCNT nanocomposite, are procured from M/s Shenzhen Nanotech Port Co., Ltd., China with 97% of purity and ash content < 3%.

3.3. Processing and Characterization of UHMWPE

3.3.1. Methodology

The present work aims to study bulk sintering behaviour of isostatically compacted GUR1050 powder to optimize the processing parameters in order to maximize its mechanical strength. Three key parameters, namely, compaction pressure, sintering temperature and sintering duration are varied one at a time in a specific range, keeping the other two parameters unaltered to find its optimum. Following this methodology, all three parameters are optimized and consequently utilized during the processing of acetabular liners. A brief methodology of the present work consisting of different processes 1-7 is shown in Figure 3.1 in the form of a flow chart and it is briefly explained below. Each of the process is repeated for at least 3 times for repeatability of the results.

3.3.1.1. Process 1

It is basically the technique of differential scanning calorimetry to discover the melting zone of GUR 1050 along with its onset melting point. Thermal studies on UHMWPE are done using very small powder compacts in the temperature range of 40°C - 200°C for the purpose.

3.3.1.2. Process 2

In process 2, the samples are prepared with different compaction pressure (**P**$_C$) and sintered in TMA keeping the sintering temperature and duration unaltered. The thermomechanical analysis revealed the sintering kinetics and diffusion point of the polymer. The best compaction pressure is identified based on the highest density and hardness of the products.

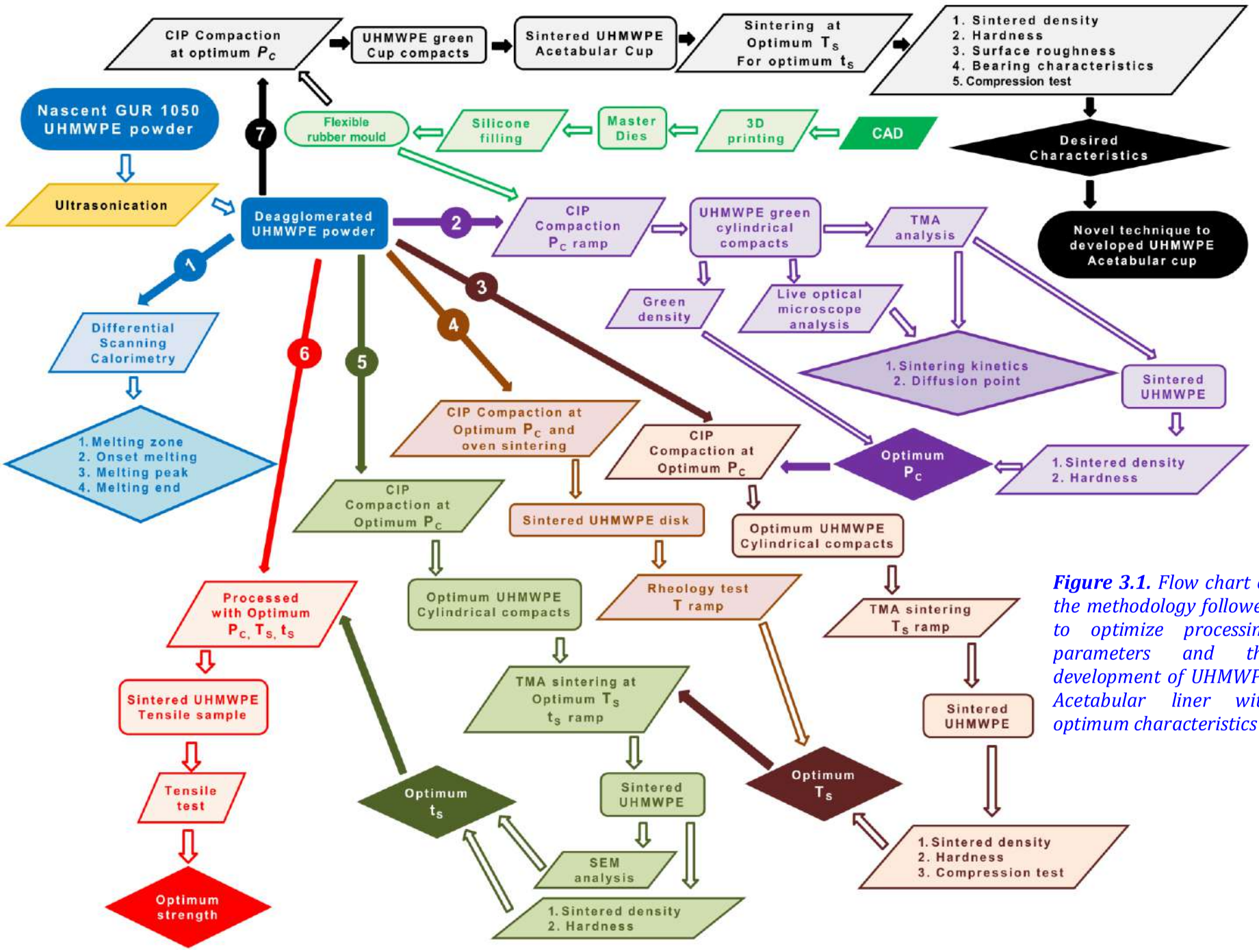

Figure 3.1. *Flow chart of the methodology followed to optimize processing parameters and the development of UHMWPE Acetabular liner with optimum characteristics*

3.3.1.3. Process 3

UHMWPE powder is compacted with the best compaction pressure identified in process 2 and sintered at different temperature (**T**S) using TMA for the same duration in process 3. The sintering temperature at which the highest density and hardness of the samples are achieved is identified as the optimum.

3.3.1.4. Process 4

Results observed through process 3 are validated by a rheology test with a temperature ramp as shown in process 4.

3.3.1.5. Process 5

It is meant to optimize the sintering duration (**t**S) for GUR 1050 samples keeping **P**C and **T**S at their optimum.

3.3.1.6. Process 6

All the optimum processing parameters found in Process 1-5 are used to prepare UHMWPE tensile samples as shown in process 6 and the optimum mechanical strength of the samples is obtained.

3.3.1.7. Process 7

Finally, a similar methodology with optimal processing parameters, shown in process 7, is applied to make UHMWPE acetabular liners.

The methodologies followed during process 1-7 are discussed below in detail.

3.3.2. Sample Preparation

3.3.2.1. Deagglomeration of powder

Nascent GUR 1050 powder is ultra-sonicated in 99.99% ethyl alcohol at 50-60 Hz for 30 minutes using an ultrasonic bath, 75-2003-220 (BUEHLER, USA) to avoid any agglomeration of particles. Thereafter, the mixture is dried at 80°C and the residual deagglomerated polymer powder is used for sample preparation. Particles are found to be near-spherical in shape and the diameter of randomly selected 500 particles is measured

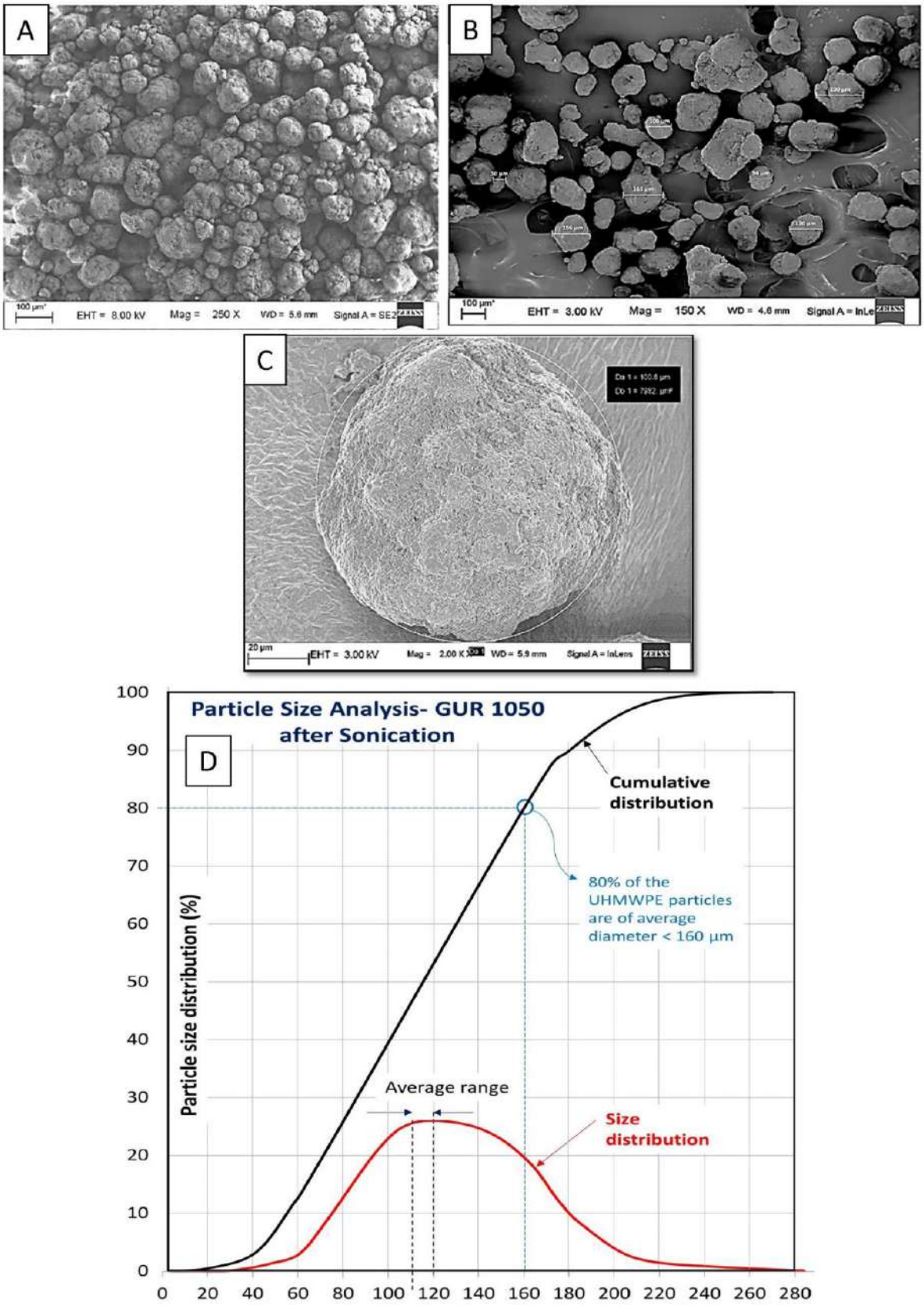

***Figure 3.2**. (A) Nascent UHMWPE particles as received (B) UHMWPE particles separated after ultra-sonication, used for sample preparation (C) A typical GUR 1050 particle of spherical shape separated by sonication (D) Particle size distribution of GUR 1050 after sonication*

by FESEM measuring scale as the conventional particle size analysis requires an abundant non-reactive liquid medium with density closely matching with that of the polymer. UHMWPE powder before and after ultra-sonication is shown in Figure 3.2(A) and Figure 3.2(B) respectively, as observed under FESEM Sigma 300 (Carl Zeiss, Germany). A representative particle of spherical shape, separated by sonication is shown in Figure 3.2(C) and the statistical size distribution of the UHMWPE particles calculated after sonication is depicted in Figure 3.2(D). It is observed that the average size of UHMWPE particles to be 115 ± 20 µm and the cumulative size distribution revealed that 80% of the GUR 1050 particles are of average diameter < 160 µm.

3.3.2.2. Rubber mould development

To make the green compact of UHMWPE with desired geometry, rubber moulds with similar shape and size are prepared incorporating necessary compaction and sintering allowance of 15% and 10%, respectively, with respect to the anticipated dimension as per the experimental experience gained by trial-and-error method. The rubber moulds are made by a three-step process, and the same for a tensile sample is shown in Figure 3.3 as an example. Firstly, the master dies are designed in SolidWorks CAD software, which are fabricated by a fused deposition modelling (FDM) 3D printing technique using a plastic material. Once the master dies are made, the die cavities are filled with commercially available liquid silicone rubber material mixed with required quantity of curing agent. After 8 hours of curing, the solid and flexible rubber moulds are ready for use. Cylindrical rubber moulds are prepared for process ❷-❺ and the same technique is followed to make the dumbbell shaped rubber mould for the process ❻, which are shown in Figure 3.1. Selection of sample size along with the pressure and temperature set points for Process ❶-❼ are listed in Table 3.1.

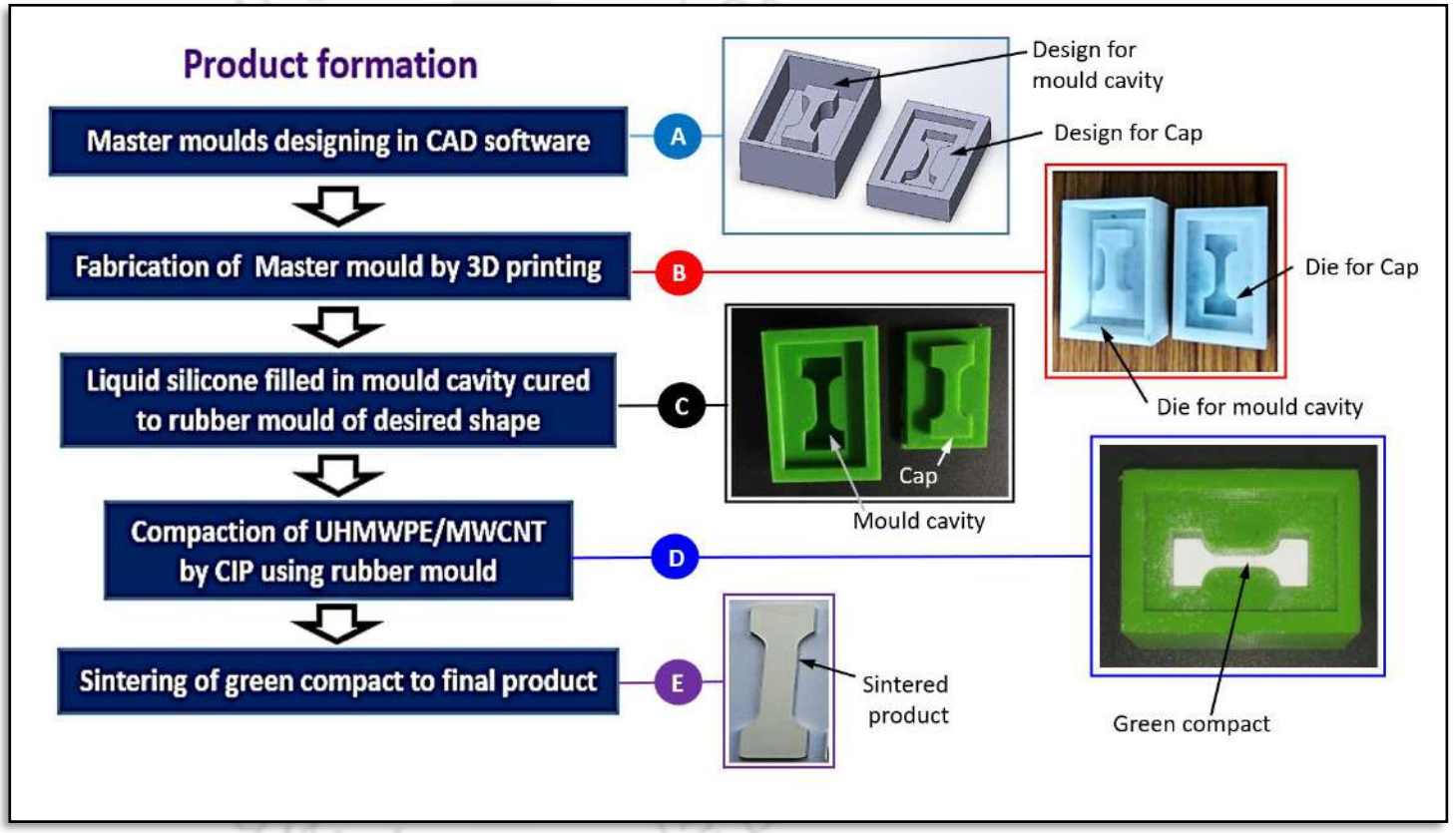

Figure 3.3. *5-Step process of Product formation (A) CAD design for Dies (B) 3D printed plastic Dies (C) Rubber mould making by cavity filling (D) Compaction of Polymer powder using developed rubber mould (E) Sintering of green compact to final product*

3.3.2.3. Compaction of UHMWPE powder

A cold isostatic press, AIP3-22-60WP (American Isostatic Presses, US) is used to compact the UHMWPE powder in desired shape and size using the in-house developed rubber moulds. Compaction pressure is gradually raised to a target pressure (P_0) at an average ramp of 5 MPa/s and held for 1 minute of dwell time, and then released at an average rate of 10 MPa/s. Figure 3.4(A) shows the pressure cycle followed during the compaction of UHMWPE powder. To identify the effect of compaction pressure on sintering kinetics and mechanical properties of UHMWPE, the samples are prepared with different compaction pressure in the range of 34.5 –276 MPa (5-40 ksi) with an increment of 34.5 MPa (5 ksi) in process ❷, as referred in Figure 3.1. The optimum compaction pressure revealed in process ❷ is used in rest of the sample preparation condition. Any measurement related to the green compacts is done after a day of stress relaxation to nullify the visco-elastic effect of UHMWPE.

***Table 3.1**. Description of sample size, process parameters for Process ❶-❼*

Process	Sample geometry	Sample size	Process parameters
❶	Powder	~10 mg	103.5MPa, 5°C/min., 40°C to 200°C
❷	Cylindrical	L = 15 mm Φ = 8 mm	34.5-276 MPa, 5°C/min, 160°C, 130 min
❸	Cylindrical	L = 15 mm Φ = 8 mm	103.5MPa, 5°C/min, 150°C – 190°C, 130 min
❹	Disc	Φ = 8mm t~ 1 mm	103.5MP, 5°C/min, 140°C – 200°C
❺	Cylindrical	L = 15 mm Φ = 8 mm	103.5MP, 5°C/min, 165°C, 30-150 min
❻	Dumbbell	ASTM D638 – type 'V'	103.5MP, 5°C/min, 165°C, 130 min
❼	Hemispherical Shell	ID = 22 mm OD =34 mm	103.5MP, 5°C/min, 165°C, 130 min

3.3.2.4. Sintering of green compacts

Sintering behaviour of GUR 1050 is studied at 160°C by process ❷, as referred in Figure 3.1, using a thermomechanical analyser, TMA/SS6000 (SEIKO, Japan). In process ❷, the samples are prepared with different compaction pressure ($\mathbf{P}_C$) as mentioned above and sintered in TMA keeping the sintering temperature and duration unaltered. The best compaction pressure is identified corresponding to the highest density and hardness of the products and utilized in all further processes.

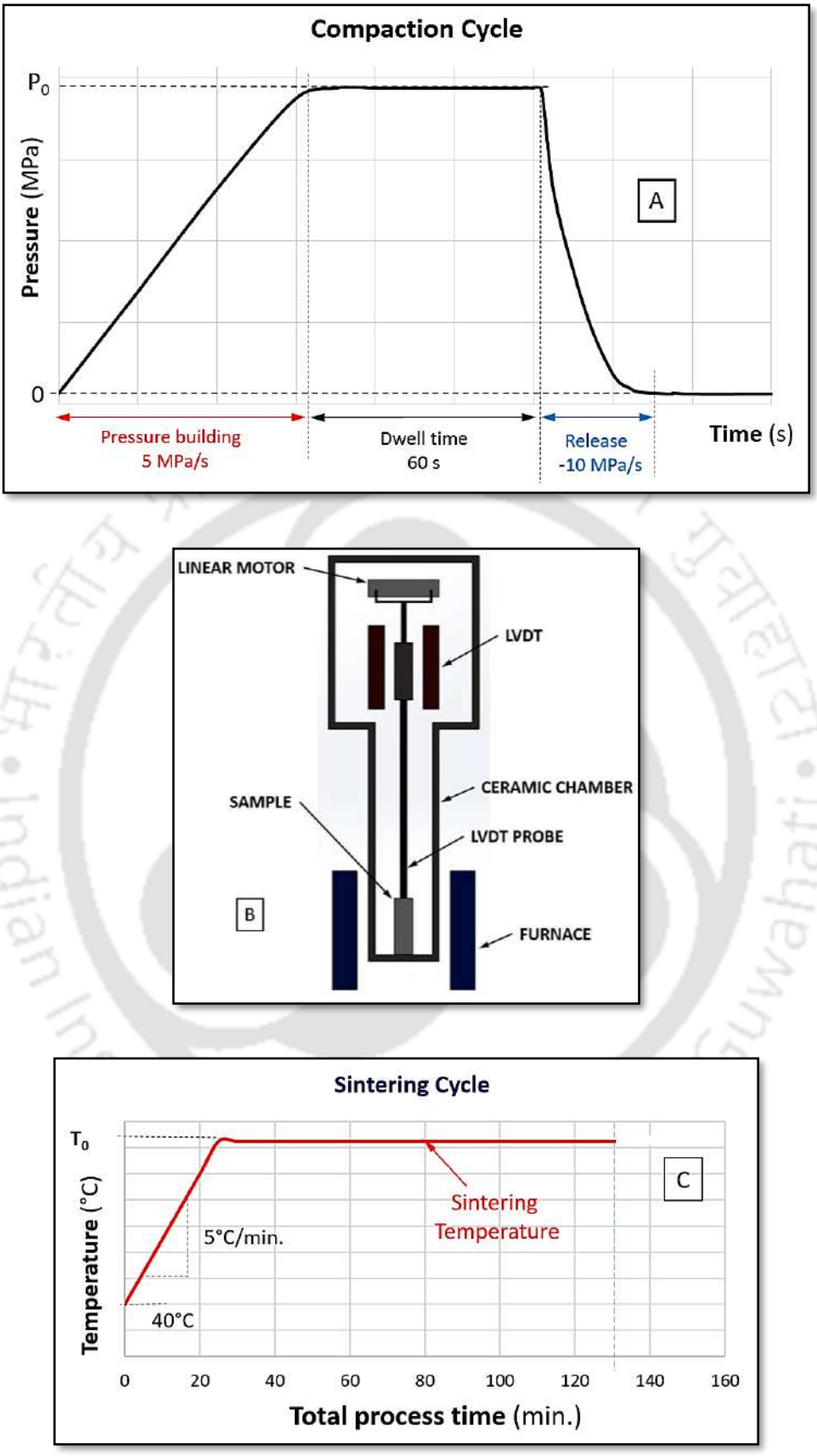

Figure 3.4. *(A) Pressure cycle during the compaction of UHMWPE powder (B) Schematic diagram of a Thermo-Mechanical Analyzer (TMA) (C) Temperature cycle during the sintering process*

The thermomechanical analyzer (TMA) is used to measure the expansion or shrinkage of the linear dimension of a sample as a function of temperature and time with the help of a linear motor-driven LVDT resting on it with negligible compressive load (50mN) ensuring perfect contact between the test sample and LVDT probe. Present study utilized the TMA as an effective tool to identify different stages, transition points and the end point of bulk sintering process of UHMWPE.

To identify the effect of sintering temperature on sintering kinetics and mechanical properties of UHMWPE, the thermo-mechanical characteristics as shown in process 3, at Figure 3.1**,** are carried out at five different isotherms ($\mathbf{T_s}$) within the temperature range of 150°C – 190°C with the heating rate of 5°C/min. from 40°C onwards and maintained at the desired temperature for a total processing time of 130 minutes. The sintering temperature at which the highest density and hardness of the samples are achieved, is identified as the optimum and all further processes utilized the said optimum sintering temperature found in process 3**.** Samples prepared in process 5 are sintered in TMA**,** whereas the green compacts obtained through the processes 4, 6 and 7**,** as referred in Figure 3.1 are sintered in a hot air oven.

Figure 3.4(B) and Figure 3.4(C) are the schematic diagram of a Thermo-Mechanical Analyzer (TMA) and the temperature cycle during the sintering process, respectively. Dwell time and heating time used during the test are shown in Figure 3.4(C).

3.3.3. Characterization Techniques

3.3.3.1. The melting zone of UHMWPE

Sintering temperature of a polymer must be higher than that of its onset melting point to obtain the defect free samples, whose properties are at par with that of conventionally melt-processed polymer [165]. Differential scanning calorimetry (DSC) studies, mentioned as process 1 in Figure 3.1, are performed on nascent polymer powder (~10mg) using DSC, STA 8000 (PerkinElmer, UK) at a heating rate of 5°C/min. under a nitrogen purge in the temperature range between 40°C to 200°C to confirm the melting zone of GUR 1050.

3.3.3.2. The diffusion point of UHMWPE

To identify the diffusion-point of the polymer, where the temperature at which coalescence and densification of UHMWPE particles start, cylindrical compacts of 15 mm length (L_0) and 8 mm diameter (D_0) are tested in the range of 40°C to 160°C at a heating rate of 5°C/min. using TMA, SS6000 (SEIKO, Japan) and the sample displacement is continuously monitored by a linear variable differential transformer (LVDT) probe to calculate the change in length of a sample (ΔL) against temperature.

3.3.3.3. Rheology analysis

The temperature ramp test is performed using a rheometer, Physica MCR 101(Anton Paar, Austria) on a circular disc-shaped UHMWPE sample of 25 mm diameter and 0.5 mm thickness to find out its least viscous point. In the process 4, the parallel plate technique is used under oscillatory mode with an angular frequency of 10 rad/s and a constant shear strain amplitude of 0.1% in the temperature range of 140°C to 200°C at a heating rate of 5°C/min. The selected temperature range is kept beyond the onset melting point of UHMWPE.

3.3.3.4. Microscopic analysis

To observe the diffusion process, live in progress, a small airtight chamber having a glass lid on top equipped with controlled heating and inert gas flow facility is attached with an optical microscope, Axiotech 100HD-3D (Carl Zeiss, Germany) and utilized for process 2, as referred in Figure 3.1. A small and flat broken part of polymer compact is placed inside the chamber and the location at which two neighbouring particles of similar size is identified using the microscope with a magnification of 50X to investigate the sintering kinetics of UHMWPE. Process 5, as referred in Figure 3.1, intended for determination of optimum sintering duration, processed the polymeric powder utilizing the optimum compaction pressure and sintering temperature identified by process 2 and 4, respectively, with different sintering duration in the range of 30-150 minutes at an increment of 20 minutes following the heating cycle as reported earlier. The evolution of cross-sectional microstructures of the samples with sintering duration is investigated under FESEM, Sigma 300 (Carl Zeiss, Germany).

3.3.3.5. Density measurement

Green density and sintered density of the test samples obtained through the processes ②, ③, ⑤ and ⑦, as referred in Figure 3.1, are calculated by the displacement method following Archimedes' principle with an in-house developed set-up, where Heptane 99.9% (density 0.7g/ml) is used as a working fluid as per **ASTM D792-13** [166].

3.3.3.6. Hardness Measurement

A micro-hardness tester, 1600-6306 (BUEHLER, USA) is used to measure the Vickers hardness of sintered polymer samples obtained through different processes at a constant normal load of 50 gf, as per **ASTM E384-17** [167]. Shore D hardness of the same samples is also measured using STECH DSHT-DIII Durometer with the precision of 1° in the scale range from 0 to100 following **ASTM D2240-15** [168].

3.3.3.7. Analysis of Mechanical properties

All the optimum processing parameters obtained in process ①-⑤ are used to prepare UHMWPE tensile samples as shown in process ⑥ and the optimum mechanical strength of the samples are studied. A digitally controlled closed-loop servo-hydraulic universal testing machine, 8801(INSTRON, US) having a dynamic loading capacity of 100 kN with a load cell accuracy of 5 N is used to evaluate the mechanical strength of UHMWPE samples in compression and tensile modes. Compression test of cylindrical samples of 15 mm length (L_0) and 8 mm diameter (D_0) is performed with three repeats at room temperature as per **ASTM D695** at a constant displacement rate of 0.5 mm/min and the offset method at a strain of 0.002 is used to define their yielding [169]. Tensile strength of the polymer is evaluated with type 'V' dumbbell-shaped test specimen as prescribed in **ASTM D638** at room temperature [170]. The crosshead speed of 0.5 mm/min. is maintained during the test till the fracture of the samples. Three samples are tested to check the repeatability and the average results are reported.

3.3.4. Results and Discussion

3.3.4.1. Melting zone and Diffusion point

Figure 3.5 shows DSC, TMA and DTMA curves against temperature generated during thermal analysis of UHMWPE powder compacts processed at 34.5 MPa (5 ksi). DSC curve represents heat flow into the test sample while heated from 40°C to 190°C at a heating rate of 5°C/min. including its melting zone. TMA curve represents the LVDT displacement generated by the test sample due to its thermal expansion or diffusion against temperature while heated from 40°C to 160°C at a heating rate of 5°C/min. including its diffusion point. Additionally, the temporal derivative of sample length i.e., **dL/dt** vs **t** curve (DTMA) obtained from TMA is plotted against the same temperature ramp for reconfirmation of the obtained peaks. The melting peak is identified from the heat flow curve. The onset melting point and melting endpoint of UHMWPE are observed to be 132°C and 161.5°C, respectively, whereas the melting peak is observed at 150°C. All these results are also matched with the peaks obtained from the DTMA curve as shown in Figure 3.5. The enthalpy of fusion of GUR1050 is observed to be 98.54 J/g from the DSC thermograms and it is closely matching with published value of 92.7 J/g [171]. The LVDT displacement is observed to change its direction at 145°C, which indicates the initiation of diffusion of polymer particles within the sample compact.

This is the minimum temperature at which the coalescence among UHMWPE particles is initiated. It is interesting to note that the diffusion point (145°C) is well above the onset melting temperature (132°C) as determined by DSC, but still substantially below the peak melting point of 150°C, which is a well-known characteristics of polymers [172].

3.3.4.2. Least viscous point

Complex viscosity of UHMWPE against temperature, beyond its onset melting point (132°C), is shown in Figure 3.6. It is observed that UHMWPE remained within its elastic limit with higher value of shear storage modulus (**G'**) compared to its loss modulus (**G"**) in this temperature range, and the temperature at which the least viscosity of molten UHMWPE ($\mathbf{T}_{VS}$) is found at 165°C. The complex viscosity ($\boldsymbol{\eta}^*$), shear storage modulus (**G'**) and shear loss modulus (**G"**) at $\mathbf{T}_{VS}$ are observed to be 61 kPa.s, 0.6 MPa, and 0.1 MPa, respectively.

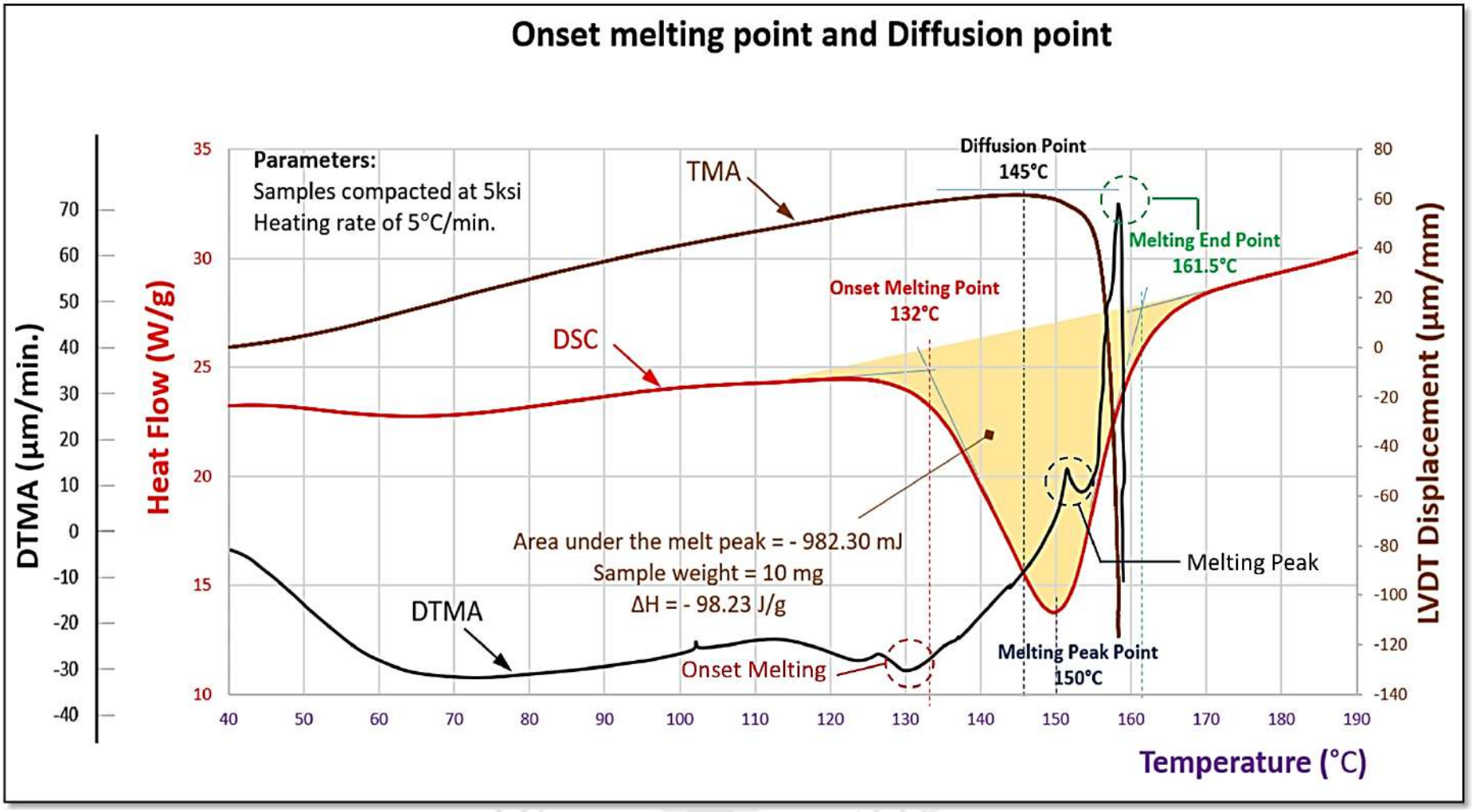

Figure 3.5. *Thermal analysis of GUR 1050 powder compacted at 5 ksi. DSC curve represents heat flow into the test sample while heated from 40°C to 190°C at a heating rate of 5°C/min. TMA curve represents the LVDT displacement generated by the test sample due to its linear thermal expansion or diffusion against temperature while heated from 40°C to 160°C at a heating rate of 5°C/min. DTMA curve (dL/dt vs t) calculated from TMA is plotted against the same temperature*

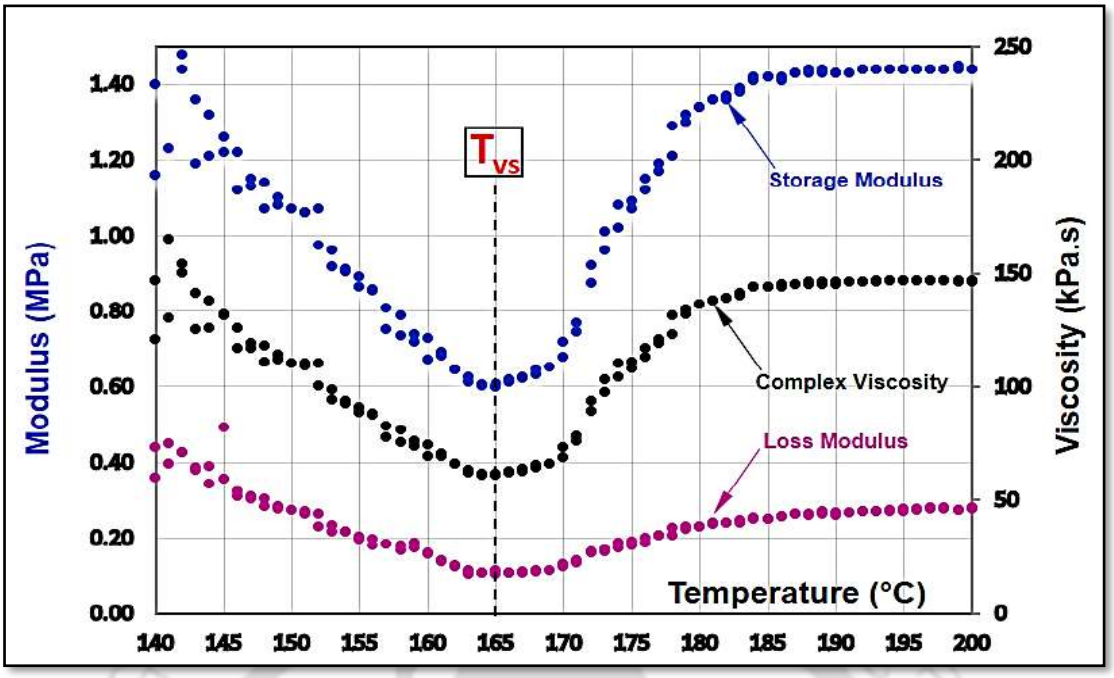

Figure 3.6. *Effect of Temperature on rheological characteristics of UHMWPE*

3.3.4.3. Sintering kinetics of UHMWPE

Figure 3.7 shows a typical LVDT displacement vs time curve (TMA) along with its temporal derivative i.e., **dL/dt** vs **t** curve (DTMA) of a sample obtained during the sintering process at 160°C from the initial temperature of 40°C (state **A**). The compact is observed to undergo thermal expansion in solid state before reaching its melting point. After initiation of polymer melting at 125°C, the DTMA peaks revealed several parameters to define the relationship between its viscosity and temperature.

The melting initiation point i.e., onset melting point ($\mathbf{T_{MO}}$ at state **B**) and melting end point ($\mathbf{T_{ME}}$ state **C**) obtained from DTMA curve are found to have a close agreement with the results observed from DSC curve, as reported in Figure 3.5. The onset temperature of viscous flow ($\mathbf{T_{VO}}$), as described in the literature, is found to be 151°C for the said polymer [173], which coincided with the peak melting point (T_{MP}) observed from the DSC analysis (150°C). The lowest viscosity of UHMWPE is achieved at a temperature of 157°C ($\mathbf{T_{VS}}$), where DTMA curve attained its maximum value [173], which is found to be within 5% variation from that of the value obtained from its rheological studies (165°C). The TMA curve revealed the starting point of diffusion process after 30 minutes (state **D**) at the heating rate of 5°C/min. which is at the diffusion temperature ($\mathbf{T_D}$) of 145°C, and it is about

a midway of its melting zone **BC**. The length of the sample is observed to be decreased when the diffusion process is progressed until the lowest value is attained by the TMA curve at 73 minutes of processing time (state **E**) with ~7.3% reduction in sample length. Thereafter, the length of the sample is observed to increase by ~1% in comparison to that at state **E** during the next 10 minutes (state **F**). After 90 minutes of processing time when heating rate of 5°C/min is maintained, the sintering kinetics is found to be stabilized, which is confirmed from the TMA and DTMA curves along the length of the sample.

Figure 3.8 shows the various stages of diffusion process of UHMWPE under live heating condition. Figure 3.8 (a) shows two neighbouring particles of similar size identified under an optical microscope. The heating profile used in TMA analysis as referred in Figure 3.4 (C) is applied here and the various stages of diffusion process between the two particles are observed under microscope live-in progress. Figure 3.8 (b) shows the snapshot of the micrograph at 30 minutes, when the particles are in a semi-solid state and on the verge of diffusion, i.e., point **D** in Figure 3.7. After 60 minutes of sintering, the particles are found to be merged together by diffusion, i.e., point **C** in Figure 3.7 and it is shown in Figure 3.8 (c).

At 90 minutes of processing time, the particles are found to be diffused completely at their common surface of contact retaining individual free surface boundary intact, i.e., point **F** in Figure 3.7, which is shown in Figure 3.8 (d). As noticed from the TMA trend, no further local diffusion of individual particles is observed, hence the end of particle diffusion (state **E** with respect to Figure 3.7) is confirmed. As shown in Figure 3.8 (e)-(h), the boundary of individual particles is diffused with surrounding particles with time and it is completely disappeared after 130 minutes to form a single-phase bulk material as desired for a product development. This instant is the end of bulk sintering, beyond which the structural integrity of the sample is lost.

But the bump appeared in the TMA curve in between 73 and 88 minutes (the points **E** and **F** with respect to Figure 3.7) of processing time is expected due to diffusion relaxation of different particles. In order to ensure repeatability of the sintering kinetics, TMA analysis of three different samples is performed and their dimension at three different sintering duration are measured using a micrometer between 73 -93 min., which are reported in Table 3.2 with respect to their initial values to determine the volumetric variation in the sample during the said range.

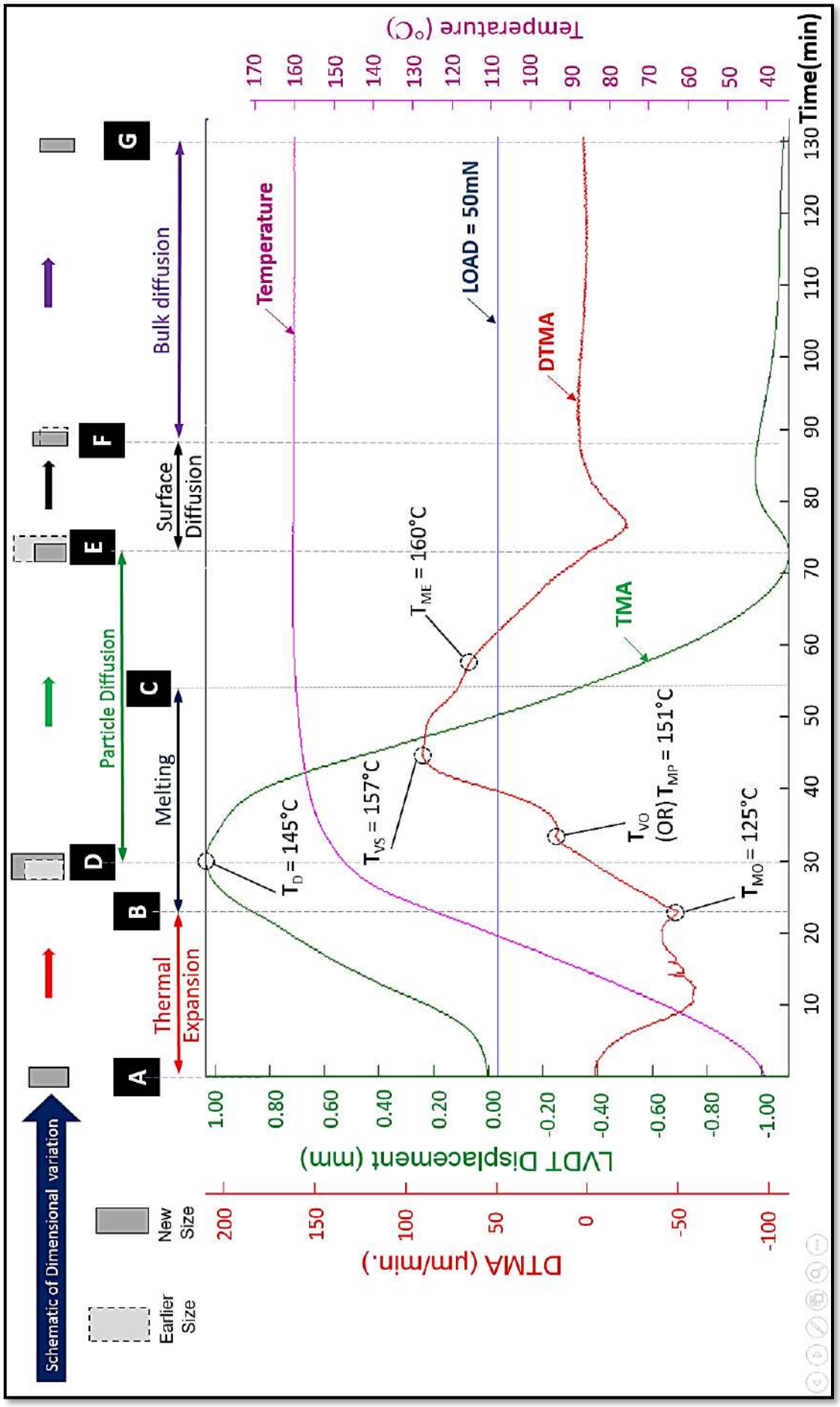

Figure 3.7. *Sintering kinetics of a GUR 1050 powder compact*

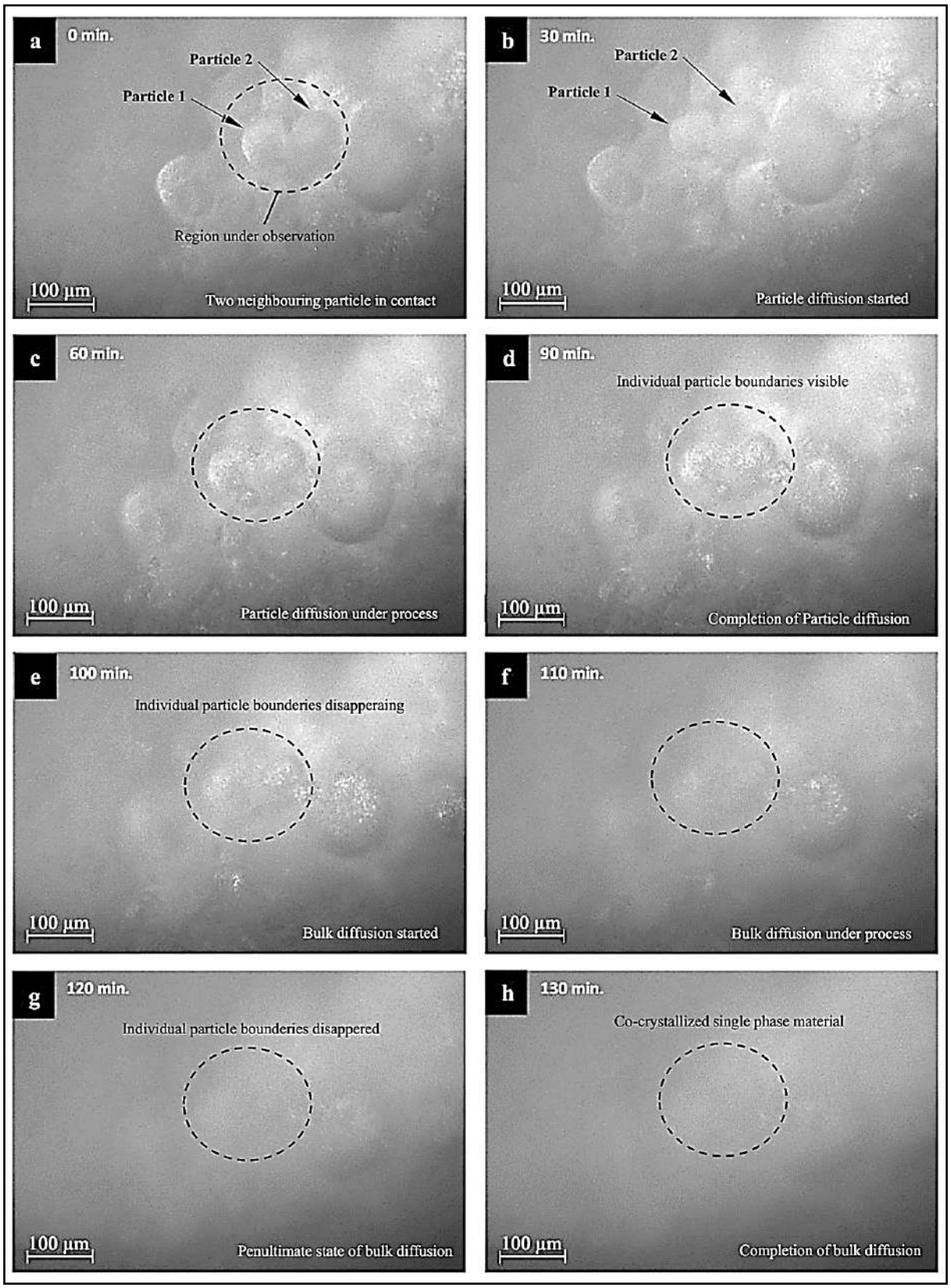

Figure 3.8. *Various stages of a diffusion process of UHMWPE particles against duration of sintering at the sintering temperature of 165°C after (a) 0 min. (b) 30 min. (c) 60 min. (d) 90 min. (e) 100 min. (f) 110 min. (g) 120 min. (h) 130 min.*

***Table 3.2**. Dimensional variation of the sample against sintering duration*

Sintering Duration (t) (min.)	$\frac{L_t}{L_0}$ x 100 (%)	$\frac{D_t}{D_0}$ x 100 (%)	$\frac{A_t}{A_0}$ x 100 (%)
73	92.73	99.37	92.33
83	93.67	99.00	92.62
93	92.87	98.88	91.86

L_0 - Initial Length of the sample

D_0 - Initial Diameter of the sample

A_0 - Total surface area of the sample at time = 0

L_t - Length of the sample at time = t

D_t - Diameter of the sample at time = t

A_t - Total surface area of the sample at time = t

At 73 min. of sintering (point **E**, i.e., before stating of surface diffusion), volume of the sample is calculated to be ~91.6% of its initial volume, which is observed to be ~91.8% and 91.5% at 83 min. (in between points **E** and **F**, i.e., during surface diffusion) and 93 min. (beyond point **F**, i.e., upon completion of surface diffusion) of sintering, respectively. It is clearly noted that the samples are undergone a quick iso-volumetric transformation during 73-93 minutes of processing time after which there is a volumetric diffusion of a sample with a rate continuously decreasing with time. In order to get complete information during the diffusion process, the cross section of the sample sintered at 83 minutes is examined under SEM and the corresponding image is shown in Figure 3.9(A). It is evident from the image that completion of sintering is not the same throughout the cross section. In the free surface region up to 0.4mm thickness, the sample is found to be co-crystallized as a single phase. However, the core region is still at the end state of particle diffusion for the same sintering duration and it is in the process of bulk diffusion, which is shown in Figure 3.9 (B).

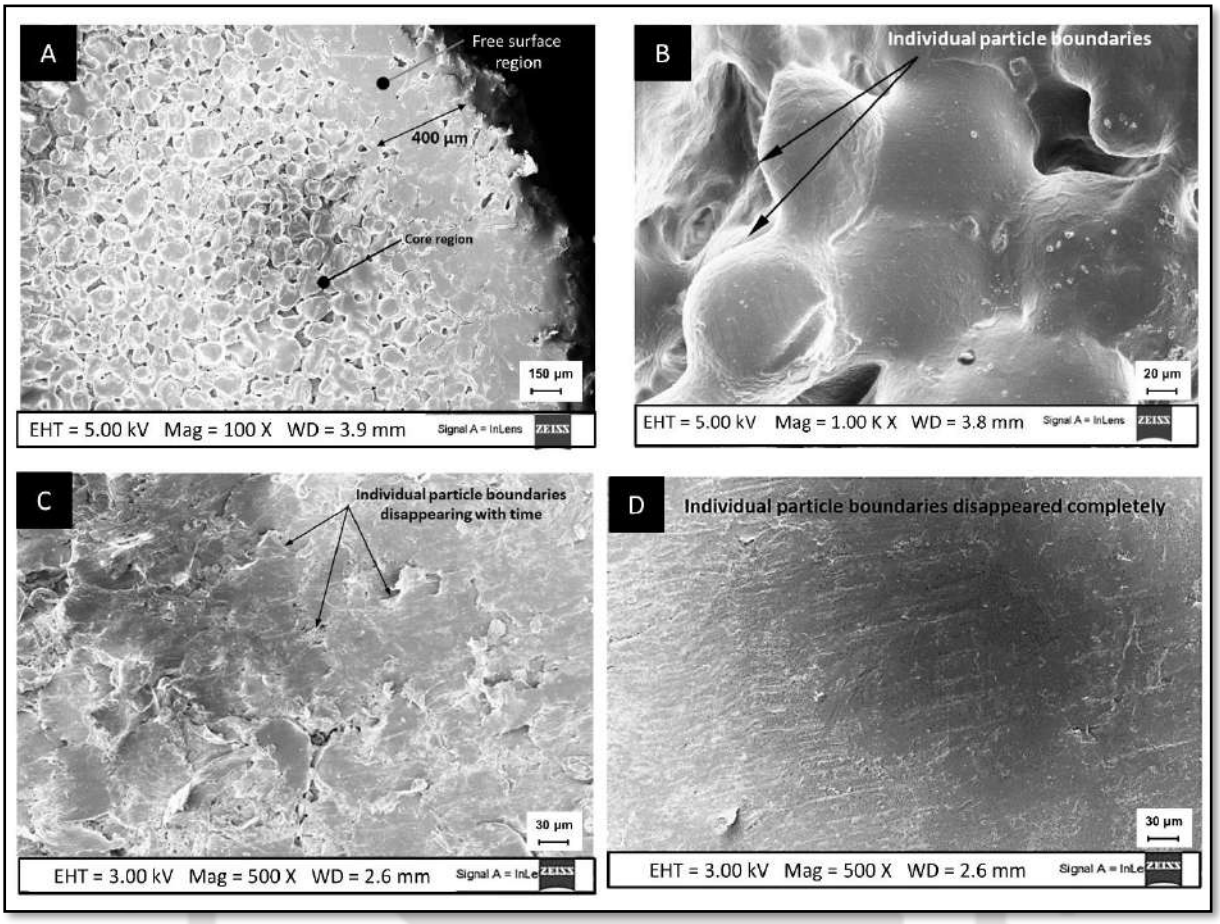

Figure 3.9. *Sintered product with compaction pressure of 15 ksi and sintering at 165°C (A) overall cross section after 83 minutes (B) the core region after 83 minutes (C) the core region of the sample after 110 min. (D) the core region of the sample after 130 min. of the heating cycle*

At this stage, the sample is found to complete its surface diffusion as reported as state **F** in Figure 3.7. During 73-93 minutes of processing time, the samples at molten state are readjusted their dimension by the 'growing together of particles' and the 'shrinking of cavities' at free surface region, where the principal motivation of sintering is to minimize the total surface free energy of the sample by decreasing its total surface area, as evident in Table 3.2. After 110 minutes of sintering, the individual particle boundaries are found to be disappeared as bulk diffusion is in progress and it is also shown in Figure 3.9 (C). Figure 3.9 (D) confirms the completion of bulk sintering after 130 minutes, which ensured a single-phase bulk material with completely disappeared particle boundaries.

- **Comparison with FRENKEL'S two-particle model of diffusion**

Frenkel's two-particle model of diffusion is shown in Figure 3.10(A) and it can be expressed mathematically in terms of nose radius $\boldsymbol{X}$ and the particle radius $\boldsymbol{a}$, where the corresponding relation between them is given in Equation (3.1) [165].

$$\frac{X^2}{a} = \frac{3}{2}\frac{\gamma}{K}t \qquad \ldots (3.1)$$

where, $\boldsymbol{\gamma}$ is the surface free energy and $\boldsymbol{t}$ is sintering duration. Flow consistency index $\boldsymbol{K}$ and flow behavior index n describe the relation between shear stress ($\boldsymbol{\tau}$) and shear strain rate ($\dot{\epsilon}_s$) of non-Newtonian fluid during its flow and the corresponding *Ostwald-de Waele power law* is given in Equation (3.2) [165].

$$\tau = K(\dot{\epsilon}_s)^n \qquad \ldots (3.2)$$

Upon completion of sintering, $\boldsymbol{X/a} = \mathbf{1}$ is achieved and the schematic representation of the same is shown in Figure 3.10(A). To observe the growth of nose radius ($\boldsymbol{X}$) with time, the core regions of test samples are observed under SEM and the neighbouring particles of similar size are compared with that of their state of diffusion with Frenkel's model. For a sample sintered till 55 minutes (**state C** with respect to Figure 3.7), the nose radius ($\boldsymbol{X}$) is found to be 22.9 μm for two adjacent particles of radii ($\boldsymbol{a}$) 51.6 μm as depicted in Figure 3.10(B) and the corresponding $\boldsymbol{X/a}$ is found to be 0.44. It is noted from Figure 3.10(C) that the nose radius is increased with time and the radius of two adjoining particles is observed to be 42.11 μm and 44.20 μm. It is also observed that the nose radius $\boldsymbol{X}$ is found to be 40.52 μm after 73 minutes of sintering, and the corresponding average value of $\boldsymbol{X/a}$ is found to be 0.94, which has an excellent agreement with the theoretically expected $\boldsymbol{X/a}$ value of 1 at the end of particle diffusion process.

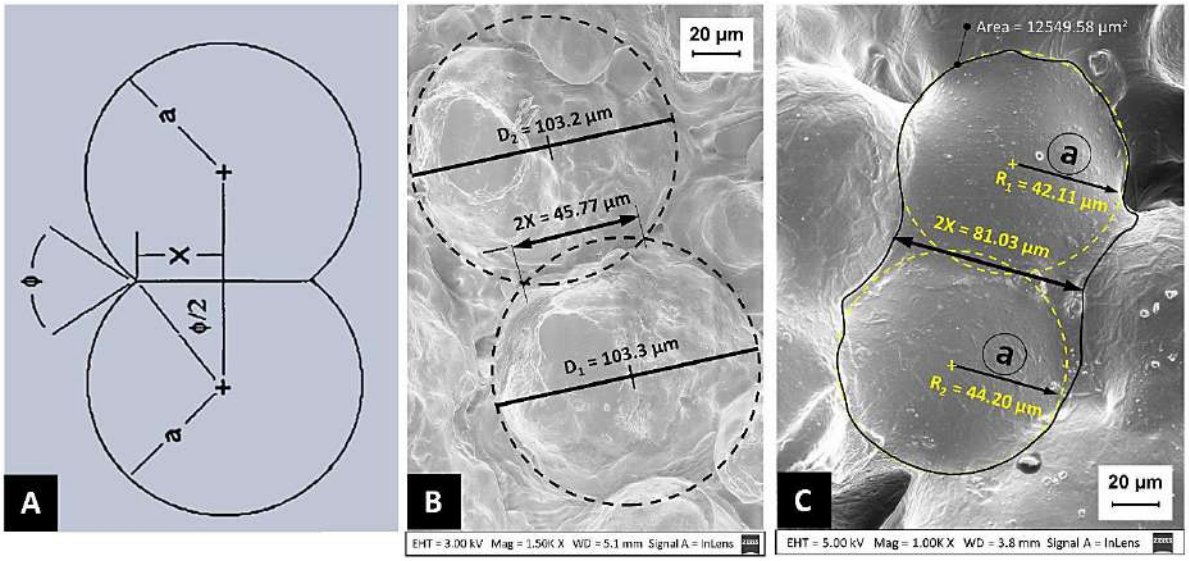

Figure 3.10. *(A) Frenkel's two particles model of diffusion [14] (B) Closer look to diffused particles in a sample compacted at 15 ksi and sintered at 165°C after 55min. (C) Closer look to diffused particles in a sample compacted at 15 ksi and sintered*

3.3.4.4. Influence of processing parameters

As the *compaction pressure*, *sintering temperature* and *sintering duration* are expected to play a major role in deciding the characteristics of a final product made of UHMWPE, their individual as well as combined influence on sintering kinetics and mechanical properties of UHMWPE based test samples are investigated.

I. Compaction pressure

The influence of compaction pressure and its optimum value for processing GUR 1050 is revealed through the process (2), as referred in Figure 3.1, and the results are discussed below in detail.

Figure 3.11(A) shows the LVDT displacement curves of the samples compacted at different pressure in the range of 34.5-276 MPa (5-40 ksi) against sintering temperature and the figure inset is focused on the diffusion region in the temperature range of 142°C to 150°C. A closer view of the TMA curves revealed that the green compacts prepared at different compaction pressure started to densify at a temperature in the range of 145°C to 148.5°C without showing any definite trend against their compaction pressure. Thus, it could be inferred that the diffusion temperature of the sample is not found to be significantly

influenced by the compaction pressure in the range of 34.5-276 MPa (5-40 ksi). Figure 3.11(B) shows the diffusion time required for the samples prepared at different compaction pressure. Diffusion time is calculated as the time interval between the diffusion point (State **D**) and the end of particle diffusion (State **E** with respect to Figure 3.7). The sample compacted at 103.5 MPa (15 ksi) is required to have the diffusion time of 70 minutes to complete its particle diffusion phase. All other types of test samples have taken ~60 ± 5 minutes to complete their particle diffusion stage. Though there was no definite trend of diffusion time against their compaction pressure, the additional 10 minutes of diffusion time taken by 103.5 MPa (15 ksi) compacted samples might be an indication for the better extent of diffusion process compared to others. Green density of compacts and sintered density of final products are plotted against their compaction pressure, which are shown in Figure 3.11(C).

It is observed that the green density of compacts varied with the applied pressure during compaction but reached a limiting value of 0.906 g/cc at a pressure of 172.5 MPa. Further increase in compaction pressure caused a slightly decreasing trend of the green density, which is a result of the spring back effect of the UHMWPE particles due to their visco-elastic characteristics [174]. Interestingly, the sintered density attained its maximum value of 0.933 g/cc for the sample prepared at 103.5 MPa (15 ksi) of compaction pressure, which is comparable to that of 0.937 g/cc as obtained by HIP processed GUR 405 samples [175]. During compaction, the particles are brought under closed packing condition providing many 'particle to particle' contact zone. During melting, these contact zones acted as sites for neck formation. However, the compaction pressure beyond 103.5 MPa (15 ksi) is not found to increase the number of such contact zones further but it is expected to increase the frictional resistance across particle boundaries and reduce the interpenetration distance of a molecular chain across an interface [15].

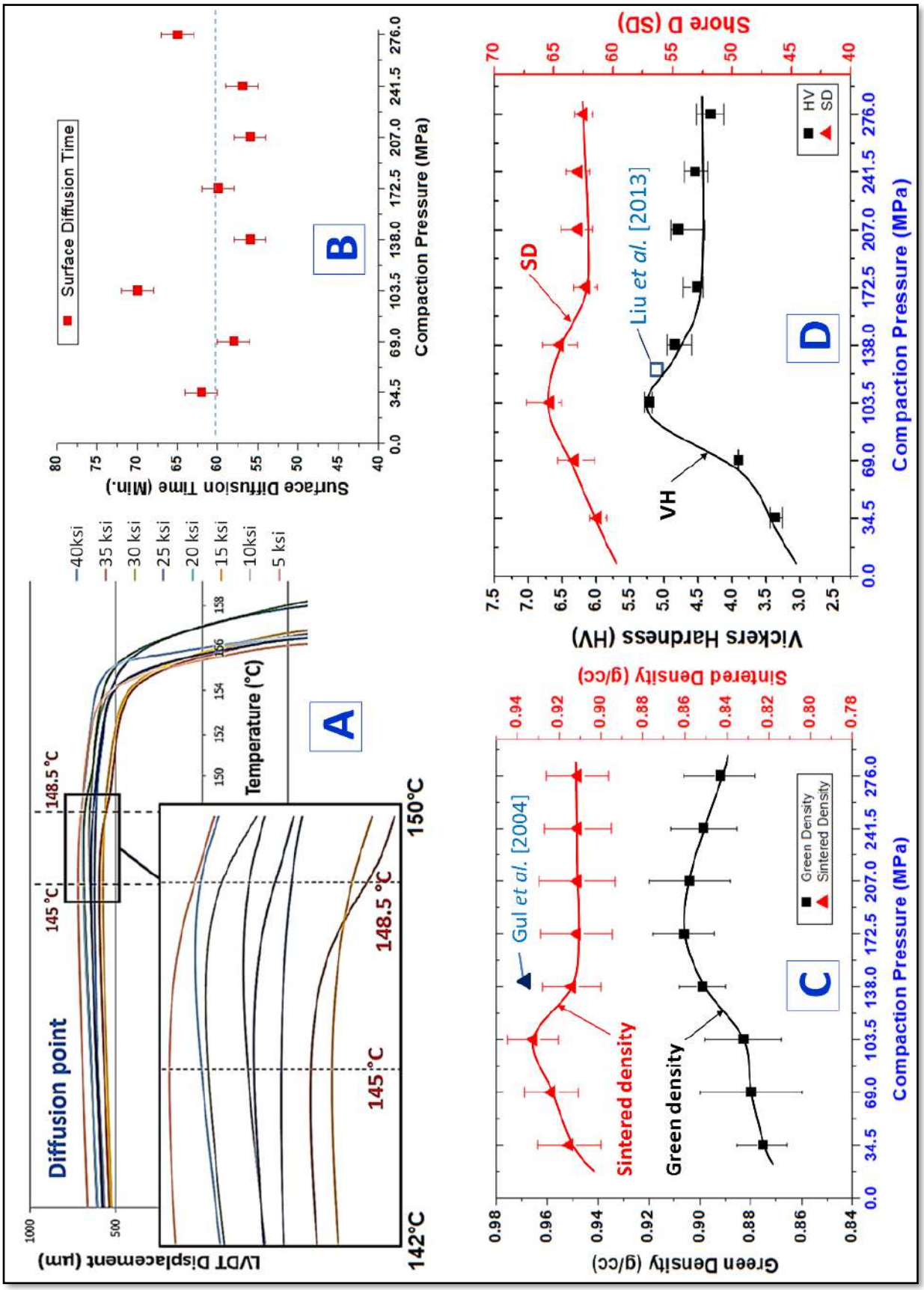

Figure 3.11. *Effect of Compaction pressure on(A) Diffusion point (B) Diffusion time (C) Density (D) Hardness of the UHMWPE*

Thus, the bulk diffusion process is hindered leading to decrease the sintered density beyond 103.5 MPa (15 ksi) compaction pressure with a stable density of 0.91 g/cc. Figure 3.11(D) shows the Vickers hardness and Shore D hardness of the UHMWPE samples against their compaction pressure and it is observed to follow a similar trend as that of sintered density. The highest value of 5.23 ± 0.06 VHN and 65.3 ± 1.5 SD is achieved for the samples processed at 103.5 MPa (15 ksi). The obtained results are found to be considerably better than that of compression moulded products having the hardness of 5.1 ± 0.7 VHN processed at 120 MPa [101].

Thus, it is inferred that a pressure of 103.5 MPa (15 ksi) is the best for compaction of GUR 1050 UHMWPE powder in terms of densification and mechanical integrity after being sintered. For all further processing, the samples are prepared at 103.5 MPa (15 ksi) compaction pressure.

II. Sintering Temperature

The mechanical properties of UHMWPE samples are obtained against different sintering temperatures in the range of 150°C – 190°C, while maintaining the compaction pressure of 103.5 MPa (15 ksi) and total process duration of 130 minutes. The test results obtained from process 3, as referred in Figure 3.1, are discussed below in detail.

Figure 3.12(A) shows the influence of sintering temperature on the sintered density of the UHMWPE samples. The density of the samples is observed to increase considerably once the sintering temperature is increased beyond the peak melting point of the polymer, i.e., 150°C. The highest density is observed to be 0.941 g/cc for the samples sintered at 170°C**.** When the sintering temperature is increased from 170°C onwards, the polymer samples changed from an opaque state to a translucent state. It is noticed that the variation in sintered density of UHMWPE samples is not observed to be more than 2%, when the sintering temperature is maintained in the range of 160°C to 190°C. It is also noted that the density of UHMWPE is further improved by ~1% through the optimization process 3 over process 2, as reported in Figure 3.1, at a sintering temperature of 170°C, which is close to its least viscous point identified in Figure 3.6.

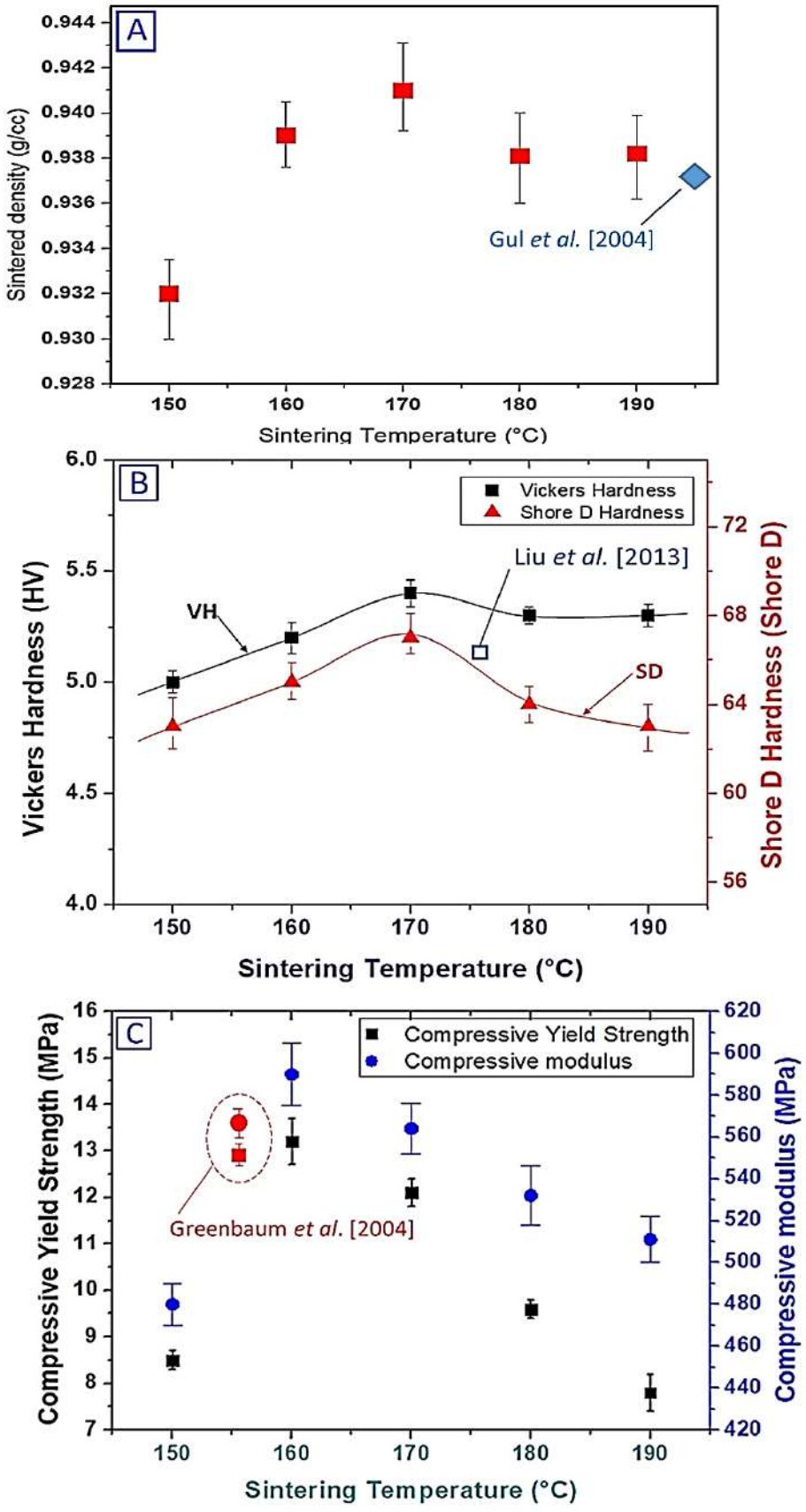

Figure 3.12. *Effect of Sintering Temperature on (A)Sintered Density (B) Hardness (C) Compressive properties of UHMWPE*

Vickers hardness and Shore D hardness of the UHMWPE samples against their sintering temperature are shown in Figure 3.12(B). It is noted that the hardness of the samples is observed to be increased with temperature in the range of 150°C to 170°C, where it reached its maximum value at 170°C beyond which the values of hardness is found to be decreased. The maximum value of 5.4 ± 0.05 HVN and 67 ± 1.4 SD is obtained by optimizing the processing condition, as reported in process 3, and the results are further improved by ~3% over the results reported by process 2, as referred in Figure 3.1.

Compressive properties of UHMWPE are investigated against sintering temperature and the results are shown in Figure 3.12(C). The maximum compressive yield strength and modulus of the samples are observed to be 13.2 ± 0.5 MPa and 721 ± 15 MPa, respectively, when they are sintered at 160°**C**. The obtained results are found to be considerably better than that of ram extruded GUR 1050 products having the compressive yield strength and modulus of 12.9 ± 0.6 MPa and 570 ± 28 MPa, respectively [176]. Both compressive strength and modulus are observed to be decreased with higher sintering temperature beyond 160°**C**. Mechanical integrity and strength are the reflection of the extent of bulk diffusion of UHMWPE samples, which is hindered at higher sintering temperature of 180°C and 190°C due to its higher melt viscosity as reported in Figure 3.6, producing mechanically inferior products. Sintering kinetics of UHMWPE is majorly governed by its viscous state at the corresponding sintering temperature. Though it has high melt flow index, a lower viscosity state is expected to facilitate the flow of material across the particle boundaries and accelerate the bulk diffusion process to improve the mechanical integrity and strength.

Bulk mechanical properties of the samples like density and compressive strength as well as sub-surface property like Shore D hardness of UHMWPE are observed to attain their peak, when the samples are sintered at 160°C-170°C due to its least viscosity state (η^*~60 kPa.s) in this range of operating temperature as noticed in Figure 3.6. At higher sintering temperature of 180°C and 190°C, the viscosity of the polymer is observed to be more than 2.5 times (η^*~150 kPa.s) as that of the value reported at 160°**C** and the bulk diffusion of

the material is hindered due to lack of flow of polymer melt. As a consequence, the mechanical properties of UHMWPE are found to reduce significantly. Thus, the least viscosity point of the polymer (T_{VS} = 165°C), as reported in Figure 3.6, is chosen as the optimum sintering temperature for the rest of the studies.

III. Optimum sintering duration

Figure 3.13 shows the SEM images representing the evolution of microstructure of UHMWPE sintered at 165°C against sintering duration. The micrograph of the compacted sample shown in Figure 3.13(A) is the starting point of the process, as reported as state **A** in Figure 3.7 and schematically shown in Figure 3.14(A).

After 40 minutes of heating cycle (in between state **D** and **C** with respect to Figure 3.7), the diffusion temperature of the sample is reached and the particle boundaries having high surface roughness are started to diffuse at their point of contact and it is depicted in Figure 3.13(B). Individual particles are found to be in enlarged state due to their expansion behaviour. Particle boundaries are observed to get merged at their surface after 90 minutes of process and it is shown in Figure 3.13(C). At this stage, the particle boundaries are not found to be completely diffused as schematically shown in Figure 3.14(B). After 10 minutes of additional sintering, bulk diffusion is observed to progress further as shown in Figure 3.13(D). However, the completion of bulk diffusion is achieved after 130 minutes of total process time, where all particles are found to be merged as schematically shown in Figure 3.14(C) in order to form a single-phase bulk material and co-crystallized during the cooling process, which is confirmed from Figure 3.13(E). Further continuation of sintering, it resulted in a translucent material with micro-voids throughout its volume and it is shown in Figure 3.13(F).

These micro voids are found to combine together to generate larger ones with time as evident in Figure 3.13(G) and (H) after 150 min. and 170 min. of sintering, respectively, though bulk density of the product is measured to be within the experimental deviation. Being in prolonged molten state, the sample is found to become translucent and unable to retain its geometry due to high viscous characteristics of the material initiated by its self-weight as schematically shown in Figure 3.14(D).

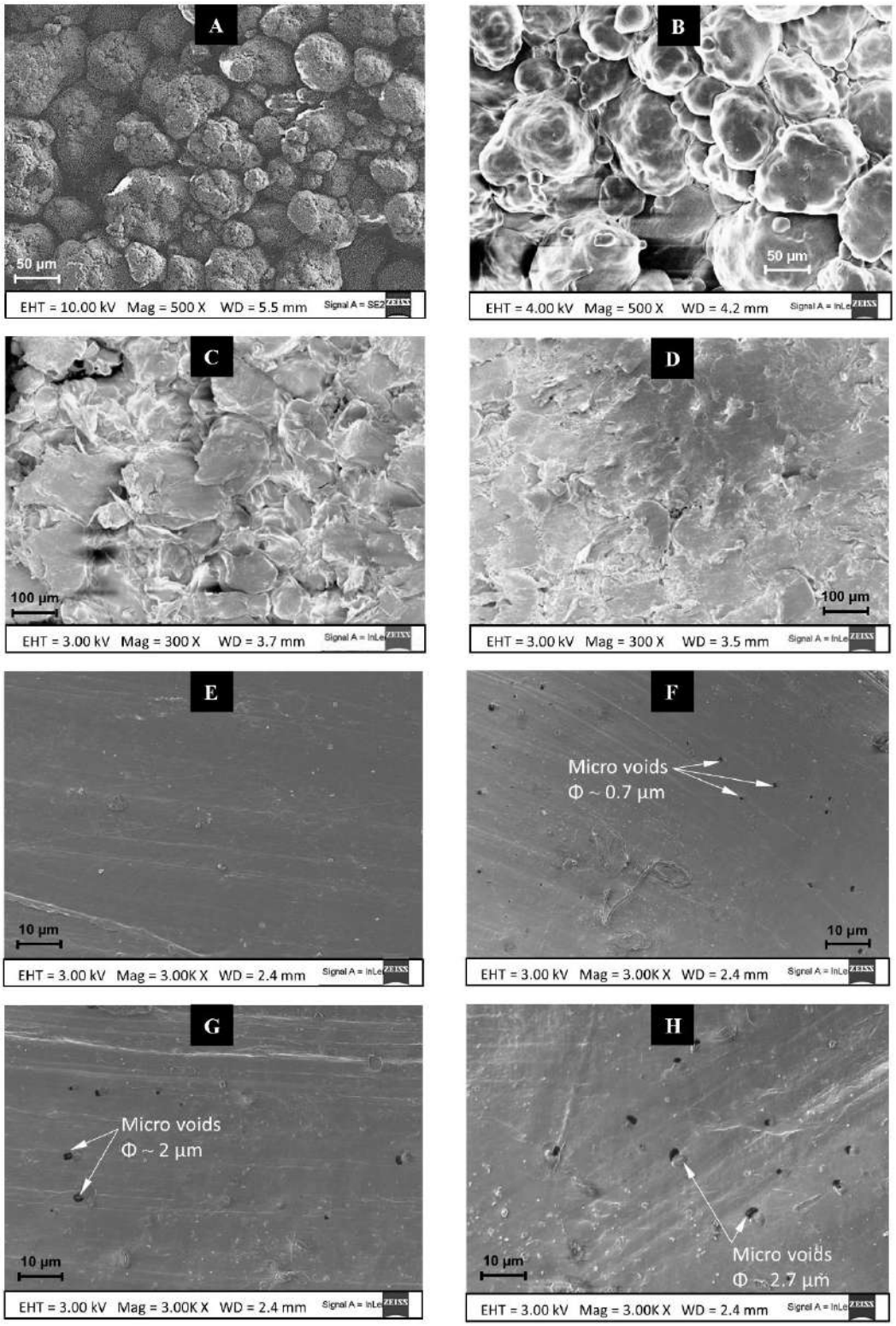

Figure 3.13. *Micrograph of UHMWPE samples compacted at 103.5 MPa sintered at 165°C after (A) 0 min. (B) 40 min (C) 90 min. (D) 110 min. (E) 130 min.(F) 150 min. (G) 170 min. (H) 190 min. of the heating cycle*

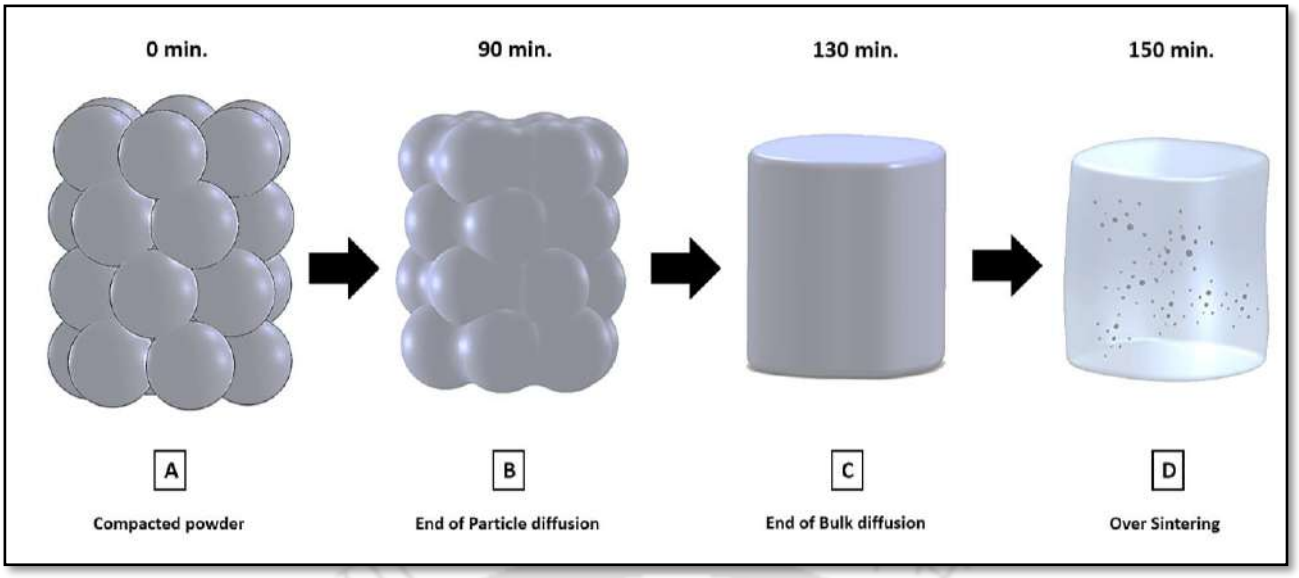

Figure 3.14. *Schematic representation of sample Morphology after the desired sintering duration*

Figure 3.15 shows the effect of sintering duration on the hardness and density of UHMWPE. After 30 minutes of sintering process, the particles are found to be in the of expansion mode, hence the overall volume of the sample is increased leading to decrease its density to 0.85 ± 0.01 g/cc, whereas its green density is observed to be 0.88 ± 0.01 g/cc. Once the diffusion process is started, the density of the sample is observed to be increased with time till 70 minutes of the process (state **E** with respect to Figure 3.7). Thereafter, the density of the sample is observed to reach its saturation limit irrespective of sintering time and it is reached its maximum value of 0.943 g/cc at 130 minutes of sintering time (state **G** with respect to Figure 3.7). Further increase in sintering time is not found to improve the sample density. Vickers hardness of the samples showed a similar trend in comparison to that of density against sintering duration and it is shown in Figure 3.15. The highest Vickers hardness of 5.4 is obtained after 130 minutes of sintering, beyond which a slight descent in hardness is noticed. Hence, the optimum sintering time of 130 minutes is used for the rest of the studies. The summary of variation in processing parameters and their optimum values, where the best characteristics are reported, are listed in Table 3.3.

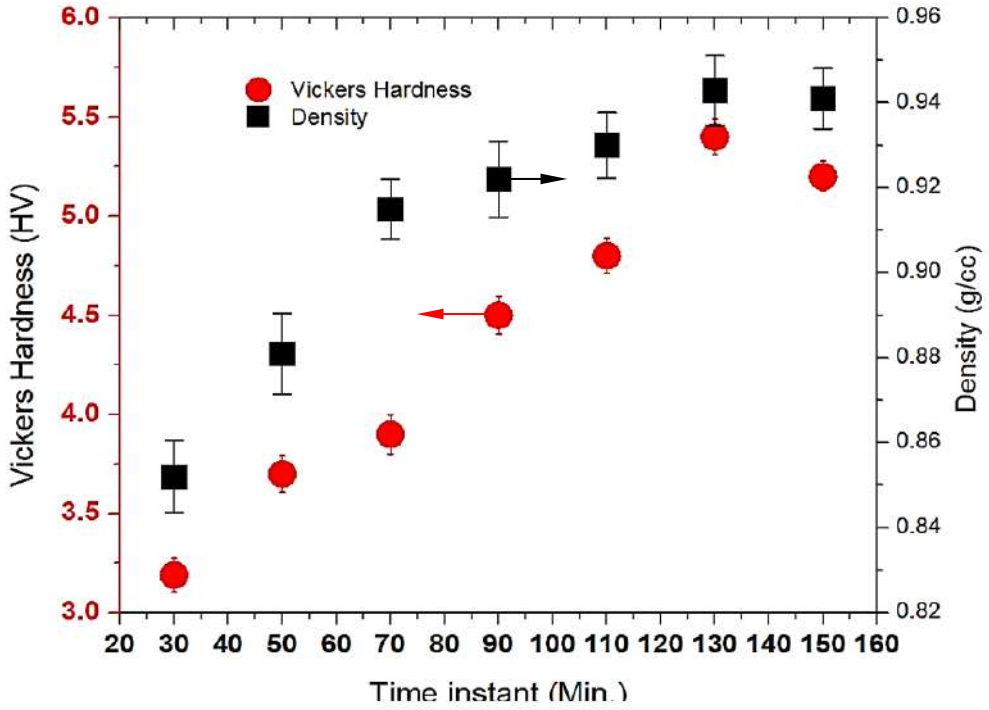

Figure 3.15. *Effect of Sintering duration on Hardness and Sintered density*

3.3.4.5. Characterization of optimally processed test sample: Tensile properties

Figure 3.16 shows the stress vs strain curve obtained from the tensile test of UHMWPE sample processed with the optimum processing parameters, i.e., 103.5 MPa (15 ksi) of compaction pressure, 165°C of sintering temperature and 130 min. of sintering time. The tensile yield strength and Young's modulus of the test sample are observed to be 22.5 $\pm$ 1.0 MPa and 625.2 $\pm$ 50 MPa, respectively. The elongation at yield and break is observed to be 12.2% and 220.0%, respectively. Toughness of the material is calculated to be 76.22 GJ/m^3. These results are compared with the datasheet of compression moulded GUR 1050 provided by the manufacturer and the variation is found to be within the limit of ± 5%.

The values obtained from the present study and that of reported results are compared in Table 3.4. Tensile properties of UHMWPE are improved by the proposed method of processing as compared to compression moulded one and at par with the reported results of the polymer processed by various methods.

Table 3.3. *Summary of variation in processing parameters and their optimum values*

Processing parameter	Compaction Pressure (P_C) (MPa)	Sintering Temperature (T_S) (°C)	Sintering Duration (t_S) (Min.)
Range	34.5-276 (5-40 ksi)	150-190	30-150
Step	34.5 (5 ksi)	10	20
Optimum	103.5 (15 ksi)	165	130
Best characteristics	**ρ** = 0.933 g/cc **VH** = 5.23	**ρ** = 0.941 g/cc **VH** = 5.4 σ_Y(C) = 13.2 MPa	**ρ** = 0.943 g/cc **VH** = 5.42 σ_Y(T) = 22.5 MPa
ρ-Sintered Density, **VH**- Vickers Hardness, σ_Y(C)-Compressive Yield Strength, σ_Y(T)- Tensile Yield Strength			

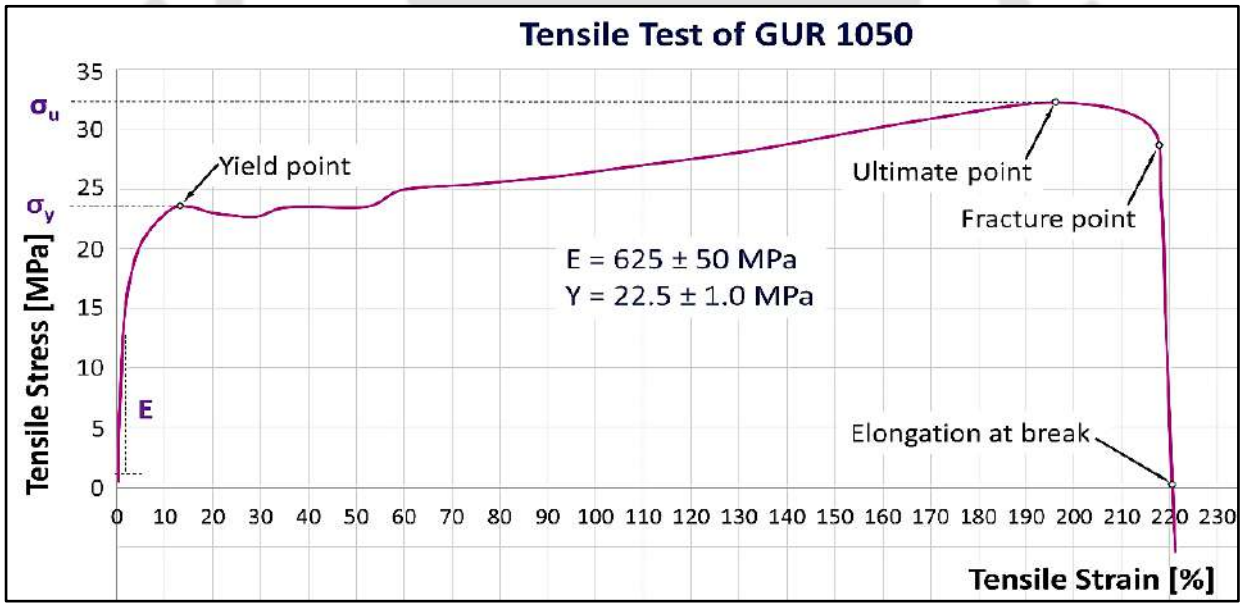

Figure 3.16. *Stress vs Strain curve of UHMWPE sample tested as per ASTM D638-14*

***Table 3.4**. Comparison of experimental data, reported data, and supplied data of UHMWPE*

Mechanical Properties	unit	ISO data	Earlier Reported Results	Present study results
Tensile Modulus	MPa	600 (ISO 527-1/-2)	670 (Pruitt [2005])	625.21 ± 50
Yield Stress	MPa	19 (ISO 527-1/-2)	19.3 ± 0.1 (Greer and Senyurt [2009])	22.52 ± 1
Density	kg/m^3	932 (ISO 1183)	942 (Liu *et al.* [2013])	941 ± 3

These results ensured that GUR 1050 powder is successfully processed in order to have the desired mechanical strength and integrity by the optimization methodology followed in this study. This novel technique for manufacturing UHMWPE products is further utilized for the development of Acetabular liner proposed to be used in total hip arthroplasty.

3.4. Processing and characterization of nanocomposites

Carbon nanotubes (CNT), carbon nanofibers (CNF) and graphene are becoming a popular choice of reinforcement among researchers for developing a new generation implant material due to their high strength, self-lubricating property and cytocompatibility. UHMWPE-MWCNT composites with different concentration of the filler are processed by the processing methodology similar to that used for UHMWPE. The methodology is designed to ensure uniform distribution and dispersion of MWCNT in highly viscous UHMWPE for enhancing its hardness, compressive properties, tensile properties and toughness to the maximum possible extent.

3.4.1. Sample Preparation

Composite specimens of required geometry are prepared by the technique explained in Section 3.3.2. with the powder mixture of UHMWPE and MWCNT after the functionalization of raw MWCNT, which is mechanically mixed with polymeric powder in a liquid medium using a magnetic stirrer and the preparation technique is described below in detail.

3.4.1.1. Functionalization of raw MWCNT

The chemical treatment of pristine MWCNT is carried out using a method described by Esumi *et al.* [177] to establish chemically active sites on its side walls for obtaining the interfacial bonding between the reinforcement and the polymer matrix apart from reducing the substrate impurity to increase its purity level. Concentrated Nitric acid (HNO_3) and Sulphuric acid (H_2SO_4) are taken in the ratio of 1:3 by volume and the required quantity of MWCNT are mixed and boiled at 140˚C for 40 min. using a magnetic stirrer and it is cooled to 30˚C. It is then followed by multiple rinsing of MWCNT with distilled water using a centrifuge REMI R-24, where the MWCNT and water is separated based on their density difference due to centripetal force until the pH value of supernatant is reached about 7 and then the wet MWCNT is dried in a hot air oven at 100 °C for 24 hr. The process flow followed for the chemical treatment of MWCNT is shown in Figure 3.17(A). The scheme of chemical functionalization of MWCNT is given in Figure 3.17(B) and the SEM micrograph of chemically treated MWCNT is shown in Figure 3.17(C). The chemically treated MWCNT are found to be undamaged in crystalline form but entangled to each other.

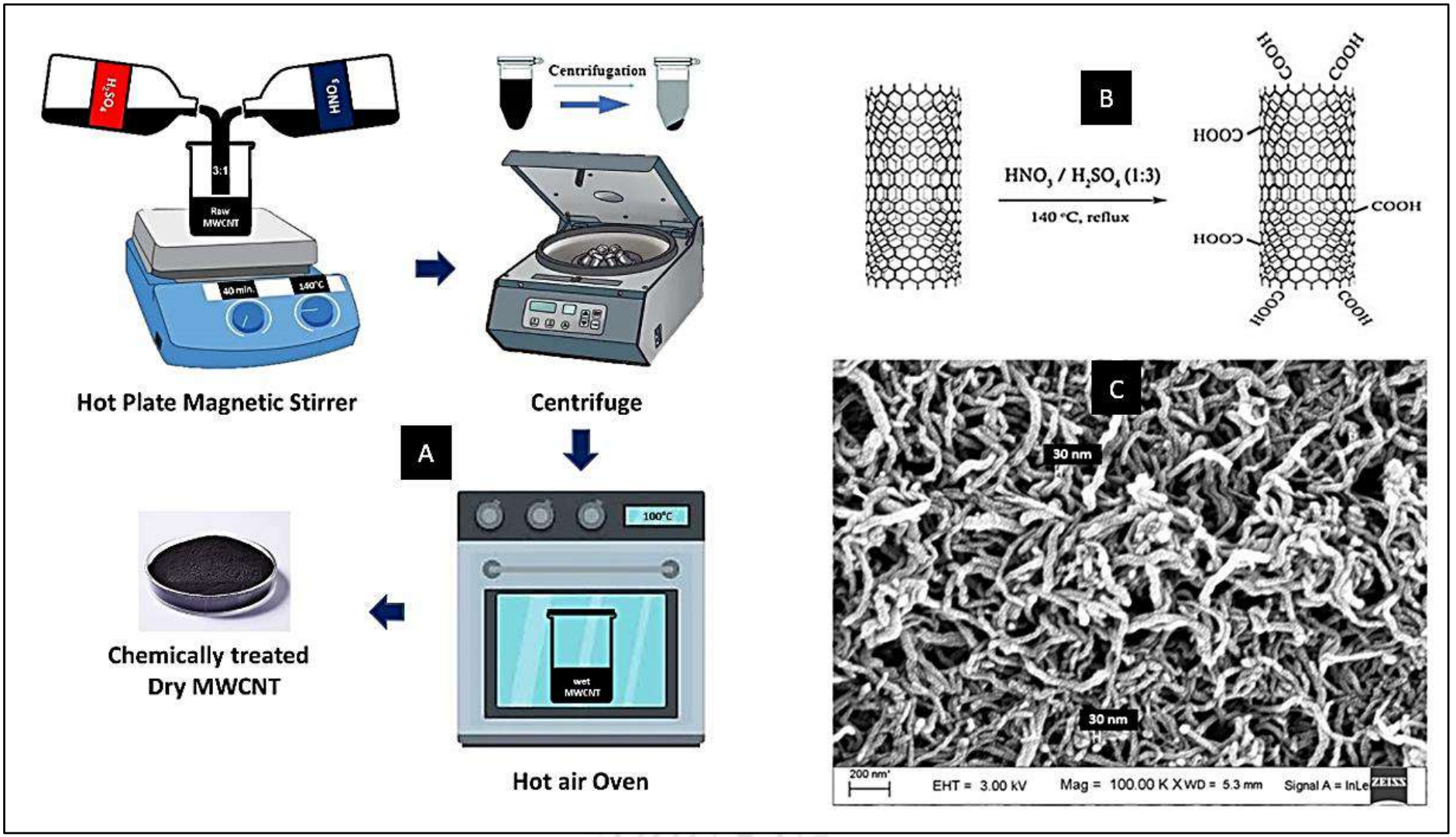

Figure 3.17.*. (A)The process flow followed for the chemical treatment of MWCNT (B) The scheme of chemical functionalization of MWCNT (C) SEM micrograph of crystalline MWCNT after chemical treatment*

3.4.1.2. Mechanical mixing of UWMWPE and MWCNT

The mechanical mixing of UHMWPE powder and chemically treated MWCNT is required to be done by a process that ensure homogeneous dispersion as well as distribution of MWCNT in UHMWPE without any physical damage on the constituents. Standard methods for the dispersion such as ultra-sonication, calendaring, and ball milling have their own limitations. Thus, it is proposed to have a unique combination of ultra-sonication and magnetic stirring at 80°C for physical blending of UHMWPE and MWCNT powder as shown in Figure 3.18 with the resultant UHMWPE/MWCNT powder mixture having different weight ratio.

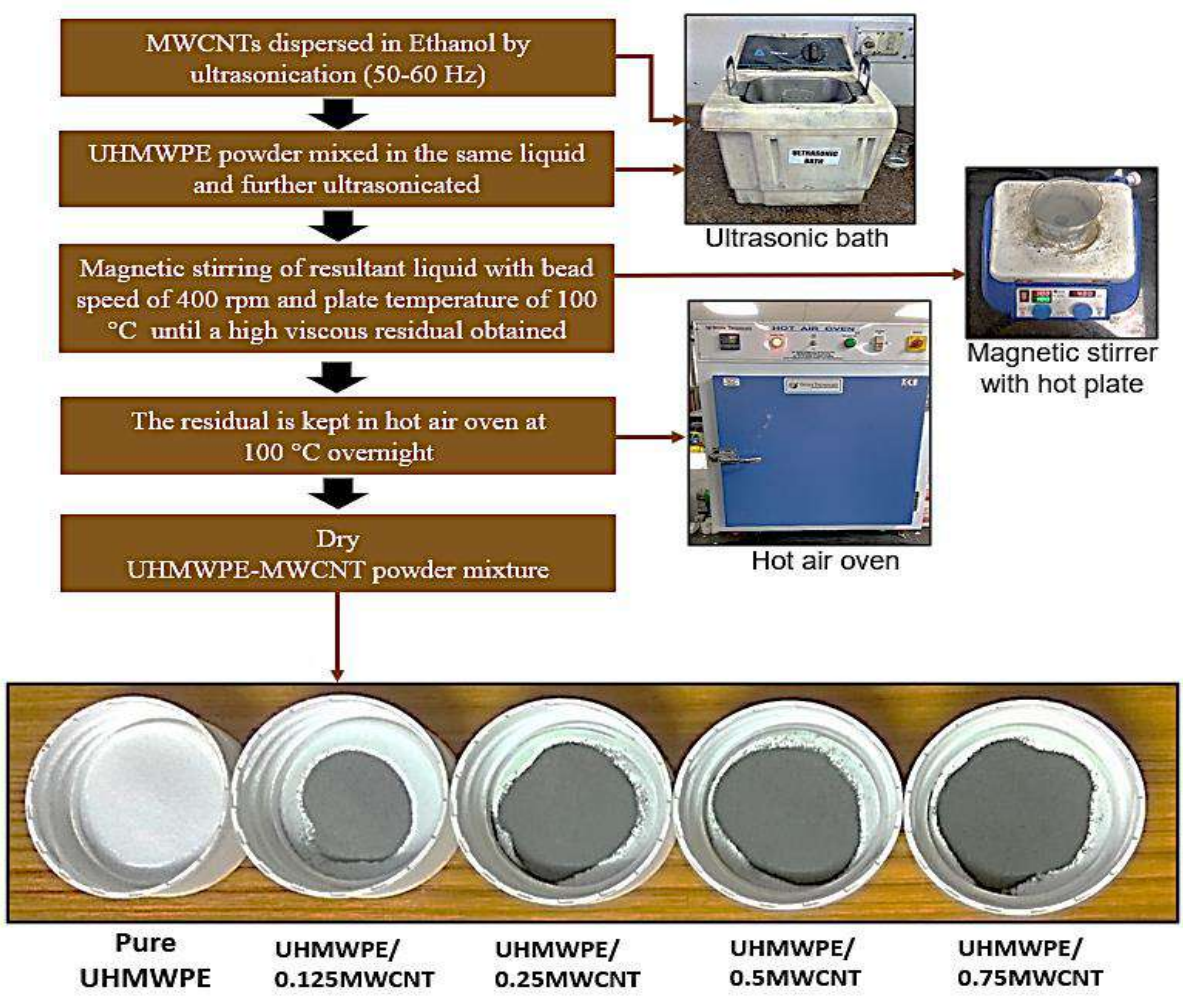

Figure 3.18. *4-Step process for mechanical mixing of UHMWPE and MWCNT powder*

Measured quantity of functionalized MWCNT in agglomerated form is shown in Figure 3.19(A) in electron micrograph, which is first dispersed in 99.9% ethanol having the density (789 kg/m^3) less than both the UHMWPE (~942 kg/m^3) and MWCNT (>1200

kg/m^3) powder using an ultrasonic bath for one hour. A low frequency of ~50-60 Hz is purposefully used for obtaining damage-free MWCNT after the sonication process and the dispersed MWCNT are evident in Figure 3.19(B).

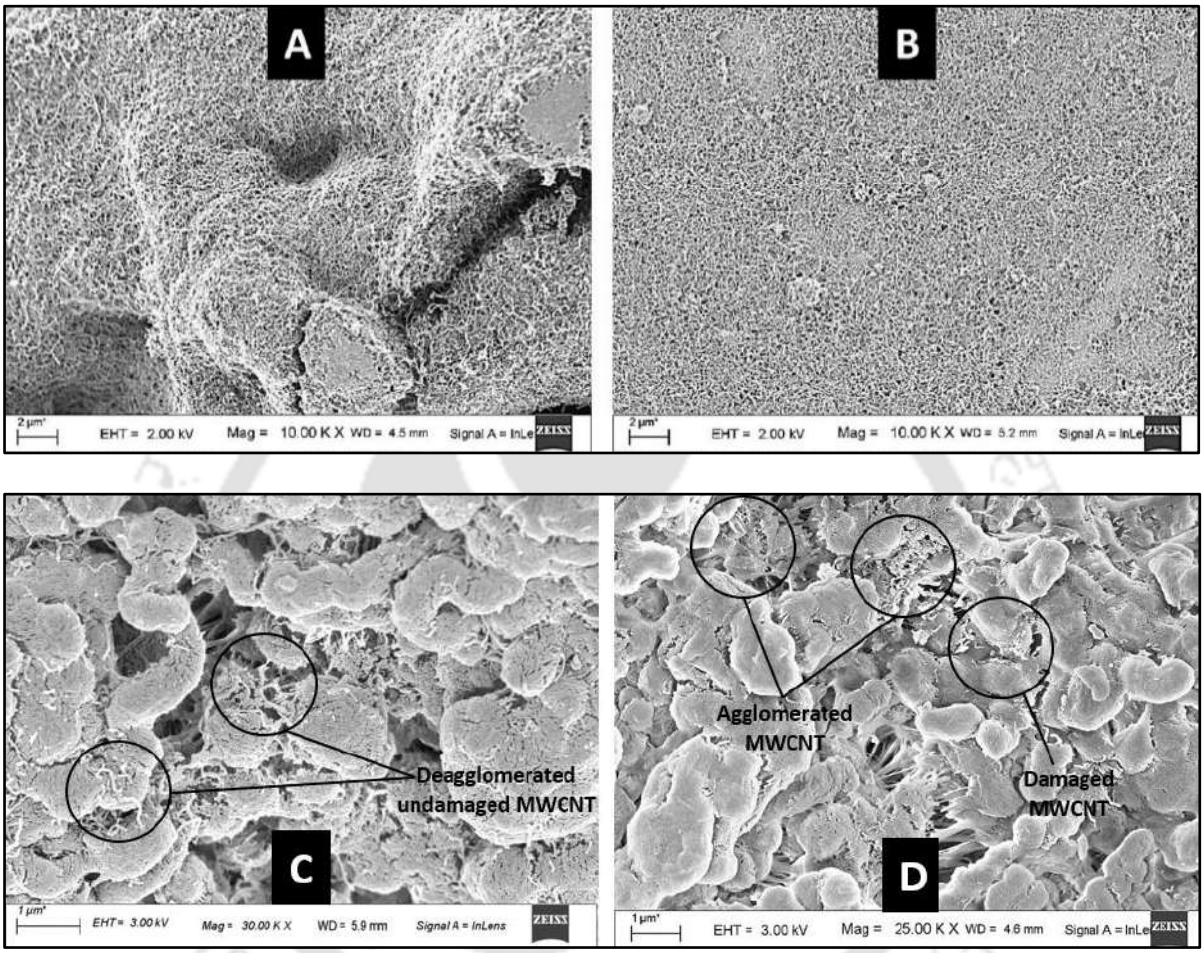

***Figure 3.19**. SEM micrograph of (A) agglomerated MWCNT after chemical treatment (B) dispersed MWCNT after ultra-sonication (C) Powder mixture of UHMWPE and MWCNT showing proper distribution and dispersion of the filler by ultra-sonication and magnetic stirring(D) Powder mixture of UHMWPE and MWCNT showing agglomerated and damaged filler due to ball milling process*

Calculated quantity of UHMWPE powder is mixed in the same liquid part by part, and the mixture is kept in ultrasonic bath for another one hour to reduce the number of agglomerates. Then the resultant liquid is kept on a magnetic stirrer with bead speed of 400 rpm at 100 °C, a temperature higher than the boiling point of ethanol (~ 79°C), for simultaneous mechanical mixing as well as evaporation of the liquid medium until a high viscous residue was obtained, which was then kept into a hot air oven at 100°C overnight

to get a dry UHMWPE-MWCNT powder mixture of calculated weight ratio, evaporating the residual ethanol from the mixture. The dispersion and distribution of MWCNT in polymer powder is confirmed by electron micrograph in Figure 3.19(C) and the same is compared with powder mixture of same composition, prepared by dry ball milling process of 1 hour with powder to ball weight ratio of 1:10 in Figure 3.19(D). UHMWPE-MWCNT powder mixture is prepared with filler concentration of 0.0 wt.%, 0.125 wt.%, 0.25wt.%, 0.375wt.%, 0.50wt.%, and 0.75 wt.%. The powder mixture having different compositions is investigated under SEM for the state of dispersion and distribution of MWCNT in UHMWPE and it is shown in Figure 3.20(A)-(F). Figure 3.20(A) shows UHMWPE without any reinforcement for reference. Figure 3.20(B) shows UHMWPE with 0.125 wt.% of MWCNT reinforcement displaying uniform dispersion and distribution of the filler which is sustained till 0.25 wt.% of MWCNT concentration as shown in Figure 3.20(C). However, the polymer composite with 0.375 wt.% of MWCNT concentration exhibited distribution of the filler without proper dispersion in Figure 3.20(D). Figure 3.20(E) and Figure 3.20(F) are showing the SEM micrograph of UHMWPE-0.5MWCNT and UHMWPE-0.75MWCNT composites, respectively, with agglomeration of the filler in polymer matrix in increasing order.

3.4.1.3. Compaction and sintering

UHMWPE-MWCNT powder mixtures are processed with the optimum parameters, i.e., 103.5 MPa (15 ksi) of compaction pressure, 165°C of sintering temperature and 130 min. of sintering time as decided in Section 3.3 and the mechanical properties of the UHMWPE-MWCNT composites are compared with those of the virgin polymer to find out the optimum MWCNT concentration in the composite and obtain desired characteristics of the composites as per the proposed application.

3.4.2. Characterization techniques

3.4.2.1. Crystallinity measurement

Crystallinity of newly processed polymer and its composites is calculated using the thermograms generated during their differential scanning calorimetry (DSC) studies with DSC, STA 8000 (PerkinElmer, UK) at a heating rate of 10°C/min. under a nitrogen purge in the temperature range between 40°C to 200°C, which includes the re-melting zone of the polymers. Enthalpy of fusion of a 100% crystalline UHMWPE is taken to be 290 J/g [178].

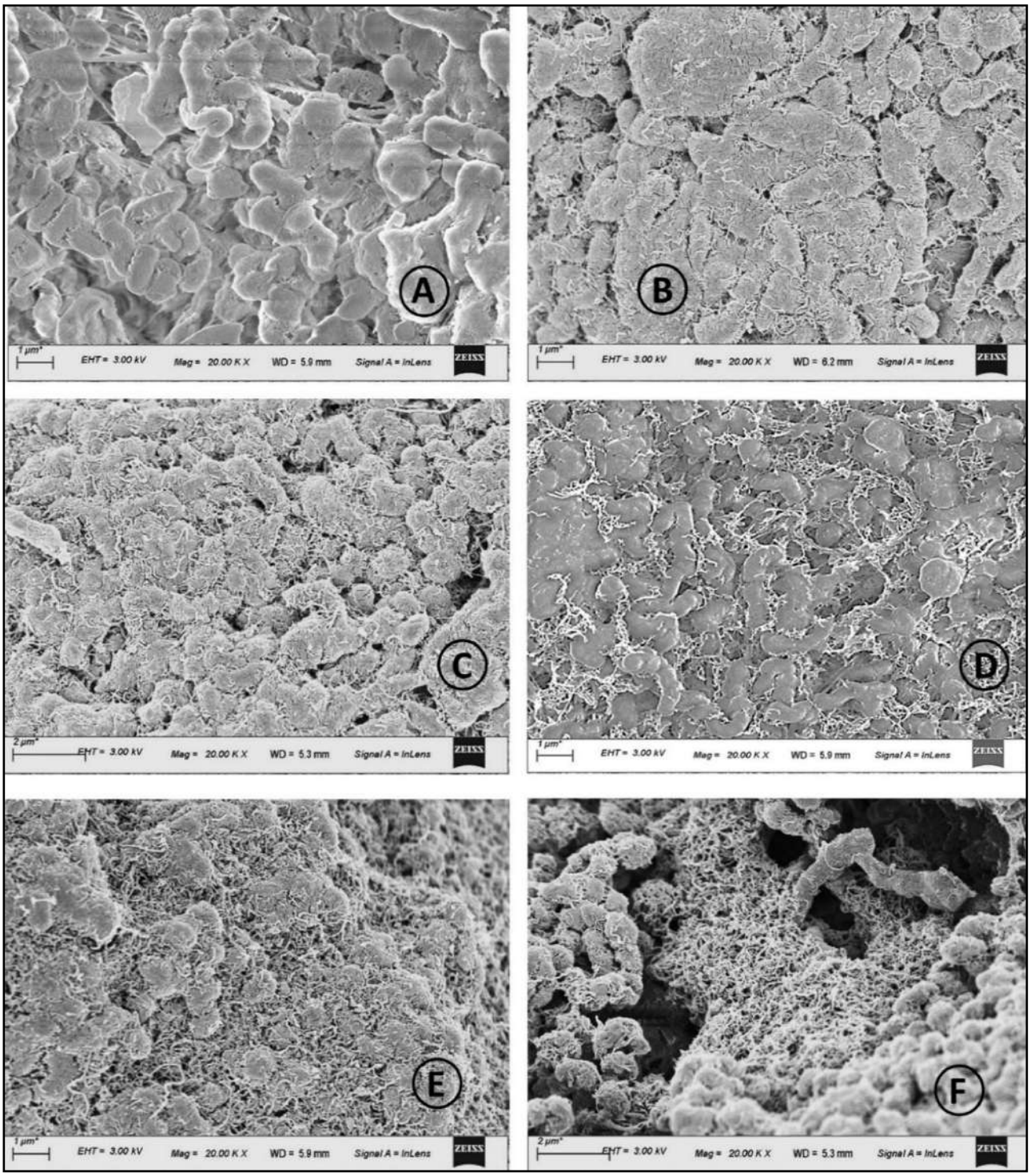

Figure 3.20. *State of dispersion and distribution of MWCNT in UHMWPE for (A) 0.0 wt.% (B) 0.125 wt.% (C) 0.25 wt.% (D) 0.375 wt.% (E) 0.5 wt.% (F) 0.75 wt.% of filler concentration. Agglomeration of MWCNT is observed beyond the concentration of 0.25 wt.%*

3.4.2.2. Hardness measurement

Micro-hardness tester is used to measure Vickers hardness of sintered pure polymer and composite samples at a constant normal load of 50 gf, as per **ASTM E384-17** [167]. Shore D hardness of the same samples is also measured using STECH DSHT-DIII Durometer with the precision of 1° in the scale range from 0 to100 following **ASTM D2240-15** [168].

3.4.2.3. Mechanical properties analysis

Universal testing machine is used to evaluate the mechanical strength of UHMWPE-MWCNT composite specimens in compression and tensile modes to compare the results with those of pure polymer. Compression test of cylindrical samples of 15 mm length ($\mathbf{L_0}$) and 8 mm diameter ($\mathbf{D_0}$) is performed with three repeats at room temperature as per **ASTM D695** [169] at a constant displacement rate of 0.5 mm/min and the offset method at a strain of 0.002 is used to define their yielding. Tensile strength of the polymer is evaluated with type 'V' dumbbell-shaped test specimen as prescribed in **ASTM D638** [170] at room temperature. The crosshead speed of 0.5 mm/min. is maintained during the test till the fracture of the samples. Three samples are tested to check the repeatability and the average results are reported.

3.4.2.4. Confirmation of Biocompatibility

The confirmation of biocompatibility of UHMWPE-MWCNT composite is very much necessary in order to validate the present work. The quantitative analysis of cell viability and cell spreading are performed on the UHMWPE and UHMWPE-MWCNT specimens to establish their cytocompatibility with Human Mesenchymal Stem Cells (hMSc) and osteoblast cells. The hemocompatibility of the composites is investigated under the controlled flow of rabbit blood in a microfluidic device. An attempt has been made to discuss the blood compatibility results in the backdrop of the bovine serum albumin adsorption kinetics. This study is carried out by IISc Bangalore team on the specimens prepared at IIT Guwahati [179].

3.4.3. Results and Discussion

3.4.3.1. Crystallinity vs MWCNT concentration

As the increase in mechanical properties of the composites is related to increase in crystallinity of the composites, an attempt is made to study the crystallinity of the composites using DSC. Figure 3.21 shows the thermograms of UHMWPE-MWCNT composites with different filler concentration. At their melting zone, the melting point of the UHMWPE is not found to be influenced by the presence of MWCNT. The onset melting points of the composites are found to be in the range of 132 ± 2°C and their melting end points are observed to be well within the range of 160 ± 2°C.

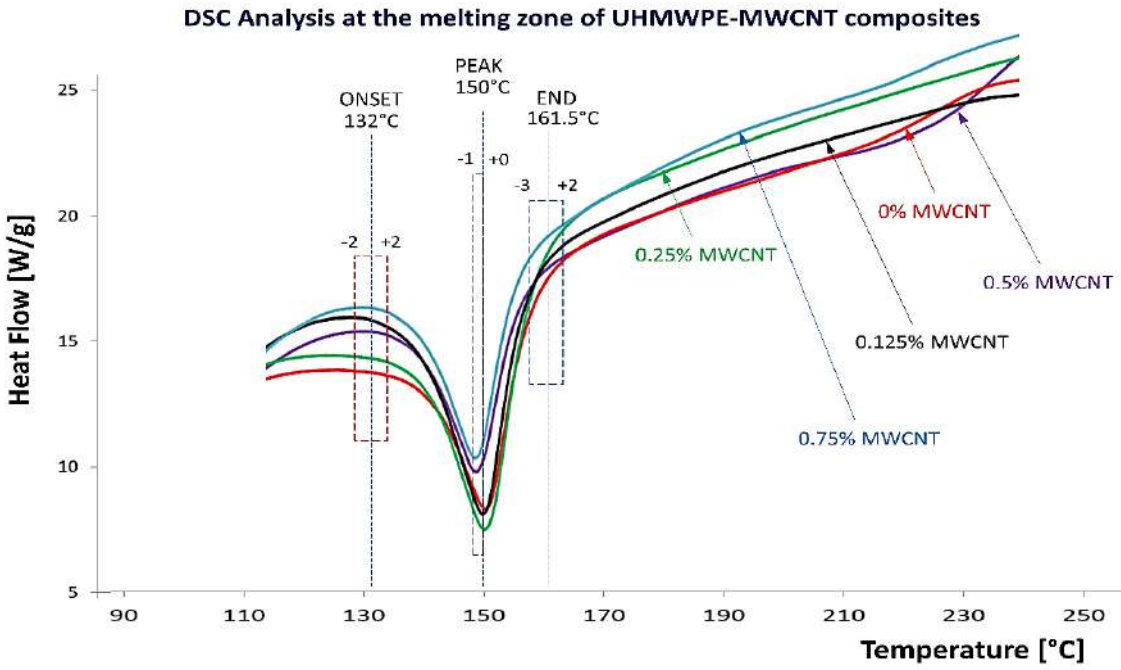

Figure 3.21. *DSC analysis of UHMWPE-MWCNT composites with different MWNCT concentration at their melting zone. Onset melting point, peak melting point and melting end point are found to be independent of filler concentration*

Figure 3.22(A) compared the crystallinity of UHMWPE-MWCNT composites incorporated with different filler concentration with that of pure polymer. Crystallinity of pure polymer is found to be ~56%. It is noted that the crystallinity of composites is increased up to ~63% with 0.25 wt.% of MWCNT but decreased further with higher concentration of the filler as shown in Figure 3.22(A). At the filler concentration of 0.75 wt.%, the composite exhibited crystallinity of ~ 54%, which is even lower than that of pure polymer. The crystallinity of

the composite is increased with the incorporation of MWCNT, acting as nucleation sites for polymer crystallization [180]. However, the decline in degree of crystallinity of the nanocomposites at higher concentration of MWCNT is caused by the friction between the filler and polymer chains hindering their mobility in the crystal growth [56].

3.4.3.2. Hardness vs MWCNT concentration

Figure 3.22(B) shows the Vickers hardness and Shore D hardness of the UHMWPE-MWCNT composite samples against their composition, and it is observed that the hardness of compacts varied with the MWCNT loading but reached a limiting value of 8.34 ± 0.06 HVN and 85.33 ± 1.5 SD at 0.25 wt.% of filler concentration. Further increase in MWCNT loading caused a slightly decreasing trend in the hardness. The corresponding hardness of 5.23 ± 0.06 VHN and 65.3 ± 1.5 SD for unfilled polymer are ~58% and ~30% inferior compared to that of maximum hardness achieved for reinforced composite in terms of Vickers hardness and Shore D hardness, respectively.

3.4.3.3. Mechanical properties vs MWCNT concentration

The mechanical properties of nanocomposites, namely, the compressive strength, compressive modulus, tensile yield strength, Young's modulus and toughness are evaluated to determine the optimum concentration of MWCNT for the best combination of mechanical properties of UHMWPE. Figure 3.22(C) shows the compressive properties of UHMWPE and UHMWPE-MWCNT composites against filler concentration. The compressive yield strength and modulus of the pure polymer samples are found to be 23.5 ± 0.5 MPa and 721 ± 15 MPa, respectively. The maximum compressive yield strength and modulus of the samples are observed to be 28.9 ± 1 MPa and 821 ± 35 MPa with an improvement of ~23% and ~14%, respectively, at the filler concentration of 0.25 wt.%. The obtained results are found to be considerably better than that of ram extruded GUR 1050 products having the compressive yield strength and modulus of 12.9 ± 0.6 MPa and 570 ± 28 MPa, respectively [176]**.** Both compressive strength and modulus are observed to be decreased with higher MWCNT loading beyond 0.25 wt.%.

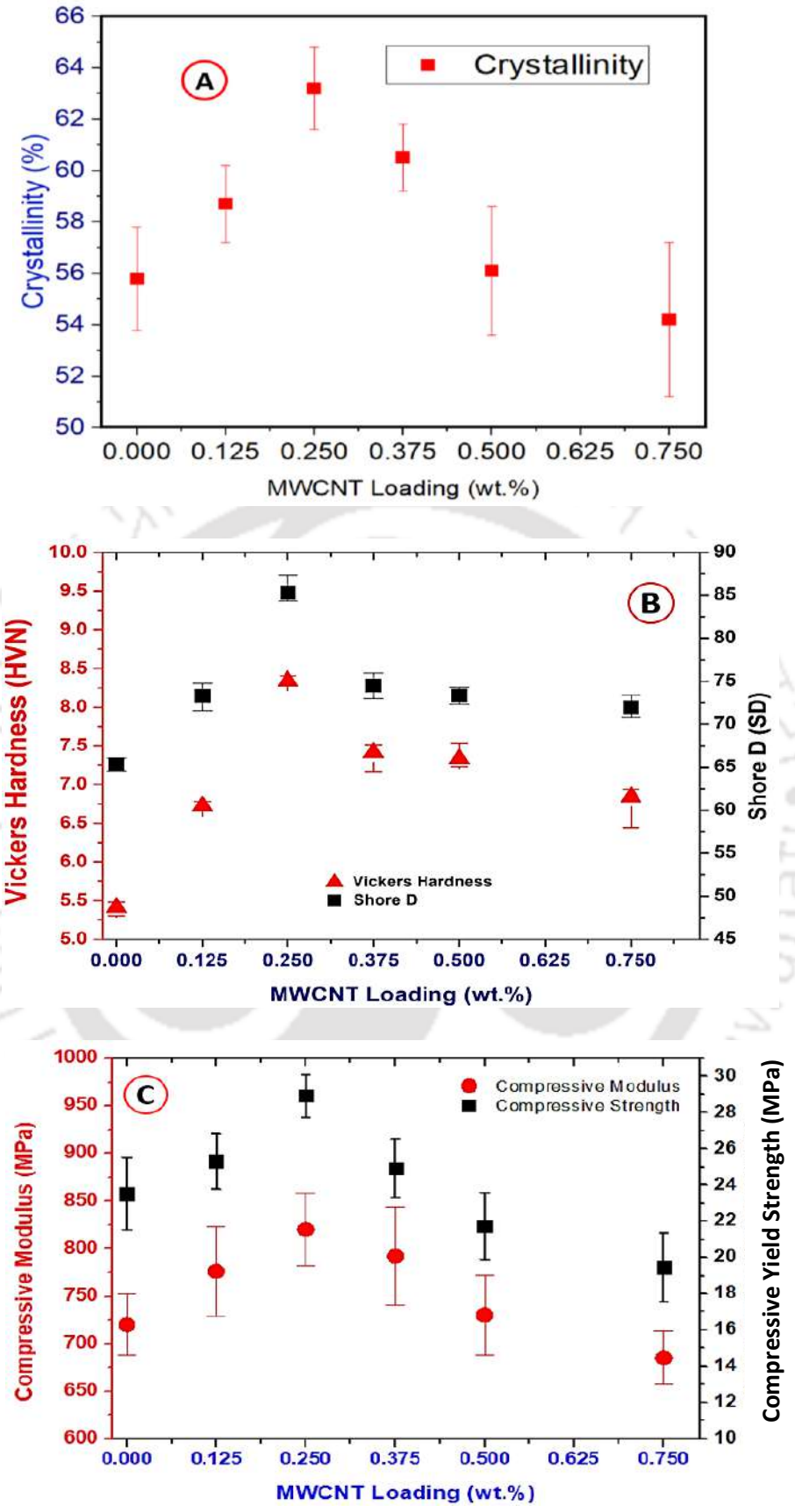

Figure 3.22. *Variation of (A)Crystallinity (B) Hardness (C) Compressive properties of UHMWPE-MWCNT composites with filler concentration*

Figure 3.23 (A) shows the variation of tensile stress against strain in polymer composites having different concentration of reinforcement and their yield strength, Young's modulus and elongation at yield are compared in Figure 3.23 (B). The calculated toughness of the samples from the area under the stress-strain curve along with their elongation at break are summarized in Figure 3.23 (C). It is observed that Yield strength, obtained using the 0.2% offset technique from the stress-strain graph, and Young's modulus UHMWPE-MWCNT composites attained their peaks of 34.2 ± 1.0 MPa and 705 ± 50 MPa, respectively, at 0.25 wt.% concentration of MWCNT and the corresponding values are ~50% and ~20% over the virgin polymer.

A similar trend is noticed in case of fracture toughness with a maximum of 94 ± 5 GJ/m^3 at 0.25 wt.% concentration of MWCNT showing ~24% increment over pure polymer. However, the elongation at yield and the elongation at break are found to be decreased with an increase of filler concentration as a result of increase in bulk hardness till 0.25 wt.% of MWCNT, beyond which material failed due to higher concentration of flaws initiated by agglomerated MWCNT in the polymer matrix as shown in Figure 3.20 (D)-(F). Polymer without filler had elongation at yield and elongation at break of 12.2 ± 0.5% and 276 ± 22%, respectively, and the corresponding values are found to be reduced to 4.0 ± 0.2% and 190 ± 10% for UHMWPE-0.75MWCNT composite which are shown in Figure 3.23 (B) and (C).

Due to the following factors, the mechanical properties of composites are increased in comparison to that of virgin polymer:

(i) MWCNT has very high mechanical properties, [95]-[103]

(ii) The attached functionalized group helps in effective stress transfer from matrix to reinforcement which is validated by a Raman Spectroscope Triax 550 (Jovin Yvon, Germany) with 488 nm blue laser (Argon) and a CCD detector, which is coupled with a monochromator having the XY step resolution of 0.1 µm, wave number accuracy of ± 1 cm^{-1} along with its resolution of 0.5 cm^{-1}. Figure 3.24(A) shows Raman spectra of UHMWPE-0.25MWCNT nanocomposite before and after the tensile test along with that of UHMWPE specimen after tensile test, where a very small peak shift was observed. The G band peak of the composite sample before the test was noticed at 1590.62 cm^{-1}, which was found to be shifted to 1584.7 cm^{-1} after the tensile test. The change in C-C bond (of MWCNT) vibrations due to tensile strain was noticed in Raman spectra in the

form of change in position and intensity and thus it confirms the effective stress transfer from matrix to the reinforcement.

(iii) Homogeneous distribution of reinforcement in the matrix, as shown in Figure 3.20(B) and Figure 3.20 (C)

(iv) (iv) Increased crystallinity of the composites, as shown in Figure 3.22(A).

However, beyond 0.25 wt.% filler concentration mechanical properties are observed to decrease due to the following reasons:

(i) The complex viscosity of composites was increased with concentration of reinforcement, and it is confirmed by temperature ramp test on UHMWPE-MWCNT composites to investigate the variation of complex viscosity with temperature as shown in Figure 3.24(B). Complex viscosity of pure polymer at 165^0 C is found to be ~15 kPa.s which further increased with addition of MWCNT and attained maximum value of ~65 kPa.s with 0.75 wt.% reinforcement loading.

(ii) Formation of voids at higher concentration of reinforcement due to more surface area of CNT and difference in thermal properties of reinforcement and matrix. At the same time, mechanical integrity and strength are the reflection of the extent of bulk diffusion of samples. Overloading of MWCNT is found to agglomerate at certain locations in UHMWPE matrix as shown in Figure 3.20 (D)-(F) and these sites are expected to act as defects in the material resulted in a declination of mechanical integrity of the material.

It is inferred that present technique is capable of dispersing and distributing MWCNT in UHMWPE up to a certain limit (0.25 wt.%). Hence further study is continued only with the UHMWPE-0.25MWCNT composite to utilize its maximum mechanical integrity and strength.

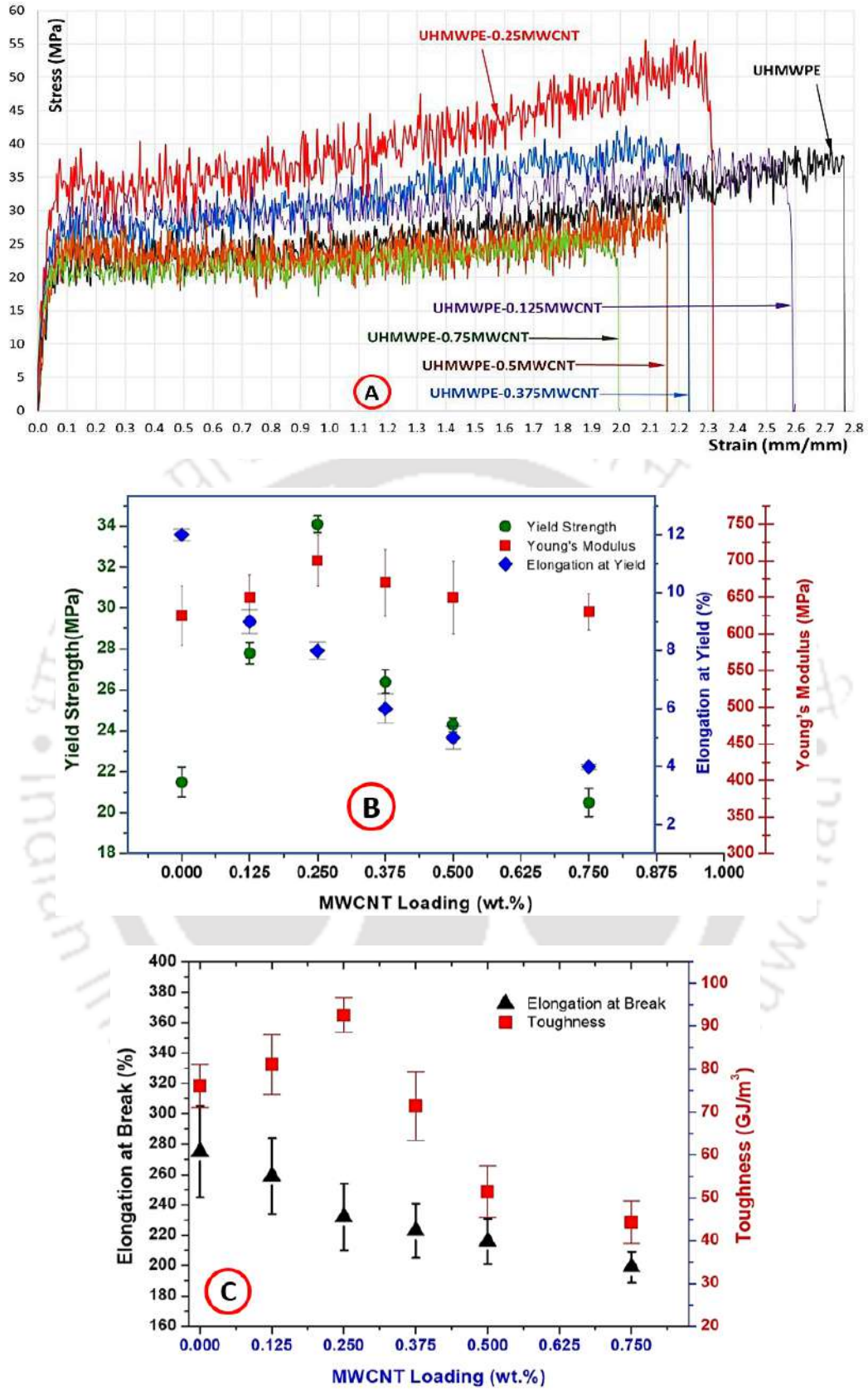

Figure 3.23.*(A) Tensile Stress vs Strain curve for UHMWPE-MWCNT composites (B)Variation of yield strength and Young's modulus and elongation at yield (C) Variation of toughness and elongation at break with MWCNT loading in polymer composites*

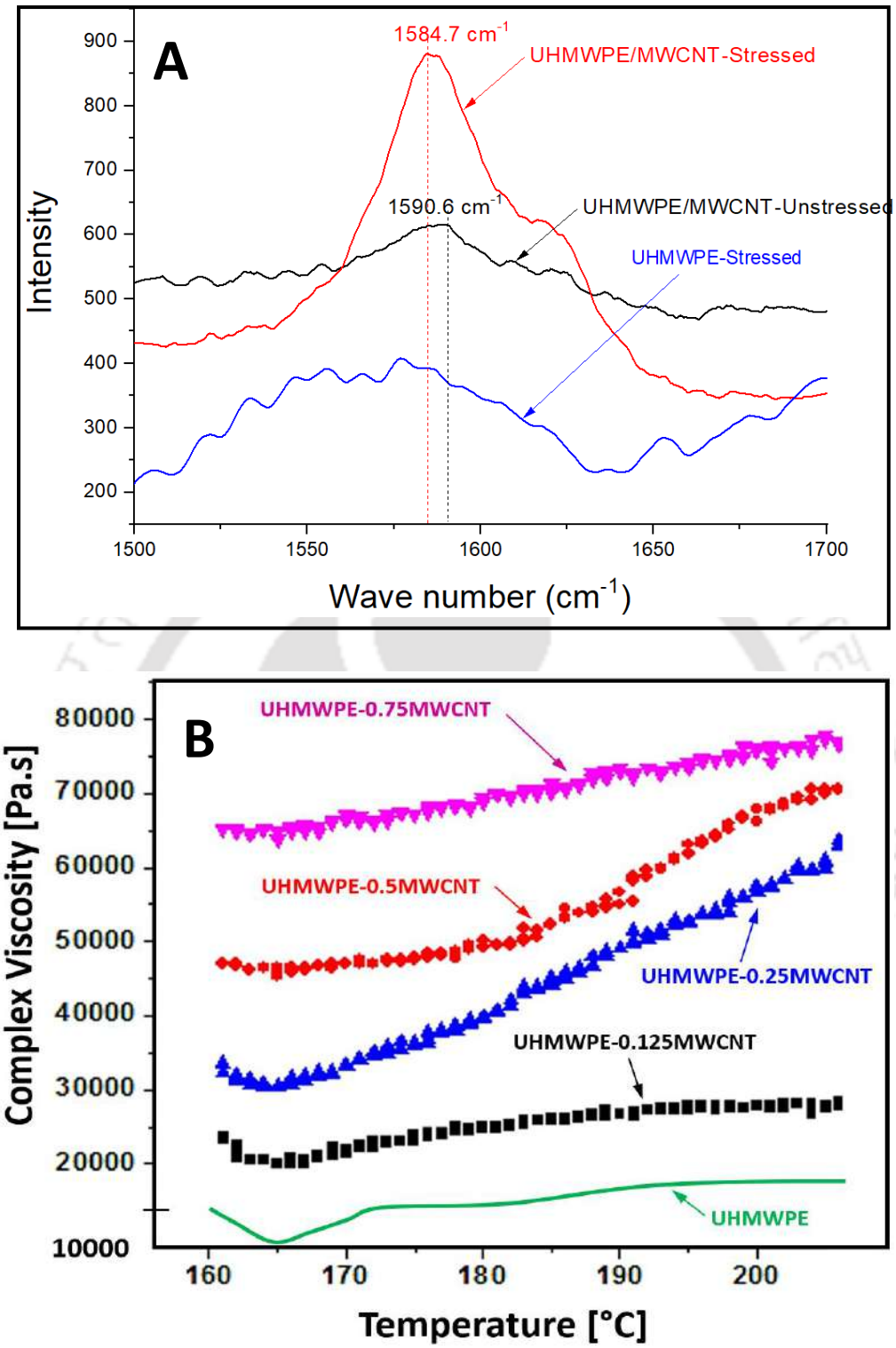

Figure 3.24. *(A) Raman spectra of UHMWPE-0.25MWCNT specimen-before and after the tensile test along with that of UHMWPE specimen after tensile test (B) Temperature ramp test of UHWMPE-MWCNT nanocomposites for the variation of complex viscosity with temperature*

3.4.3.4. Biocompatibility

Cellular interaction with polymer composite depends on the protein adsorption on the surface. Adsorption parameters of UHMWPE with and without nanofibers reinforcement are shown in Figure 3.25(A) indicating Langmuir isotherm as the most appropriate model of adsorption. The hydrophobic surfaces of UHMWPE exhibited a high amount of Bovine Serum Albumin protein adsorption but is comparatively lesser than UHMWPE-0.25MWCNT due to the presence of hydrophilic patches of functionalized MWCNT dispersed in the hydrophobic matrix of UHMWPE. Figure 3.25(B) shows the results obtained from hemocompatibility study on lab-on-chip to realize the controlled shear flow of blood in the physiological environment. The percentage of hemolysis in UHMWPE and UHMWPE-0.25MWCNT nanocomposite indicates a statistically significant difference ($\mathbf{p} < 0.05$) with respect to control and the composite sample exhibited uncompromised cytocompatibility with osteoblast and human mesenchymal stem cells. Exhibition of sufficient protein adsorption and uncompromised cytocompatibility can qualify UHMWPE-0.25MWCNT composites as articulatory implant materials.

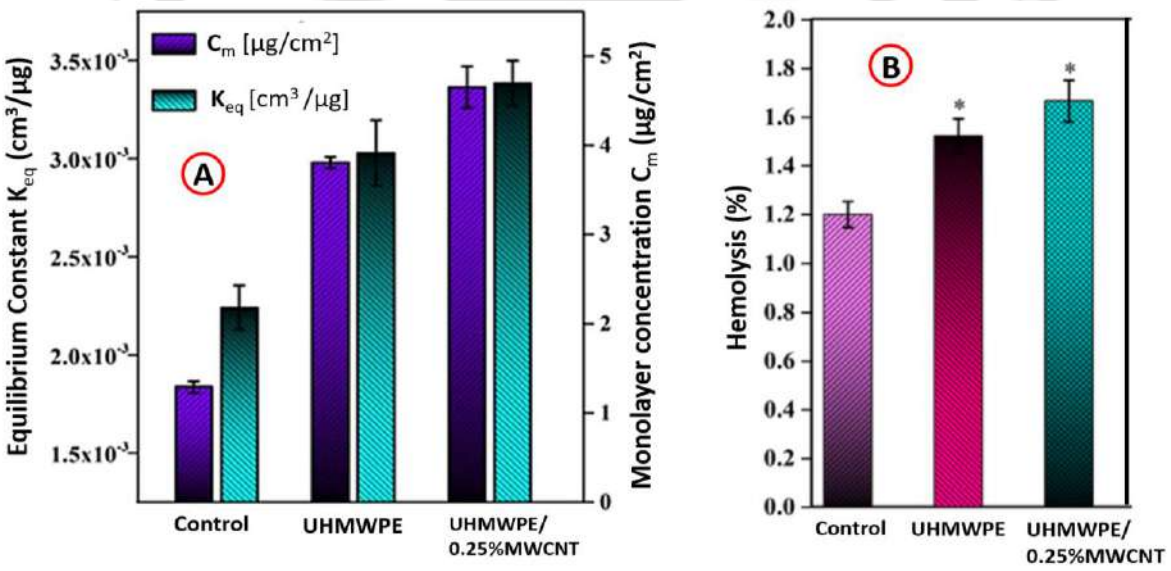

Figure 3.25. *(A) Adsorption parameters of UHMWPE with and without reinforcement (B)Percentage of hemolysis in UHMWPE and UHMWPE-MWCNT nanocomposite*

3.5. Summary

- The proposed technique processed medical grade UHMWPE-GUR1050 with experimentally obtained optimum value of compaction pressure, sintering temperature and sintering duration to get products having the properties at par with hot isostatic processed (HIPped) products, viz., relative density of ~ 97% and Vickers hardness of ~ 5.0.

- UHMWPE-MWCNT composites with different concentrations of the filler are processed with a methodology, designed to ensure homogeneous distribution and dispersion of MWCNT in highly viscous UHMWPE for enhancing the hardness, compressive properties, tensile properties and toughness of virgin polymer to the maximum possible extent.

- Up to 0.25 wt.% of MWCNT is successfully dispersed and distributed homogeneously in UHMWPE by ultra-sonication and magnetic stirring, where the hardness and compressive yield strength of UHMWPE are improved by 77% and 43%, respectively, with 60% increase in tensile yield strength.

- Uncompromised biocompatibility of UHMWPE-0.25MWCNT nanocomposite is confirmed.

भारतीय प्रौद्योगिकी संस्थान गुवाहाटी
Indian Institute of Technology Guwahati

CHAPTER 4

DEVELOPMENT OF ACETABULAR LINERS

4.1. Introduction

Acetabular liner is an integral part of the THA and provides the bearing surface to an artificial hip joint as shown in Figure 4.1. Compression moulding and bulk extrusion have been used for making commercially available UHMWPE-based acetabular liners and these techniques rely on diffusion of polymer particles under simultaneous application of heat and uniaxial pressure without any bulk flow of material leading to anisotropic characteristics with numerous flaws, such as fusion defect and weak bonding [31]. Imperfect boundary diffusion leads to crack initiation and its propagation in the product. Moreover, the unworn bearing surface of some of the retrieved implants [28], possibly due to non-uniform stress distribution in the liner acted upon an asymmetric load profile during its usage, makes evident of intact machining marks on it. These machining mark asperities are expected to initiate the wear process at the high stress zone on the liner with a drastic material removal rate during its usage. It demands an alternative manufacturing technique for processing UHMWPE to develop a defect-free acetabular liner to exploit its full potential as a bearing material in THR. The main objective of this chapter is to develop an ingenious technique to fabricate acetabular liners having the inner diameter (Φ_i) of 22 mm and thickness of 6 mm incorporated with desired bearing characteristics and surface finish innately by sintering UHMWPE and UHMWPE-0.25MWCNT powder after their cold isostatic compaction with optimum processing parameters as described in Chapter 3. Methodology described earlier as process ⑦ in Figure 3.1. has been followed for the development of a 6 mm thick acetabular liner having the Φ_i of 22 mm. The steps followed to develop the product are reported into four major parts, namely, (1) conceptualization, (2) development of rubber moulds, (3) compaction, and (4) sintering, which are shown in Figure 4.2 and discussed below in detail.

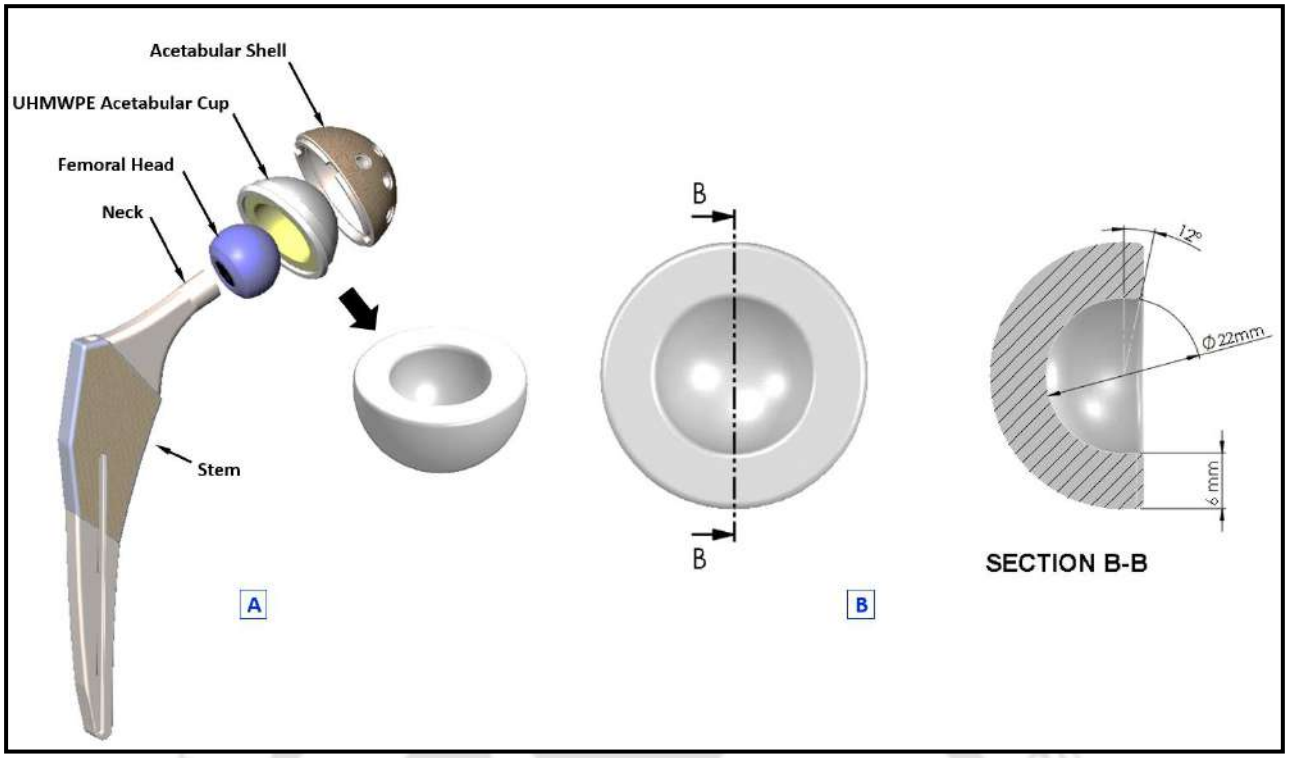

Figure 4.1. *(A) Metal-On-UHMWPE THA components (B) Dimension of the Acetabular liners to be manufactured.*

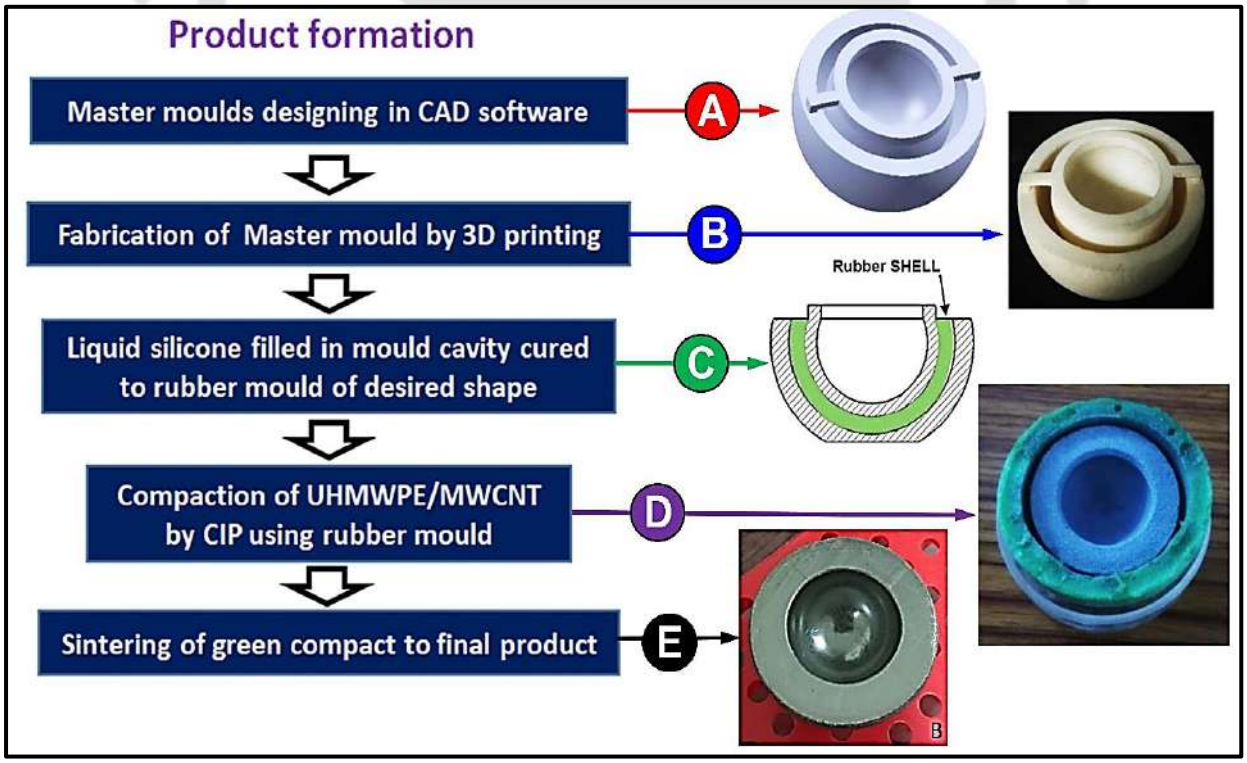

Figure 4.2*. 5-Step process of Product formation (A) CAD design for Dies (B) 3D printed plastic Dies (C) Rubber mould making by cavity filling (D) Compaction of Polymer powder using developed rubber mould (E) Sintering of green compact to final product*

4.2. Conceptualization

First step for the development of acetabular liner is the conceptualization of isostatic compaction of UHMWPE powder into a typical shape with desired dimension. The major challenges are to generate the bearing surface with sphericity ~ 1.0, dimensional deviation < ± 0.5%, and desired surface finish having $\mathbf{R_a}$ < 2 μm**.** For this purpose, a compaction process is visualized as shown in Figure 4.3(A), where a hemispherical rubber mould is used with a rigid hemispherical stainless-steel ball at core, placed concentrically in it. Due to their difference in diameter, a mould cavity of hemispherical shell geometry is generated. A sealed assembly of this conceptual rubber mould is expected to generate a cup-shaped compact as a result of isostatic pressing of the polymer powder filled in the cavity against the rigid spherical surface of the ball at core. With this process conceptualization, the following inbuilt characteristics of the product are expected to be obtained as desired for a next-generation acetabular liner.

1. Isotropic characteristics of a product due to usage of isostatic compaction pressure, as shown in Figure 4.3(B1), where the grains are noticed to be oriented along the direction of load, resulting in uniform mechanical strength in all direction. On the other hand, Figure 4.3(B2) shows grain orientation of a product while formed by uniaxial compaction, leading to non-uniform mechanical strength and integrity in the product.
2. A zero-tolerance limit for the dimensional accuracy of the bearing surface S" as generated by the rigid spherical counter face S' of the ball at core with desired dimension as shown in Figure 4.3(C).
3. A desired thickness of the product as per the calculated radial clearance between the ball and the rubber mould along with other allowances.
4. A desired bearing surface finish as generated against the mirror finished counter face of the metallic ball.
5. A product without any machining process having the desired dimension and surface finish

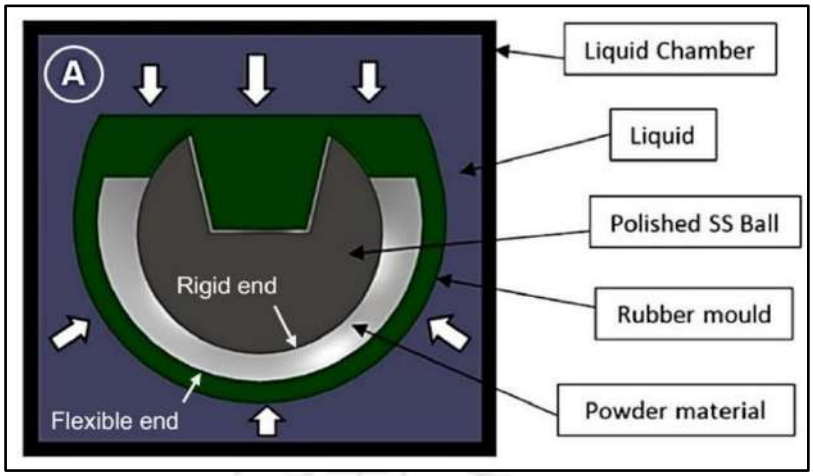

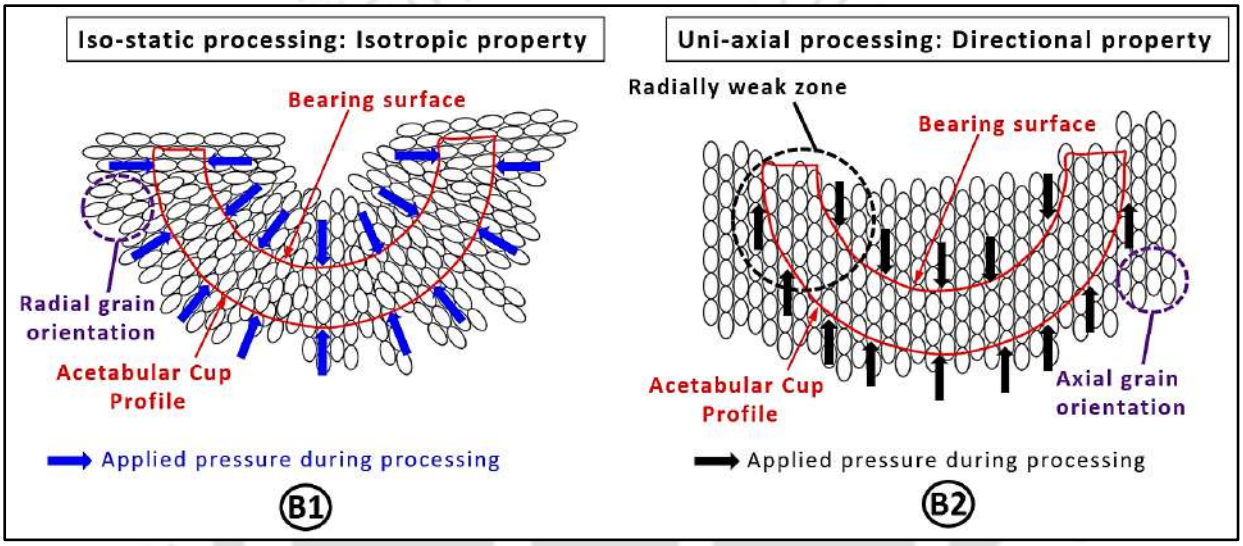

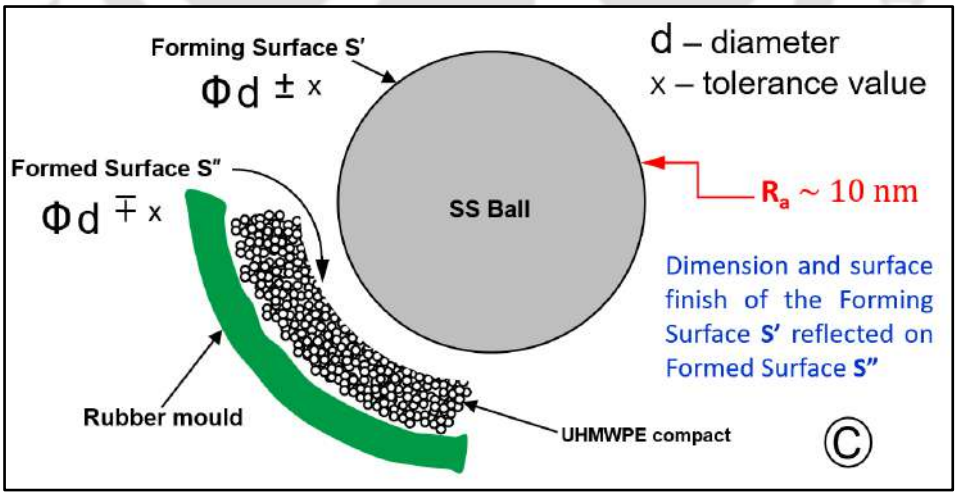

Figure 4.3. *(A) Conceptualization of acetabular liner development by isostatic pressure. (B) Grain orientation during compaction: uniaxial pressure versus isostatic pressure. (C) Sphericity, dimension, and surface finish of compacting surface S' are reflected on compacted surface S" during compaction*

4.3. Design and development of a novel rubber mould

The rubber moulds are designed in three parts, namely, CAP, SHELL, and SS ball, keeping the conceptualization in mind. The femoral head part of an actual stainless-steel THA with mirror finished surface of $\mathbf{R_a}$ = 0.02 μm is used as a SS ball in order to get accurate dimension and desired surface finish on the product. In order to make the rubber parts, suitable dies are designed using SOLIDWORKS CAD software and manufactured by FDM 3D printing using ABS plastic material. These die cavities are filled with commercially available silicon rubber material mixed with curing agent. After sufficient curing time, the rubber parts are produced with desired dimension. Figures 4.4(A) and Figures 4.4(B) show the stepwise development of CAP and SHELL, respectively, with their corresponding CAD designs in A-(I) and B-(I), 3D-printed plastic dies in A-(II) and B-(II) and the final rubber products in A-(III) and B-(III). Assembled view of the rubber CAP with SS ball in its core is shown in Figure 4.4(C)-(I) and the mould cavity filled with UHMWPE powder before compaction is schematically shown in Figure 4.4(C)-(II). UHMWPE powder is compacted in an acetabular liner geometry using the in-house-developed mould at 103.5 MPa (15 ksi) with a pressure cycle reported earlier and the compacted samples are obtained. The SS ball fitted at the centre of the rubber cap is expected to ensure the formation of a concentric cavity with exact dimension and desired surface finish at compaction stage and retain the same after sintering.

4.4. Compaction and sintering

The AIP made cold isostatic press (CIP) is used to compact UHMWPE and UHMWPE-0.25MWCNT powder in a hemispherical shell shape with inner diameter of 22 mm and thickness of 6 mm using the in-house developed rubber moulds. Compaction pressure is gradually raised to 103 MPa (15ksi) and held for 1 min. of dwell time, and then released at a slow rate within 30 seconds to produce the green compacts in the shape of hemispherical shells as shown in Figure 4.5(A1) and Figure 4.5(A2). Shape constrained sintering of the green compacts is done inside a rubber holder at 165°C for 130 min. in a hot air oven after a day of relaxation to nullify the visco-elastic effect of UHMWPE and the final sintered products are shown in Figure 4.5 (B1) and Figure 4.5 (B2). All the above mentioned

processing parameters are decided by an unique optimization process, which are all discussed in Chapter 3 [181]. To retain the surface finish of the bearing generated during compaction, the SS ball is kept inside the cavity during the sintering process. As a result, the final bearing surface is formed with sphericity ~ 1, dimensional deviation < ± 0.5%, and superior surface finish having $\mathbf{R_a}$ < 2 μm, reflecting its parent surface [182].

4.5. Inborn features and their relevance

4.5.1. Relative density

Density of the developed UHMWPE acetabular liners is measured using the Archimedes' Principle as described earlier and the relative density of the products is found to be more than 97% with respect to the highest density value 0.97 g/cm^3 reported for gel-spun UHMWPE fibers [183].

4.3.2. Surface quality

Surface roughness at the inner surface of developed acetabular liner is measured using a Taylor-Hobson non-contact type profilometer. The arithmetic mean roughness ($\mathbf{R_a}$) of the representative surface shown in Figure 4.6(A1) is found to be 85.6 ± 11 nm and 100.2 ± 12 nm along the two mutually perpendicular directions with their corresponding root mean square roughness ($\mathbf{R_{RMS}}$) of 104.8 ± 25 nm and 126.1 ± 35 nm. Average surface roughness of the developed acetabular liner is ~60% and ~75% less, respectively, compared to the $\mathbf{R_a}$ of 229.5 ± 18 nm and $\mathbf{R_{RMS}}$ 445.0 ± 55 nm observed from the non-worn surface of commercially available UHMWPE liners retrieved from human body [184]. Skewness of height distribution of the surface asperities is found to be -1.156 confirming a good bearing characteristic of the surface and the corresponding Abbott-Firestone curve shown in Figure 4.6(A2) revealed that the bearing surface is observed to be smooth on top and rough underneath as schematically shown in Figure 4.6(B). Negative skewness of a bearing surface is found to yield lower friction in low-speed sliding wear tests [185]. The maximum height of a peak ($\mathbf{S_p}$) is observed to be 1.65 μm with respect to the mean plane, and it is approximately 0.5 times of the maximum depth of a valley ($\mathbf{S_v}$ = 3.03 μm) as observed in Figure 4.6(A2).

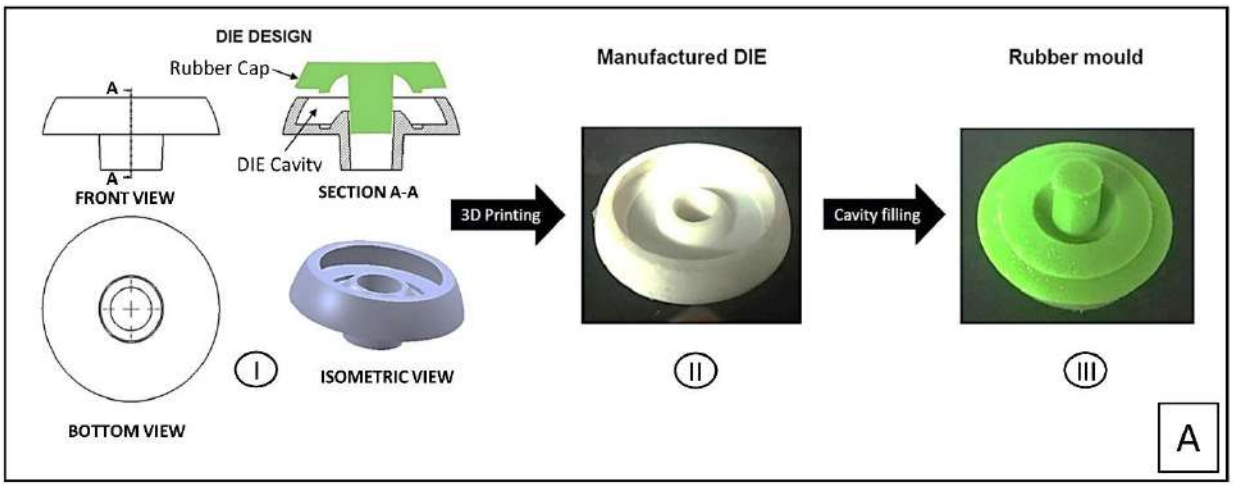

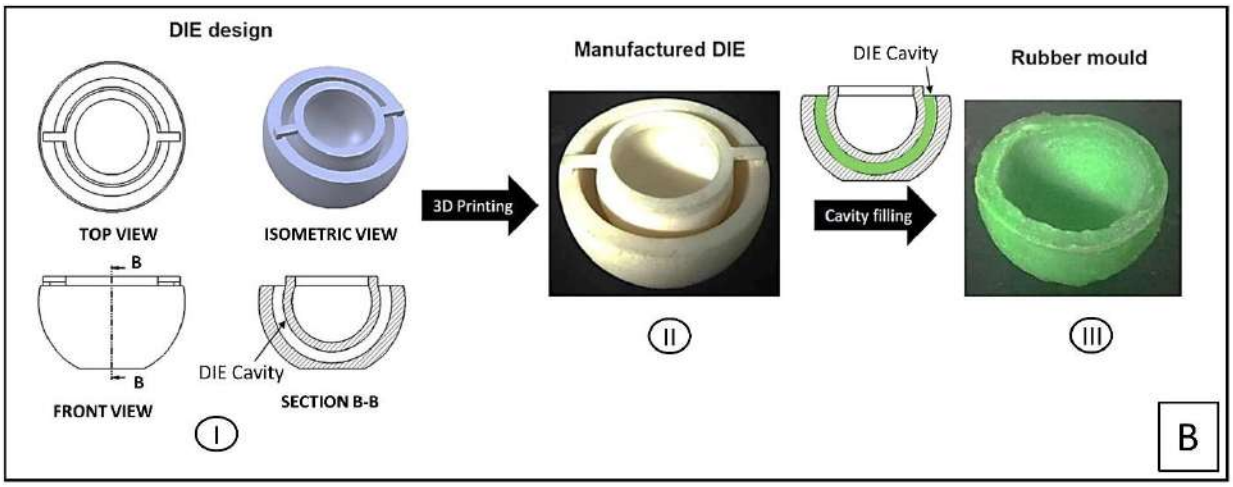

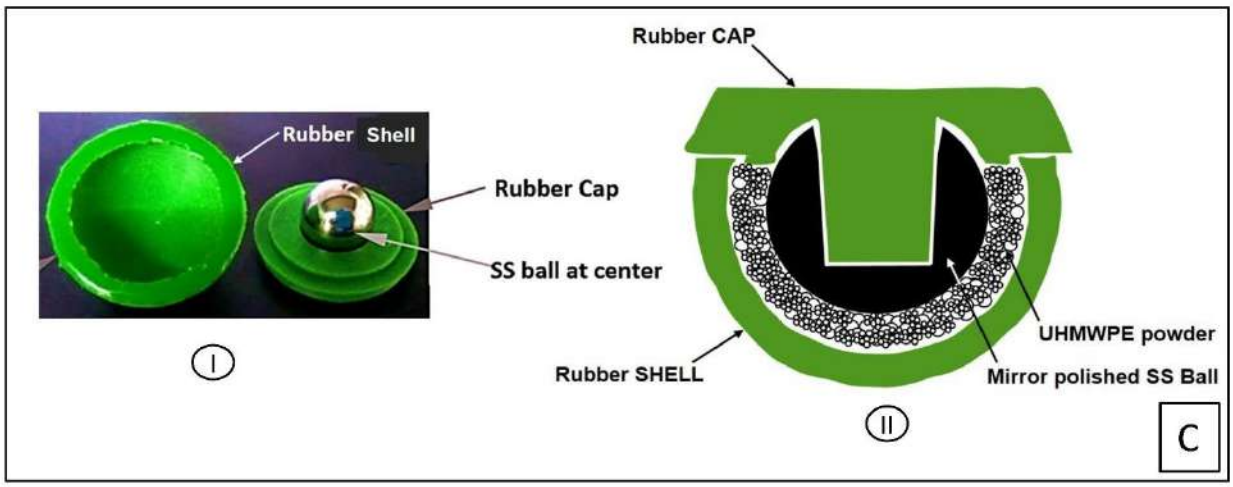

Figure 4.4*. Stepwise development of (A) rubber CAP, (B) rubber SHELL, and (C) assembled view of developed rubber mould for acetabular liner*

Figure 4.5.*(A1) UHMWPE powder after compacted in acetabular liner shape (A2) UHMWPE-0.25MWCNT powder mixture after compacted in acetabular liner shape (B1) UHMWPE liners finally obtained after sintering (B2) UHMWPE-0.25MWCNT liners finally obtained after sintering without any machining or finishing operation.*

The material ratio 1 at the peak zone (M_{r1}) and material ratio 2 at the valley zone (M_{r2}) are found to be 9% and 81%, respectively. Thus, it is inferred that the bearing surface of the acetabular liner has only 9% material volume in the peak zone, whereas the void volume in its valley zone is as high as 81%.

Additionally, kurtosis value ($\mathbf{S}_{ku}$) of height distribution of the surface asperities is found to be 4.52 (>3), which indicates that the surface is a leptokurtic one having sharp asperities, majorly valleys, ensuring a substantial effective bearing area for the counter-face. This type of surface, known as plateau-finished one, is an ideal choice for any bearing applications, which is usually generated by honing process. But the proposed technique does not require any machining process to obtain the same surface profile.

Wear loss of the material is likely to be reduced significantly due to absence of micro peaks on the bearing surface whereas, the improved lubrication control and retention are expected by the trapped lubricant in the micro valleys. This would reduce the coefficient of friction between the femoral head and the acetabulum during its usage and improve the life of the implant. Vickers hardness at the bearing surface is measured to be 5.6 ± 0.5 and a representative indent on the bearing surface under the load of a 50 gf is shown in Figure 4.6(C). Hence, it is inferred that surface hardness of UHMWPE samples is further increased by ~ 4% compared to its maximum value reported earlier due to retention of the inborn surface.

4.3.3 Defect-free product with dimensional accuracy

For the measurement of dimensional accuracy of the developed acetabular liner, it is sectionally cut by a precision saw and observed under Nikon SMZ 24 stereo microscope. The bearing surface diameter is found to be 22.00 ± 0.00 mm as desired and the liner thickness is measured to be 5.2 ± 0.9 mm. It is evident that the inner surface of the acetabular liner is formed radially eccentric to the outer surface by approximately 1 mm leading to a gradually decreasing thickness of the product in top to bottom direction, which is possibly due to a slight misalignment of the SS ball at core with respect to the rubber mould during compaction of polymeric powder and can be rectified by a minor refinement in the design of the mould. Cross-sectional surface of the acetabular liner is observed under FESEM, where no visible defects are found at a magnification of 5000. Figure 4.7 is referred for the dimensional accuracy of the acetabular liner achieved with flawless cross-sectional area.

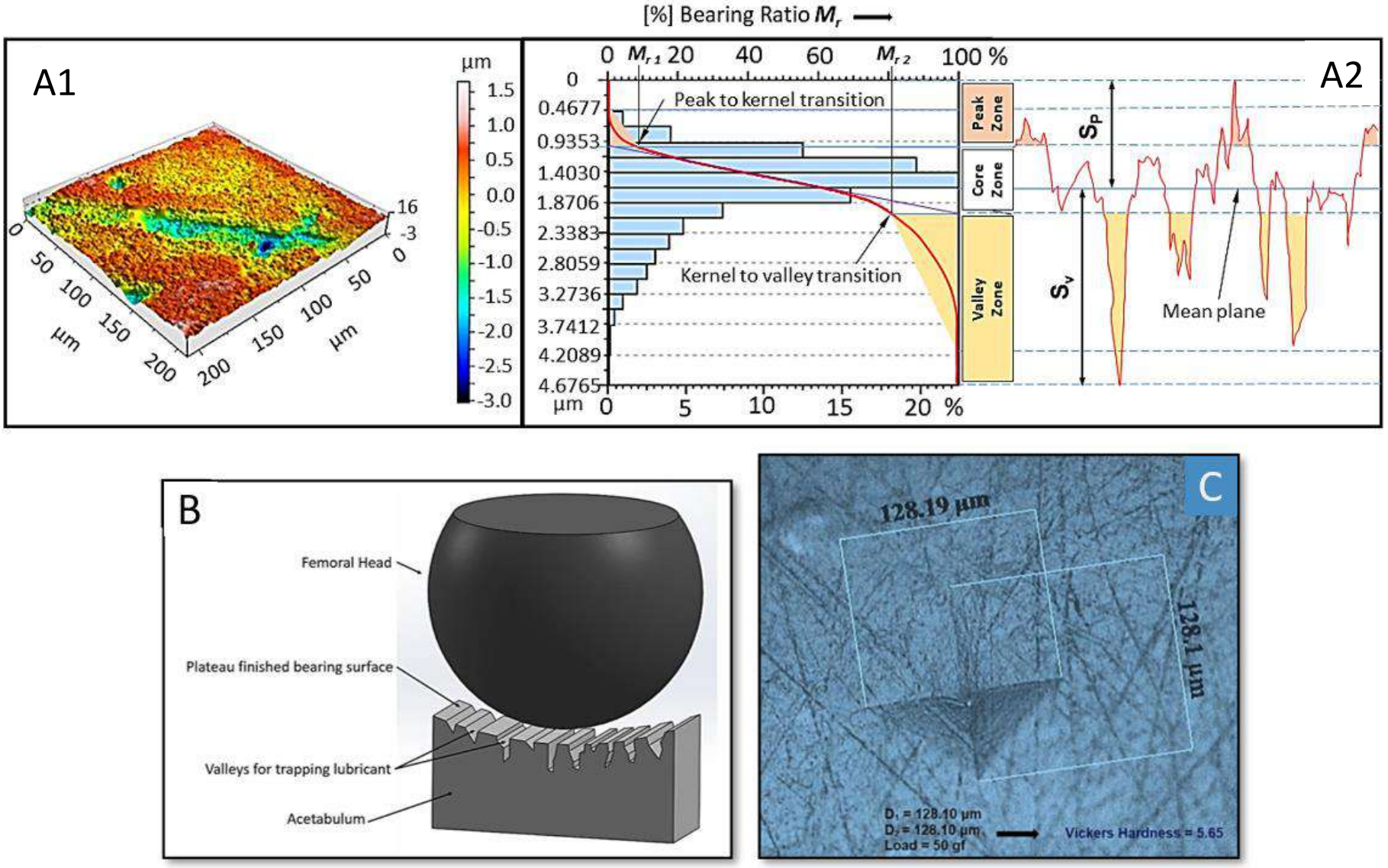

Figure 4.6*. Bearing surface characteristics of the developed acetabular liner by proposed technique (A) Abbott-Firestone curve of a randomly selected zone on the bearing surface showing more valleys compared to peaks. (B) schematic representation of the generated bearing surface similar to a plateau-finished one, (C) a representative indent during Vickers hardness test of the bearing surface*

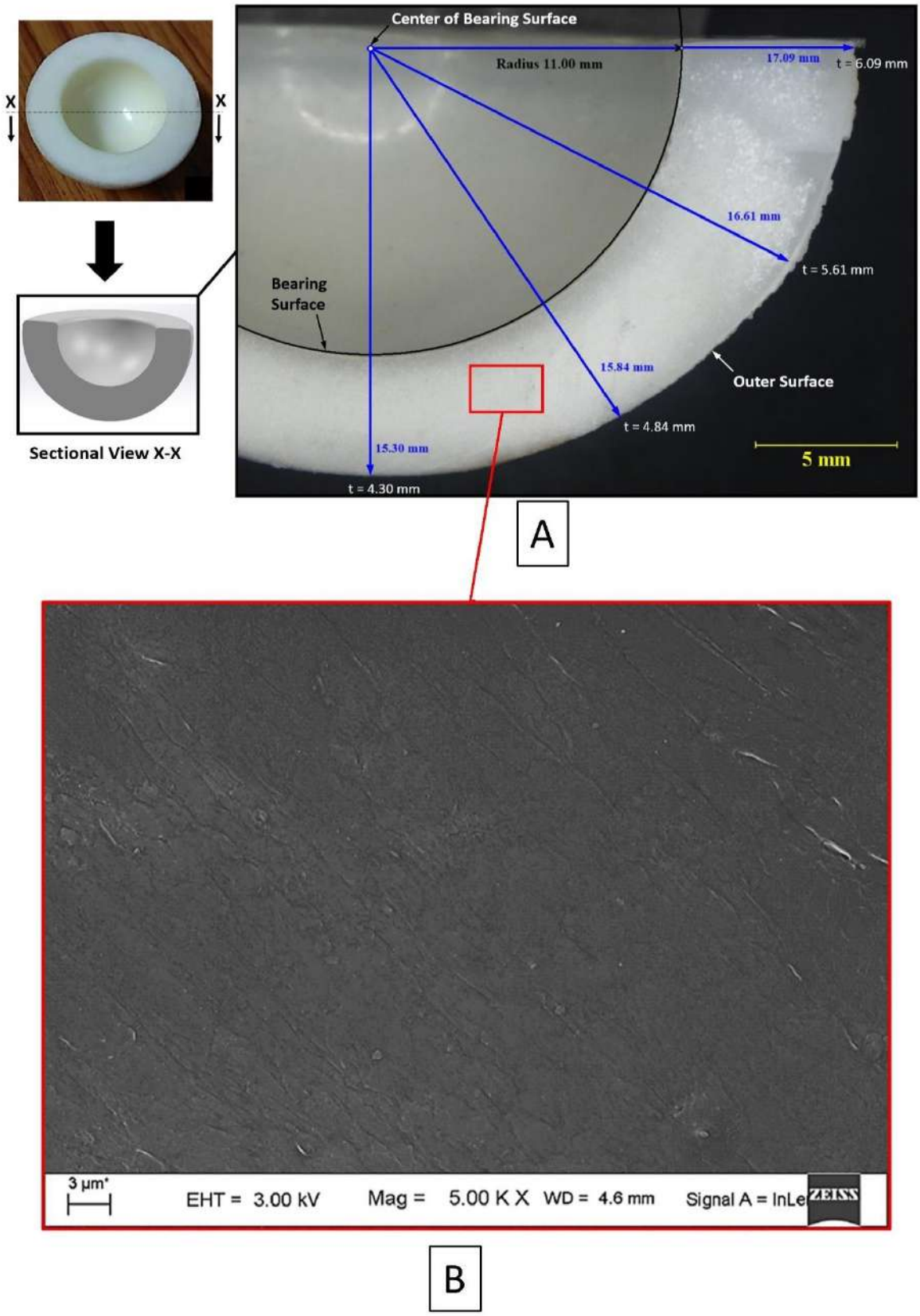

Figure 4.7. *Acetabular liner fabricated by the proposed technique achieved with (A) Exact dimension of Φ22 mm for the bearing surface (B) No visible flaws in the cross-sectional material under SEM at 5000X*

4.6. Discussion on the novelty

As described in the present work, the compacts in acetabular shape are sintered at 165°C to produce the final products. To retain the surface finish of the bearing generated during compaction, the SS ball is kept inside the cavity during the sintering process. As a result, the final bearing surface is formed with perfect sphericity ~ 1.0, dimensional deviation < ± 0.2%, and superior surface finish having $\mathbf{R}_a$ < 100 nm reflecting its parent surface.

Two types of sintering are possible after compaction of UHMWPE powder.

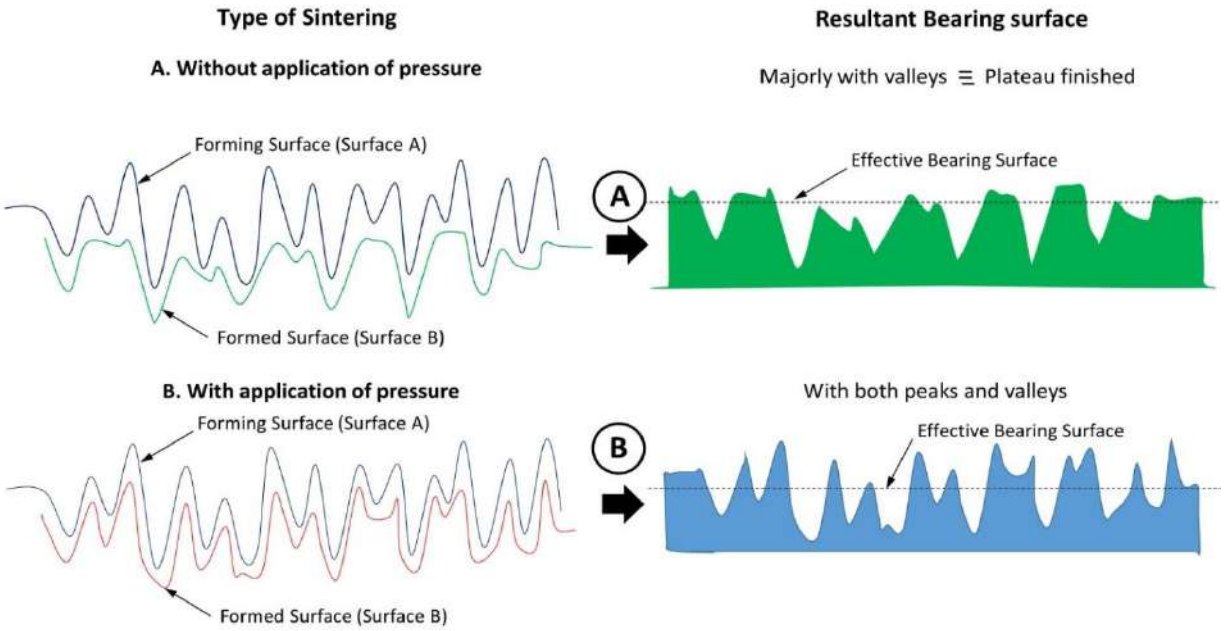

Figure 4.8. *UHMWPE bearing surface formed against stainless steel counter-face by sintering (A) without application of pressure (B) with application of pressure*

A. Without application of pressure

This type of sintering may be called as free sintering as described in the present work resulting in a bearing surface majorly having valleys in its profile. The peaks present in stainless steel counter-face penetrate through the molten polymer surface during its sintering to form valleys on it. But, the valleys on the stainless-steel counter-face are remained unfilled by molten UHMWPE due to lack of flow in it because of its high melt viscosity and absence of processing pressure. As a result, the bearing surface is formed without considerable number of peaks as shown schematically in Figure 4.8(A).

B. With application of pressure

This type of sintering may be called as forced sintering which is the case for hot isostatic pressing or compression moulding. Due to application of pressure during sintering, the molten polymer is forced to replicate the profile of the stainless-steel counter-face despite of the high melt viscosity of UHMWPE, as schematically shown in Figure 4.8(B). In this way, the peaks and valleys on the stainless-steel counter-face are imitated on the polymer bearing surface as the valleys and peaks, respectively, maintaining a surface roughness of similar order. Generally, hot isostatic pressing is considered to be superior to cold isostatic pressing and free sintering for material processing. However, the present study preferred free sintering over forced sintering to achieve a bearing surface without having a considerable number of peaks. This kind of surface, known as a Plateau finished surface, is an ideal choice for any bearing applications, which is usually generated by honing process, but the proposed technique does not require any machining process for the same. Wear loss of the material is likely to be reduced significantly due to absence of micro peaks on the bearing surface whereas the improved lubrication control and retention are expected by the trapped lubricant in the micro valleys. This would reduce the coefficient of friction (COF) between the femoral head and the acetabulum during its usage and improve the life of the implant.

4.7. Summary

- An ingenious technique is proposed for the manufacturing of Acetabular liner using medical grade UHMWPE-GUR1050 polymer and UHMWPE-0.25MWCNT composite powder by a cold isostatic compaction against a mirror finished metallic surface, followed by shape constrained sintering.

- The newly developed acetabular liners are found to possess inborn Plateau finished bearing surface with R_a <100 nm and a negative skewness of 1.156, altogether making it an ideal choice for any bearing applications.

- UHMWPE and UHMWPE-0.25MWCNT acetabular liner are manufactured having desired dimensional accuracy without any visible defects.

भारतीय प्रौद्योगिकी संस्थान गुवाहाटी
Indian Institute of Technology Guwahati

CHAPTER 5

ESTABLISHMENT OF SIMULATED *IN VIVO* CONDITION

5.1. Introduction

The imprimatur to a next generation acetabular liner primarily depends on the success in recreation of *in vivo* human joint biomechanics under *in vitro* environment during its preclinical testing. Hence, evaluation of next generation bearing materials under a realistic kinetic profile and tribological environment is not possible without testing them in a hip joint wear simulator under a lubricant, a rheologically equivalent to the synovial fluid**.** A joint simulator along with a synovial fluid analogue can mimic the *in vivo* conditions of the hip joint under *in vitro*. However, the hip joint simulators are not popular to the researchers due to its operational complexity, unavailability and expensive nature. At the same time, a rheological analogue of synovial fluid is not naturally abundant. Objective of the present chapter is to design an orbital bearing machine (OBM) simulator to apply the tribological conditions to a THA as per international guidelines having the simplicity of a wear screening device. A modular mechanism is designed to transform a conventional *Pin-On-Disc* tribometer into a *Ball-On-Cup* tribometer for testing the actual prosthetic joints as per **ISO 14242-3** guidelines and validated with an analytical model. This device is integrated with a bio-lubricant chamber, and a single DC motor is used to generate the recommended bi-axial angular motion and a load profile. Additionally, an attempt is made to synthesize a rheological equivalent synovial fluid to imitate the realistic contact stresses and wear mechanism of a THA under *in vitro* condition.

5.2. Development of a single station hip joint simulator

5.2.1. Design requirements as per ISO 14242-3

The OBM hip joint simulator is found to successfully evaluate the wear characteristics of THA bearing surface, hence, it is very popular worldwide. Test results produced by OBM simulator are found to correlate well within the clinical findings.

Standardization of parameters is very important for this kind of widely used machines for uniformity and comparability of results between the laboratories. ISO 14242-3 prescribes the relative angular motion and load profile to be applied on the articulating components of a THA during its *in vitro* OBM wear testing along with the frequency, duration and environment, which are described below in detail.

I. The simulator must be capable to produce the angular motions shown in Figure 5.1(A) with an accuracy of ± 3° at the minima and maxima of the motion in synchronisation with the corresponding load profile prescribed in Figure 5.1(B) with an accuracy of ± 3% of the maximum load at an operating frequency of 1 ± 0.1 Hz.

II. The test specimen must be mounted and enclosed using a corrosion resistant material, capable of holding acetabular and femoral components, with an enclosure to isolate the test specimen from third-body contamination.

III. Positioning and alignment of both femoral and acetabular components of the test specimen with respect to the axes of rotation must be reproducible following removal of the specimen for cleaning and measurement at regular interval as per the testing protocol.

IV. Lubrication system must keep the contact surfaces immersed under the test fluid of a minimum volume of 200 ml.

V. Temperature of the test fluid must be maintained at 37 °C ± 2 °C by the temperature control system.

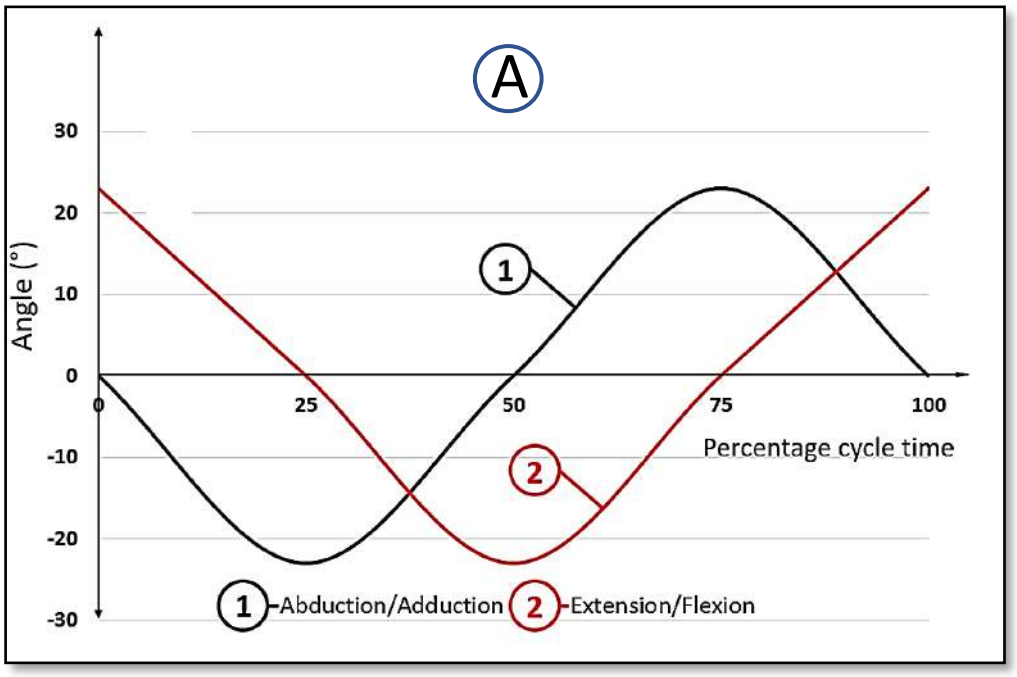

Cycle % ± 1%	0	25	50	75	100
Angle of Flexion (+) Extension (-) ± 3°	23°	0°	-23°	0°	23°
Angle of Abduction (+) Adduction (-) ± 3°	0°	-23°	0°	23°	0°

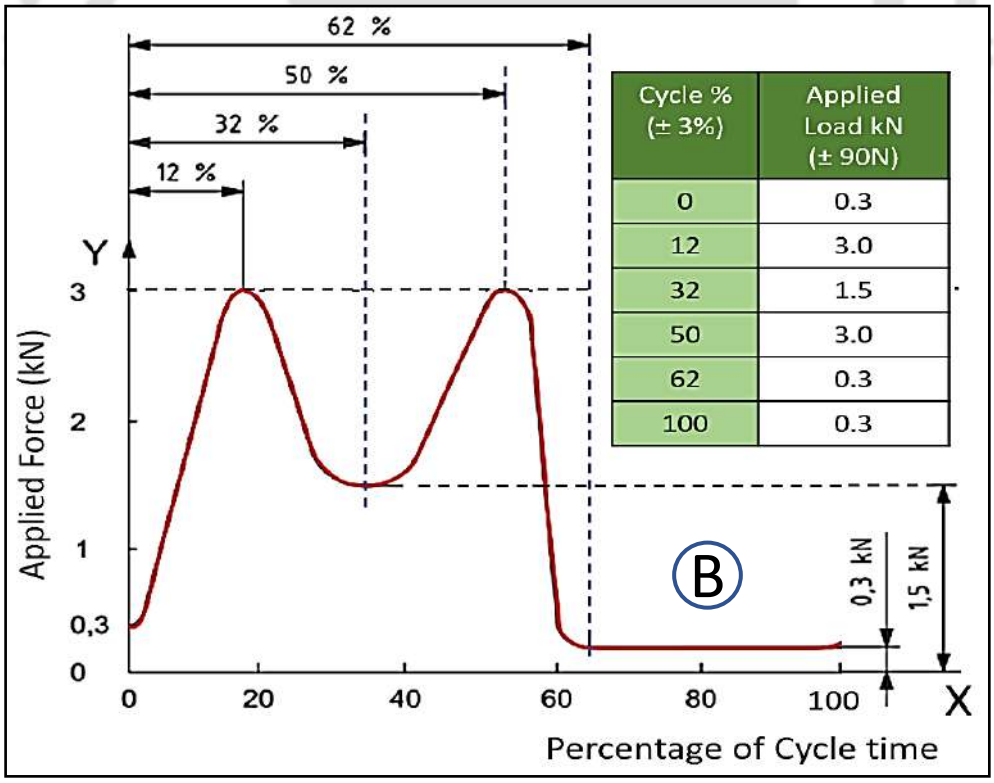

Cycle % (± 3%)	Applied Load kN (± 90N)
0	0.3
12	3.0
32	1.5
50	3.0
62	0.3
100	0.3

Figure 5.1. *(A) Variation with time of angular movement to be applied to the femoral test specimen [158] (B) Variation with time of the force to be applied along the loading axis [158]*

5.2.2. Design constraints in modification of a Pin-on-Disc to a OBM simulator

I. A typical Pin-On-Disc tribometer is equipped with a single motor which can rotate the disc at variable angular speed in horizontal plane and cannot produce the bi-axial angular motion.

II. In a Pin-On-Disc tribometer, dead load is applied on the pin sample against the rotating disc by a lever pulley mechanism, which cannot generate a dynamic load.

III. The THA components cannot be mounted in a Pin-On-Disc machine without a fixture, specifically designed for the purpose.

IV. A typical Pin-On-Disc device is not equipped with a lubricant chamber to keep the contact surfaces of a THA immersed under the test fluid during the testing.

V. Additionally, there are some geometrical constraints and limit of space depending upon the design of a Pin-On-Disc tribometer.

VI.

5.2.3. Design of the Mechanism

Working principle of an eccentric sheave is used to generate the biaxial rotational motion of a ball (femoral head) relative to its socket (acetabular liner) with an eccentric rod in reciprocation for the generation of dynamic load as shown in Figure 5.2. Generally, two independent servo motors are required to be synchronised along with the electronic control system to generate a similar kind of bi-axial angular motion profile, and a third one is required for the generation of a load profile. The proposed mechanism eliminates the challenges of synchronising the biaxial angular motion profile with load profile using a single motor.

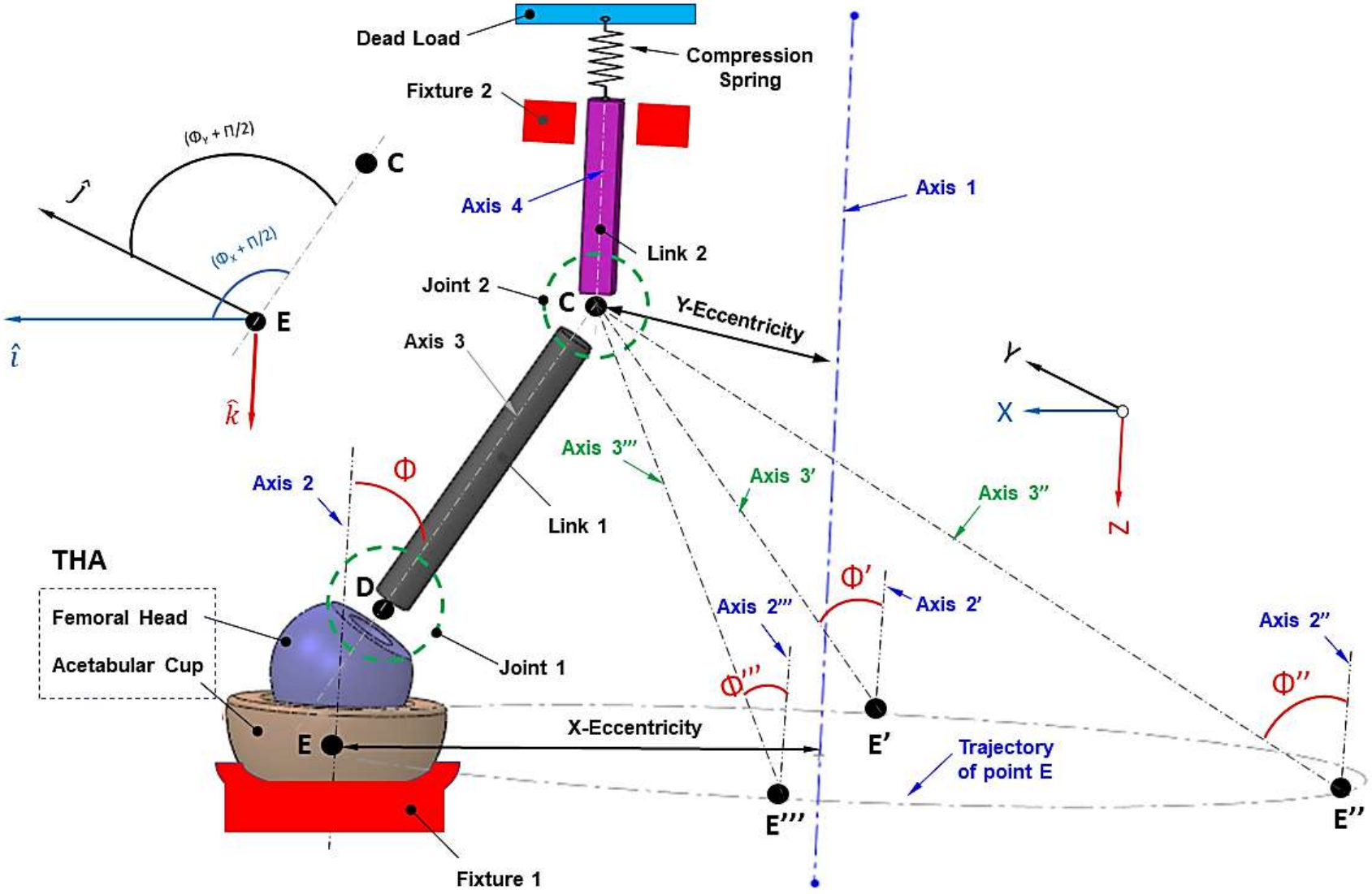

Figure 5.2. *Design concept of the mechanism based on the principle of an eccentric sheave*

5.2.3.1. Conceptualization

To explain the design requirements and working principle of the mechanism, the conceptual design with schematic diagram is shown in Figure 5.2 and explained below in detail.

The conceptual design consists of a THA, a motor with its shaft Axis 1, Link 1 with Axis 3, Joint 1 with centre D, Link 2 with Axis 4, Joint 2 with centre C, and a compression spring. The total hip arthroplasty comprising of a femoral head and an acetabular liner acts as a ball and socket joint. When the head or ball component is placed concentrically inside the acetabular socket, it is bound to have three degrees of rotational freedom. Link 1 is a connecting rod attached to the femoral head co-axially with zero degree of freedom by Joint 1. Link 2 is a reciprocating rod against the compression spring maintaining its axis at parallel to the Axis 1 with a Y-offset and connected to Link 1 by Joint 2 with three rotational degrees of freedom. If the acetabular liner with its centre at E is made to rotate about the axis of the motor shaft with an X-eccentricity in a specific horizontal plane, Axis 3 would make an asymmetric cone with vertex at C. As a result, the femoral head would be compelled to roll and pitch with respect to the acetabular liner, which are correlated to flexion-extension and abduction-adduction of a hip joint, respectively. At the same time, Link 2 would be compressed against the spring and the generated spring force can be utilized as the dynamic load applied on the THA. During the execution of the above motion, the following parameters would undergo periodic changes:

i. Length $\overline{CD}$ along Axis 3
ii. Φ- the angle between Axis 2 and Axis 3
iii. Φ_X – Component of Φ in X direction
iv. Φ_Y – Component of Φ in Y direction
v. Spring force

Φ_X and Φ_Y can be controlled by X-eccentricity of the acetabular liner, Y-offset of Link 2 with respect to Axis 1 and dependent on length $\overline{CD}$. They can attain the desired profile of flexion-extension and abduction-adduction with proper selection of these parameters. Spring force in association with some dead load can be modulated in order to provide the desired dynamic load profile after calculative selection of the spring constant and dead weight.

For the realization of the above, following major components are to be designed:

Fixture 1: A properly designed fixture is needed to rotate the acetabular liner about Axis 1 in a specific horizontal plane, keeping the Axis 2 parallel to the Axis 1 at a desired X-eccentricity. The Components *disc*❶, *cup holder*❷, *linear guideway*❸ and *washer*❹, as shown in Figure 5.3, are designed for these purposes.

Link 1: As per the requirement of the mechanism, length of Link 1 should be variable with self-adjusting ability. The Components s*lider*❺, *spring holder*❻ and *spring*❼, as shown in Figure 5.3, are designed for the said purpose.

Joint 1: Link 1 and femoral head is connected by Joint 1 with zero degree of freedom and the design of component s*lider*❺ ensured the same.

Joint 2: Link 1 and Link 2 are connected through Joint 2 to provide three degrees of rotational freedom between them, hence component *ball and socket joint*❽ is selected**.**

Link 2: It is a spring-loaded reciprocating rod which is meant to serve as a load applicator. The components *square bar* 1❾, *reciprocator*❿, *load cell*⓫, *Square Bar 2*⓬, *loading spring*⓭, *spring casing*⓮, *transmitter*⓯, *load pan*⓰, *dead load*⓱ and *limiter*⓲, as shown in Figure 5.3, are designed to constitute as a load applicator.

Fixture 2: it is meant to restrict the motion of the Link 2 to reciprocate at a desired Y-offset to the Axis 1. The component *square bar* 1❾ in combination with component *reciprocator*❿ is designed to fulfil the requirement.

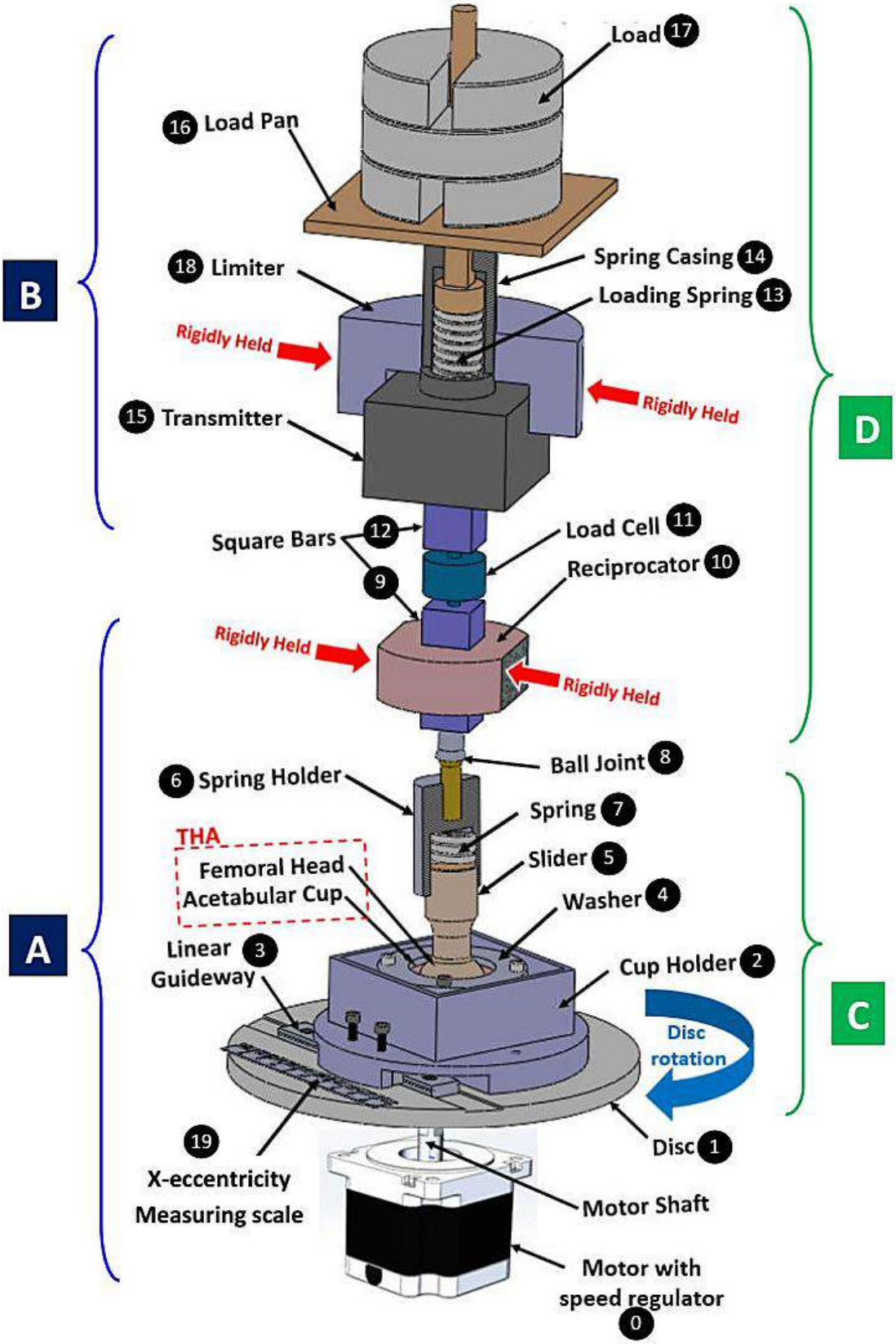

Figure 5.3. *Assembly design of Ball-On-Cup Tribometer Mechanism A Core Mechanism B Loading Mechanism C Rotating Mechanism and D Reciprocating mechanism*

5.2.3.2. Components and features

An assembly design of the novel *ball-on-cup* tribometer is shown in Figure 5.3. The design of the proposed mechanism includes two major units in terms of utility, viz., core mechanism and loading mechanism and two major segments in terms of generated motions, viz., rotating mechanism and sliding mechanism as referred in Figure 5.3. The core mechanism is responsible for imposing desired angular motion to the THA to be tested, whereas loading mechanism generates the necessary load profile to be applied on it and they are connected through a compression-extension type load cell as shown in Figure 5.3. Rotating mechanism is the segment of the simulator which is performing only rotary motion, while the sliding mechanism is performing reciprocation in vertical direction. Rotating mechanism and sliding mechanism are connected through a ball and socket joint as shown in Figure 5.3. The major components and their functions are described below:

I. The Core Mechanism

❖ **The Rotating Mechanism**

The rotating mechanism comprises the assembly of six components, viz., *disc*❶, *cup holder*❷, *linear guideway*❸, *slider*❺, *spring holder*❻ and *spring*❼, connected with the motor shaft as shown in Figure 5.3. The *Disc*❶ is a stainless-steel disc, which is coaxially attached to a DC motor shaft by means of the projected shaft at its bottom using a bellow coupling as shown in Figure 5.4. The *disc*❶ coupled with the DC motor rotates at a desired speed. A rectangular slot of 1mm depth with prescribed width of rail (WR) mentioned in Table 5.1(Row A) is made on top of its surface to accommodate a commercially available *linear guideway*❸. A disc of 8 mm thickness and 165 mm diameter is selected as per the geometric constraints of the pin-on-disc device, where it is to be attached.

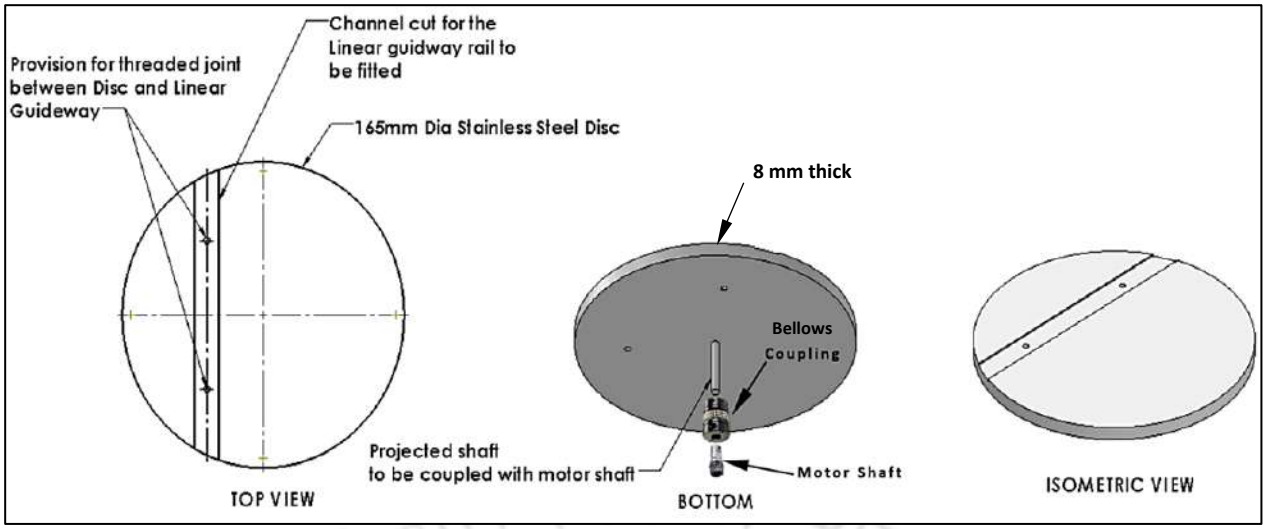

Figure 5.4. *The DISC❶ with its design specifications*

The *cup holder*❷ is made of stainless steel and it is specially designed to meet two major requirements. Firstly, it holds the Acetabular liner rigidly at the central cavity shown in Figure 5.5(I). During the testing, the Acetabular prosthesis is fixed at a desired eccentricity with respect to the *disc*❶ centre by means of a linear guideway❸. Secondly, the *cup holder*❷ has an integrated small chamber surrounding the Acetabular liner for holding the sufficient quantity of bio-lubricant during its tribological characterization. A channel is cut at the bottom of the *cup holder*❷ for fixing the linear guideway sliding block in it. A set of threaded holes (type D) is used to fix three levelling screws in order to ensure perfect alignment of the *cup holder*❷. Another set of threaded holes (type E) is used for fixing the sliding block at the channel. A third set of threaded holes (type G) is made to have a provision for fixing a *washer*❹ on the acetabular liner assembly. Sectional view of the *cup holder*❷ is shown in Figure 5.5(II) for better visualization of the internal design. Figure 5.5(III) and Figure 5.5(IV) show the solid view of the *cup holder* ❷ from its top and bottom, respectively, indicating the cavity to place acetabular liner with the lubricant chamber, and the channel to accommodate linear guideway. Figure 5.5(V) shows all the assembly provisions when the cup holder is seen from its bottom.

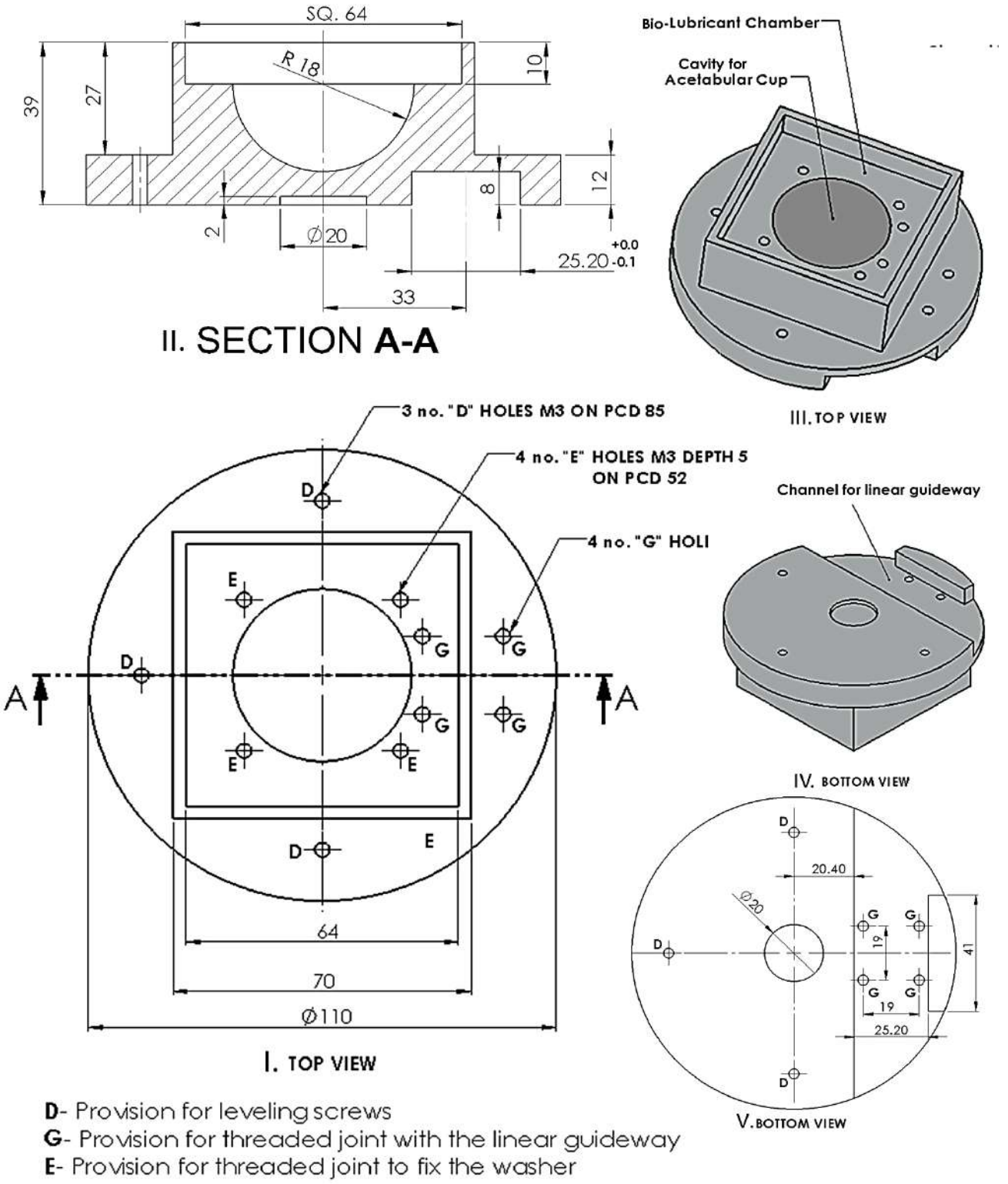

Figure 5.5*.(I)Top view of the CUP HOLDER❷ with its design specifications (II) Sectional view of the Design with all the assembly provisions (III) Top view showing the cavity to place acetabular liner with the lubricant chamber (IV) Bottom view showing the channel to accommodate linear guideway (V) Bottom view with all the assembly provision.*

A standard *linear guideway*❸ is required to make a sliding contact between the *cup holder*❷ and the *disc*❶, where HIWIN MGW 7H model linear guideway is selected as per the dynamic requirement of the mechanism listed in Table 5.1(Row A). The rail is fitted in the channel with M4 screws, while the sliding block, which is fitted on the rail, is fixed in the bottom channel of *cup holder*❷ by means of four type-E screws as shown in Figure 5.6(A).

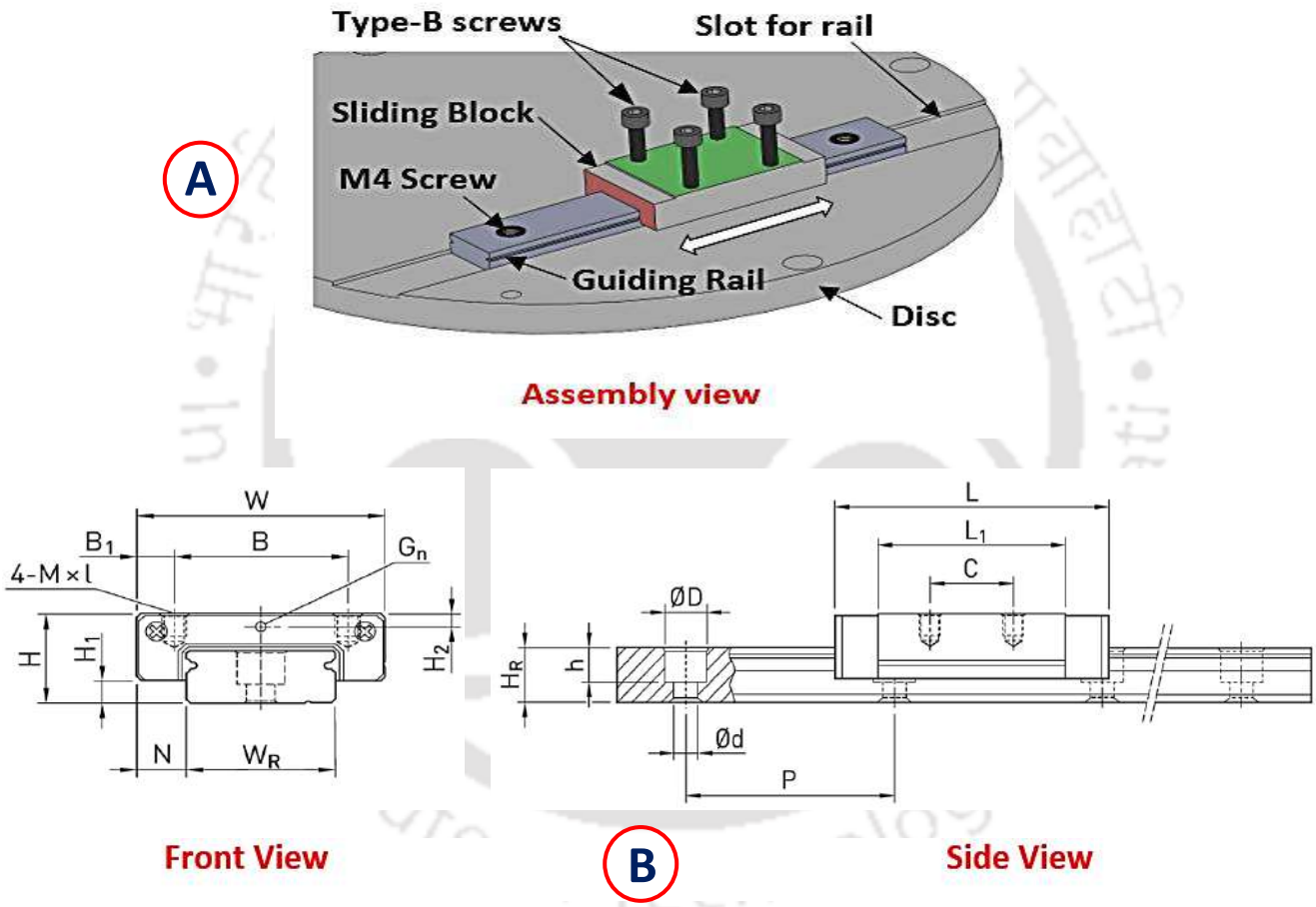

H	H1	N	W	B	B1	C	L1	L	Gn	M	l	H2
9	1.9	5.5	25	19	3	19	30.8	41	Φ1.2	M3	3	1.85

Figure 5.6. *(A)HIWIN MGW 7H Linear guideway❸ assembly with Disc❶(B) HIWIN MGW 7H linear guideway❸ specifications (www.hiwin.com) [all dimensions are in mm]*

Thus, the linear guideway❸ would provide a sliding contact between the *disc*❶ and the *cup holder*❷ in X-direction, as shown in Figure 5.6(A), allowing the *cup holder*❷ to be positioned at a desired eccentric position along the X-axis with respect to the *disc* centre. Figure 5.6(B) is referred for detailed design of the selected *linear guideway*❸.

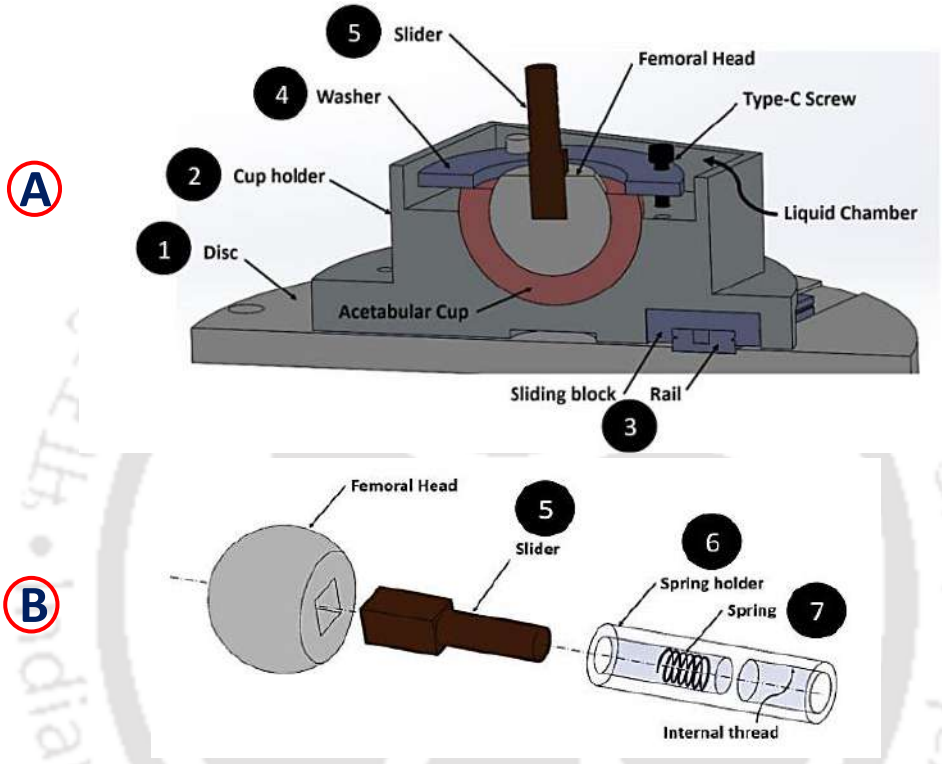

Figure 5.7. *(A) Cross sectional view of the assembled DISC❶ + LINEAR GUIDEWAY❸ + CUP HOLDER❷ + acetabular liner + WASHER❹ + femoral head + SLIDER❺ (B) Assembly sequence - Femoral head + SLIDER❺ + SPRING❼ + SPRING HOLDER❻*

A stainless-steel *washer*❹ is used for locking the Acetabular liner in the central cavity of *cup holder*❷. This *washer*❹ is fit into the liquid chamber and sit on the top surface of Acetabular liner to fix it rigidly with the *cup holder*❷ by means of type-G screws, and the assembly is shown in Figure 5.7(A). Any displacement of Acetabular liner relative to the *cup holder*❷ will be restricted by the clamping force given by the *washer*❹ in the form of friction. The central hole in the *washer*❹ provides the passage for insertion of the femoral head and its necessary movements during the testing of the prostheses.

If the inner and outer diameter of the acetabular prosthesis, which is to be tested, are D_i and D_o respectively, then a washer with inner diameter $(D_i + D_o)/2$ and outer diameter $(D_o + 5)$ with 3 mm thickness is selected for the purpose. The *Slider*❺ is a stainless-steel component used to make a force contact between the femoral head and the *spring*❼. It has a square cross-section at the femoral head end and circular cross-section at the *spring holder*❻ end, matching with their respective female ends. Square end will restrict its rotational degree of freedom with respect to femoral head, whereas the other end is free to slide co-axially inside the cylindrical *spring holder*❻ against the compression *spring*❼ held in the cavity, and the assembly is shown in Figure 5.7(B).

*Slider*❺*-spring-holder* assembly is acting as a linear link with variable length under a compressive load, necessary for eccentric rotation of the acetabular liner with respect to the *disc* axis. For maintaining the contact between these components during operation, a compression *spring* is incorporated in the mechanism. Design parameters and the calculated dimensions of *slider*❺ are shown in Figure 5.8(A) and listed in Table 5.1(Row B).

As shown in Figure 5.7(B), the *spring holder*❻ having two separate hollow sections is designed to confine the compression *spring* ❼ coaxially with it against the sliding movement of the *slider*❺ at one end. The other end of the hollow section of the spring holder is incorporated with an internal thread in order to connect a *ball and socket joint*❽ along its axis. Dimension of *spring holder*❻ is calculated based on the dynamic requirements of the mechanism as reported in Table 5.1(Row C) and depicted in Figure 5.8(B). A helical compression *spring*❼ is designed as per the kinetic requirement of the mechanism during testing of the prostheses. The *spring*❼ is set under pre-compression under the dead load at static condition and acts as a connecting link between the *spring holder*❻ and the *slider*❺ by maintaining cyclic contact between them when they are in relative reciprocation during operation. The *spring*❼ must withstand the maximum load applied to the mechanism and selected accordingly as listed in Table 5.1 (Row D).

Table 5.1. *Dynamic requirements and design of the components*

SL NO.	COMPONENT	MATERIAL PROPERTIES	MAXIMUM LOAD	CRITICAL EQUATION	CRITICAL DIMENSION
(A)	Linear Guideway ③ Figure 5.6	Commercially purchased HIWIN MGW 7H Stainless Steel	$F_X = 3 \times \sin 22°$ ~ 1.03 kN $M_Z = F_X \times a$ ~ 22.15 N.m a = 21.5 Figure 5.14(A)	$F_R > F_X$ $M_C > M_Z$	**ASSEMBLY** H = 9 mm, H1 = 1.9 mm, N= 5.5 mm **BLOCK** W= 25 mm, B=19 mm, B1=3 mm C=19 mm, L1=30.8 mm, L=41 mm H2=1.85 mm **RAIL** WR=14 mm, HR=5.2 mm, D=6 mm H=3.2 mm, d=3.5mm P=30 mm, E=10 mm **Dynamic Load Rating = 1.77 kN** (F_R) **Static Load Rating = 3.14 kN** **Rated Moment = 23.45 N.m** (M_C)
(B)	Slider⑤ Figure 5.8(A)	Stainless Steel 304 [207] Elastic Modulus = 200 GPa Proof Stress (σ_c)= 190 MPa Shear Modulus = 75 GPa Critical shear Stress(τ_c)= 90 MPa	$F_Z = 3.0$ kN $F_X = 3 \times \sin 22°$ ~ 1.03 kN $F_Y = 3 \times \sin 22°$ ~ 1.03 kN fos = 1.5	$\sigma_c / fos > 4F_Z / \Pi D^2$ $\tau_c / fos > 4F_X / \Pi D^2$ L/D < 12 (Short column)	**D_c = 6 mm** **L_1 < 72 mm**
(C)	Spring Holder ⑥ Figure 5.8(B)	Stainless Steel 304 [207] Elastic Modulus = 200 GPa Proof Stress (σ_c)= 190 MPa Shear Modulus = 75 GPa Critical shear Stress(τ_c)= 90 MPa	$F_Z = 3.0$ kN $F_X = 3 \times \sin 22°$ ~ 1.03 kN $F_Y = 3 \times \sin 22°$ ~ 1.03 kN fos = 1.5	$\tau_c / fos > F_X / \Pi db$ $\tau_c / fos > F_X / \Pi dc$	**d = D** **$(b_2)_c$ = 1 mm** **b_1 = 8 mm (M8 thread)** **$(b_3)_c$ = 3 mm** **$L_2 = L_3 + L_1/2$ = 55 mm**

Table 5.1. *Dynamic requirements and design of the components*

SL NO.	COMPONENT	MATERIAL PROPERTIES	MAXIMUM LOAD	CRITICAL EQUATION	CRITICAL DIMENSION
(D)	Spring ⑦ Figure 5.6	Commercially purchased LEE SPRING LHL 1260D 01 Helical Compression type Material: Oil tempered Chrome Silicone	F_Z = 3.0 kN	Solid Height < 40 mm Rate > 250 N/mm Compression < 15 mm No. of Spring = 1	**Outer diameter = 30.61 mm** **Casing Diameter = 31.75 mm (CD1)** **Wire Diameter = 6.35 mm** **Rate = 284.591 N/mm** **Free Length = 50.8 mm (L_3)** **Solid Length = 38.1 mm** **Total Coils = 5.97** **Active Coils = 3.97** **End Type = SQUARE & GROUND** **d = D = CD1**
(E)	Square Bar 1 ⑨ Figure 5.8(C)	Stainless Steel 304 [207] Elastic Modulus = 200 GPa Proof Stress (σ_c)= 190 MPa Shear Modulus = 75 GPa Critical shear Stress(τ_c)= 90 MPa	F_Z = 3.0 kN fos = 1.5	σ_c /fos > F_Z /e^2 $0.5L_4/e < 12$ (Short Column)	**e_c = 5mm** **L_4 < 120 mm**
(F)	Reciprocator ⑩ Figure 5.8(D)	Stainless Steel 304 [207] Elastic Modulus = 200 GPa Proof Stress (σ_c)= 190 MPa Shear Modulus = 75 GPa Critical shear Stress(τ_c)= 90 MPa	$F_X = 3 \times \sin 22°$ ~ 1.03 kN $F_Y = 3 \times \sin 22°$ ~ 1.03 kN fos = 1.5	τ_c / fos > F_X /2et	**e = 5 mm** **t = 5 mm** **f_c = 2mm**

Table 5.1. *Dynamic requirements and design of the components*

SL NO.	COMPONENT	MATERIAL PROPERTIES	MAXIMUM LOAD	CRITICAL EQUATION	CRITICAL DIMENSION
(G)	Square Bar 2⑫ Figure 5.8(E)	Stainless Steel 304 [207] Elastic Modulus = 200 GPa Proof Stress (σ_c)= 190 MPa Shear Modulus = 75 GPa Critical shear Stress(τ_c)= 90 MPa	F_Z = 3.0 kN	σ_c /fos > F_Z /e^2 0.5L_5/e < 12 (Short Column)	**e_c = 5mm** **L_5 < 120 mm**
(H)	Loading Spring⑬	Commercially Purchased LEE SPRING LHL 1250C 07 Helical Compression type Material: Oil tempered Chrome Silicone	F_Z = 3.0 kN	Solid Height < 40 mm Rate > 100 N/mm Compression < 10 mm No. of Spring = 4	**Outer diameter = 30.35 mm** **Casing Diameter = 31.75 mm (CD2)** **Wire Diameter = 6.17 mm** **Rate = 109.458 N/mm** **Free Length = 101.6 mm (L_3)** **Solid Length = 70.1 mm** **Total Coils = 11.29** **Active Coils = 9.29** **End Type = SQUARE & GROUND**

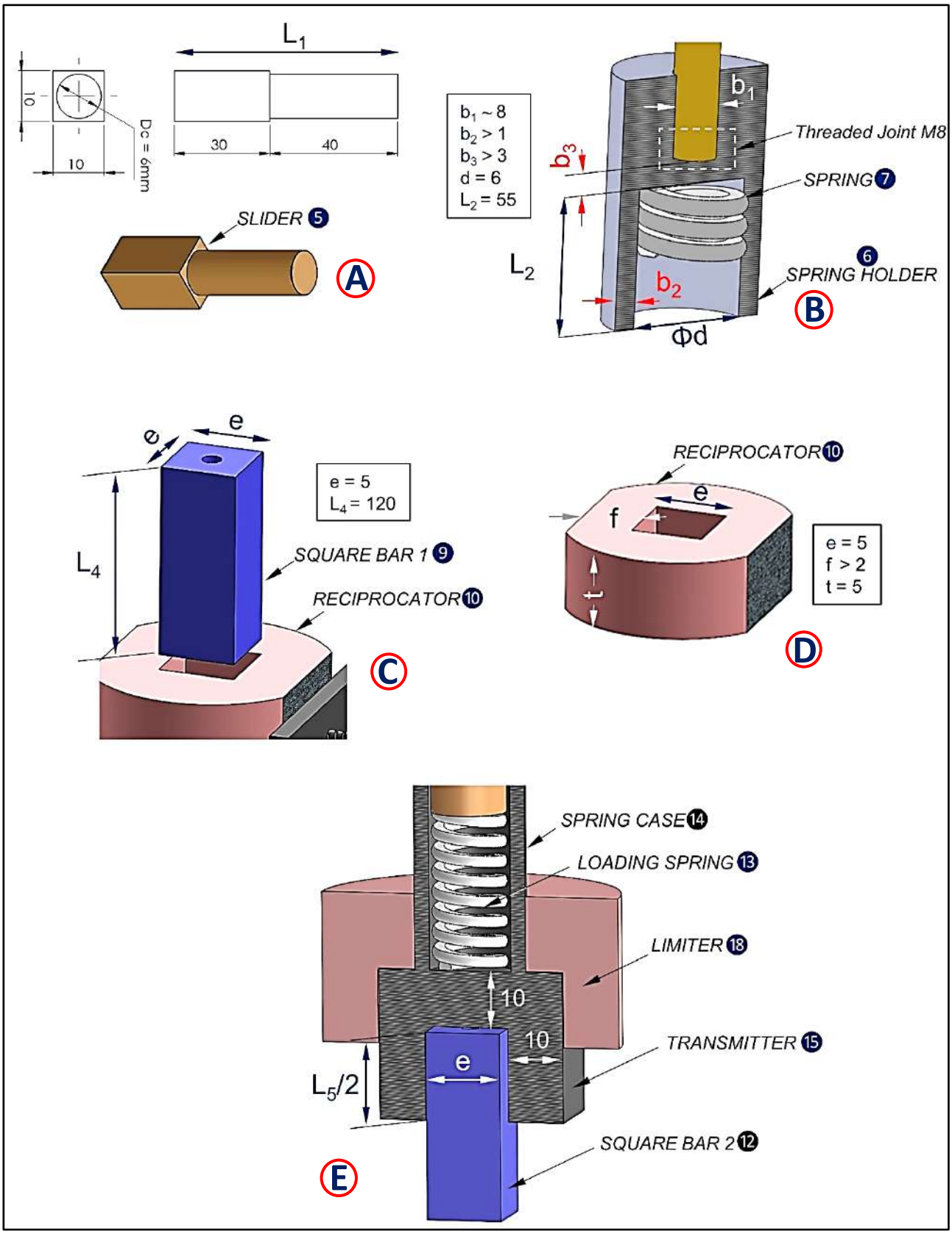

Figure 5.8. *Dimension of the components (A) Slider 5 (B) Spring Holder (C) Square Bar 1 9 (D) Reciprocator 10 (E) transmitter 15*

❖ **Ball and Socket Joint❽**

A *ball and socket joint*❽ with a dynamic load rating of 5 kN (~160% of maximum applied load) as per the requirement of the mechanism is used to connect the rotating part of the mechanism to the reciprocating part. The socket end is connected to the *square bar 1*❾ and the ball end is threaded into the *spring holder*❻ by means of a threaded joint in order to provide three degrees of rotational freedom in it, and it is shown in Figure 5.9(B).

❖ **The Reciprocating Mechanism**

The reciprocating mechanism comprises the assembly of four components, viz., Square Bar 1❾, Reciprocator❿, Load cell⓫ and Square Bar 2⓬, connected with the rotating mechanism by means of the ball and socket joint ❽ as shown in Figure 5.3.

Square bar 1❾ is the connecting link between the *Load cell*⓫ and the *Ball and socket joint*❽ by means of threaded joints, making sliding contact with the *reciprocator*❿. Threads are made in order to match the counterpart of load cell. Rotational freedom of the bar is restricted by its geometry, and it is shown in Figure 5.10(A). Dimension of *Square bar* 1❾ is decided based on the kinetics of the mechanism as reported in Table 5.1(Row E).

As its name suggests, the *reciprocator*❿ provides reciprocating motion to the entire loading mechanism in vertical direction (Z) through the *square bar 1*❾ by limiting its motion to a vertical sliding. It helps to transmit a purely vertical load to the mechanism. The *reciprocator*❿ is clamped by an adjustable vice having the provision of horizontal travel ± 50 mm and its position can be locked at a desired Y co-ordinate. This can provide a calculated Y-eccentricity in the range of 0-50 mm to the mechanism on both side, and the assembly to achieve the same is shown in Figure 5.10(A). Critical dimension of *reciprocator*❿ is calculated based on the stress analysis of the component as reported in Table 5.1(Row F).

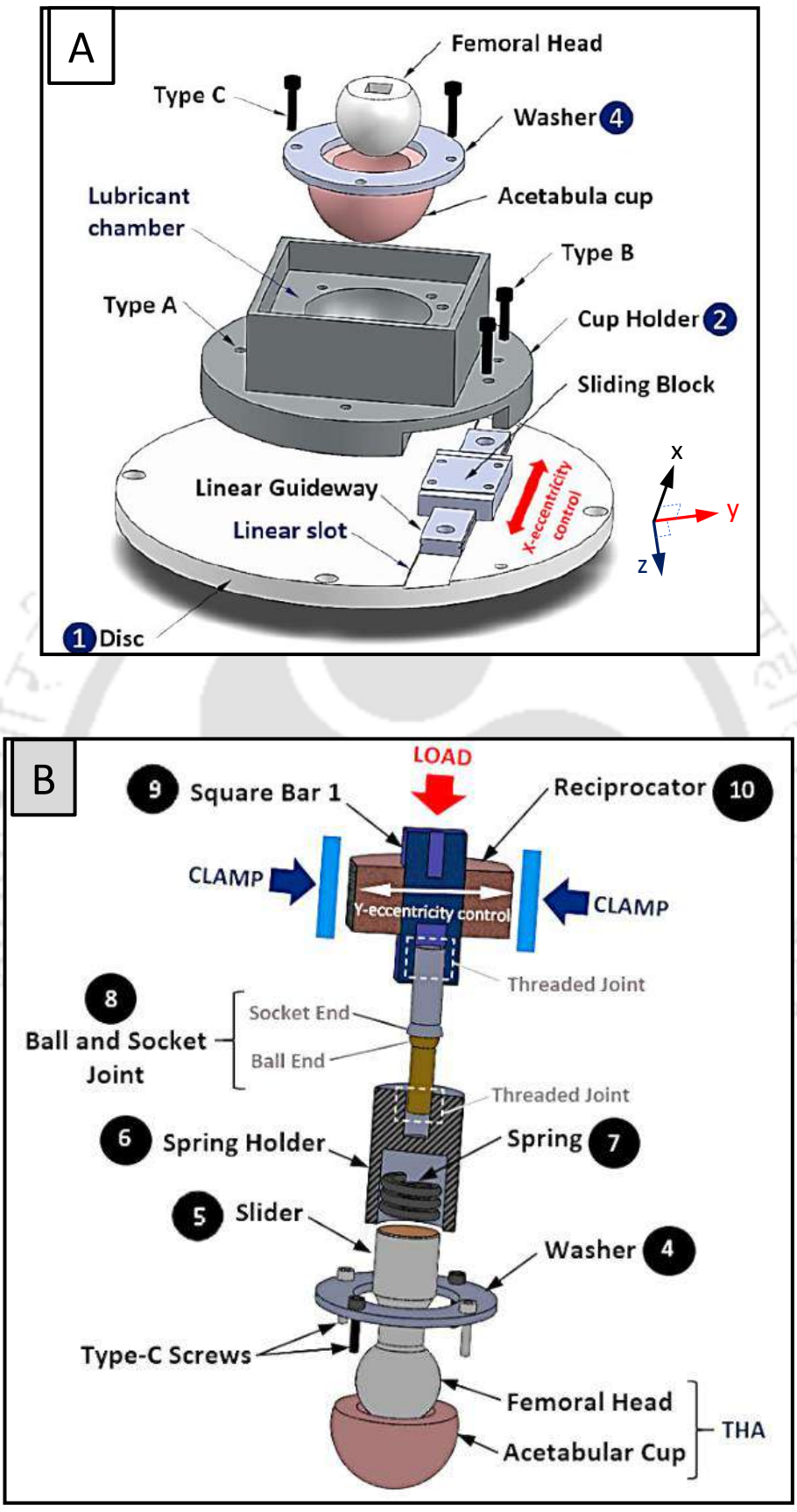

Figure 5.9. *Assembly sequence-(A) Disc❶+Linear Guideway❸+Cupholder❷ + Acetabular liner + Washer❹+ Femoral Head (B) Acetabular liner + Washer❹+ Femoral Head+ Slider❺+Spring❼+Spring Holder❻+ Ball Joint❽+ Square Bar+ Reciprocator❿*

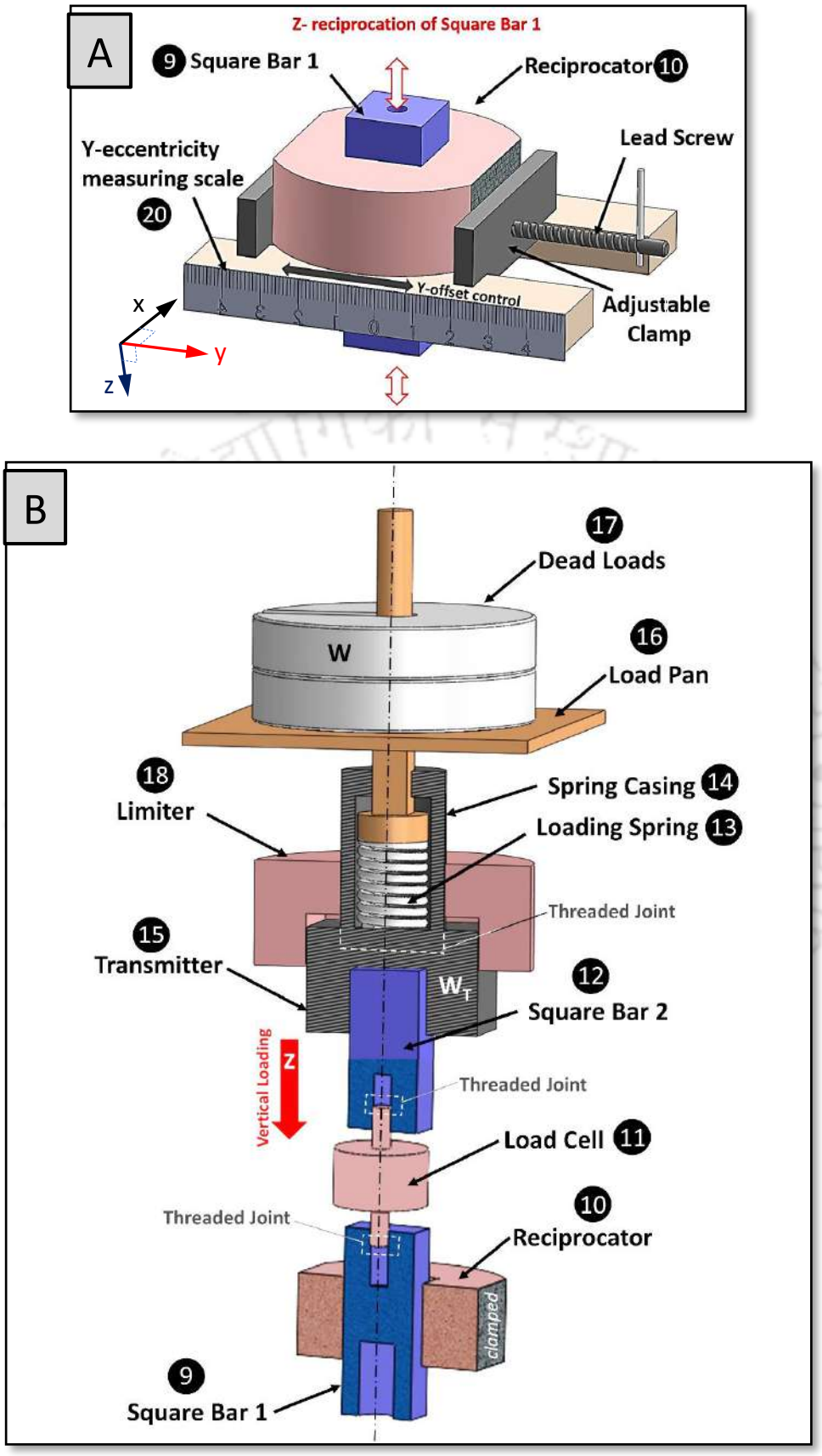

Figure 5.10. *(A) Fixture for Reciprocator including Y-eccentricity measuring scale and adjustable clamp (B) Loading Mechanism consisting of Loading spring 13, Dead load 17, Transmitter 15 and Limiter 18*

As per the ISO 14242-3, the maximum normal load of 3kN is to be applied on the prosthesis during its testing. Thus, a compression-extension *load cell*⓫ with a load rating of 5kN (~160% of the maximum applied load of 3kN as per the ISO 14242-3) is connected in between the *square bar 1* ❾ and the *square bar 2* ⓬ by means of threaded joints, as shown in Figure 5.10(B). The *load cell*⓫ is used to continuously measure the transmitted normal load generated by the loading mechanism to the Hip prostheses during their characterization. *Square Bar 2*⓬ transmits the load applied on the *load pan*⓰ resting on its head to the mechanism through the *Load cell*⓫, which is connected co-axially to it by means of threaded joint and it is shown in Figure 5.10(B). Threads are made in order to match the counterpart of load cell UNV 0.5 (Sensomatic, India). Dimension of *Square bar 2*⓬ is decided based on the kinetics of the mechanism as reported in Table 5.1(Row G).

II. The Loading Mechanism

Loading mechanism consists of a *load pan*⓰ with a *dead load*⓱ on its top resting on the *loading spring*⓭ confined in the *spring casing*⓮, as shown in Figure 5.10(B). The components and their functions are briefly described below:

*Loading spring*⓭, as shown in Figure 5.10(B), is a helical compression spring selected as per the dynamic requirement of the simulator during testing of the prostheses. Its bottom end is fixed with the *spring casing*⓮ by welding while the top end is set free. The *loading spring*⓭ is under the action of *dead load*⓱ on its top through the *load pan*⓰ and get excited at its bottom end by the *transmitter*⓯. The parameters for the selection of *loading spring*⓭ are reported in Table 5.1(Row H) and a combination of four springs connected in parallel is used to serve the purpose. The *spring casing*⓮ is a stainless-steel hollow cylinder as prescribed in Table 5.1(Row H) to hold the *loading spring*⓭ coaxially with itself and it prevents the spring from buckling. Its top end allows the *load pan*⓰ to sit on the spring and reciprocate in vertical direction following spring compression or extension, while the bottom end is rigidly attached to the *transmitter*⓯ as shown in Figure 5.10(B). The *transmitter*⓯ is a stainless-steel square block, rigidly attached with the *spring casing*⓮ at its top end by means of threaded joint and sits on the *square bar 2*⓬ as shown in Figure 5.10(B). It reciprocates vertically inside the *limiter*⓲ and transmits the displacement excitation generated by *square*

*bar 2*⓬ to the *loading spring*⓭ through its casing. The square profile of the *transmitter*⓯ restricts its rotational degrees of freedom inside the *limiter*⓲. The square slot at the bottom end of *transmitter*⓯ is made to accommodate *square bar 2*⓬ and the selected dimensions are shown in Figure 5.8(E). The *load pan*⓰ holds the *dead load*⓱ on its top and applies the collective load directly on the *loading spring*⓭. This dead load is converted into a dynamic load by the *loading spring*⓭ when excited by the mechanism and conveyed *to square bar 2*⓬ through the *transmitter*⓯ in the vertical direction and it is shown in Figure 5.10(B).

The *limiter*⓲ acts as a hub for the *transmitter*⓯. It is clamped at a desired position for restricting the motion of the *transmitter*⓯ to a vertical reciprocation with a certain upward limit. The limit for *transmitter*⓯ motion is set to cut-off its motion beyond the equilibrium position of the *loading spring*⓭ to nullify the upward spring force acted upon the mechanism during spring expansion.

III. Attachability to a pin-on-disk tribometer

The core mechanism is designed as a modular attachment to be fixed in a *pin-on-disc* tribometer with *Disc*❶, *Reciprocator*❿, *Square Bar 1*❾, ***Y****-eccentricity Control*⓴ and a variable speed *Motor*⓿ as the common components as shown in Figure 5.11**,** where the equivalent components between the pin-on-disc tribometer and the proposed mechanism are shown and identified**.** The existing *Counter Disc*❶' of the pin-on-disc tribometer can be used as the *Disc*❶ with some modifications, as described above**.** The *pin holder*❿' may be utilized as the *Reciprocator*❿ to hold *Square Bar 1*❾ in place of the pin❾'. The wear track radius adjustment mechanism of the tribometer can work as the **Y**-eccentricity control of the simulator. As this mechanism needs only one motor for its functioning, a motor attached to a regular tribometer with speed regulator will serve the purpose. In case of pin-on-disc instrument, the dead loads are used for the application of loads and the same loading mechanism can be utilized with a few minor modifications.

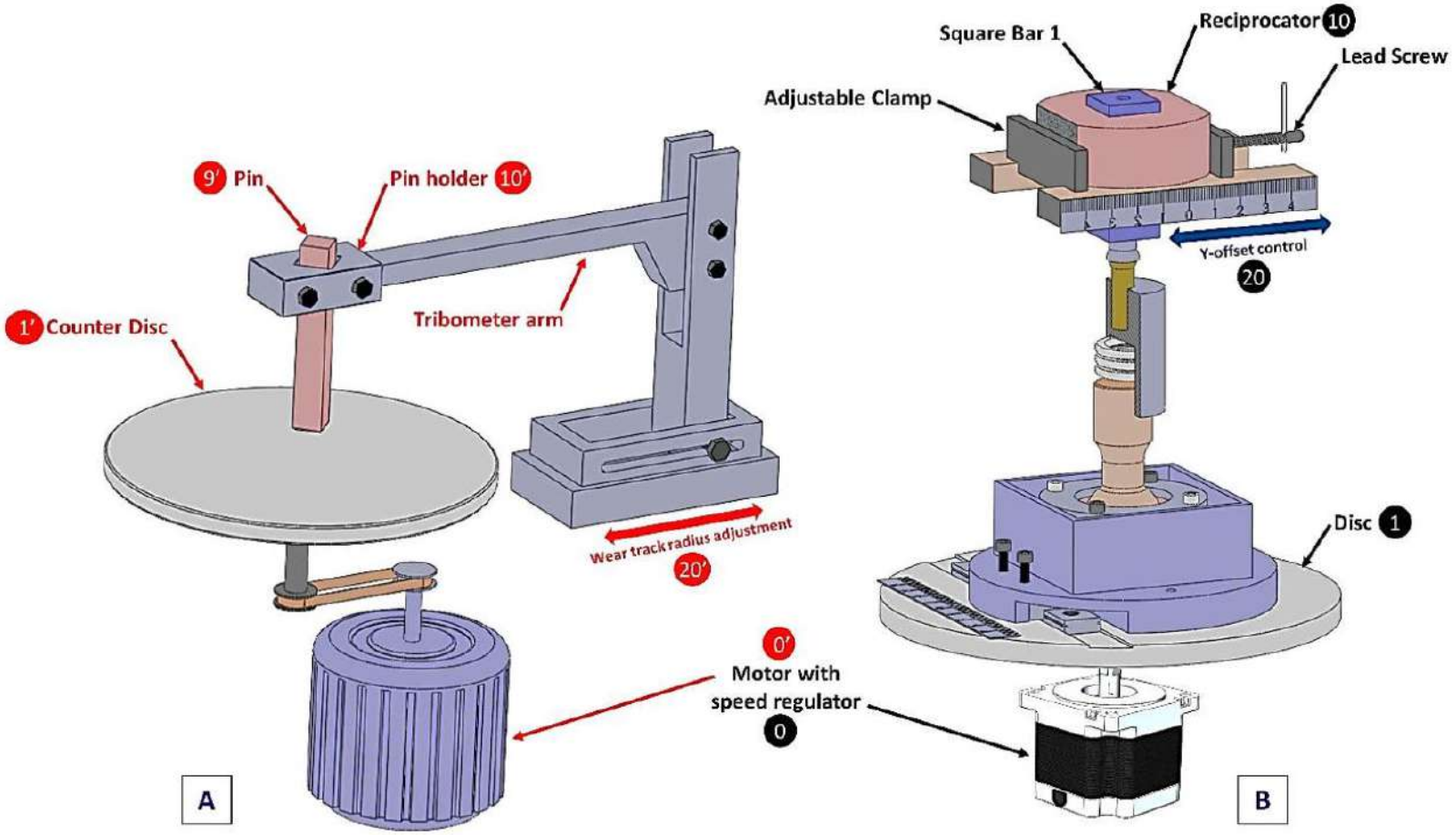

Figure 5.11.(A) *Schematic of a Pin-on-disc Tribometer (B) Core mechanism designed as a modular attachment to the Pin-on-disc Tribometer with DISC 1, RECIPROCATOR 10, SQUARE BAR 1 9, Y-ECCENTRICITY CONTROL 20 and variable speed MOTOR 0 as the common components*

It is to be noted that the *Disc*❶ has a diameter of 165 mm and **X**-eccentricity of the acetabular liner can be varied in the range of 0 to ± 27.5 mm after accommodating the cup holder of external diameter of 110 mm. The **Y**-eccentricity is limited by the **Y**-travel of tribometer arm and it can be varied in the range of 0 to ±80 mm. Components *disc*❶, *cup holder*❷, *linear guideway*❸ and *washer*❹, *slider*❺, *spring holder*❻ and *spring*❼, *ball and socket joint*❽, *square bar* 1❾ are to be placed in the vertical space available between the disc and the pin holder, which is limited to 120 mm.

5.2.3.3. Working Principle

To explain the working principle of the designed setup, some significant points are marked on the mechanism, and it is shown in Figure 5.12(A). Point ***A*** is the point of load application on the *square bar 1*❾. When the load is transferred to the acetabular liner, it generates a reaction force. The vertical component of this reaction force is measured by the *load cell*⓫. Point ***B*** is the center of *reciprocator*❿ and it is clamped at the desired location. ***C*** is the centre of the *ball and socket joint*❽. Hence, ***AC*** is the axis (Z) of load application. ***D*** is a point on axis of *slider*❺. ***E*** is the centre of acetabular liner as well as femoral head. The linear guideway❸ on which the acetabular liner -femoral head assembly is fixed via the *cup holder*❷, as shown in Figure 5.9(A), is used to provide a desired eccentricity to the Acetabular liner in X direction with respect to the motor shaft. Using the adjustable clamping mechanism as shown in Figure 5.10(A), axis ***BC*** is made at desired Y-eccentricity to the *disc* axis. This way, axes ***CE*** and ***BC*** are made to intersect at a desired angle at ***C.***

I. Generation of Bi-axial Angular Motion

When the *disc*❶ is rotated, the Acetabular liner is made to rotate about a point non-collinear with ***BC***. At the same time, axis ***CE*** is compelled to rotate about ***C*** in a conical profile, adjusting the length ***CE*** accordingly and it is shown in Figure 5.12(B). As a result, the femoral head is made to roll, and pitch with respect to the Acetabular liner, which can be correlated into flexion-extension and abduction-adduction of the hip joint, respectively, as shown in Figure 5.12(C). Figure 5.12(B) (i)-(v) shows the angular position of femoral head with respect to

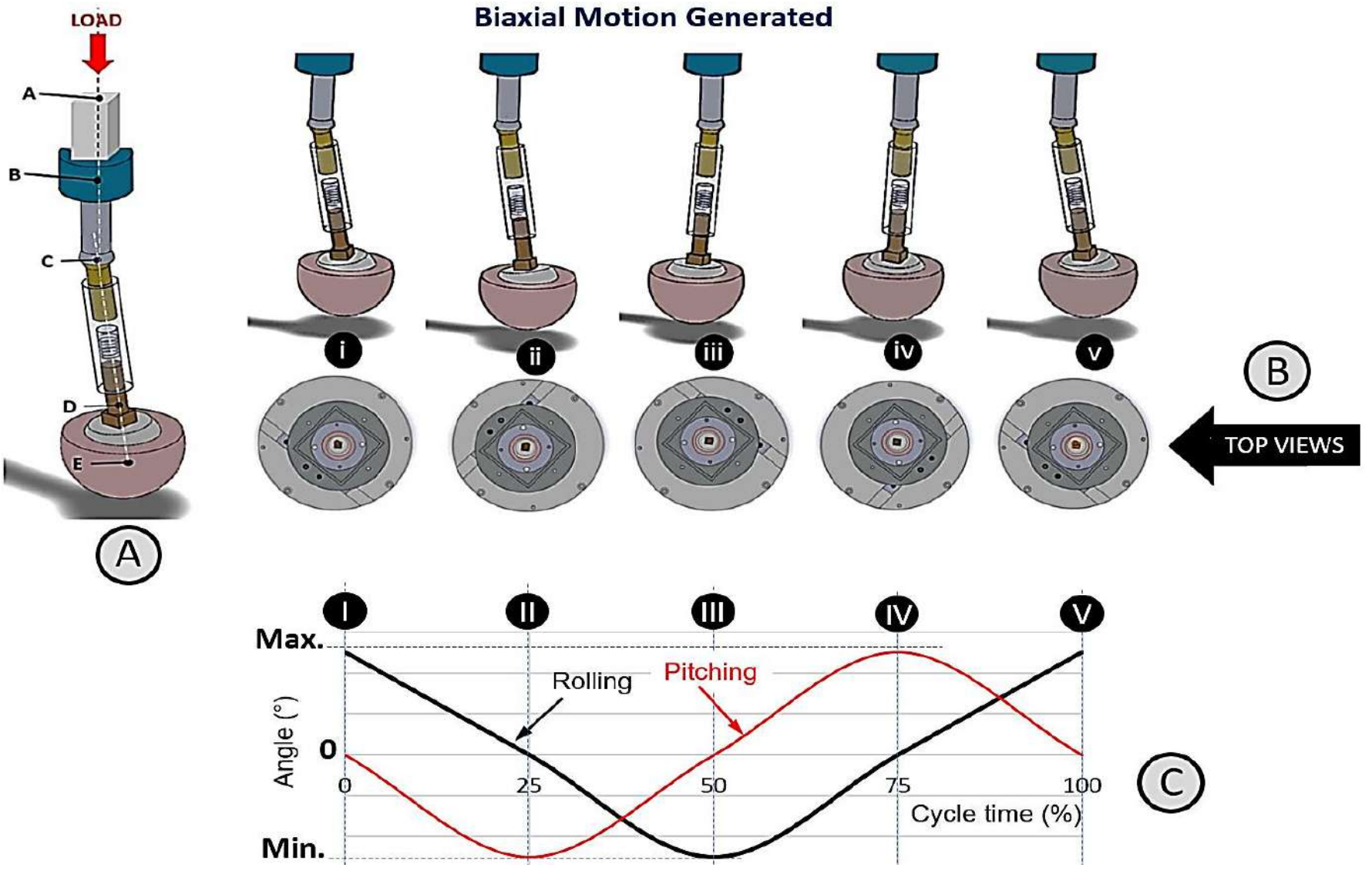

Figure 5.12. *(A)Working principle of the mechanism (B) Instants of the operational cycle at (i) t=0 (ii) t=T/4 (iii) =T/2 (iv) t=3T/4 (v) t=T (C) The rolling and pitching motion generated by the simulated motion of the mechanism*

Acetabular liner at each quarter of the working cycle and the corresponding angles w.r.t. **X** and **Y** axis are shown in Figure 5.12(C) (i)-(v) on the **F-E (Simulated)** and **AB-AD (Simulated)** curves, respectively. Figure 5.12(B) (i) corresponds to the angular position of femoral head with zero abduction-adduction angle and maximum flexion-extension angle in positive direction with respect to acetabular liner as shown in Figure 5.12(C) (i). Figure 5.12(B) (ii)corresponds to zero flexion-extension angle and maximum abduction-adduction angle in negative direction as shown in Figure 5.12(C) (ii) after completion of the first quarter of the cycle. At the end of second quarter of the cycle, the angular position of femoral head with respect to acetabular liner is shown in Figure 5.12(B) (iii), which is the zero abduction-adduction with maximum negative flexion-extension position as depicted in Figure 5.12(C) (iii). Figure 5.12(B) (iv) is related with Figure 5.12(C) (iv), which depicts the angular position of Acetabular liner after the completion of third quarter of the cycle and the same at the end of the cycle is shown in Figure 5.12(B) (v) which corresponds to Figure 5.12(C) (v). By this way, the **X** and **Y** eccentricity of the mechanism can be controlled in order to apply the desired angular movement to the femoral head relative to the Acetabular liner.

II. Generation of Load profile

Figure 5.13(I) shows the working principle of the loading mechanism and the generated load profile is compared with the prescribed one by **ISO 14242-3** in Figure 5.13(II). In order to achieve variable length of the link *CD* during operation of the mechanism, *square bar 2*⓬ is compelled to reciprocate in a sinusoidal manner and this cyclic displacement is used as the excitation for the *loading spring*⓭ through the *transmitter*⓯. Under a sinusoidal excitation, the *loading spring*⓭ with dead loads on its top generates a dynamic load of same nature on the *transmitter*⓯ which consequently conveyed to the test section. Amplitude of the load profile will be based on the stiffness (**k**) of the *loading spring*⓭ and the dead weight (**W**), while the average load depends on the combined self-weight of the *spring holder*❻, *square bar 1*❾, *square bar 2*⓬, *transmitter*⓯, and *spring casing*⓮. The limiter⓲ is provided to restrict the upward motion of the *transmitter*⓯ beyond a certain limit. By this way, the *transmitter*⓯ is compelled to convey only the desired range of the loading cycle generated by the loading mechanism to the *square bar 2*⓬ without restricting the oscillating motion of the *loading spring*⓭ inside its casing.

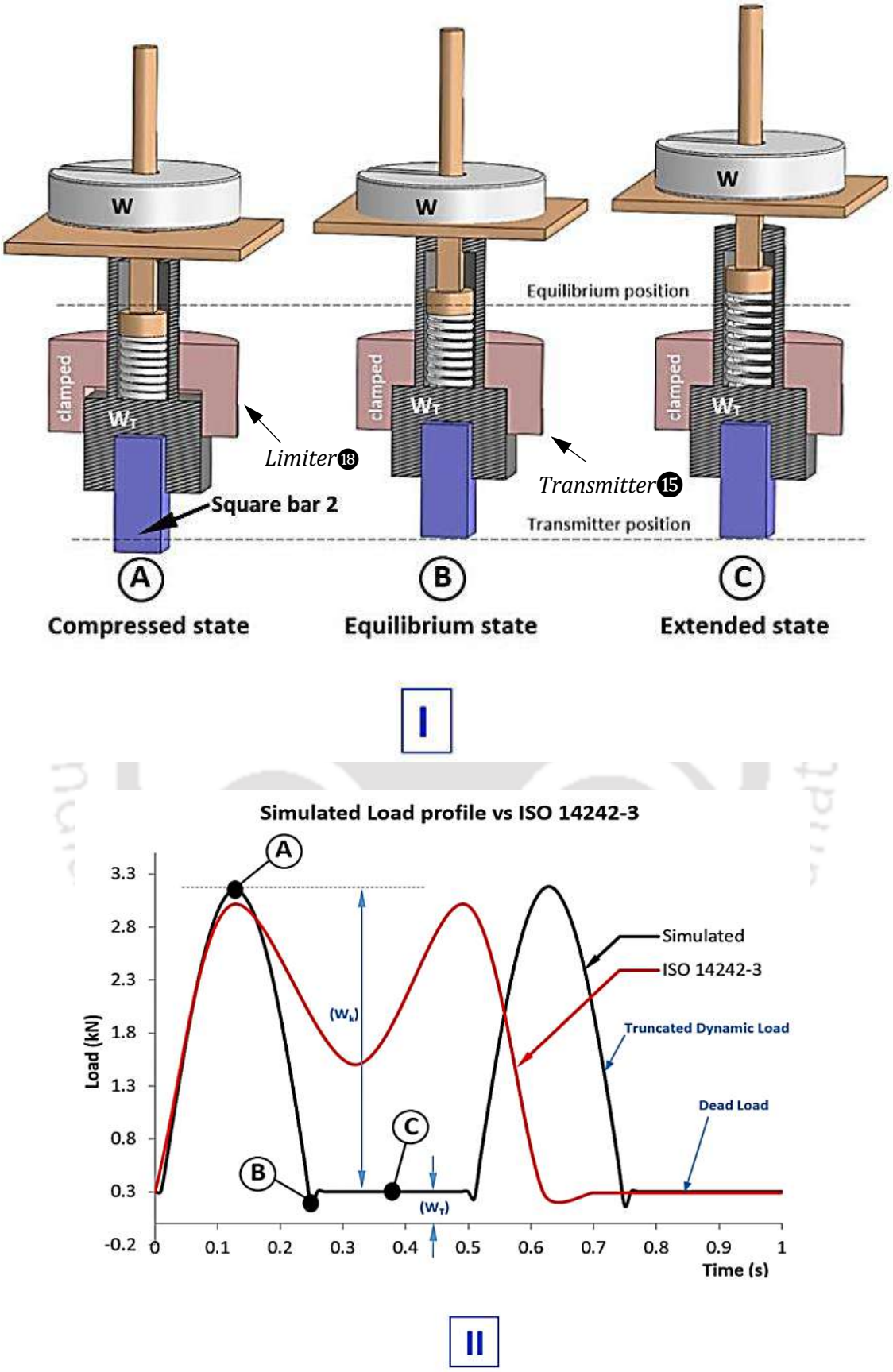

Figure 5.13. *(I) Working principle of Loading Mechanism (II) Comparison between the recommended load profile with the simulated one*

Figure 5.13(I)-(A) shows the position of the *square bar 2*⓬ at the maximum compression of the *loading spring*⓭ generating the maximum compressive load indicated as (A) in Figure 5.13(II). Figure 5.13(I)-(B) shows the equilibrium position of the *loading spring*⓭ at which only the dead load of the system is acted upon the THA as indicated as (B) in Figure 5.13(II). Figure 5.13(I)-(C) shows the *loading spring*⓭ in expanded position. However, the *limiter*⓲ does not allow the *transmitter*⓯ to loose contact with *square bar 2*⓬. At this position the spring force is detached from the mechanism resulting as indicated as (C) in Figure 5.13(II).

5.2.3.4. Analytical Model for parameter selection

An analytical model is developed for the validation of motion profile generated by the mechanism. Figure 5.14(A) shows an instantantaneous position of the femoral head during its motion inside the acetabular liner. Orientation of the flat circular surface **Q** on the top of femoral head is continuously changing w.r.t. the **XY** plane, i.e., the orientation of the acetabular liner and inclination between these two planes in **X** and **Y** directions can be considered as the Abduction-Adduction and Flexion-Extension angles, respectively, for the THA under simulation.

The acetabular liner is made to rotate about the motor shaft with an eccentricity of $\boldsymbol{a}$ w.r.t. the disc center **O**, taken as origin for the analysis. **Z**-axis is considerd to be the axis of motor shaft with direction vector $\hat{k}$. The center of the *ball and socket joint*❽ is located at **R** with a **Y**-eccentricity of $\boldsymbol{b}$ w.r.t. the origin. Thus, the vector equations can be written as:

O (0,0,0) – Reference

$$\vec{a} = a.cos\omega\ \hat{\imath} + a.sin\omega\ \hat{\jmath} \quad \text{... (5.1)}$$

$$\vec{b} = b\,\hat{\jmath} \quad \text{... (5.2)}$$

$$\vec{d} = b\,\hat{\jmath} + c\,\hat{k} \quad \text{... (5.3)}$$

$$\vec{q} = \vec{a} - \vec{d} \quad \text{... (5.4)}$$

$$\hat{q} = \frac{a.cos\omega\ \hat{\imath} + (a.sin\omega\ - b)\hat{\jmath} - c\,\hat{k}}{\sqrt{[(a.cos\omega)^2 + (a.sin\omega\ - b)^2 + c^2]}} \quad \text{... (5.5)}$$

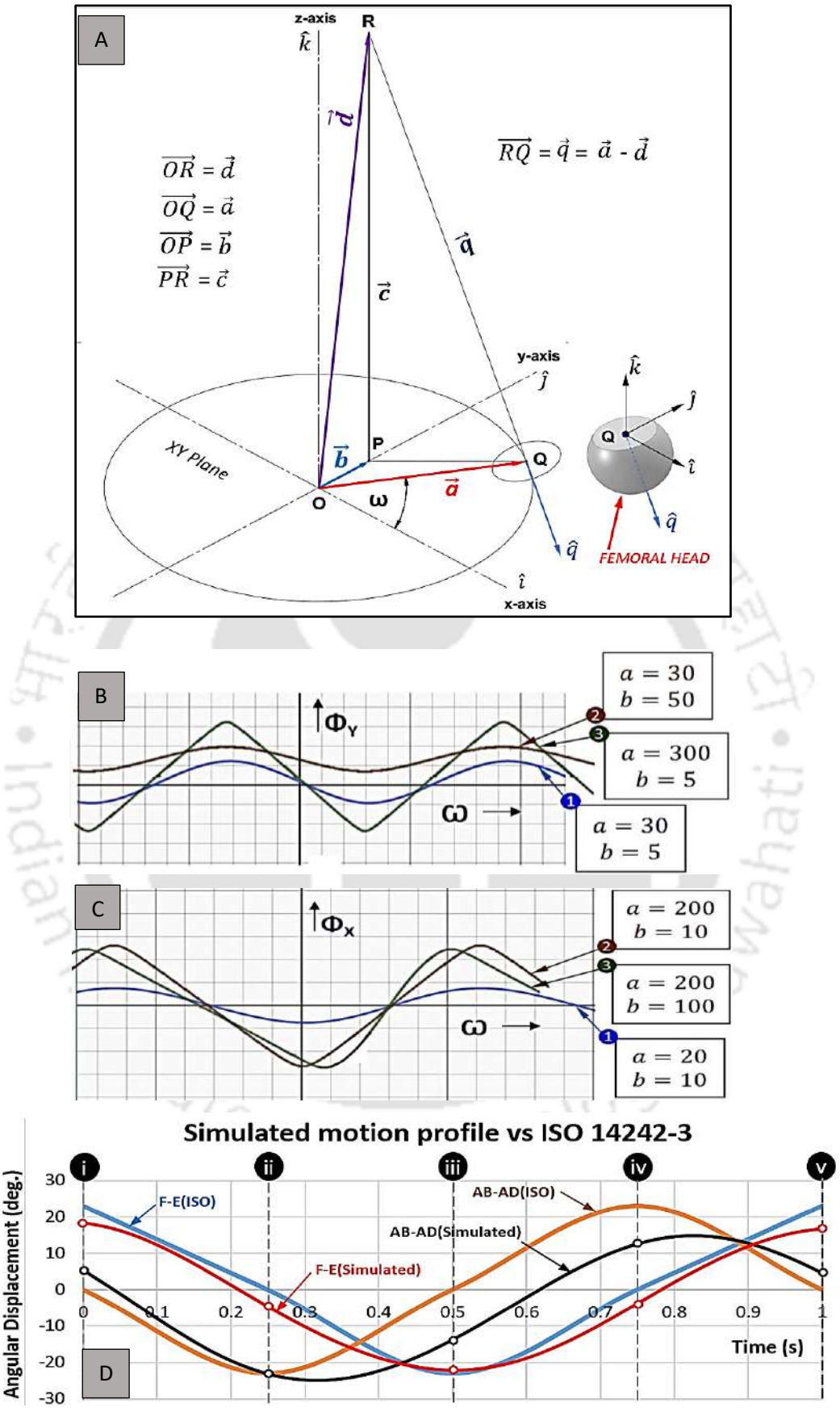

Figure 5.14. *(A) Vector diagram of the Rotating Mechanism (B) Curve Φ_Y at various parameters (C) Curve Φ_X at various parameters (D)comparison between achieved motion profiles by simulation with the prescribed one by ISO 14242-3*

Where, $\hat{\imath}$, $\hat{\jmath}$ *and* $\hat{k}$ are the unit vectors along **X**, **Y** and **Z** axis, respectively. The positions of **Q** and **R** are given by the vectors $\vec{\boldsymbol{a}}$ *and* $\vec{\boldsymbol{d}}$ with $\boldsymbol{c}$ being the height of *ball and socket joint*[8] w.r.t. acetabular liner. The instantaneous angular position of the radius vector $\vec{\boldsymbol{a}}$ w.r.t. **X**-axis is denoted by $\boldsymbol{\omega}$. The normal vector to the flat circular surface **Q** is represented as $\hat{q}$. If Φ_X and Φ_Y are the angles between the Acetabular liner and Femoral head, i.e., between the planes **XY** and **Q** in **X** and **Y** direction, respectively, they are given by

$$\cos\left(\Phi_X + \frac{\pi}{2}\right) = \hat{\imath}.\hat{q} = \frac{a.cos\omega}{\sqrt{[(a.cos\omega)^2 + (a.sin\omega - b)^2 + c^2]}}$$

$$\Phi_X = cos^{-1}\left[\frac{a.cos\omega}{\sqrt{[(a.cos\omega)^2+(a.sin\omega - b)^2+c^2]}}\right] - \frac{\pi}{2} \qquad \ldots (5.6)$$

$$\cos\left(\Phi_Y + \frac{\pi}{2}\right) = \hat{\jmath}.\hat{q} = \frac{(a.sin\omega - b)}{\sqrt{[(a.cos\omega)^2 + (a.sin\omega - b)^2 + c^2]}}$$

$$\Phi_Y = cos^{-1}\left[\frac{(a.sin\omega - b)}{\sqrt{[(a.cos\omega)^2+(a.sin\omega - b)^2+c^2]}}\right] - \frac{\pi}{2} \qquad \ldots (5.7)$$

Both $\Phi_X(\omega)$ and $\Phi_Y(\omega)$ are continuous periodic functions with a period of $T = 2\pi$ and bounded between their maximum and minimum values. Nature of the curves defined in equation (5.6) and (5.7) is depending on the ratio $\boldsymbol{a}$: $\boldsymbol{b}$: $\boldsymbol{c}$ and exactly the same curve is reproduced if the ratio is maintained. The function $\Phi_X(\omega)$ is a symmetric function about the line $\Phi_X = 0$ but, $\Phi_Y(\omega)$ is not a symmetric function about the line $\Phi_Y = 0$. As per **ISO 14242-3** prescribed motion profile, both $\Phi_X(\omega)$ and $\Phi_Y(\omega)$ should be symmetric about the ω-axis and proper selection of the parameters $\boldsymbol{a}$, $\boldsymbol{b}$ and $\boldsymbol{c}$ is vital to fulfil the requirement. Due to the geometrical constraints explained in section 5.2.2, the value of $\boldsymbol{c}$ is kept constant at 50 mm with $0 < \boldsymbol{a} < 27.5$ mm and $0 < \boldsymbol{b} < 80$ mm. In order to recognize the diverse effects of parameters $\boldsymbol{a}$ and $\boldsymbol{b}$ on the nature of the function $\Phi_Y(\omega)$, these parameters are varied in a range of $\boldsymbol{a} \in [30, 300]$ and $\boldsymbol{b} \in [5, 50]$. For the function $\Phi_Y(\omega)$, parameter $\boldsymbol{a}$ majorly decides the amplitude of the curves whereas, $\boldsymbol{b}$ decides its line of symmetry parallel to ω-axis. Three representative curves are shown in Figure 5.14(B).

Curve 1 is corresponding to $\boldsymbol{a} = 30, \boldsymbol{b} = 5$, sinusoidal in nature and symmetric about ω-axis. As the value of $\boldsymbol{a}$ is reset to 300 keeping $\boldsymbol{b} = 5$, amplitude of the corresponding curve 2 is increased without changing the nature of the curve and its line of symmetry.

When the value of $\boldsymbol{b}$ is reset to 50 keeping $\boldsymbol{a} = 30$, the curve 3 is a sinusoidal one similar to curve 1 without changing its amplitude significantly but the line of symmetry is shifted. Similarly, the parameters $\boldsymbol{a}$ and $\boldsymbol{b}$ are varied in a range of $\boldsymbol{a} \in [20, 200]$ and $\boldsymbol{b} \in [10, 100]$ for the analysis of function $\Phi_X(\omega)$. It is found that the parameter $\boldsymbol{a}$ majorly decides the amplitude of the curves $\Phi_X(\omega)$ whereas, $\boldsymbol{b}$ decides its nature. Three representative curves are shown in Figure 5.14(C). Curve 1 is corresponding to $\boldsymbol{a} = 20$, $\boldsymbol{b} = 5$, sinusoidal in nature and symmetric about Y-axis. When the value of $\boldsymbol{a}$ is reset to 200 keeping $\boldsymbol{b} = 10$, amplitude of the corresponding curve 2 is increased without changing the nature of the curve. When the value of $\boldsymbol{b}$ is reset to 100 keeping $\boldsymbol{a} = 200$, the curve 3 turned into a non-sinusoidal and asymmetric about Φ_X -axis without changing its amplitude significantly. Hence, the parameters $\boldsymbol{b} = 5$ and $\boldsymbol{c} = 50$ ensured both $\Phi_X(\omega)$ and $\Phi_Y(\omega)$ curves to be sinusoidal and symmetric about ω-axis. As per the **ISO 14242-3** recommendations, extremums of both $\Phi_X(\omega)$ and $\Phi_Y(\omega)$ should be equal to ± 23° w.r.t. the ω-axis and to achieve that parameter $\boldsymbol{a}$ is to be selected properly.

To find the maximum value of Φ_Y during a cycle rotation, it is differentiated w.r.t. **ω.**

$$f(\omega) = \Phi_Y = cos^{-1}\left[\frac{(a.sin\omega - b)}{\sqrt{[(a.cos\omega)^2+(a.sin\omega - b)^2+c^2]}}\right] - \frac{\pi}{2} \quad \text{... (5.8)}$$

$$\frac{df(\omega)}{d\omega} = -\frac{cos\,\omega[a^2.sin^2\omega - a.b.sin\omega + a^2.cos^2\omega + c^2].a}{[(a.sin\,\omega - b)^2 + a^2.cos^2\omega + c^2]^{\frac{3}{2}}.\sqrt{1-\frac{(a.sin\,\omega-b)^2}{(a.sin\,\omega-b)^2+a^2.cos^2\omega+c^2)}}} \quad \text{... (5.9)}$$

The equation $\frac{df(\omega)}{d\omega} = 0$ has roots at $\boldsymbol{\omega} = \frac{\pi}{2}$ *and* $\frac{3\pi}{2}$ and correspond to its extremums.

Similarly, the extreme values of Φ_X are obtained at $\boldsymbol{\omega} = \pi, 0$. Moreover, Φ_Y and Φ_X are out of phase by $\frac{\pi}{2}$ or $\frac{T}{4}$ and for $0 < \boldsymbol{a} < 27.5$ mm, the ranges of $0° < \Phi_X < 28.7°$ and $0° < \Phi_Y < 28.6°$ are achieved. Further calculation revealed that extreme values of ±23° for both Φ_X and Φ_Y is achieved at $\boldsymbol{a} = 21.5$ mm. It is observed that the calculated Abduction-Adduction (Φ_X) of ±23° is found to be out of phase with the Flexion-Extension (Φ_Y) of ± 23° by $\frac{\pi}{2}$ or $\frac{T}{4}$, which are the exact recommendations of **ISO 14242-3**. A 3D model of the mechanism is developed with SOLIDWORKS CAD package and these results are further validated by SOLIDWORKS motion simulation of the mechanism, which are discussed in section 5.2.3

and the simulated kinematic profiles are shown in Figure 5.14(D). An independent simulator is developed at IIT Guwahati as per the design discussed above and it is shown in Figure 5.15.

Figure 5.15. *Independent simulator developed as per the design at IIT Guwahati*

5.2.4. Basic Features of the Simulator

5.2.4.1. Feature followed as per ISO 14242-3

I. Kinematic profile

International guideline **ISO 14242-3** prescribes the testing parameters for the characterization of THA in a bi-axial Orbital bearing Machine (OBM) hip joint simulator. The kinetics of the mechanism is solved analytically with **X**-eccentricity of **a** and **Y**-

eccentricity of **b** as input variables. The results revealed that the angular motion of the femoral head w.r.t. the acetabular liner as per **ISO 14242-3** can be achieved very closely by imparting a certain combination of ***a*** and **b** to the mechanism. The simulated kinematic profiles are compared with the recommended pattern and it is shown in Figure 5.14(D).

II. Load Profile

The typical load profile as suggested by **ISO 14242-3** cannot be achieved without an independent and programmable loading system. However, the proposed loading mechanism in this simulator, in spite of being dependent on the core system for its excitation, can provide a truncated sinusoidal loading pattern with reasonable agreement in comparison to **ISO 14242-3**. The steady part of the load is generated by a calculated self-weight of transmitter (W_T). The maximum load to be applied is given by $\mathbf{W_T + W_k}$, where $\mathbf{W_k}$ is the amplitude of spring force and can be set to a desired value by proper selection of loading spring(k) and dead load (**W**). When the limiter⓲ is rigidly fixed at the equilibrium state of the loading spring⓭, 50% of loading cycle corresponding to its extension is cut-off from the core system and the acting load remains to be steady at $\mathbf{W_T}$. The working principle is depicted in Figure 5.13(I) and the simulated load cycle is compared with the recommended one by **ISO 14242-3** in Figure 5.13(II).

III. Frequency

ISO 14242-3 prescribes to operate the testing machine at a frequency of 1 ± 0.1 Hz. The desired operating frequency of the simulator can be achieved by rotating the *disc*❶ at a speed of 60 ± 6 RPM.

5.2.4.2. Bio-lubricant chamber

In vitro characterization of a prosthetic joint is required to be done under the bio-lubricant in order to reproduce the physiological state under which wear condition is experienced by a THA implanted in a human body. The *cup holder*❷ described in section **3.1.2** is designed with an integrated lubricant chamber as a provision for testing THA under different lubrication environment.

5.2.4.3. Comparison with the existing technologies

Table 5.2 summarises the existing bi-axial hip joint simulators worldwide based on the literatures [38], [146]-[149] and the major differences in their features are listed below:

I. The mechanism is mainly designed to transform a conventional *Pin-On-Disc* tribometer into a single channel OBM simulator. However, the other listed simulators are standalone type with multi-channel option.

II. None of the reported simulators is observed to follow the kinematic profile as suggested by the **ISO 14242-3** except the newly proposed one.

III. The dynamic range of applied force is prescribed to be 300N to 3000N by the **ISO 14242-3** guidelines which is not strictly followed by most of the simulators unlike the newly designed one.

IV. Design of the hip simulators listed in Table 5.2 is expected to have 3 independent prime movers in synchronization to execute bi-axial angular motion coupled with the dynamic load profile. The newly proposed device can generate a load profile similar to the suggested one by **ISO 14242-3** synchronized with the bi-axial kinematic profiles with a single DC motor as the only prime mover.

5.2.5. Additional features to be incorporated

5.2.5.1. Online Temperature measurement

Online temperature variation in the bio-lubricating environment can be monitored during experiments using a simple probe type thermocouple. The influences of articulating materials, lubrication characteristics of synovia against the temperature, and their biological consequences are the topic of interest for many researchers[186]. Such knowledge is essential for optimizing the implant materials and identifying the risk of implant loosening, which is an essential part of a joint simulator.

Table 5.2. *Summary of modern bi-axial hip joint simulators worldwide*

Simulator's name	Angular Motion	Load data	Features	ISO 14242-3 Guidelines
HUT-4 [146] Custom-Made Finland	AA: ±6° FE: ±23°	Type: Pneumatic Profile: Double Peak L_{max}: 2000N L_{min}: 400N	•12 channels •Anatomical	FE: ±23°
MARK I [38] Custom-Made UK	FE: ±25° IO: +8° to −20°	Type: Pneumatic Profile: Paul L_{max}: 2000N	•Five channels •Anatomical	Not followed
MARK II [147] Custom-Made UK	FE: +30° to −15° IO: +8° to −20°	Type: Pneumatic Profile: Square wave L_{max}: 2000N	•Five channels •Anatomical	Not followed
PA II [148] Custom-Made UK	FE: +30° to −15° IO: ±10°	Type: Not Specified Profile: Paul L_{max}: 3000N	•Six channels •Anatomical	L_{max}: 3000N
PROSIM [149] Commercial UK	FE: +30° to −15° IO: ±10°	Type: Pneumatic Profile: Paul L_{max}: 2780 N	•10 channels •Anatomical	Not followed
OBM Simulator IITG India [208]	AA: ±23° FE: ±23°	Type: Mechanical Profile: Sinusoidal L_{max}: 3000 N L_{min}: 300 N	•Single channel •Inverted •ISO 14242-3	AA: ±23° FE: ±23° L_{max}: 3000 N L_{min}: 300 N

5.2.5.2. Online Wear measurement

An LVDT or other equivalent probe may be incorporated with the designed mechanism during its operation to measure the online position of *square bar 1*❾ with time. These measurements can be regarded as the average penetration rate of femoral head inside the acetabular liner in vertical direction (Z) during its testing and may be correlated with the online wear rate of the prosthesis.

5.2.5.3. Testing parameters

The device can be used to investigate the effects of different elements like the contact surfaces, load, lubricant, articulating surfaces, relative position and speed, motions, surface roughness and temperature on the life of a THA.

5.3. Development of Synovial fluid analogue

It is broadly acknowledged that the utilization of bovine serum as a lubricant for *in vitro* testing of artificial joints is not ideal and there is a need to develop a test lubricant with mechanical properties that are more biologically relevant.

5.3.1. Materials

Low acyl Gellan Gum (Kelcogel) and high viscosity Sodium Alginates are purchased from M/s Sigma-Aldrich, USA.

5.3.2. Methodology

A synovial fluid analogue with bio-relevant rheology is developed for *in-vitro* wear testing of implants to provide a realistic simulation of the *in vivo* conditions. This study investigated rheological behaviour of Sodium alginate (2% w/v), Gellan gum (0.75% w/v) and mixtures of both at different volumetric ratio as proposed by Smith *et al.* [161] using a rheometer, Physica MCR 101(Anton Paar, Austria) equipped with 55 mm diameter parallel plate geometry maintaining a gap of 1 mm at 37°C temperature with a shear ramp in the frequency range of 0.1-100 s^{-1} and compared with that of a synovial fluid published in the literature. The volumetric ratio of Sodium alginate and Gellan gum at which their solution is found to be rheologically equivalent to the synovial fluid is identified as synovial fluid analogue (SFA) and used as a lubricant for *in vitro* testing of THA.

5.3.3. Results and discussion

Figure 5.16 shows the comparison between the viscosity of Synovial fluid and 0.75% w/v Gellan gum, 2% w/v Sodium alginate and mixture of 0.75% w/v Gellan and 2% w/v Sodium alginate in 1:2, 1:1 and 2:1 volumetric ratio. It is difficult to obtain a synthetic SFA for the entire range of frequency. However, this study requires a SFA for the operating range of 1-5 Hz during the testing of THA.

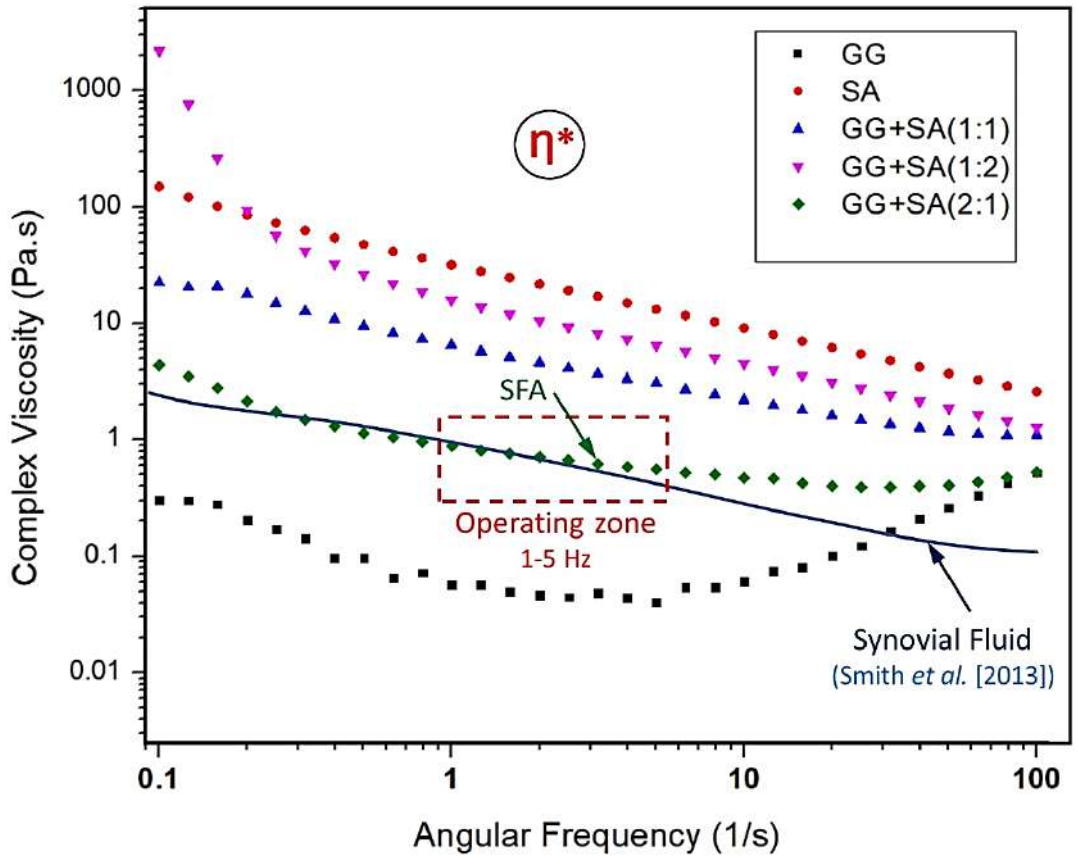

Figure 5.16. *Viscosity vs shear rate of the Synovial Fluid, represented in solid line [161], compared with 0.75% w/v Gellan gum, 2% w/v Alginate and their mix in 2:1, 1:1, and 1:2 volumetric ratio*

The 0.75% w/v Gellan gum showed significantly lower viscosity (η*) than Synovial fluid (SF) at low shear rates and higher viscosity at high shear rates. Sodium alginate (2% w/v) showed considerably higher viscosity than Synovial fluid in the entire shear rate range. These polysaccharides are mixed in different proportion in order to attain rheological behaviour of the resulting solution analogous to SF. Among all the Gellan gum/Sodium alginate mixtures, 2:1 volumetric blend is found to be the closest one to SF in terms of viscosity in the operating range of 1 to 5 Hz, indicated as SFA in Figure 5.16.

Figure 5.17(A) and Figure 5.17(B) show the storage modulus (G') and loss modulus (G"), respectively, of the SF with those of 0.75% w/v Gellan gum, 2% w/v Sodium alginate and their mixture in 1:2, 1:1 and 2:1 volumetric ratio. The SF has shown a typical mechanical spectrum of an entangled polymer solution i.e., dilute solution rheology at low frequencies G" ≥G' and an elastic response at high frequencies G'≥G". These properties enable the synovial fluid to perform a dual physiological role of a lubricant as well as a shock absorber [187]. The 0.75% w/v Gellan sample appeared to exhibit similar elastic properties as the SF at a frequency range of 6 to13 s^{-1} as evident in Figure 5.17(A). At operating frequencies of 1-5 Hz the Gellan showed weak gel behaviour that is unlike SF with G' slightly greater than G". The alginate sample on the other hand, showed a small amount of shear thinning only at higher shear rates. Hence, the Alginate/Gellan mixture is expected to demonstrate viscoelastic behaviour similar to that of SF with the alginate providing the viscous response at low frequencies and the Gellan contributing to the elastic response at high frequencies. The 2:1 Gellan gum/Sodium alginate mixture exhibited viscoelastic behaviour similar to that of SF in the operating range of 1 to 5 Hz, indicated as SFA in Figure 5.17(A) and Figure 5.17(B). Hence this fluid has the potential to execute a realistic simulation of the *in-vivo* rheology of a THR during its simulator testing.

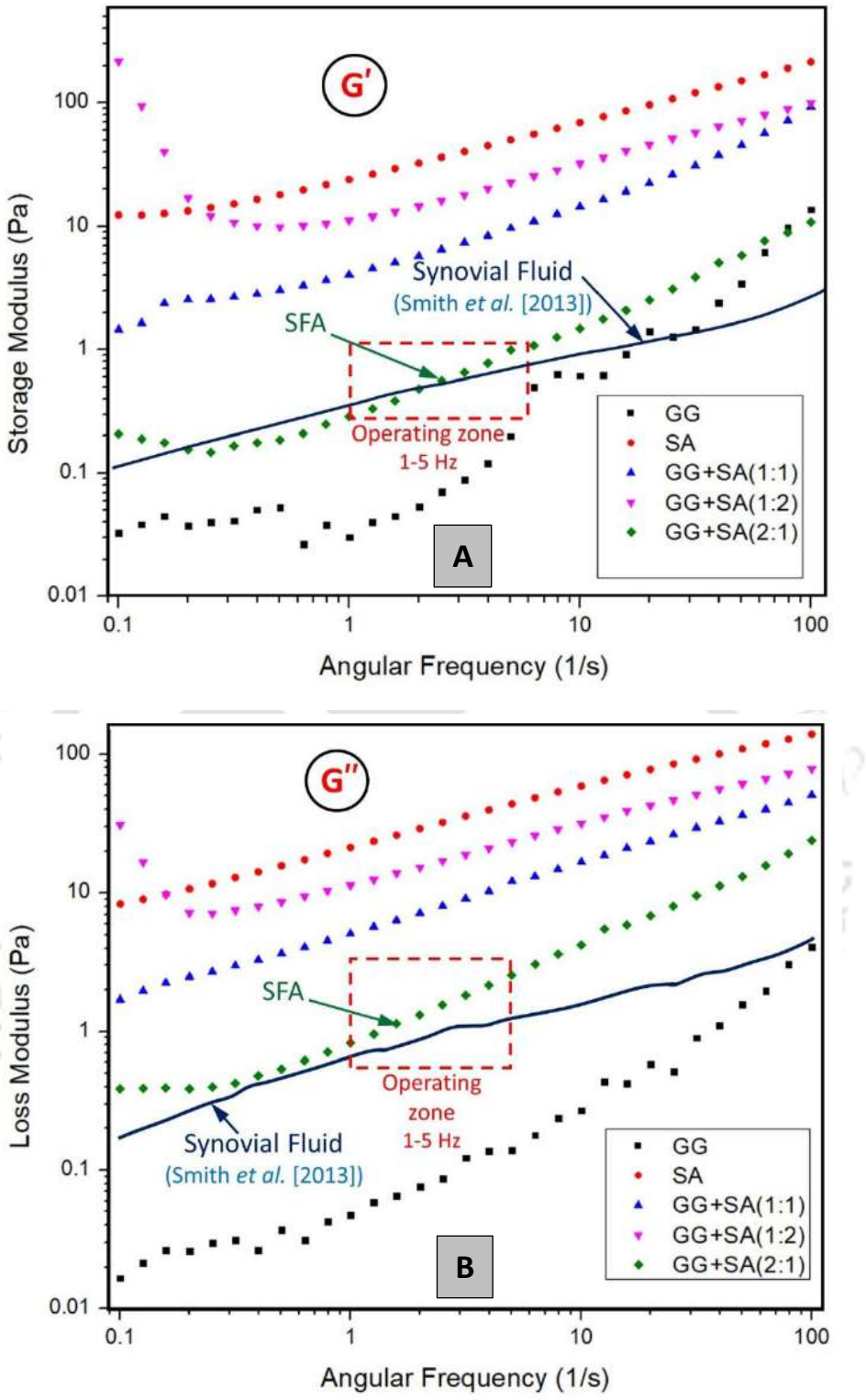

Figure 5.17. *(A) Storage Modulus vs. shear rate (B) Loss Modulus vs. shear rate of the Synovial Fluid, represented in solid line [161], compared with 0.75% w/v Gellan gum, 2% w/v Alginate and their mix in 2:1, 1:1, and 1:2 volumetric ratio*

5.4. Summary

- A modular mechanism is designed, which can be attached to a conventional *Pin-On-Disc* tribometer to modify the same into a *Ball-On-Cup* device for testing the actual total hip arthroplasties.

- The analytical solution of the simulator kinematics and its numerical validation confirmed that the device is capable of imparting flexion/extension and abduction/adduction of ± 23° to the THA under testing condition while operating at 1 Hz as per the **ISO 14242-3** recommendations.

- The device may be categorized as an orbital bearing machine (OBM) hip simulator which can approximately generate a load profile similar to the suggested one by **ISO 14242-3** in addition to the bi-axial angular motion with a single DC motor as the only prime mover.

- An independent simulator, integrated with a bio-lubricant chamber, has been designed for *in vitro* testing of THA in a simplistic way.

- The 'Ball-on-Cup' tribometer can reproduce the tribological test results similar to that of *in vivo* in a simplified manner taking into account of the influence of geometry and morphology of a THA while reflecting the lubrication regime and wear mechanism, imitating the realistic contact stresses during its usage.

- A mixture of 0.75% w/v Gellan and 2% w/v sodium alginate in 2:1 volumetric ratio is found to be rheologically similar to the synovial fluid and to be utilized as a synovial fluid analogue ((SFA) for the tribological characterization of any new material proposed to be used as the bearing surface for metal-on-polymer THA.

भारतीय प्रौद्योगिकी संस्थान गुवाहाटी
Indian Institute of Technology Guwahati

CHAPTER 6

WEAR TESTING

6.1. Introduction

Preclinical wear testing of an artificial hip joint is a complex task, which is a key factor affecting its survivorship. Wear resistance of surfaces is not being an intrinsic property of the parent material and it depends strongly on the system variables such as environment, operating condition, type of counter face etc. Wear screening device like Pin-On-Disc uses simplified specimens rather than actual prosthetic joints, hence, it is incompetent to look into their distinguishing morphological aspects. However, it is capable to evaluate the intrinsic properties of material exclusively and is used in present study for a rapid comparative study on the frictional coefficient and linear wear rate of pure UHMWPE and UHMWPE-MWCNT composite against SS 316L under different lubricating conditions. 'Ball-On-Cup' tribometer, on the other hand, is used to conduct accelerated protocols to test the newly developed acetabular liners against SS 316L femoral heads under conditions approximating those occurring in the human body under the best lubricating condition found in wear screening tests.

6.2. Apparatus and Materials

6.2.1. Wear Screening Tests

The primary wear screening tests of UHMWPE and UHMWPE-0.25MWCNT composite pins having 8 mm diameter and 15 mm length are done against a stainless steel (SS 316L) plate in a Pin-On-Disc (POD), TR-301 (Ducom, USA) rotary tribometer, attached with a lubricant chamber and a lubricant feed system. Figure 6.1(A) shows the experimental setup used for wear screening test of the developed materials.

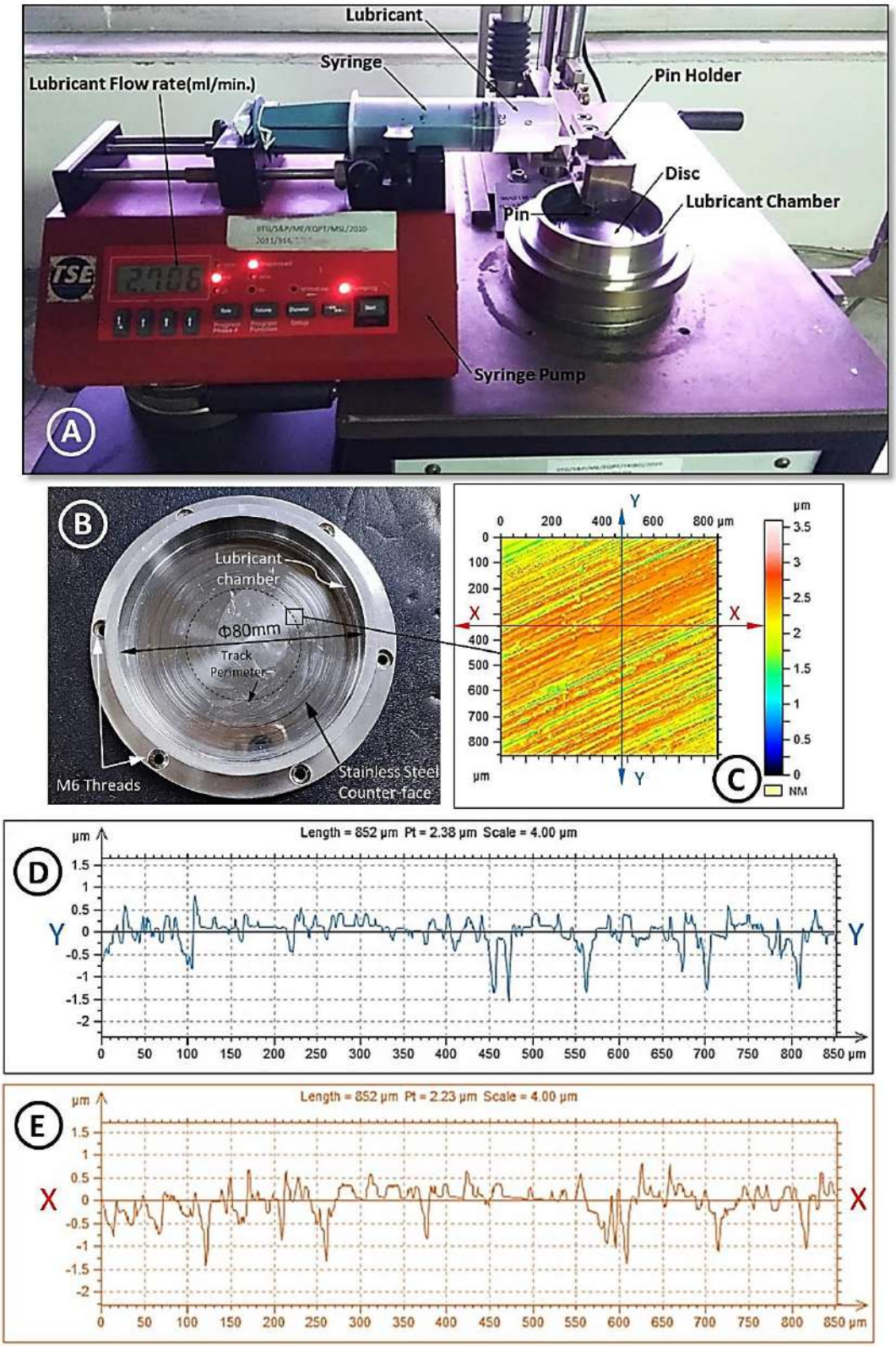

Figure 6.1. *(A) Pin-On-Disc (POD) experimental set up incorporated with lubrticant feed system for wear testing of polymer samples (B) The SS 316L Disc used for POD experiments (C) micrograph of a selected area on SS counter face located at the track perimeter (D) Linear surface roughness characteristics of the of the selected area in Y-Y direction (E) Linear surface roughness characteristics of the of the selected area in X-X direction*

The lubricant feed system integrated with a syringe is used for continuous lubricant feeding at the contact zone between the polymer pin and stainless steel (SS 316L) disc. Figure 6.1(B) shows the design of the SS disc of 80mm diameter integrated with a liquid chamber to hold sufficient lubricant during the testing. Figure 6.1(C) shows the micrograph of a selected area 800 µm × 800 µm on SS counter-face located at the track perimeter with 50 mm diameter, opted for POD experiment using a high precision non-contact type surface profilometer Talysurf CCI lite (Taylor Hobson, UK). Figure 6.1(D) and Figure 6.1(E) show the linear surface roughness along Y-Y and X-X direction, respectively, on the selected surface as indicated in Figure 6.1(D). The average surface roughness ($\mathbf{R_a}$) values along Y-Y and X-X are found to be 0.17 µm and 0.20 µm, respectively, keeping the average surface roughness ($\mathbf{R_a}$) of the SS counter-face in the range of 0.01 - 0.05 µm, which is at par with the prosthetic femoral head [188].

6.2.2. Simulator Test

The wear simulator tests are performed in the in-house developed 'Ball-On-Cup' tribometer described in Section 5.2. The ingeniously developed UHMWPE and UHMWPE-0.25MWCNT acetabular liners having the inner diameter of 22 mm as discussed in chapter 4 are tested against a SS 316L femoral head having the average surface roughness ($\mathbf{R_a}$) in the range of 0.01 - 0.05 µm [188]. The corresponding diameter of femoral head is chosen to be 21.8 mm to provide a radial clearance of 0.1 mm, sufficient for a lubricant film between the mating surfaces and avoid overheating during testing of the prosthesis.

6.3. Preparation of Specimens

6.3.1. Wear Screening Test

6.3.1.1. Polishing of samples

Cylindrical specimens of 8 mm diameter and 15 mm length are prepared with in-house developed rubber moulds by the methodology discussed earlier in Section 3.3.1.2. Contact surface of the specimens are polished using 800/P1500 silicon carbide grinding papers followed by polishing cloth till the average surface roughness ($\mathbf{R_a}$) within a range of 0.1-0.3 µm is achieved which are at par with the commercial prosthetic bearing surfaces [182]. Figure 6.2(A) shows the condition of UHMWPE pin contact surface before POD test.

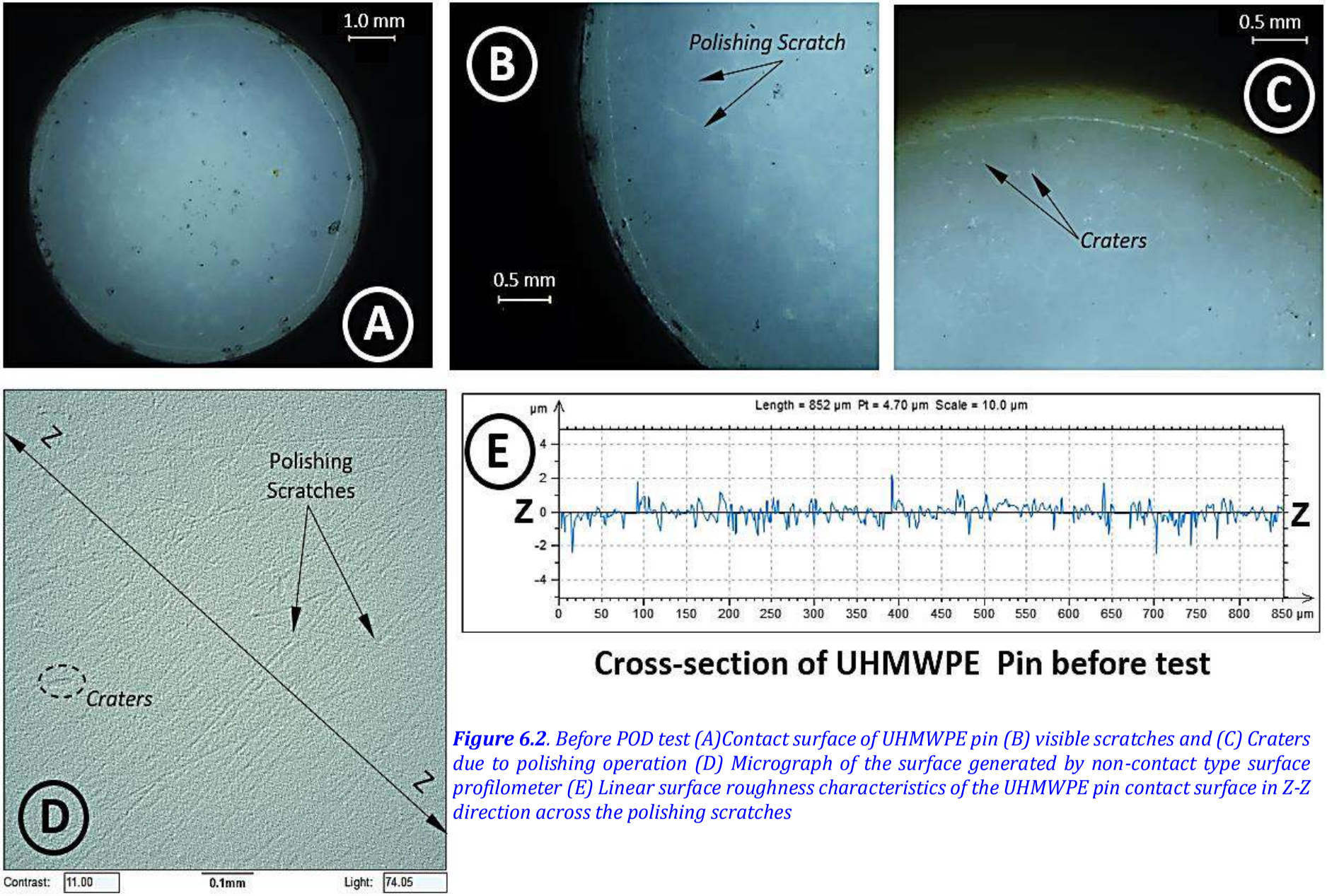

***Figure 6.2**. Before POD test (A)Contact surface of UHMWPE pin (B) visible scratches and (C) Craters due to polishing operation (D) Micrograph of the surface generated by non-contact type surface profilometer (E) Linear surface roughness characteristics of the UHMWPE pin contact surface in Z-Z direction across the polishing scratches*

The pre-test polishing resulted in some minor polishing scratches visible in Figure 6.2(B) with some minute craters as identified in Figure 6.2(C). Figure 6.2(D) shows the micrograph of a selected area of 800 µm × 800 µm at the central region of UHMWPE pin surface captured by surface profilometer indicating similar characteristics of polishing scratches and craters. Linear roughness characteristics of the selected test surface in Z-Z direction across the polishing scratches is shown in Figure 6.2(E). The average surface roughness (R_a) of the UHMWPE samples is found to be ~0.2-0.3µm before their use.

Figure 6.3(A) shows the typical condition of UHMWPE-0.25MWCNT pin contact surface before its use. Similar to UHMWPE samples, some minor polishing scratches and minute craters are visible in Figure 6.3(B) and Figure 6.3(C), respectively. Figure 6.3(D) shows the surface morphology of a selected area of 800 µm × 800 µm on UHMWPE-0.25MWCNT pin contact surface observed under surface profilometer and the corresponding linear roughness characteristics is shown in Figure 6.3(E). The **R_a** of the UHMWPE-0.25MWCNT pin surface is found to be ~ 0.1-0.2µm before testing.

6.3.1.2. Cleaning and Drying

After polishing and prior to wear testing, contaminants from the polymer specimens are removed by careful cleaning process. The sequence of cleaning and drying the specimens is described below:

I. Rinse with tap water to remove the presence of bulk contaminants, if any
II. Wash in an ultrasonic cleaner in distilled water for 15 min.
III. Rinse in a stream of distilled water
IV. Rinse in an ultrasonic cleaner in ethyl alcohol-water mixture (70:30) for 5 min.
V. Rinse in a stream of distilled water
VI. Dry with lint-free tissue
VII. Air-dry in a dust-free environment at room temperature for 30 min.

6.3.1.3. Pre-soaking in lubricant

Finally, the polymeric and composite specimens are pre-soaked in the wear test lubricant for 48 hr. to minimize fluid-sorption during the wear test and avoid a net increase in weight or volume during the initial wear intervals [189]. After pre-soaking for sufficient period of time, the specimens are cleaned for 10 min. in deionized water using an ultrasonic bath followed by rinsing in deionized water to make them all set for wear test.

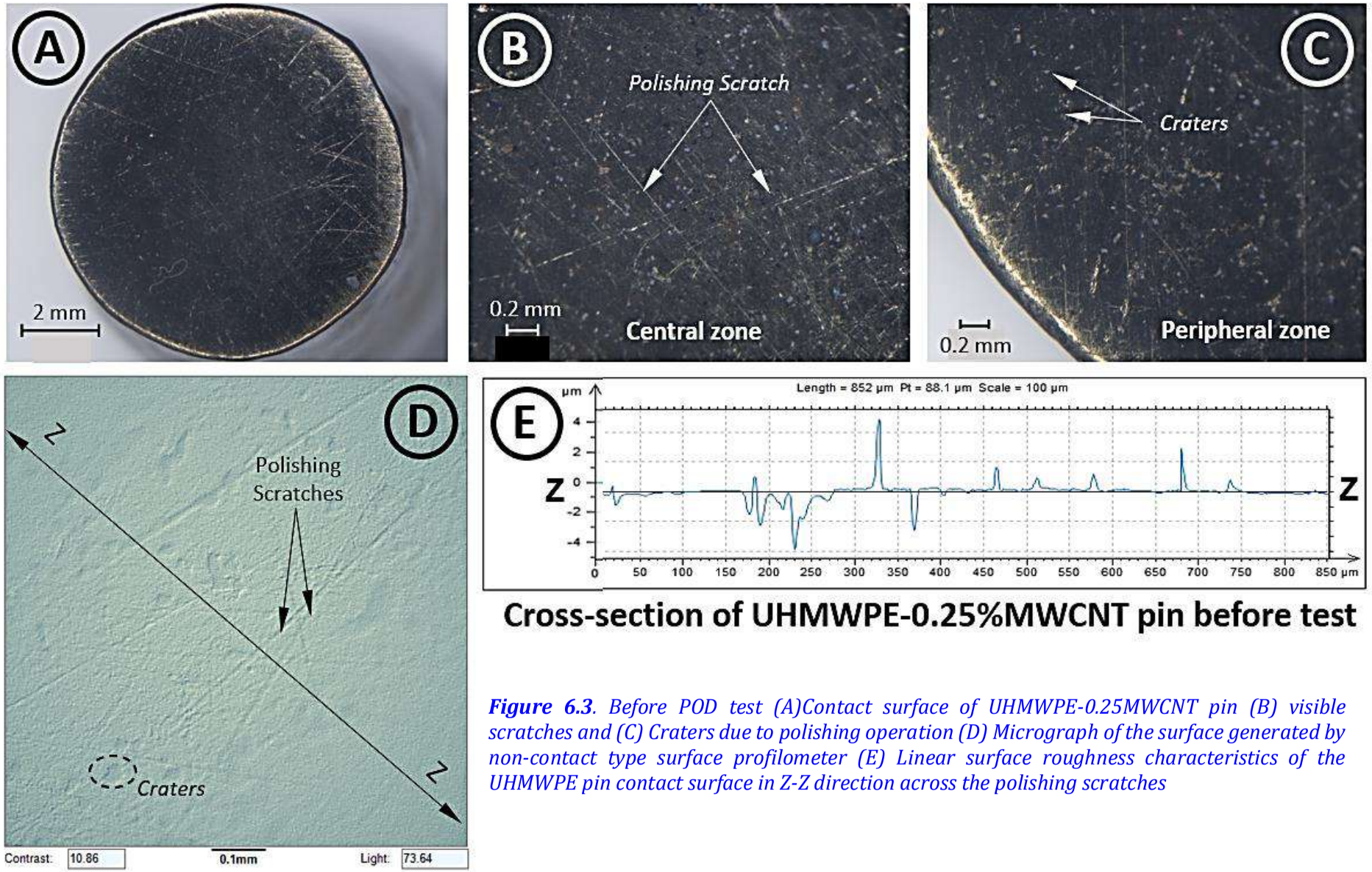

***Figure 6.3**. Before POD test (A)Contact surface of UHMWPE-0.25MWCNT pin (B) visible scratches and (C) Craters due to polishing operation (D) Micrograph of the surface generated by non-contact type surface profilometer (E) Linear surface roughness characteristics of the UHMWPE pin contact surface in Z-Z direction across the polishing scratches*

6.3.2. Simulator Test

The polymeric and composite liner specimens are soaked in the wear test lubricant for 48 hr. before each test to minimize fluid-sorption during the wear test and avoid a net increase in weight or volume during the initial wear intervals [189]. After pre-soaking, the specimens are cleaned by a typical cleaning protocol using an ultrasonic bath as described in **ISO 14242-2**[190]**,** which is reported below in sequence.

I. Vibrate for 10 min in deionized water
II. Rinse in deionized water
III. Vibrate for 10 min in deionized water
IV. Rinse in deionized water
V. Vibrate for 3 min in deionized water
VI. Rinse in deionized water
VII. Dry in a vacuum heating chamber
VIII. Soak in ethyl alcohol for 15 min.
IX. Dry in a vacuum heating chamber

6.4. Methodology

6.4.1. Wear Screening Test

After polishing, cleaning, and pre-soaking the pin specimens, they are tested against SS 316L disc under distilled water and SFA as lubrications along with dry sliding condition. POD experiments are started with a dry sliding condition and continued for an initial travel of 1.5 km, after which the lubricant is added dropwise at the contact zone between the pin specimen and the disc, and the tests are continued for another 7 km of sliding distance in wet condition. The experiments are designed to identify three regimes of lubrication, viz., a dry regime until stabilized, a transient regime from dry to lubrication and a stable lubricant regime. At the same time the experimental errors are eliminated which can arise during sample changing procedure or variation in specimen characteristics to identify difference between dry and wet run outcomes of the same specimen in exact manner. All the POD experiments are carried out at constant sliding speed of 1.2 m/s with contact pressure of 1.5 MPa for a total sliding distance of 8.5 km as recommended by **ASTM F732 - 17** [191]. Three

specimens for each combination of pin materials and lubricating conditions are tested for achieving repeatability of the results.

6.4.2. Simulator Test

The *in vitro* wear tests of the developed acetabular liners are performed as per the **ISO 14242-3** for a biaxial angular motion of Abduction (+)/Adduction (-) and Flexion (+)/Extension (-) relative to the metallic femoral head (SS316L) in the of range ±23°. The metal-on-plastic type THAs are tested at an accelerated operation frequency of 5 Hz under a double-peaked dynamic contact load described in section 5.2.3.3, under 100 ml of SFA lubricant. Each test is carried out at the room temperature, which is maintained between 25°C -30°C for 5.0 million cycles, where wear of the samples is measured at each 1.0 million cycles and the lubricant was replaced during the same period. Wear debris are collected from the lubricant chamber of the tribometer at the end of each million cycles and investigated under SEM for their morphology and size distribution. Three specimens of each type are tested for achieving repeatability in the test results. The specimens are cleaned and dried following the regime discussed in Section 6.3.1.2 before further characterizations.

6.4.3. Numerical Validation

Numerical models of THA with UHMWPE/SS-316L and UHMWPE-0.25MWCNT/SS-316L bearing combinations are designed using ANSYS software package to validate the experimental results obtained from simulator test. Figure 6.4(A) shows the geometry of the ball and socket type joint representing the THR developed using CAD package. The numerical model is incorporated with the motion and load profiles as per the **ISO 14242-3**. The femoral head is defined to execute the Abduction-Adduction motion with the load profile on the acetabular liner, performing the Flexion-Extension motion during the simulation. Material properties of UHMWPE and UHMWPE-0.25MWCNT are obtained from experimental results, reported earlier and the same for SS 316L are acquired from the data sheet. Tetrahedral mesh with element size of 0.2 mm is used to discretize the model. However, a finer mesh size of 0.1 mm is used at the contact zone for more accuracy. Figure 6.4(B) shows the discretized THR model used for simulation.

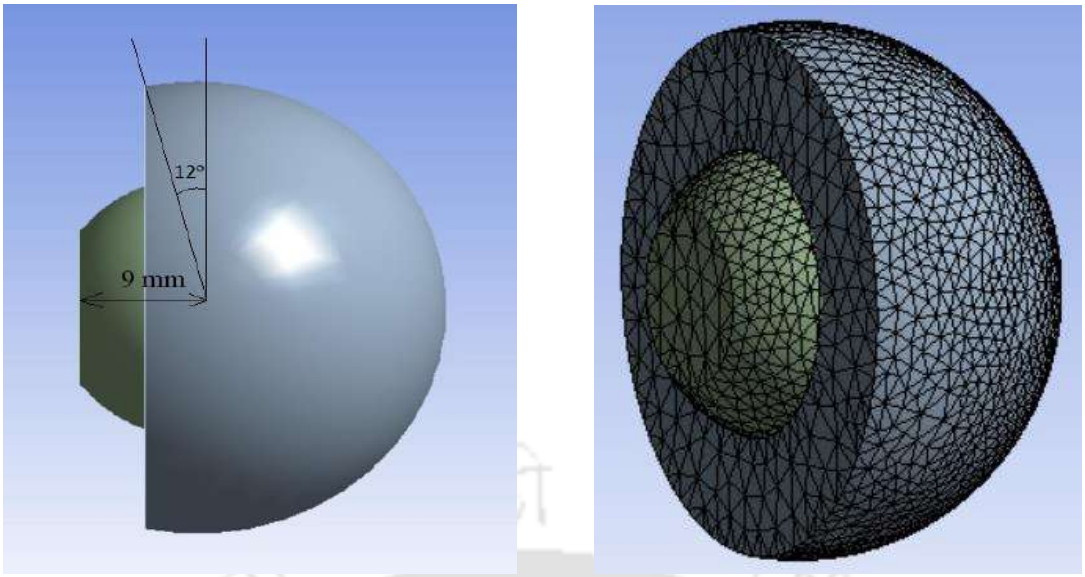

Figure 6.4. *(A) CAD model of THA for numerical simulation (B) Discretized model of THA with tetrahedral elements used for numerical simulation*

6.5. Characterization techniques

6.5.1. Wear Screening Test

A. A stereo microscope SMZ 24 (Nikon, Japan) is used to observe the surface morphology of the wear samples and identify the corresponding wear mechanism

B. Surface roughness parameters of the worn surface are measured using a high precision non-contact type surface profilometer

C. Wear debris, after being separated from the lubricant, are cleaned, dried and gold coated before observed under FESEM for assessing their morphology and confirming the type of wear mechanism. In order to eliminate the effects of lubricant on the analysis of the morphology of wear debris, a careful regime for their cleaning and drying is followed after the used lubricant containing wear debris collected from the lubricant chamber, which is described below in sequence:

I. Used lubricant containing wear debris is diluted and sonicated in water for 1 hr.
II. Sonicated solution is rested for 24 hr. for wear debris floatation.
III. Upper part of the solution is separated and diluted in water by 1 hr. of sonication
IV. Drops of resultant solution are poured into some handmade Aluminium foil crucibles
V. Aluminium crucibles are put into a hot air oven operating at 80°C overnight

VI. Dry Aluminium crucibles are left with wear debris after evaporation of the liquid

VII. Part of the Aluminium foil is cut and observed under FESEM to find the shape and size of wear debris

6.5.2. Simulator Test

A. Volume of the liners is calculated by the displacement method following Archimedes' principle with an in-house-developed setup, where Heptane 99.9% (density 0.7 g/ml) is used as the working fluid as per **ASTM D792-13** [42] at an interval of 1 million cycles after following the cleaning protocol as described in section 6.3.2.

B. Bearing surface of the acetabular liners is expected to suffer zone-wise uneven wear depth during their usage in THR due to asymmetric working load [139] as shown in Figure 6.5(A). Hence, every test samples are marked into 4 quadrants as shown in Figure 6.5(B) and visualized as shown in Figure 6.5(C). Diameter of the newly formed spherical bearing surface obtained after suffering wear loss is measured in each of the zones using a CMM, Spectra (Accurate, India) with a resolution of 0.5 µm. The difference in radius of the bearing hemisphere before and after the test is recognized as the linear wear depth suffered by the liners.

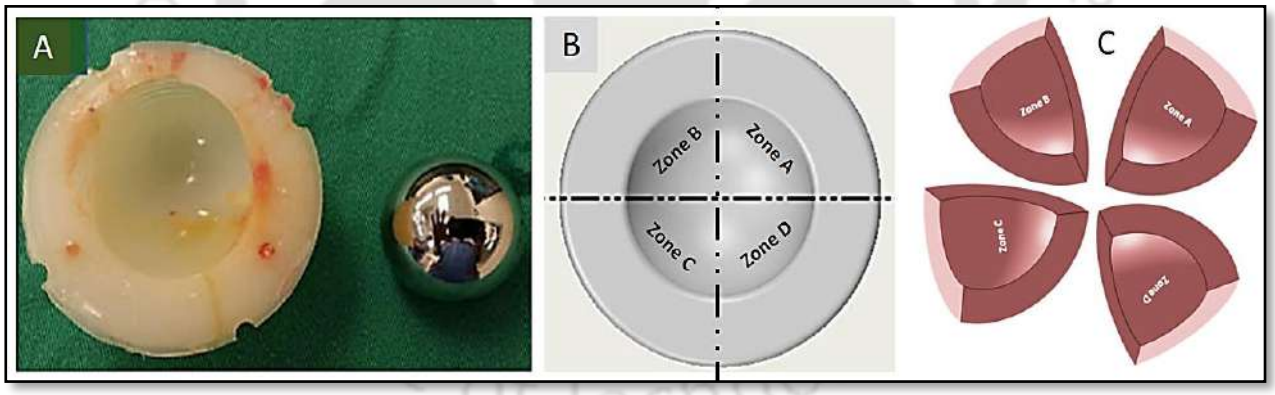

Figure 6.5. *(A) Visualization of zone-wise uneven wear depth attainment during usage of THR due to Asymmetric working load (Shahemi et al. [139]) (permission sought) (B)Acetabular liners marked into 4 quadrants and (C) Visualized Zone A, Zone B, Zone C, Zone D by solid modelling*

C. Before arriving at any conclusion and validation of simulation results, stability of the lubricant is ensured by comparing Viscosity (η), Storage modulus (G') and Loss modulus (G") characteristics of unused lubricant against frequency in the range of 0.1

to 100 Hz with those of used one, taken out of the simulator chamber after each million cycles of testing.

D. In order to eliminate the effects of SFA on the analysis of the morphology of wear debris, it is necessary to separate the wear debris from the used lubricant and collect it. The separation method of the UHMWPE and UHMWPE-0.25MWCNT wear debris from the used lubricant fluid is described in the Section 6.2.3.

E. Wear debris, after being separated from the used lubricant, are gold coated and observed under FESEM for assessing their morphology, size distribution and wear mechanism.

6.6. Results and Discussion

6.6.1. Wear Screening Test

The result and discussion section of wear screening test gives a detailed technical insight of the following:

- Linear wear rate and coefficient of friction of UHMWPE and UHMWPE-0.25MWCNT pin samples sliding against SS-316L disc in dry, water and SFA lubricating conditions
- Wear mechanism encountered by the polymeric pin surface against SS-316L counter face under different lubricating conditions

6.6.1.1. Coefficient of Friction and linear wear

Figure 6.6(A) shows the coefficient of friction (COF) of UHMWPE and UHMWPE-0.25 MWCNT pins during their dry sliding test against SS-316L disc. The coefficient of static friction (μ_s) is achieved for UHMWPE/SS combination after the completion of 0.25 km sliding distance and a stable value of kinetic friction is observed after a sliding distance of 4 km. The said transition is achieved at 0.05 km of sliding distance in case of UHMWPE-0.25MWCNT/SS combination, where kinetic friction is observed to be stable at a similar sliding distance of ~4 km.

Pin-on-disc experiment in dry condition revealed that the kinetic coefficient of friction (μ_k) of UHMWPE and UHMWPE-0.25MWCNT against Stainless steel is observed to be ~0.6 and ~0.4, respectively, where a 33% reduction of COF is observed for the composite sample compared to that of virgin polymer. It is mainly due to the self-lubricating characteristics of the filler present in the polymer matrix.

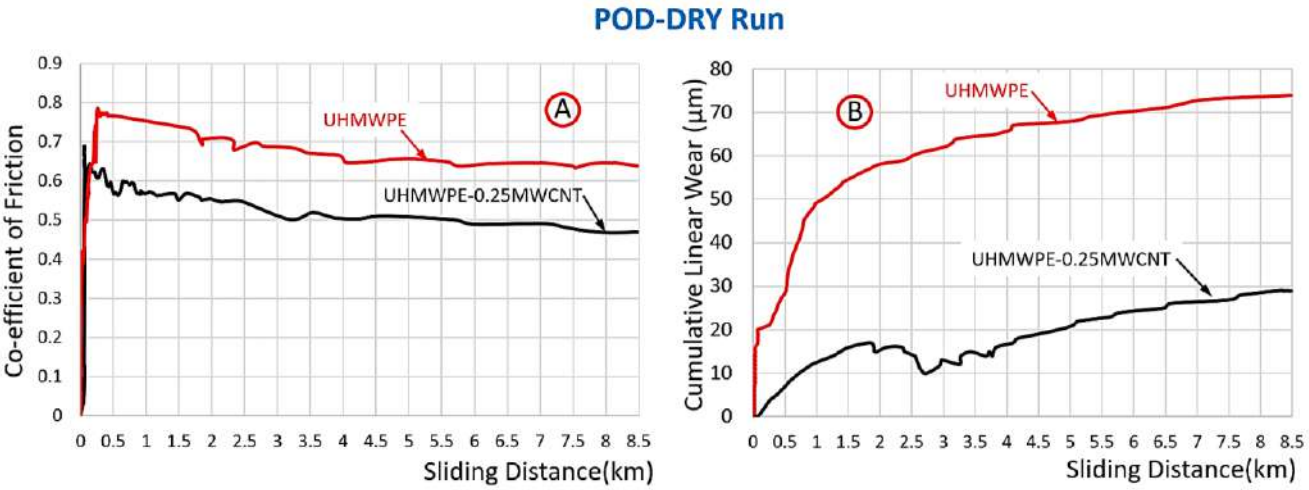

Figure 6.6. *Results obtained from Pin-On-Disc Dry test of UHMWPE and UHMWPE-0.25MWCNT pins against SS disc (A) Coefficient of friction vs sliding distance(km) (B) Cumulative linear wear(µm) vs sliding distance(km)*

Figure 6.6(B) depicts the cumulative linear wear of the polymer and composite samples against sliding distance in dry condition. Both the UHMWPE and UHMWPE-0.25MWCNT samples are observed to undergo significant a high linear wear rate (LWR) till an initial travel distance of 1.0 km followed by a stable wear rate thereafter. The average LWR of UHMWPE specimen during its dry sliding condition is found to be 3.3 µm/km, which is reduced to 2.6 µm/km, i.e., ~21% reduction in case of UHMWPE-0.25MWCNT composite. But the wear rate of UHMWPE specimen during its initial sliding of 1.0 km is found to be 50 µm/km, which is ~300% higher compared to that of composite sample having the initial wear rate of ~12 µm/km. The kinetic friction is at an early stage in case of UHMWPE-0.25MWCNT specimen compared to the pure UHMWPE specimen, which clearly indicates the lower coefficient of friction of the composite against SS counter face, assisting it to attain the operating speed of 1.2 m/s much earlier compared to the virgin polymer. The reduction in coefficient of friction of the composite specimen might be attributed by the presence of MWCNT, which has self-lubricating characteristics [192], [193].

As a consequence, the composite pin applied a tangential force ($F_t = F_N/\mu$, where F_N is set fixed) much less compared to that of UHMWPE on the SS disc during their mutual sliding and the operating speed of 1.2 m/s is achieve at ~80% less sliding distance.

The combined effect of increased hardness by 58%, increased toughness by 20% and reduced COF by 33% is expected to reduce the overall wear rate of the polymer composite significantly by ~60% during its dry sliding against SS compared to UHMWPE/SS combination. This result is supported by the steady state wear equation [194], which is given as

$$V = K \frac{PL}{3H} \quad \text{... (6.1)}$$

$$K \propto \mu_k \quad \text{... (6.2)}$$

Where, H is the hardness of the softer material, P is the normal load applied during experiment, L is the sliding distance, and V is the volumetric loss. K is the dimensionless standard wear coefficient which is proportional to COF (μ_k) of the bearing combination.

Figure 6.7(A) shows the COF of UHMWPE/SS and UHMWPE-0.25MWCNT/SS bearing combinations during POD test using distilled water and SFA as the lubricants with a noticeable transition from dry regime to lubricant regime at ~1.25 km sliding distance. The COF between Stainless steel and the polymers is found to drop drastically compared to that of the dry regime after the introduction of both water and SFA as lubricants and a stable value of COF (μ_k) is obtained after ~2.0 km sliding distance as depicted in Figure 6.7(A). The COF (μ_k) between UHMWPE and SS in distilled water is found to be 0.1, and it is further reduced to 0.05 by using SFA as the lubricant, which are 83% and 91% less compared to dry sliding of the same bearing combination, respectively. In case of UHMWPE-0.25MWCNT/SS bearing combination, the COF (μ_k) is found to be 0.05 and 0.03 under the distilled water and SFA lubrication, respectively, with 87% and 92% reduction compared to its dry sliding. Hence, the COF between UHMWPE and SS under water and SFA lubrication is found to be reduced by 50% and 40%, respectively, when the polymer is reinforced with 0.25 wt.% MWCNT.

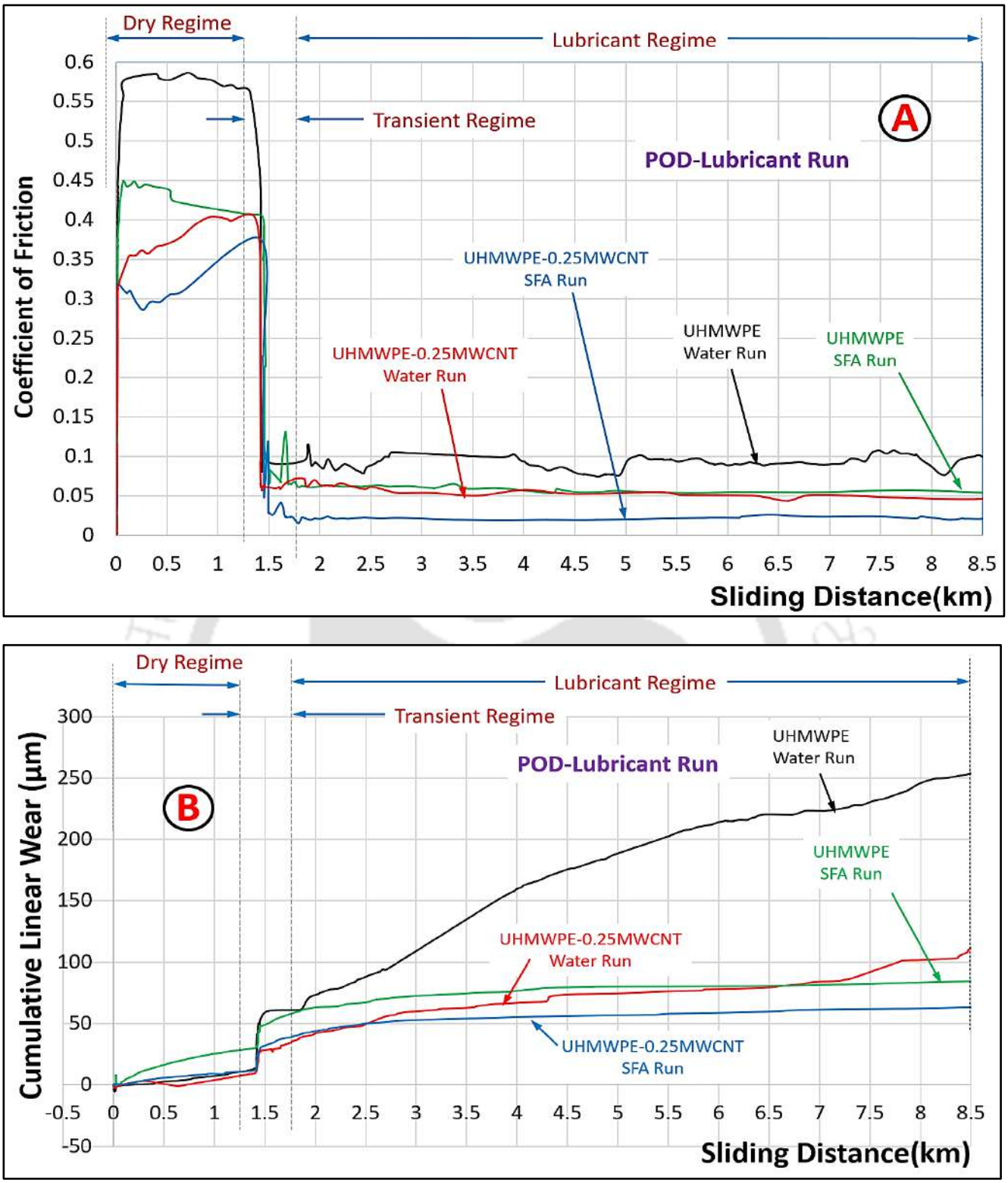

Figure 6.7. *Results obtained from POD test of UHMWPE and UHMWPE-0.25MWCNT pins against SS disc under distilled water and SFA lubrication (A) Coefficient of friction vs sliding distance(km) (D) Cumulative linear(µm) wear vs sliding distance(km)*

It can be inferred that UHMWPE-0.25MWCNT/SS under SFA lubrication is the best bearing combination among all tests carried out in this study when least frictional hindrance is desired with 95% reduction in COF in comparison to UHMWPE/SS in dry sliding, and the summary of the results is reported in Table 6.1.

Figure 6.7(B) depicts the cumulative linear wear of the UHMWPE/SS and UHMWPE-0.25MWCNT/SS bearing combinations during POD test with distilled water and SFA lubrication with an observable transition from dry regime to lubricant regime between the sliding distance of 1.25 – 1.75 km. The dry regime is designed for initial travel of 1.5 km to provide sufficient time to achieve a stable wear rate of the specimen. During the transient regime, all the polymer samples are observed to undergo a sudden jump in their cumulative linear wear under both the lubricants. After going through the transient regime, both UHMWPE and UHMWPE-0.25MWCNT specimens are found to continue with an unstable wear rate having the average rates of 25µm/km and 8 µm/km, respectively, under distilled water lubrication, which are 4-8 times higher compared to that of obtained values in dry runs as shown in Figure 6.7(B). This is possibly due to water absorption by the UHMWPE and UHMWPE-0.25MWCNT specimens during test resulting in the swelling of the samples thus decreasing their shear strength. As a result, an unsteady and high wear rate is observed for both the specimen against the hard SS counter face with water lubrication [195]. However, the linear wear rate of the polymer and composite samples is found to be very stable under SFA lubrication with their respective linear wear rate of 5 µm/km and 2.5 µm/km. These wear rates are comparable to their corresponding dry runs.

The sudden jump in linear wear of all the samples during transition of the test condition from dry to lubricated regime, as observed in Figure 6.7(B), might be due to the flushing effect of the lubricants. High COF and the corresponding frictional drag during dry sliding of the samples against SS counter face generated a considerable amount of heat, subsequently results in a significant temperature rise at the contact zone, sufficient enough to promote adhesive wear of the samples.

The wear debris generated are diffused back to the parent material due to the heat and pressure at contact zone. However, these wear particles, loosely bound to parent body, are flushed out with the lubricant after the introduction of lubricants in the test causing the abrupt peak in wear rate of the specimens during transient regime. Here, it may be inferred that the actual material removal rate in dry runs, in absence of a flushing agent, is not

reflected in the wear measurement leading to a visibly slow wear rate. During the usage of lubricants the scope of heat generation in the contact zone is very limited and the continuous flow of lubricant flushes out the wear debris immediately after their generation, leading to a realistic wear measurement during the experiments.

It can be inferred that in the presence of distilled water both UHMWPE and UHMWPE-0.25MWCNT performed the worst in terms of wear resistance among all the combinations tested in this study even though it reduced the COF(μ) by 83% and 87%, respectively, against SS compared to their dry runs. If one revolution of the disc is considered as one cycle of test, the sliding distance per cycle is calculated to be 157 mm considering the track diameter of 50mm. Hence, the linear wear rate of UHMWPE and UHMWPE-0.25MWCNT under water lubrication is converted into ~186 mg/million cycle and ~60 mg/million cycle, respectively, (refer Annexure 1 for detailed calculation) considering the density of the polymer to be 0.941 g/cc, which are 2-5 times more than that of reported values in simulator tests [196] and that reported from well-functioning THA retrieved at autopsy [197]. However, SFA has emerged out to be the best lubricant for wear performance of UHMWPE and its composite against SS with least frictional hindrance and the rate of material loss is in the same order of the simulator tests (~35 mg/million cycle) [161], [195] as well as implanted UHMWPE liner (~30 mm^3/year) considering 1 million cycle to be equivalent to 1 year of usage [197]. Hence, it may be inferred that the SFA is capable of reproducing a realistic tribological environment during POD test for UHMWPE and its composites to generate a wear rate comparable to that of achieved in a hip joint simulator test with bovine serum or observed *in vivo* in presence of the synovial fluid.

6.6.1.2. Wear Mechanism

A. Dry POD Test

Figure 6.8 shows the topological characteristics of UHMWPE and UHMWPE-0.25MWCNT specimen test surface after executing POD test in dry sliding mode evaluated by stereo microscope. Figure 6.8(A1) shows UHMWPE pin surface exhibiting some polymer layer separation along with scratches parallel to sliding direction. Figure 6.8(A2) is the micrograph of the pin surface where plastic flow is evident with some parallel scratches. The average surface roughness (R_a) along orthogonal direction to sliding is found to be 0.5-0.7 μm using a non-contact type profilometer.

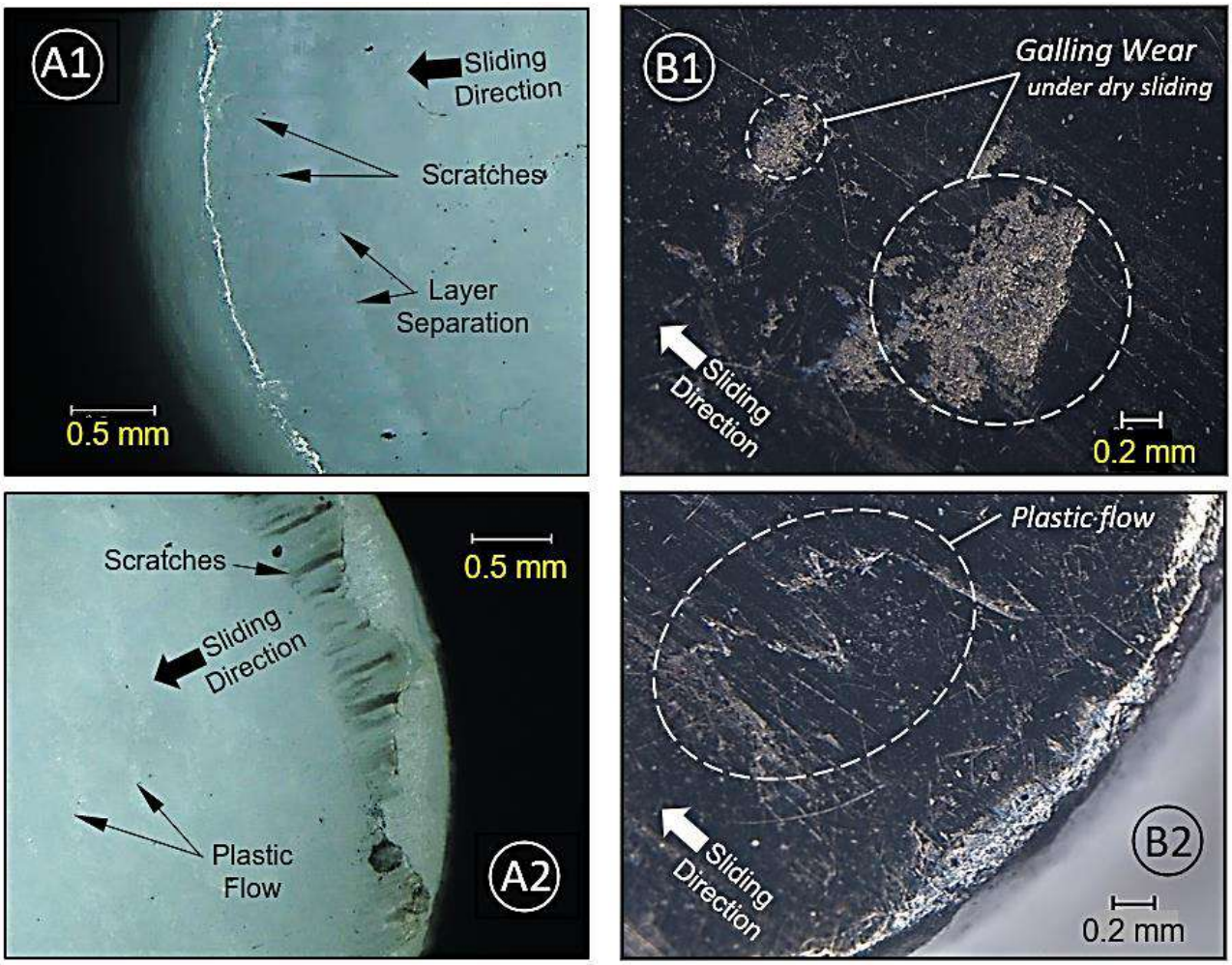

Figure 6.8. *Micrographs after Dry sliding POD test (A1) Layer separation on UHMWPE surface (A2) Plastic flow and scratches on UHMWPE surface (B2) Galling wear on composite surface (B3) Plastic flow on composite surface*

High friction coefficient between UHMWPE and SS as evident in Figure 6.6(A) due to lack of lubricant generated high frictional hindrance at the contact region resulting in overheating of the dry sliding zone. As a result, micro-adhesion and plastic flow of UHMWPE specimen are found to be the dominant wear mechanism during its sliding against SS along with minor abrasion and fatigue.

Figure 6.8(B1) shows the stereo microscopic image of UHMWPE-0.25MWCNT pin surface where wear patches are evident along with some scratches parallel to sliding. These wear patches are the result of adhesion, specifically known as galling wear mechanism which is caused by microscopic transfer of material during sliding [198], [199]. Figure 6.8 (B2) is the micrograph that identifies plastic flow on the composite surface. So, the composite specimen exhibited similar wear mechanism to that observed for pure polymer during its dry sliding against SS. However, the wear patches due to galling are observed due to higher brittleness of the composite compared to pure polymer. The average surface roughness (R_a) along Z-Z is ~ 0.8-0.9 μm with some accumulation of peaks and valleys due to plastic flow and micro-ploughing, respectively. However, some of the region on the test surface is found to be very smooth unlike the surface profile of UHMWPE specimen obtained after dry POD test due to higher Vickers hardness of the composite after dry polishing against the SS disc.

Figures 6.9(A1) and (A2) show the SEM micrographs of two typical wear debris of average diameter (Φ_{avg}) ~ 30 μm obtained after dry sliding POD test on UHMWPE pins against SS disc. These kind of lacerated wear debris come from the cracked surface because of the fatigue stress and the separation from wear surface at the weak points by adhesive force. Sharp ripples are observed on the surface of the wear debris as shown in Figure 6.9(A1) which are the indication of plastic flow of the polymeric material due to fatigue stress generated during testing. Figure 6.9(A2), on the other hand, shows another lacerated wear debris with faint ripples indicating coalescence phenomena on its surface after being detached from the parent body due to the generation of heat and pressure during experiment.

Hence, both the test surface and wear debris morphology suggest plastic flow of UHMWPE to be the major wear phenomena during its dry POD test resulting in layer separation in addition to minor signs of abrasion. The large size and lacerated shapes of the debris suggest deep cuts on the pin surface during sliding against a hard surface in dry condition.

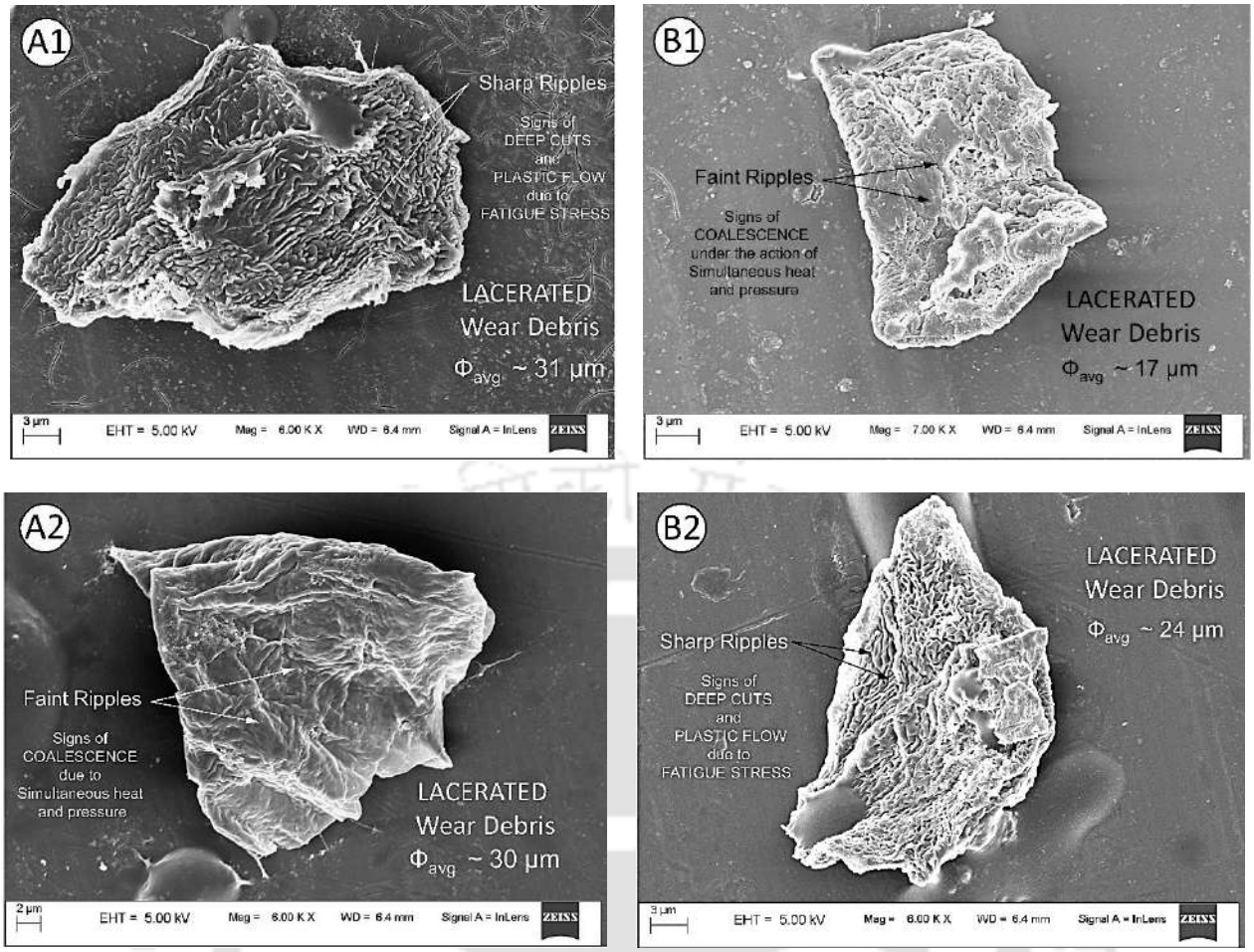

Figure 6.9. *SEM images of Lacerated wear debris obtained from dry POD test of polymer pins UHMWPE debris with (A1) sharp ripples on its surface (A2) faint ripples on its surface UHMWPE-0.25MWCNT debris with (B1) faint ripples on its surface (B2) sharp ripples on its surface*

Figures 6.9(B1) and (B2) show the SEM micrographs of two representative wear debris generated during POD test on UHMWPE-0.25 MWCNT pins against SS disc in dry condition in lacerated shape with an average diameter of 17 µm and 24 µm, respectively. These debris are typically similar to those obtained from dry POD test of UHMWPE against SS disc as shown in Figures 6.9(A1) and (A2) with similar morphological features explained earlier. Sharp ripples as well as coalescence zones are evident on the surface of UHMWPE-0.25MWCNT wear debris confirming the same kind of wear mechanism in both composite and pure polymer. In addition, there is a reduction in average diameter of the composite wear debris by 40% compared to those obtained from pure polymer due to brittleness of the composite.

B. POD test under water lubrication

Figure 6.10 shows the surface characteristics of UHMWPE and UHMWPE-0.25MWCNT specimen test surface evaluated by stereo microscope after performing POD test under water lubrication. Figure 6.10(A) shows the stereo micrograph of the UHMWPE test surface where micro-cutting is evident throughout the surface in the form of parallel scratches, which is the indication of abrasive wear. The average surface roughness (R_a) is found to be 1.0-1.5 µm. and some sudden crests are observed on the surface.

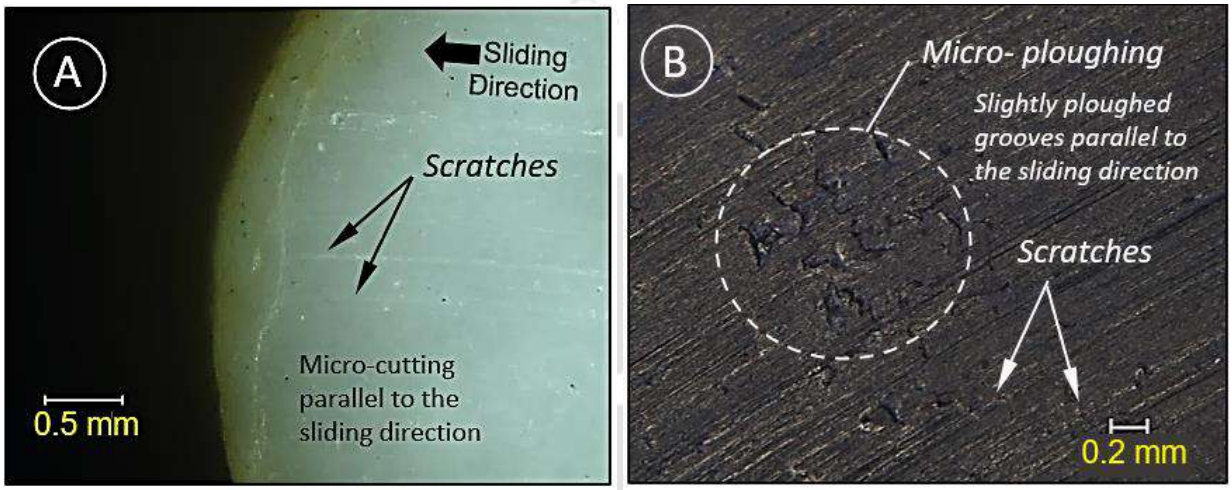

Figure 6.10. *Microscopic images After POD test with water lubrication (A) Contact surface of UHMWPE showing abrasive scratches parallel to sliding direction at centre (B) Contact surface of UHMWPE-0.25MWCNT showing ploughed grooves and scratches parallel to sliding direction*

Figure 6.10(B) shows the SEM images of UHMWPE-0.25MWCNT sample surface after slid against SS disc under water lubrication identifying ploughed grooves of ~0.1-0.3 mm with prominent parallel scratches throughout the whole area. These scratches are the outcome of abrasive wear of the composite similar to that of pure polymer.

However, the composite specimen exhibited an additional feature of micro-ploughing as a consequence of its increased brittleness due to presence of the MWCNT as the reinforcement. The profile of resultant test surface is identified to be wavy in nature, unlike the surface profile of UHMWPE specimen obtained after water test, with an average surface roughness (R_a) of ~ 0.5-0.6 µm.

Figures 6.11(A1) and (A2) show the SEM images of two sites containing typical strip-shaped wear debris obtained after POD test on UHMWPE pins against SS disc under water lubrication. These debris are typically of 500 μm length in average and it is formed after the harder abrasive material continuously scrapes on the soft basal body in the presence of a low viscous fluid. Hence, both the test surface and wear debris morphology confirmed to have micro-cutting on UHMWPE which confirmed that abrasion is one of the major wear mechanisms during its POD test under water lubrication. However, these kind of wear mechanism and wear debris are rarely observed in the artificial joints in human body [9], [200].

Figures 6.11(B1) and (B2) show the SEM micrographs of strip wear debris generated during POD test on UHMWPE-0.25 MWCNT pins against SS disc under water lubrication with average length of 200 μm and 300 μm, respectively. These debris are very similar to those obtained from water test of UHMWPE as shown in Figures 6.11(A1) and (A2) with approximately 50% reduction in length confirming the wear mechanism noticed in the composite to be identical with that of pure polymer. The reduced 'elongation at break' value of the composite debris compared to pure polymer is mainly due to its increased brittleness as a result of filler incorporation as explained in Section 3.4.3.3, which justified the reduction of wear debris length. It is already reported that in presence of water UHMWPE and its composite get feeble in terms of their shear strength.

As a result, abrasive wear is predominantly observed for both polymer and its composite when slid against a harder SS counter face in presence of water lubricant and the corresponding wear debris generated is consolidated in the form of strips or ribbons as shown in Figure 6.11.

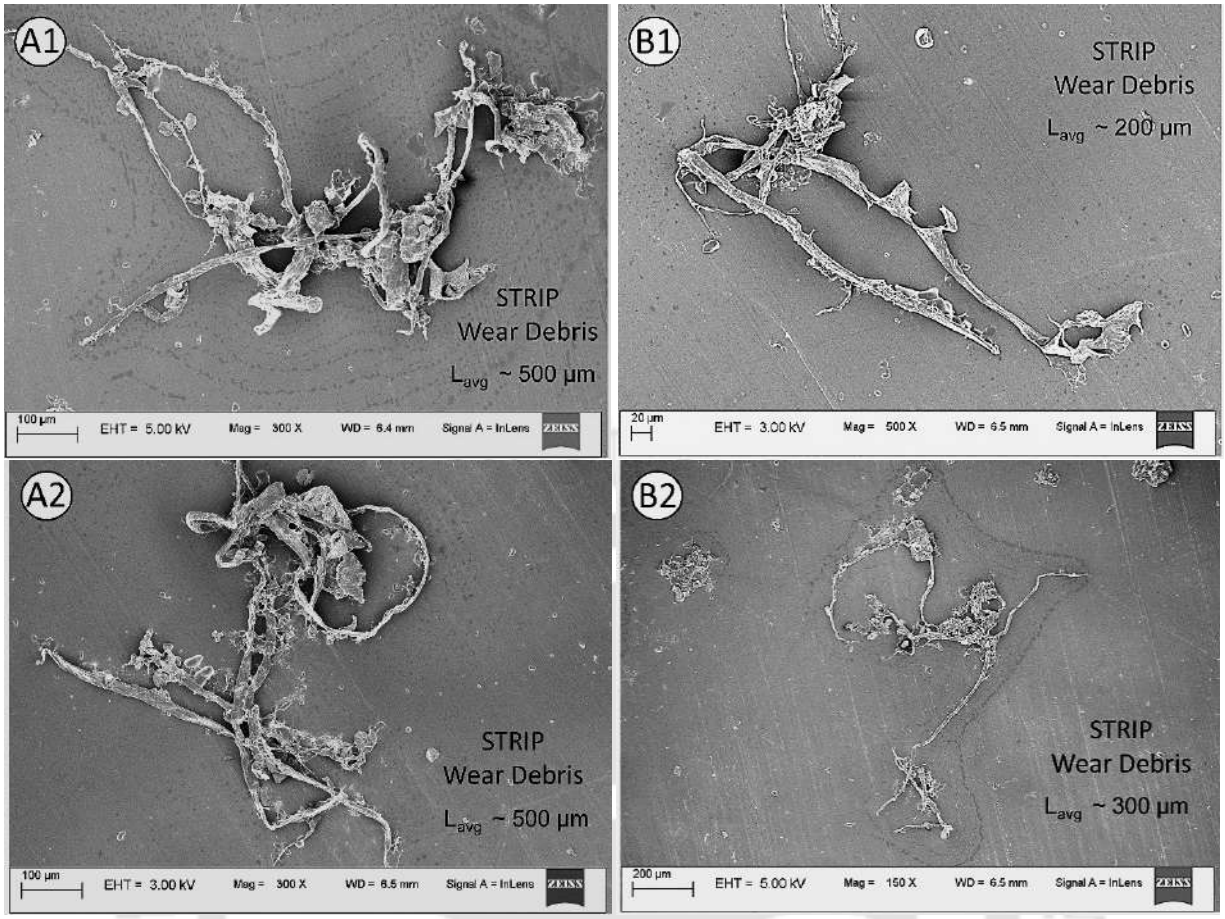

Figure 6.11. *SEM images of Strip-shaped wear debris obtained from Pin-On-Disc in water lubrication UHMWPE wear debris with average length of 500 µm (A1) site 1 (A2) site 2 and UHMWPE-0.25MWCNT wear debris (B1) with average length of 200 µm and (B) with average length of 300 µm*

C. POD test under SFA lubrication

Figure 6.12 shows the stereo microscopic topography of pure polymer and composite specimen surface after executing POD test under SFA lubrication. Figure 6.12(A1) identifies abrasive wear with parallel scratches on UHMWPE test surface. Figure 6.12(A2) is the micrograph of polymer surface indicating plastic flow of the material parallel to the sliding direction as the predominant wear mechanism as the highly viscous SFA lubricant adheres to the surfaces of friction pair keeping the friction coefficient to the lowest. The average roughness (R_a) of the surface is observed to be ~ 5.0-6.0 µm, where some sharp crests and troughs are observed due to the plastic flow on the polymer surface. However, most of the profile is found to be smooth without any undulations.

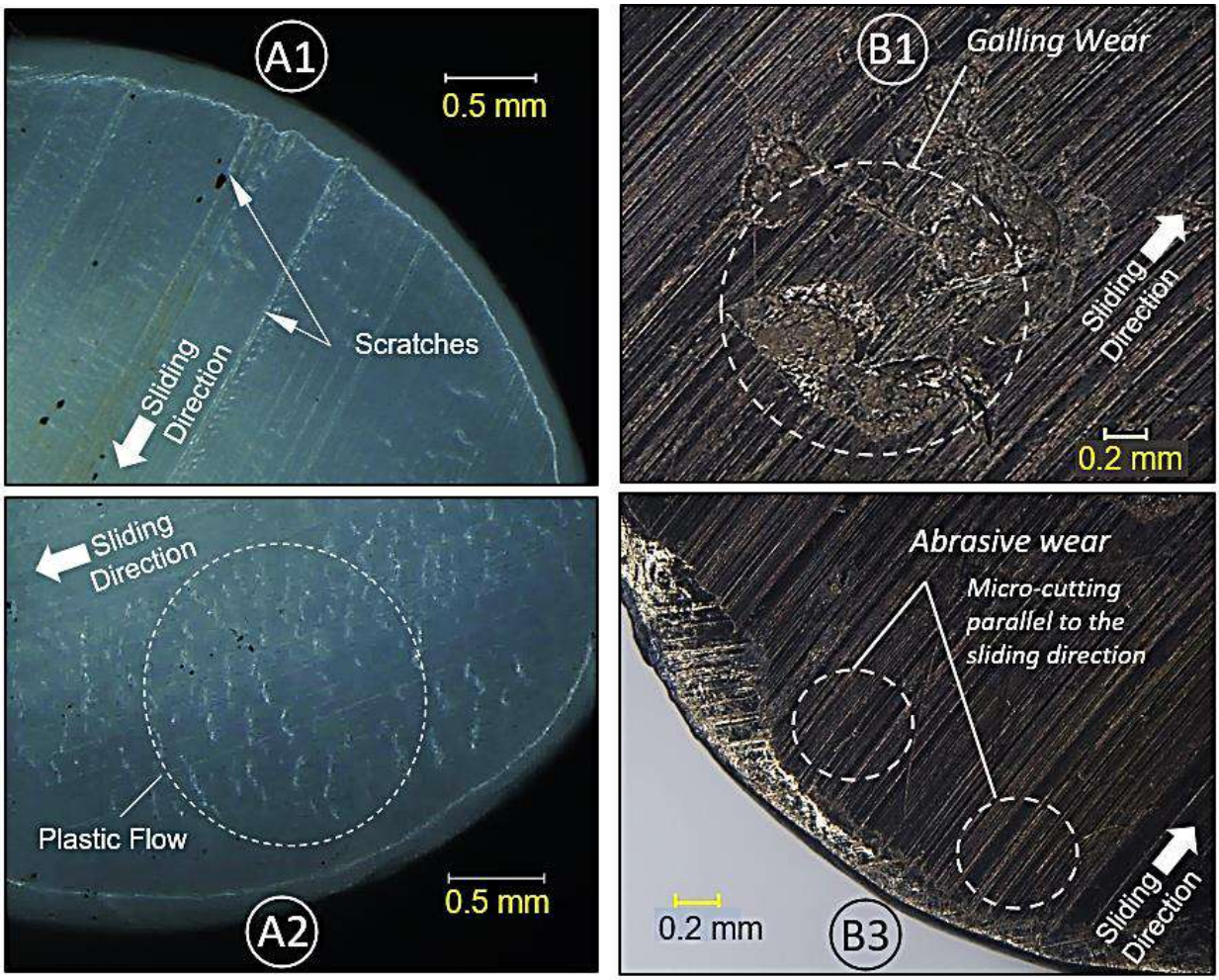

Figure 6.12. *Microscopic images of pin surface after POD test under SFA lubrication (A1) Contact surface of UHMWPE Micro-cutting parallel to sliding (A2) Plastic flow UHMWPE surface (B1) Contact surface of UHMWPE-0.25MWCNT pin showing Galling wear (B2) Micro-cutting parallel to sliding direction on UHMWPE-0.25MWCNT surface*

Figure 6.12(B1) shows the microscopic image of composite pin contact surface identifying some wear patches as a result of galling wear mechanism as a consequence of adhesion. Figure 6.12(B2) is the micrograph of composite surface showing abrasive scratches parallel to sliding as the major wear mechanism along with some polished patches on it. The profilometer recorded the average surface roughness (R_a) of ~ 0.8-0.9 µm featuring some sudden troughs followed by flats as marked due to the galling and polishing on the composite surface. However, the plastic flow characteristics seen in case of UHMWPE sample after POD test under SFA lubrication are absent in case of the composite due to its increased toughness and yield strength compared to pure polymer at the cost of galling wear due to its brittleness.

Figure 6.13(A1) shows the SEM image of wear debris of different shapes and sizes which are generated during POD test on UHMWPE pins against SS disc in presence of SFA. Figures 6.13(A2) and (A3) show the SEM micrographs of two representative wear debris from the collection in prismatic flake shape with an average diameter of 15 μm and 24 μm, respectively. These debris are typically comprised of sharp edges and smooth surfaces, and they are formed from UHMWPE samples with SFA as a result of composite motion of friction pairs, and are most irregular in all UHMWPE wear debris [201]-[203]. Profile of the test surface suggests plastic flow of UHMWPE to be the most dominant wear phenomena over abrasion. The flake like wear particles is a direct result of adhesive wear [203].

Figure 6.13(B1) shows a collection of wear debris of different shapes and sizes as observed under SEM which are generated during POD test on UHMWPE-0.25MWCNT pins against SS disc under SFA lubrication. Figures 6.13(B2) and (B3) show the SEM micrographs of two representative wear debris from the collection in block shape and flake shape with an average diameter of 4 μm and 5 μm, respectively. These debris typically have of sharp edges and smooth surfaces, and they are generated from UHMWPE samples during their wear test under the lubrication of SFA. Profile of the test surface suggests abrasion of the composite to be the dominant wear phenomena in addition to some galling wear. However, the scratches or texture observed on the surface of wear debris in Figures 6.13(B1) and (B2) suggest the occurrence of adhesive wear during the test.

Figure 6.13(C) shows a typical morphology of UHMWPE wear debris found in small amount from the implanted artificial hip joint as observed under SEM by Hongtao *et al.* [9] having a significant resemblance with those produced from both UHMWPE and UHMWPE-0.25MWCNT specimens under SFA lubrication. The outcomes of POD tests are briefly summarized in Table 6.1.

Based on the experimental results, it is reported that the morphology and size of UHMWPE wear debris produced by the POD tribometer are found to be influenced by the type of the lubricant used in the test as well as brittleness of the test material. Overall observations revealed that both UHMWPE and UHMWPE-0.25MWCNT underwent similar wear behaviour when testing conditions are remained unchanged. It is supported by the morphological resemblance of the wear debris produced under the same test lubricant. While testing under water lubricant, it produced strip-like wear particle, some of which are several millimetres in length.

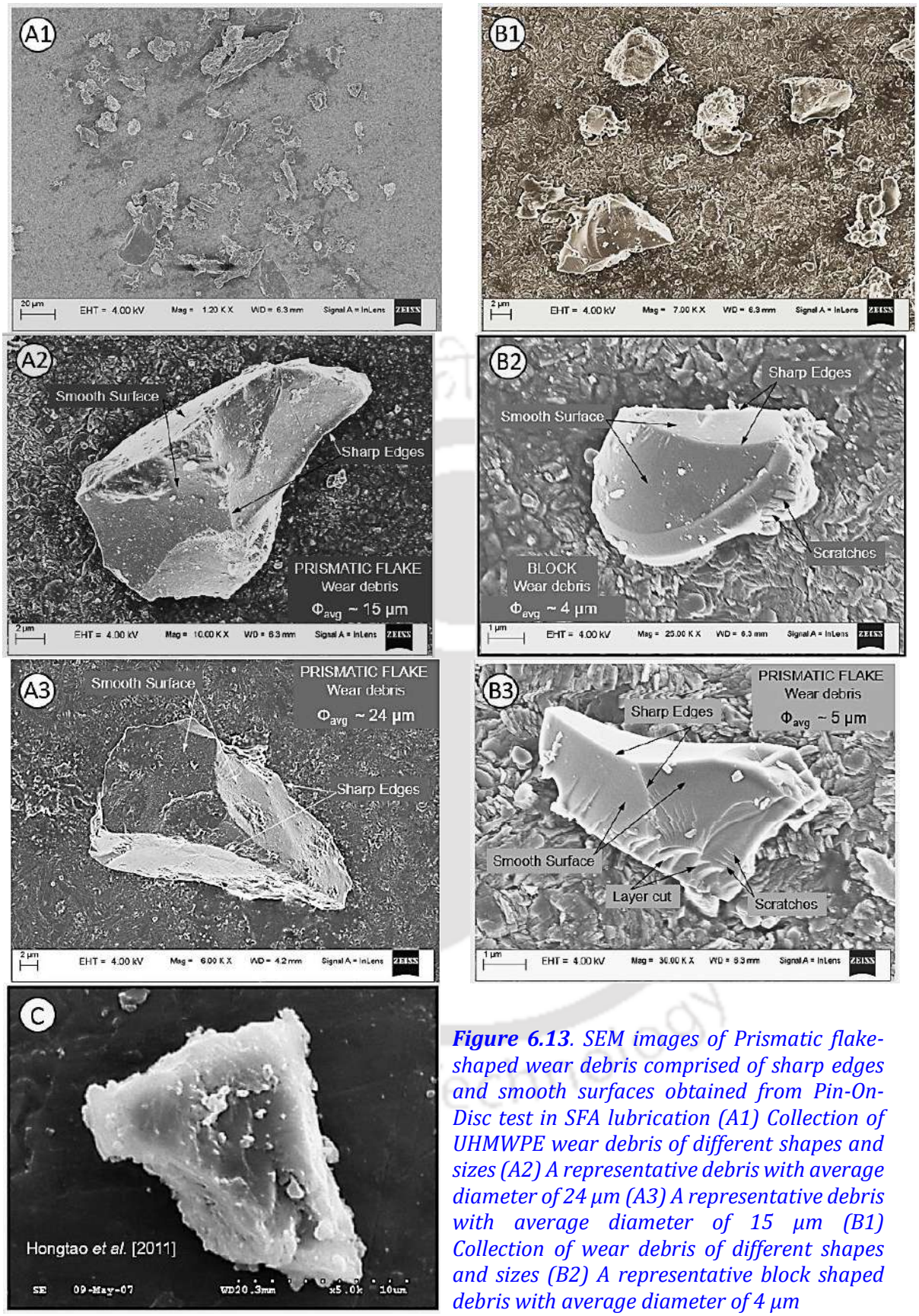

***Figure 6.13**. SEM images of Prismatic flake-shaped wear debris comprised of sharp edges and smooth surfaces obtained from Pin-On-Disc test in SFA lubrication (A1) Collection of UHMWPE wear debris of different shapes and sizes (A2) A representative debris with average diameter of 24 µm (A3) A representative debris with average diameter of 15 µm (B1) Collection of wear debris of different shapes and sizes (B2) A representative block shaped debris with average diameter of 4 µm (B3) A representative flake-shaped debris with average diameter of 5 µm (C) Typical morphology of UHMWPE wear debris found in small amount from the implanted artificial joint [9]*

However, testing under SFA lubrication it produced small wear debris in the form of prismatic flakes, blocks or spindle shapes, mostly in the order of micron and submicron size. However, the average size of UHMWPE-0.25MWCNT wear debris is observed to be 0.3-0.5 times of those generated from UHMWPE reflecting to the total wear volume measurements of the specimens.

This indicates a less severity in the wear process of the composite compared to pure polymer as a result of the improved hardness and integrity of the composite due to incorporation of MWCNT. In addition, every UHMWPE-0.25MWCNT specimen underwent material removal process by micro-ploughing at their central zone independent of the test lubricant used, which is a brittle failure of the material due to its increased hardness, which is absent in UHMWPE specimen for exhibiting enough ductility in pure form.

Studies on the size and shape of UHMWPE wear debris retrieved from periprosthetic tissues during revision of THA indicated that the majority of the wear particles were found to be in the order of micron and submicron size. These particles were in spherical, sub-spherical or a small amount of unbroken plate shape [9], [197], [204]. These observations are similar to what is observed in case of SFA lubricated POD test, bear no resemblance to what is noticed for the water lubricated case with long strip shaped wear debris. In other words, SFA lubrication is confirmed to produce similar kind of wear mechanism observed clinically in UHMWPE/SS. It has long been recognized that water alone is not a good boundary lubricant for UHMWPE/Metal bearing couples as there are no long-chain molecules in the liquid that can adhere to the articulating surfaces [205]. The formation of transfer films on the SS counter face is a direct consequence of the ineffectiveness of water as a boundary lubricant. In order to have joint simulation study, it is required to mimic the *in vivo* situation as close as possible and thus, SFA is the best choice to be used as a lubricant in polymer/metal bearing tribology studies.

Table 6.1. *Summary of POD test results*

	UHMWPE/Stainless Steel					
Lubricating condition	**μ**	**LWR**	**Pin surface topology**	**Wear debris Morphology**	**Wear mechanism**	**Explanations**
DRY	0.6	3.3	Plastic flow Layer separation Scratches	LACERATED	**Plastic flow (major)** Micro-Adhesion (minor) Abrasive wear (minor)	▪ High friction due to lack of lubricant ▪ Overheating and adhesion ▪ Fatigue
WATER	0.1	25	Scratches	STRIP	**Abrasive wear**(major) Micro-cutting	▪ Water absorption and swelling of UHMWPE ▪ Decreases in shear strength of UHMWPE ▪ Cumulative effect
SFA	0.05	5	Plastic flow orthogonal to sliding Scratches	PRISMATIC FLAKES	**Adhesive wear** (major) Abrasive wear (minor)	▪ Highly Viscous SFA adheres to friction pair surfaces ▪ Wear debris from cracked surface by adhesive force ▪ Block shaped wear debris
	UHMWPE-0.25MWCNT/Stainless Steel					
Lubricating condition	**μ**	**LWR**	**Pin Surface topology**	**Wear debris morphology**	**Wear mechanism**	**Explanations**
DRY	0.4	2.7	Wear patches Plastic flow Scratches	LACERATED (40% reduced size)	**Galling wear** (major) Plastic Flow (minor) Abrasion (minor)	▪ Lack of lubrication and heating ▪ Friction lowered by 33% compared to PE ▪ Increased brittleness of the composite
WATER	0.05	8	Scratches Grooves	STRIP (40% reduced size)	**Abrasive wear** (major) Micro-cutting Micro-ploughing	▪ Water absorption, ▪ Swelling of composite ▪ Decreases of shear strength ▪ Cumulative effect
SFA	0.03	2.5	Scratches Wear patches	PRISMATIC FLAKES & BLOCKS (75% reduced size)	**Abrasive wear** (major) Galling wear (minor)	▪ Highly Viscous SFA adheres to friction pair surfaces ▪ Lowest friction coefficient ▪ Yield strength increased with MWCNT addition ▪ Plastic flow is absent

6.6.2. Simulator Test

6.6.2.1. Gravimetric analysis

Residual volume of the acetabular liners, calculated by displacement method, against number of cycles of simulator test performed on it is plotted in Figure 6.14(A). The difference in volume before and after a million cycle of operation is considered as the volumetric wear loss experienced by the specimen during the particular period. It is observed that the wear rate of the test sample is found to be stabilized after 2 million cycles. During the initial testing period, a higher average volumetric wear rate of ~90 mm^3/MC and ~60 mm^3/MC is observed for pure polymer and composite liners, respectively.

The higher wear rate during initial phase of the test is due to the well-known fact of 'initial seating' during the usage of THR [206]. After the 'initial sitting' period, the average volumetric wear rate of UHMWPE and UHMWPE-0.25MWCNT liner is found to be stable at ~20 mm^3/MC and ~9 mm^3/MC, respectively, where a 70% reduction in wear rate of the composite specimen is observed. The obtained results of UHMWPE sample are compared with volumetric wear rate of crosslinked polyethylene liner against metallic femoral head, obtained by different laboratories worldwide and the same is shown in Figure 6.14(B) [162]. The wear rate of unirradiated UHMWPE acetabular liner against SS femoral head obtained in this study is found to be comparable with the results reported by SW 12ST, MARK II and MATCO EW08 simulators for the similar bearing combination where the polymer is crosslinked. Thus, the wear rate of the ingenious UHMWPE liners is expected to be reduced by ~ 90% after its irradiation, and it is also supported by Essner *et al.* [137].

6.6.2.2. CMM Measurements

Diameter of the spherical bearing surface is measured zone-wise as depicted in Figure 6.5(C) and the results are reported in Table 6.2. The difference in diameter before and after the simulator test is considered as the measure of linear wear depth in this study and it is found to be asymmetric as predicted earlier with reference to the retrieved THR shown in Figure 6.5(A) due to the asymmetry in loading profile. Zone C is found to suffer the maximum linear wear in both UHMWPE and UHMWPE-0.25MWCNT liners.

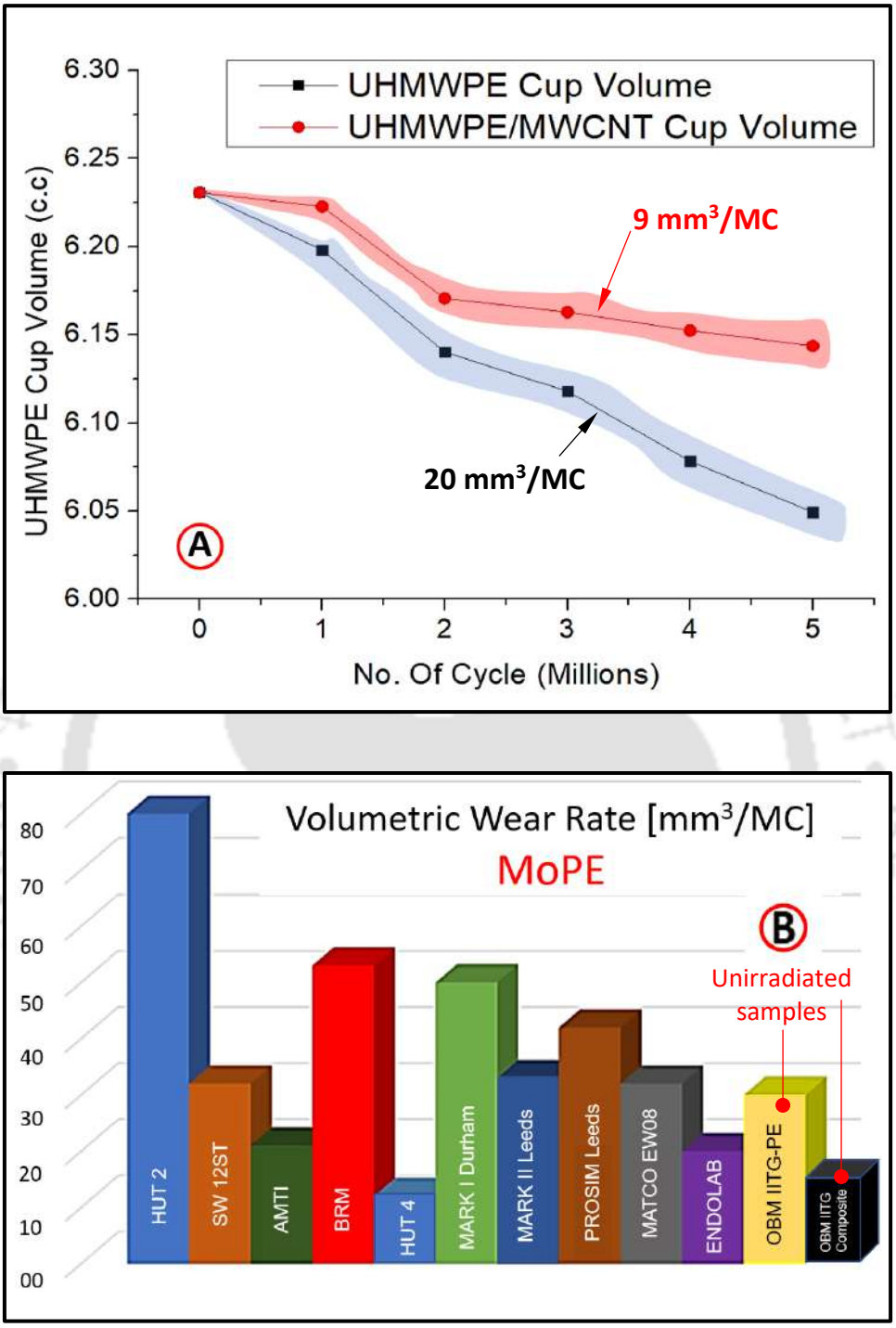

Figure 6.14. *(A)Volumetric Measurement of the Acetabular liners after Simulator test with an interval of 1 million cycles (B)Comparison of volumetric wear rate for MoPE THA reported by different laboratories worldwide with that found in present work [162]*

Table 6.2. *Zone-wise bearing surface diameter measurement before and after test*

NO. OF CYCLES	PE LINER DIAMETER (mm)				COMPOSITE LINER DIAMETER (mm)			
(Millions)	Zone A	Zone B	Zone C	Zone D	Zone A	Zone B	Zone C	Zone D
0	22.021	21.999	22.012	22.009	22.021	22.009	22.02	22.013
1	21.954	21.876	22.211	22.085	21.911	21.994	22.123	22.095
3	21.868	21.793	22.452	22.101	21.869	21.989	22.301	22.099
5	21.771	21.762	22.533	22.124	21.835	21.974	22.359	22.103

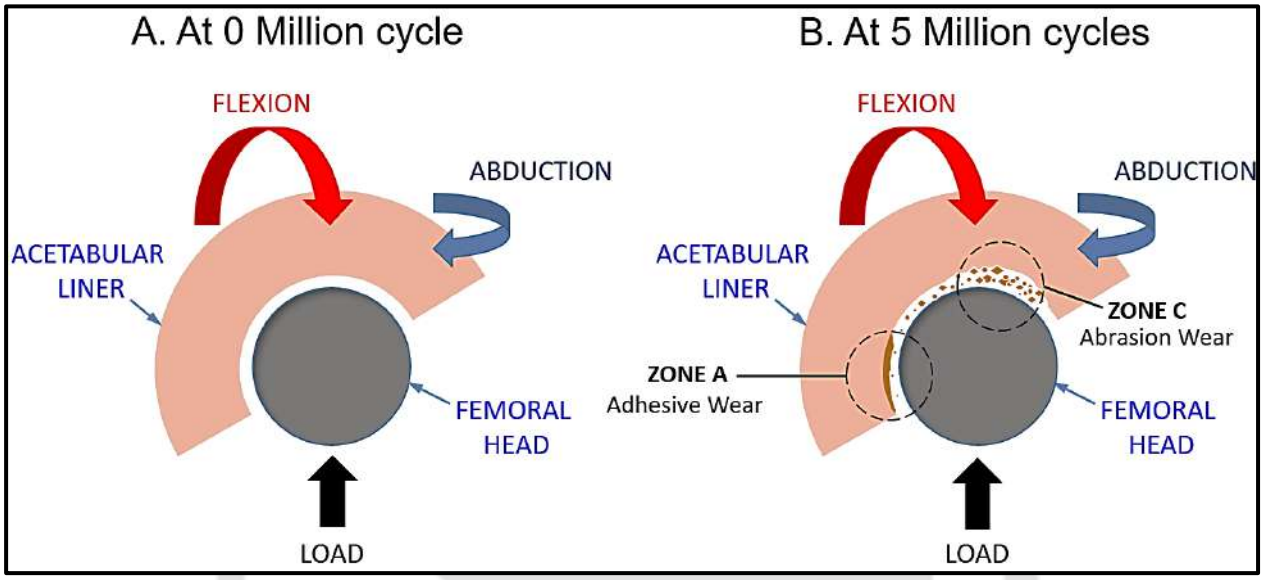

Figure 6.15 *Zone-wise wear phenomena in the acetabular liner (A) at the beginning of wear test (B) after 5 million cycles of testing*

The maximum linear wear depth in UHMWPE acetabular liner is observed to be ~260 µm, and it is reduced to ~170 µm for the reinforced composite with a 32% reduction. An apparent negative wear is observed in Zone A and Zone B for both pure polymer and composite liners indicating an adhesive wear in those zones. The wear debris generated from zone C and zone D are anticipated to be welded back to the parent material on Zone A and Zone B located diametrically opposite to them due to the heat and pressure generated at the contact zones in absence of any flushing agent during the testing as schematically shown in Figure 6.15.

Figure 6.16 shows the variation in diameter of the UHMWPE and UHMWPE-MWCNT liners with number of cycles of test at different zone. Diameter at Zone C and Zone D for both the liners are observed to increase with number of test cycles while that of Zone A and B are reduced effectively due to deposition of wear debris with the mechanism depicted in Figure 6.15.

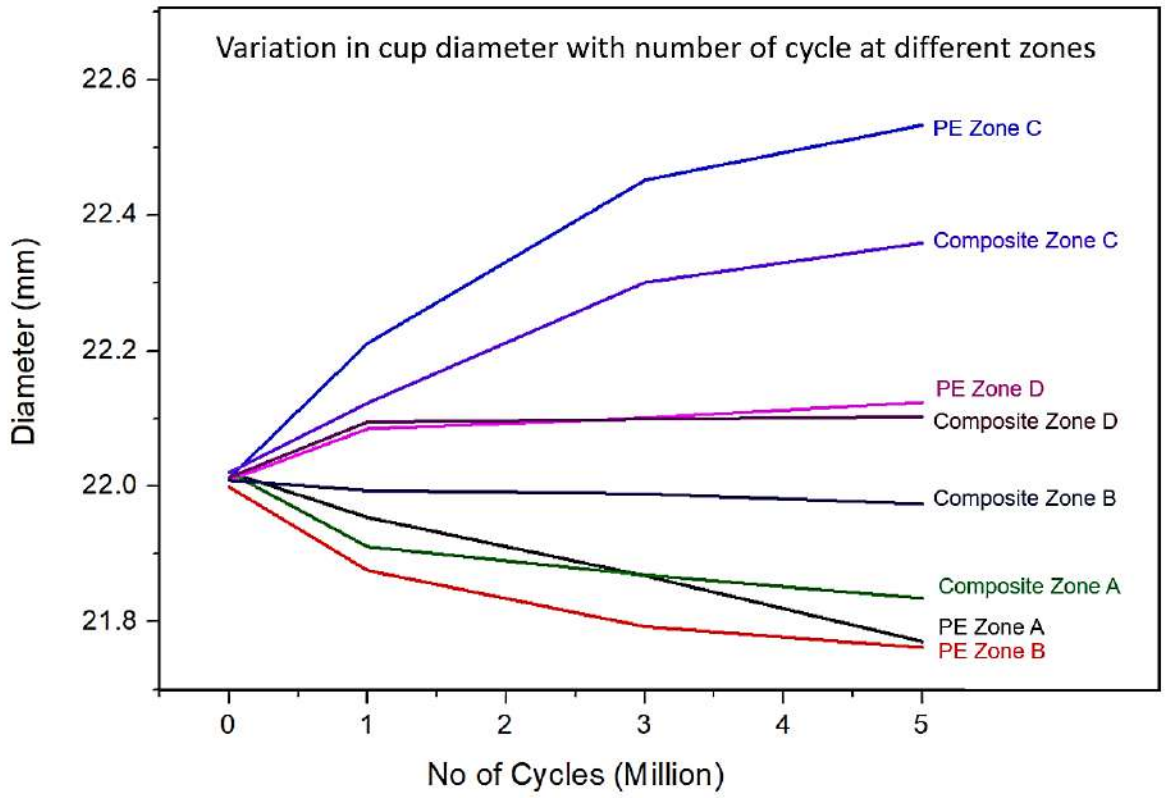

Figure 6.16. *variation in diameter of the UHMWPE and UHMWPE-MWCNT liners with number of cycles of test at different zone*

6.6.2.3. SFA Stability analysis

Figures 6.17(A), (B) and (C) show the comparison of Viscosity (η), Storage modulus (G') and Loss modulus (G"), respectively, of unused lubricant against frequency in the range of 0.1 to 100 Hz with those of used one, taken out of the simulator chamber after each million cycles of testing. No visible deviation in the rheological characteristics of used and unused lubricant is found in the operating zone of 1-6 Hz. Hence, it is confirmed that the lubricant was rheologically consistent during its usage in the simulator.

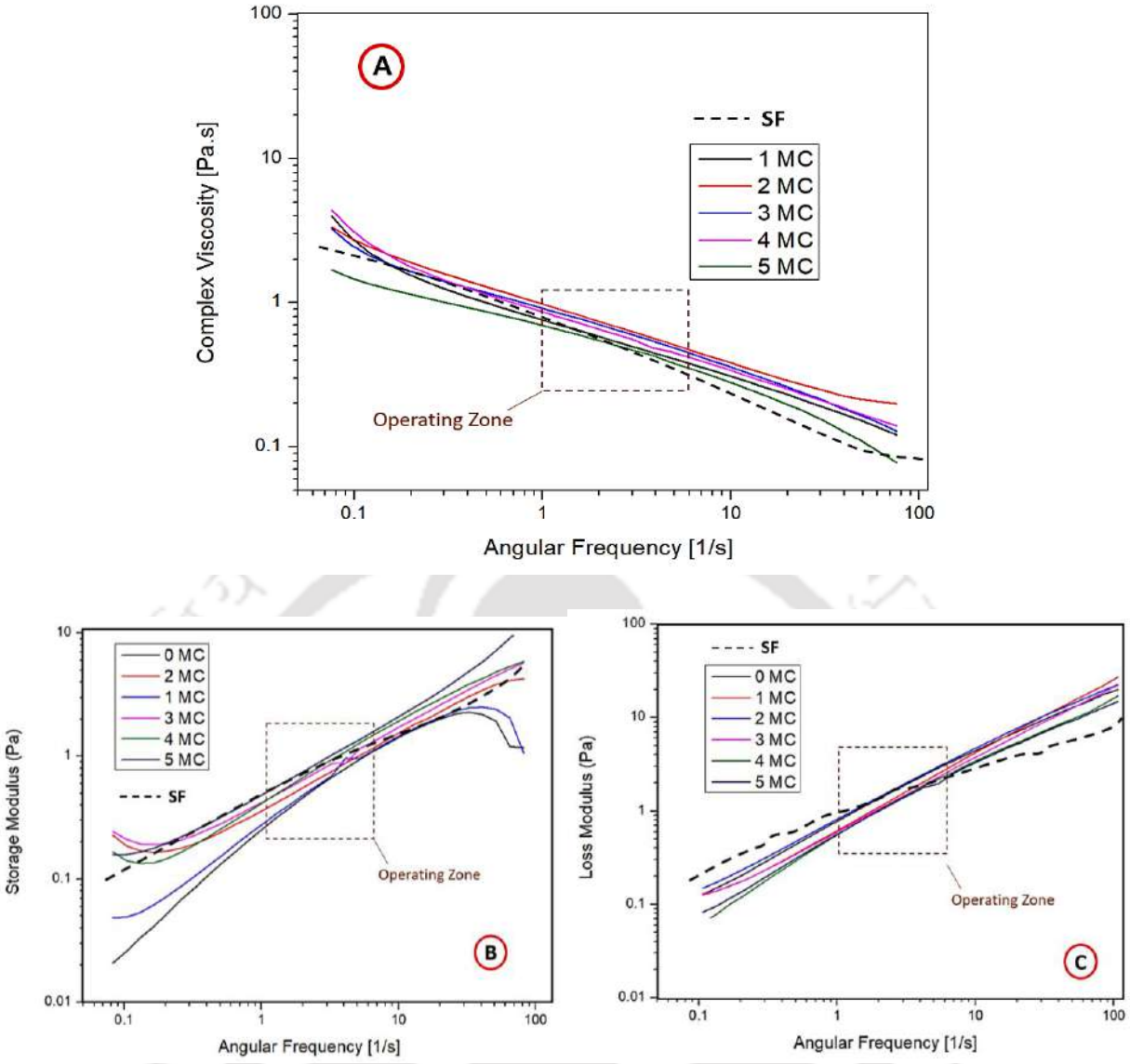

Figure 6.17. *Comparison of (A)Viscosity (B)Storage modulus (C) Loss modulus of unused lubricant with used lubricant taken out of the simulator chamber after each million cycle of testing ensuring the stability of the lubricant during usage.*

6.6.2.4. Wear Debris Analysis: Wear Mechanism

The UHMWPE wear debris of artificial joint obtained in the simulator test shows a variety of morphologies due to the complicated kinetics of artificial joint. However, most wear debris generated in SFA lubricating condition are found to be spherical or sub-spheroidal in shape. Figures 6.18(A1) – (A4) show the SEM images of four typical representative wear debris in spherical shape having Φ_{avg} in the range of 4 µm – 30 µm, which are separated from the test lubricant after the wear simulation studies of UHMWPE liners.

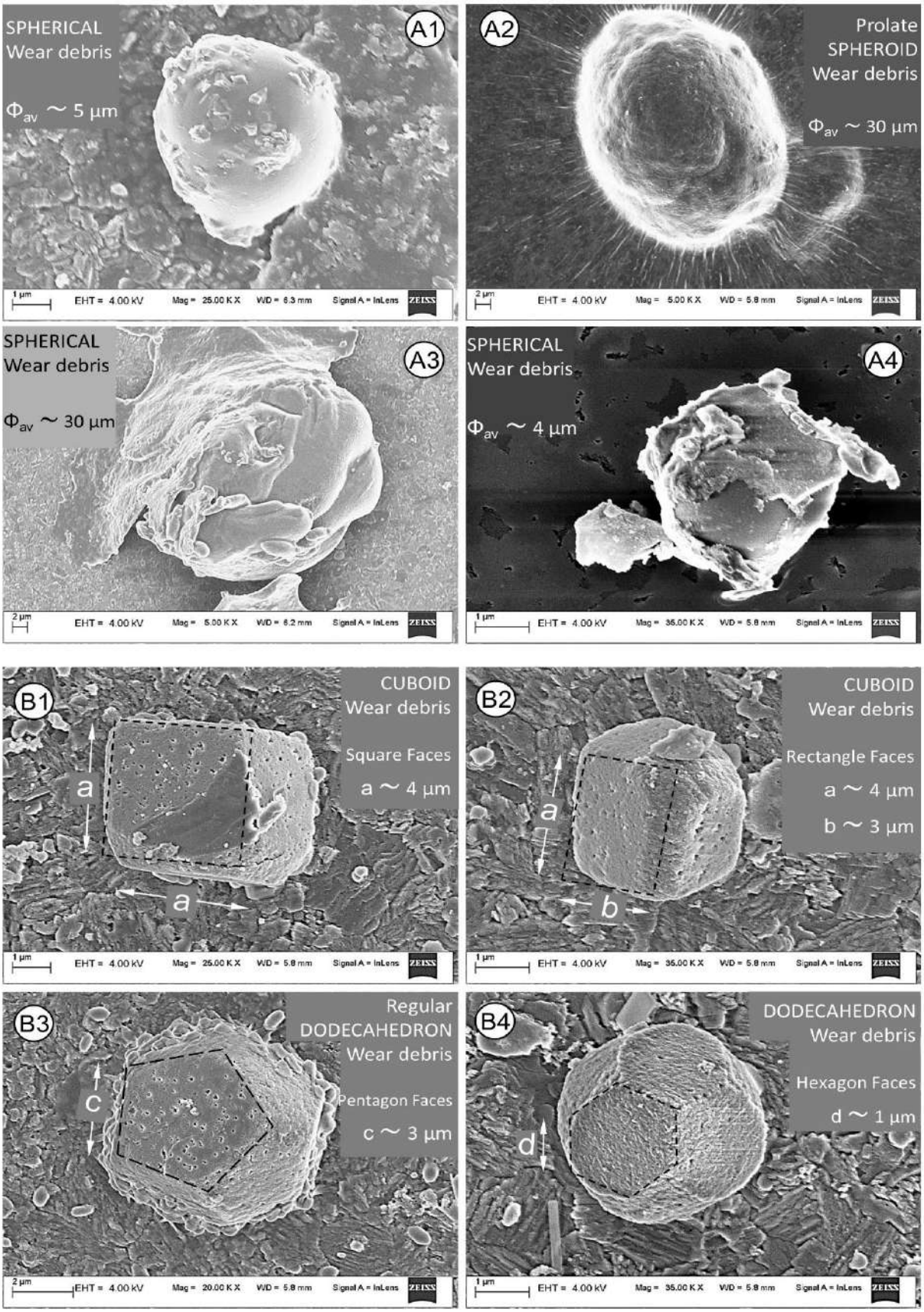

Figure 6.18. *SEM images of some representative wear debris generated after simulator test in SFA lubrication (A1-A4) UHMWPE wear debris (B1-B4) UHMWPE-0.25MWCNT wear debris*

Figures 6.18(B1) – (B4) show the similar SEM images of wear particles having Φ_{avg} in the range of 1 µm – 5 µm, which are obtained from UHMWPE-0.25MWCNT liners after the simulator tests. The UHMWPE-0.25MWCNT wear particles are found to be in cuboid as shown in Figures 6.18(B1) and (B2) or regular dodecahedron shapes as shown in Figures 6.18(B3) and (B4) unlike spherical shapes in case of pure polymer shown in Figures 6.18(A1) – (A4) with a size reduction of ~ 75%. However, these wear particles of near spherical shape may be considered to be under the process of becoming spheroidal with more number of test cycles, which have been delayed possibly due to higher hardness of the composite wear particles compared to UHMWPE wear debris as a result of MWCNT reinforcement. Figures 6.19 (A1) – (A6) show the SEM micrograph of UHMWPE wear debris obtained from a hip joint simulator studies after the *in vitro* testing of UHMWPE liners against Co-Cr-Mo alloy head for 1 million cycles as per the ISO 14242-1 recommendations under 25% calf serum lubrication [203]. It is observed that the wear debris have different sizes and shapes such as Spheroidal wear debris [Figure 6.19(A1)], Block wear debris [Figure 6.19(A2)], Tearing wear debris [Figure 6.19(A3)], Sheet wear debris [Figure 6.19(A4)], Rod wear debris [Figure 6.19(A5)] and Zonary wear debris [Figure 6.19(A6)] without any majority. Though the shape of wear debris is complicated, it still can be found that the size of wear debris is larger and the shape is more complicated. When the wear debris is small enough, its shape tends to be spherical or near-spherical.

Fatigue wear is the major wear mode when the artificial joint is implanted in a human body [200], [203]. As the wear debris in spherical shape possesses the lowest energy structure, all the wear debris tend to turn into sub-spheroidal shape if they persist enough time in the lubricant. It is confirmed by the morphology of the extracted wear debris of the artificial joint, which are shown in Figures 6.19(B1) and (B2). The substantial resemblance in morphology of the *in vivo* UHMWPE wear particles with those shown in Figure 6.18(A1) – (A4) confirmed the similarity in wear mechanism followed by them. On the other hand, comparing Figure 6.19 (A1) – (A6) with Figure 6.19(B1) – (B2), it is noticed that the reported hip joint simulators could not regenerate the *in vivo* environment and wear mechanism even after following the ISO 14242-1 for the same pair of material under calf serum lubrication. This inconsistency in the results may be explained by two major incongruities, viz., (i) execution of a smaller number of wear cycles, (ii) difference in rheological behaviour between calf serum and the synovial fluid, which resulted in a dissimilar wear mechanism and wear debris during the reported simulator test which are eliminated in the present study by using SFA.

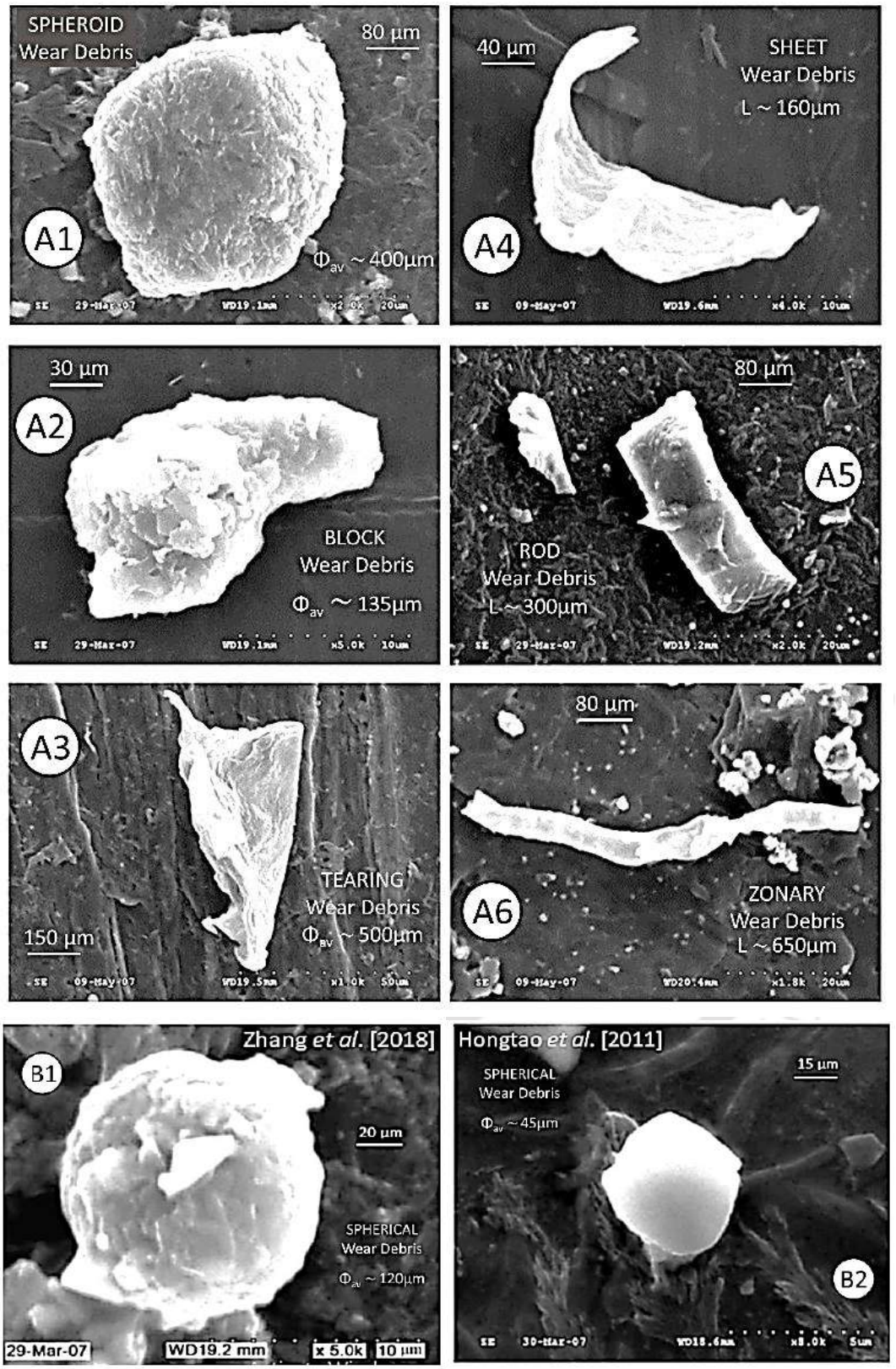

Figure 6.19. *(A1-A6) Wear debris of various morphology obtained by Hongtao et al. [9] by simulator test of UHMWPE liner (B1-B2) Typical morphology of UHMWPE wear debris obtained from human body after total hip replacement [200]*

Particle size distribution of the wear debris generated from UHMWPE and UHMWPE-0.25MWCNT liners are evaluated using FESEM micrographs, samples of which are shown in Figure 6.20(A) and Figure 6.20(B), respectively. Average diameter of each visible wear particle in the cluster is measured using in-built FESEM software and statistical normal distribution of the same is plotted in Figure 6.20(C). Diameter of the wear debris generated from UHMWPE liner after the Ball-On-Cup tribometer test are found to be in the range of 0.6 µm to 82.5 µm**.** They are mostly concentrated between 2.5 µm and 20 µm, with 31% of the wear debris having the average diameter of 7.14 µm.

Compared to the UHMWPE wear debris, the wear debris of UHMWPE-0.25MWCNT liner generated by the 'Ball-On-Cup' tribometer presents a relatively smaller size. The size distribution of UHMWPE-0.25MWCNT wear particles ranges from 0.2 µm to 70.1 µm. They are mostly concentrated between 0.5 µm and 15 µm, with 24% of the wear debris having the average diameter of 4.23 µm. Figure 6.20(C) compares the size distribution of wear debris obtained in the present study with that of UHMWPE wear debris obtained from the artificial joint simulator test performed by Hongtao *et al.* [9] along with the size distribution of wear debris retrieved from the implanted artificial joint.

The wear debris produced by the reported simulator [9] were found to have an average diameter of 7.54 µm, whereas 18% of the *in vivo* wear debris is reported to have an average size ~ 1.33 µm. It can be inferred that UHMWPE wear debris obtained from the present study and the reported hip joint wear simulator study [9] are found to have similar size distribution with ~ 10% particles having $\Phi_{avg} > 7$ µm.

However, the size distribution of ~ 10% *in vivo* UHMWPE wear particles is reported to have $\Phi_{avg} < 2$ µm. This disparity is possibly due to execution of a smaller number of wear cycle by the simulators compared to the actual number of cycles undergone by the THA inside the human body. The wear debris are expected to turn into smaller in size if they persist enough time in the lubricant for higher number of cycles. In terms of average particle size, UHMMWPE-0.25MWCNT wear debris with ~10% particles having $\Phi_{avg} \sim 4$ µm are found to be much similar to that of *in vivo* particles and these two size distribution curves are observed to be closer to each other which is noticed in inset of shown in Figure 6.20(C). From the particle size distributions of all the wear debris obtained from both *in vitro* and *in vivo* studies, it is noticed that they are mostly within 50 µm in size.

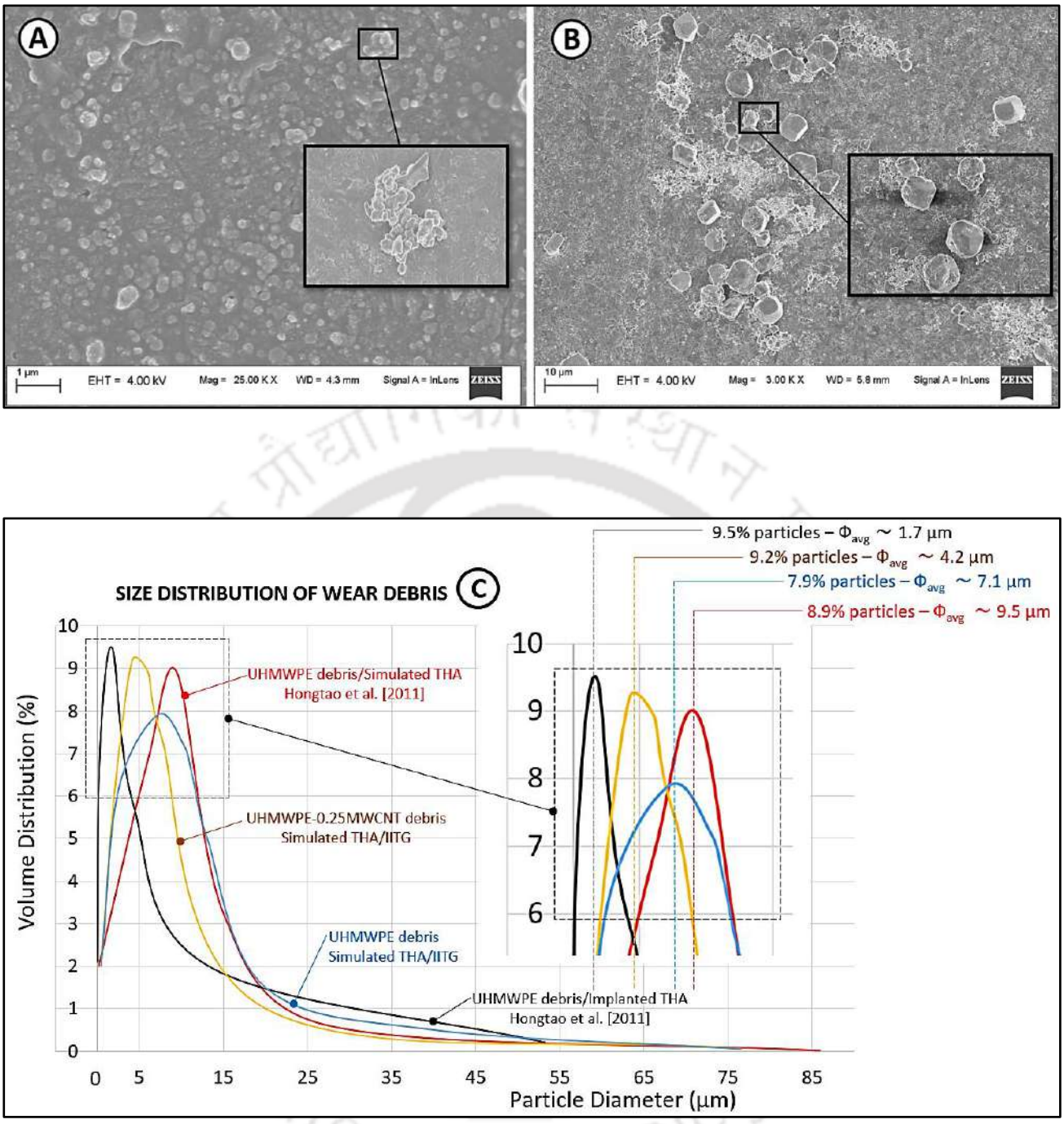

Figure 6.20*. Sample cluster of wear debris generated from (A) UHMWPE liner (B) UHMWPE-0.25MWCNT liner for the evaluation of particle size distribution (C) Comparison of Wear debris size distribution obtained from IITG simulator with published one [198]*

6.6.3. Numerical Validation of experimental observations

Both UHMWPE and UHMWPE-0.25MWCNT acetabular liners are observed under SEM after they have completed 5 million test cycles to evaluate the residual surface morphology and confirm the wear mechanism. Figures 6.21(A1-D1) and Figures 6.21(A2-D2) show the SEM micrographs to identify four distinct wear profiles on UHMWPE and UHMWPE-0.25MWCNT liners, respectively, along their meridian. Figures 6.20(E) shows the results obtained from numerical stress-strain analysis of the liner for the time instance 0.5 s when the applied load and extension angle reached their maximum of 3.0 kN and 23°, respectively as per the ISO 14242-3. Figure 6.21(A1) shows the SEM micrograph of Zone 1 of UHMWPE liner which is found to undergo the most severe damage due to adhesive wear mechanism. The numerical analysis also identified that the Zone 1 is bound to have the highest stress (~ 3.5 MPa) on the transverse section of the liner shown in Figure 6.21(E).

Similarly, Figure 6.21(B1) shows that the Zone 2 of UHMWPE liner is undergone through micro ploughing predominantly, and the corresponding stress on the zone is found to be ~ 2.6 MPa by the numerical stress analysis. Zone 3 is found to undergo plastic flow as shown in Figure 6.21(C1) under the action of a moderate stress of ~ 1.8 MPa and the corresponding strain value is ~0.15%. Surprisingly, Zone 4, i.e., the bottom region of UHMWPE liner is found to be unworn when looked under SEM, shown in Figure 6.21(D1), and the surfaces retained their inborn morphology. The experimental observation is well supported by the numerically obtained stress of negligible order at Zone 4 with insignificant strain at the region. The numerical model also identified that the maximum strain of ~0.2% is developed at Zone 1, which is also consistent with the experimental observations.

Similarly, UHMWPE-0.25MWCNT liner is inspected under SEM and four distinct wear mechanism, viz., adhesive wear (Zone 1), micro-ploughing (Zone 2), plastic flow (Zone 3) and no wear (Zone 4) are identified as shown in Figures 6.21(A2), (B2), (C2) and (D2) respectively.

From the above studies, it is inferred that both UHMWPE and UHMWPE-0.25MWCNT liners exhibited four distinct wear zones of similar wear mechanism but the severity of it is found to be much less in case of composite sample, which is consistent with the results discussed earlier.

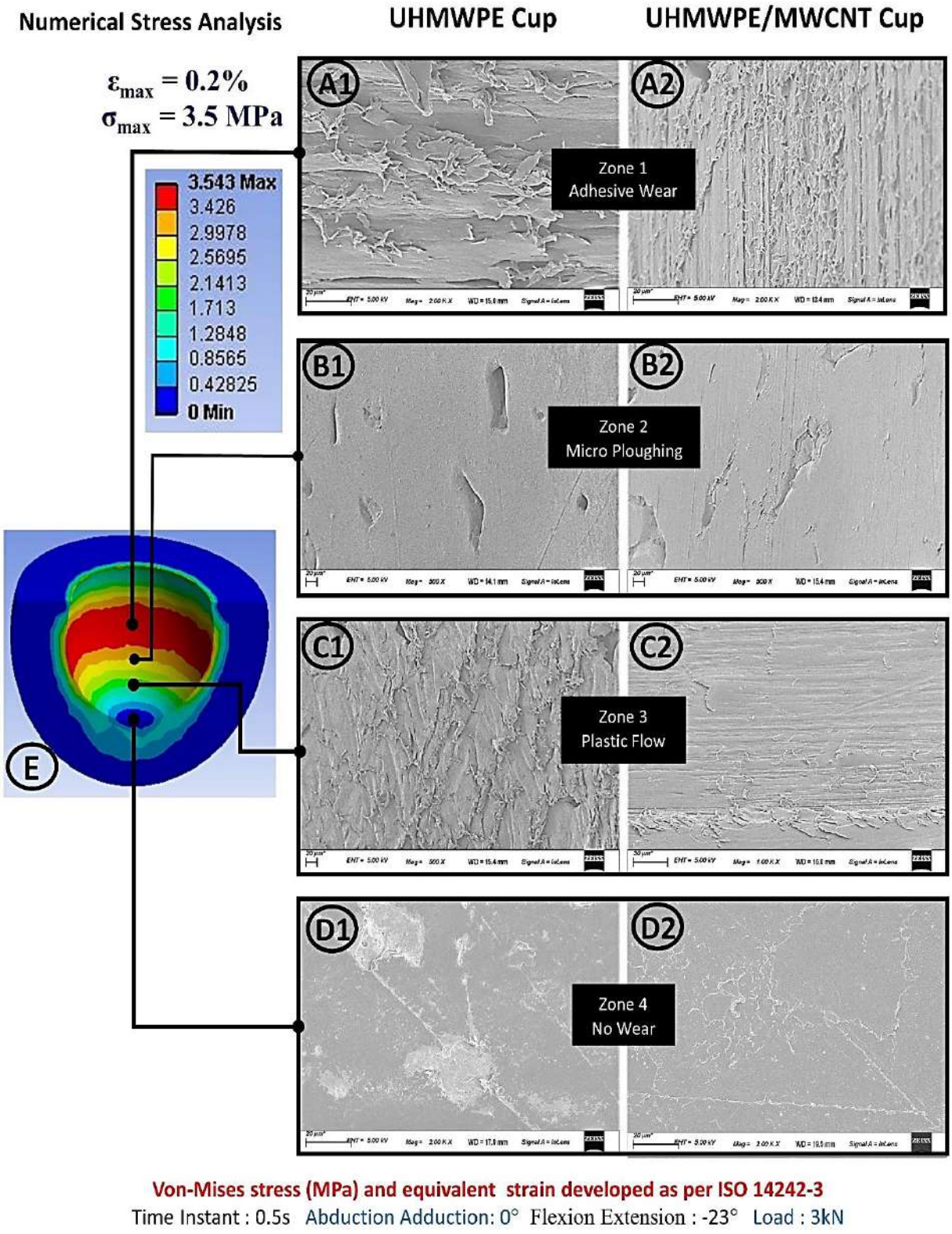

Figure 6.21. *Wear profile observed under FESEM (A1) Zone 1-UHMWPE liner (A2) Zone 1-UHMWPE-0.25MWCNT liner (B1) Zone 2-UHMWPE liner (B2) Zone 2-UHMWPE-0.25MWCNT liner (C1) Zone 3-UHMWPE liner (C2) Zone 3-UHMWPE-0.25MWCNT liner (D1) Zone 4-UHMWPE liner (D2) Zone 4-UHMWPE-0.25MWCNT liner (E) Transverse section of the numerical model of liner to identify distinct stress zones*

6.7. Summary

- Experimental results revealed that the morphology and size of UHMWPE wear debris produced by the POD tribometer depends strongly on the type of lubricant used in the test as well as hardness of the test material. Strip wear debris is generated by micro-cutting and under water lubrication and the lacerated wear debris is produced by dry sliding condition. These are found to be dissimilar by their morphology when compared with the *in vivo* wear particles. However, SFA lubrication POD test is found to be predominated by adhesive wear mechanism which produced typical flake and block shaped wear debris. These type of wear debris are found in human body after the total hip replacement. In order to have hip joint wear simulation studies, the test conditions are expected to closely mimic the *in vivo* situation, where SFA is used as the lubricant.

- Overall observations on hip simulator test revealed that both UHMWPE and UHMWPE-0.25MWCNT underwent similar wear phenomena while testing condition remained unchanged and this statement is supported by the morphological resemblance of the wear debris produced under the same test lubricant. However, the severity of wear damage is found to be much less in case of composite specimen due to its superior hardness compared to that of pure polymer. Morphology and size distribution of wear debris are signatures of friction and wear behavior of the implanted joints. Hence, the observed morphological resemblance and similarity in the range of particle size distribution between the wear debris generated by 'Ball-On-Cup' tribometer and those retrieved from the implanted hip joint indicated a significant success in recreating *in vivo* conditions under *in vitro* with the help of in-house developed simulator along with the synovial fluid analogue (SFA). Rheological analogy of synthetic SFA with the synovial fluid and the ISO 14242-3 protocols played an important role in this accomplishment, lack of which may generate a completely diverse set of wear debris morphologies under a different wear mechanism incongruent with the *in vivo* outcomes.

- Four distinct wear mechanism, viz., adhesive wear, micro-ploughing, plastic flow, and no wear are identified under SEM on the bearing surface of the tested acetabular liners. However, fatigue wear is the major wear mode when the artificial joint is tested in the hip joint wear simulator as the wear debris with the spherical structure possesses the lowest energy structure. However, the wear debris tend to turn into sub-spheroidal structure if it persists enough time in the test lubricant which is also the case for *in vivo* wear particles in synovial fluid.

- The numerical model is used to validate four distinct wear zones observed in the experimental studies with the calculated stress distribution pattern.

भारतीय प्रौद्योगिकी संस्थान गुवाहाटी
Indian Institute of Technology Guwahati

CHAPTER 7

CONCLUSIONS AND FUTURE SCOPE

7.1. Conclusions

Medical grade UHMWPE GUR 1050 is processed with apposite processing parameters in order to maximize its mechanical integrity and characteristics. UHMWPE is reinforced with different concentrations of MWCNT ranging from 0.125 to 0.75 wt.%. The homogeneity in distribution and dispersion of the filler in polymer matrix is also studied. The various mechanisms involved to enhance the mechanical properties of UHMWPE up to an optimum filler concentration and the reduction thereafter are suggested and confirmed. Further studies on the nanocomposites are limited at the optimum concentration of MWCNT only. Optimally processed UHMWPE and UHMWPE-MWCNT composite pin specimens are tested for wear screening using a pin-on-disc tribometer against a stainless-steel disc for a comparative study on the frictional coefficient and linear wear rate among all the bearing combinations under different lubrications, viz., dry, water and SFA. Ingeniously developed acetabular liners made of UHMWPE and UHMWPE-MWCNT composite with optimum MWCNT concentration are tested under simulated *in vivo* condition using an in-house developed novel 'Ball-on-Cup' tribometer and a synthetic lubricant engineered to be analogous to synovial fluid. The simulated wear mechanism is compared with that of reported mechanism for total hip arthroplasties operated under *in vivo* condition.

The important findings of the present work are reported as follows:

- Optimum compaction pressure, sintering temperature and sintering duration of medical grade GUR 1050 UHMWPE are found to be 15 ksi (103.5 MPa) 165°C and 130 min., respectively, in order to obtain machining free polymer products with the best characteristics for the proposed application without any visible defects.

- The final product achieved at a relative density of more than 97% with respect to the gel-spun UHMWPE fibers having an average hardness of 5.4 HVN and tensile strength of 21.5 MPa, where these properties are found to be at par with hot isostatic pressed (HIPped) products.
- UHMWPE is reinforced with different concentration of MWCNT (0.125, 025, 0.375, 0.5 and 0.75 wt.%) using a novel combined technique of ultra-sonication and magnetic stirring for effective dispersion and distribution of the filler in the UHMWPE matrix.
- At 0.25 wt.% of MWCNT loading, the mechanical properties of nanocomposite, namely, compressive strength, tensile yield strength, Vickers hardness, and toughness are enhanced by ~120%, ~62%, ~60%, and ~20%, respectively, in comparison to that of virgin polymer.
- The UHMWPE and UHMWPE-MWCNT samples exhibited uncompromised cytocompatibility with osteoblast and human mesenchymal stem cells.
- An ingenious technique is developed to fabricate UHMWPE and UHMWPE-0.25MWCNT acetabular liners with excellent inborn surface finish and bearing characteristics, and it required no machining or finishing process for generating the bearing surface with an average surface roughness (Ra) of ~90 nm.
- Bearing surfaces of the acetabular liners are generated with the desired bearing surface diameter of 22.00 ± 0.01 mm and the liner thickness of 5.2 ± 0.9 mm.
- No visible defects in the cross-sectional surface of the Acetabular liner are observed while following the optimized processing parameters.
- A modular mechanism is designed and developed, which can be attached to a conventional *Pin-On-Disc* tribometer to modify the same into a *Ball-On-Cup* tribometer for testing the total hip arthroplasty.
- The *Ball-On-Cup* tribometer may be categorized as an orbital bearing machine (OBM) hip simulator, which approximately generates *a* load profile comparable to the suggested one by **ISO 14242-3** in addition to the bi-axial angular motion using a single DC motor as the only prime mover.
- The *Ball on Cup* device can reproduce the tribological test results similar to that of *in vivo* usage in a simplified manner taking into account of the influence of geometry and morphology of a THA while reflecting the lubrication regime and wear mechanism, imitating the realistic contact stresses during its usage.

- A mixture of 0.75% w/v Gellan and 2% w/v sodium alginate in 2:1 volumetric ratio is found to be rheologically similar to the synovial fluid and it is proposed to be utilized as a synovial fluid analogue (SFA) for the tribological characterization of any new polymeric liner in metal-on-polymer THA.
- SFA lubricated POD test is found to be predominated by adhesive wear mechanism and produced typical flake and block shaped wear debris which are also found in human body after total hip replacement.
- UHMWPE-0.25MWCNT are found to be 50% more wear resistant with 40% reduction in COF under SFA lubrication in comparison to that of pure polymer.
- Recreating *in vivo* conditions under *in vitro* is successfully done with the help of in-house developed 'Ball-on-Cup' tribometer along with the synovial fluid analogue (SFA).
- Most of the wear debris generated in SFA lubricated simulator test of SS-on-UHMWPE bearing couple are of spherical or sub-spheroidal in shape showing a significant morphological resemblance with the wear debris generated in an implanted artificial joint *in vivo* condition, which is the signature of adhesive and fatigue wear.
- The simulator test results of UHMWPE sample are compared with volumetric wear rate of M-o-P THA reported by different laboratories worldwide and the wear rate of the developed unirradiated pure UHMWPE acetabular liner is observed to be ~20 mm^3/MC, which is found to be at par with irradiated polymer liner. In addition, the wear rate of UHMWPE and UHMWPE-MWCNT samples after cross-linking is expected to reduce further.
- Volumetric wear rate and maximum wear depth of UHMWPE acetabular liner produced by the simulator are reduced by 70% and 32%, respectively with the reinforcement of 0.25 wt.% of MWCNT under the same tribological environment.
- UHMWPE and UHMWPE-MWCNT composite processed with the proposed technique may be considered as a potential aspirant for the next generation acetabular liner having inborn plateau finish bearing surface in the metal-on-polymer THR in order to increase its longevity.

7.2. Scope of future work

The work presented in this thesis opens up several avenues for further development and characterization of UHMWPE and its composite based material for biomedical applications, especially in the field of orthopaedic implants. The scope of future work is outlined as follows:

- Hot isostatic press or an autoclave may be used for processing UHMWPE using the existing mould design. The simultaneous application of pressure and heat may produce products with higher relative density and mechanical strength but with completely different set of operating parameters.
- The wear resistance of UHMWPE and UHMWPE-MWCNT products developed in the present study is expected to improve further significantly if the polymer molecular chains are cross-linked by gamma irradiation. Hence, the study on the existing acetabular liners may be taken further after they are exposed to gamma irradiation of prescribed dose.
- The study can be extended further with a biological analogue of the synovial fluid incorporating protein and hyaluronan to study some additional phenomenon like tribo-corrosion and protein deposition on the THA during its simulator testing.
- The existing liners may be tested against commercially available ceramic heads for further study, which is approved by FDA.
- A complete numerical model of the developed liners against various femoral heads may be designed and simulated as per the ISO 14242-1 including the prescribed motion and load profiles for wear study.
- The developed acetabular liners may be tested further using a tri-axial hip simulator as per the ISO 14242-1 and the outcome may be compared with the existing results.
- Before human trial of the developed prosthesis, they must be tested and approved by an *in vivo* animal study as per the ISO 10993-1.

ANNEXURE 1

Conversion of linear wear rate (µm/km) to volumetric wear rate (mg/million cycle)

Linear wear rate (LWR) for UHMWPE specimen in water lubrication is reported to be 25 µm/km.

LWR = 25 µm/km = 25 × 10^{-3} mm/km

Pin (8mm diameter) area = A= $\pi d^2/4$ = 50.25 mm^2

So, volumetric wear rate (VWR) may be calculated as

VWR = LWR × A = 25 × 10^{-3} mm/km × 50.25 mm^2 = 1256.25 mm^3/km

Track diameter during POD test = 50mm

One cycle of POD test = one revolution = πD = (3.14 × 50) mm =157 mm

1 km = 10^6 mm = 10^6 / 157 cycles

Density of UHMWPE is reported to be 0.941 g/cc = 0.941 mg/mm^3

Hence, VWR = 1256.25 mm^3/km = 1256.25 × 157 mm^3/MC

= 1256.25 × 157 × 0.941 mg/MC

= 185.6 mg/MC

So, as per the calculation shown above,

25 µm/km = 185.6 mg/MC

REFERENCES

[1] P. Hernigou, "Earliest times before hip arthroplasty: From John Rhea Barton to Themistocles Glück," *Int. Orthop.*, vol. 37, no. 11, pp. 2313–2318, Nov. 2013, doi: 10.1007/s00264-013-2004-4.

[2] P. Hernigou, "Smith-Petersen and early development of hip arthroplasty," *Int. Orthop.*, vol. 38, no. 1, pp. 193–198, Jan. 2014, doi: 10.1007/s00264-013-2080-5.

[3] I. D. Learmonth, C. Young, C. Rorabeck, and B. Bs, "The operation of the century : total hip replacement," vol. 370, 2007, doi: 10.1016/S0140-6736(07)60457-7.

[4] B. M. Wroblewski, P. D. Siney, and P. A. Fleming, "The principle of low frictional torque in the Charnley total hip replacement," *J Bone Jt. Surg [Br]*, no. 7, pp. 91–855, 2009, doi: 10.1302/0301-620X.91B7.

[5] L. Neumann, K. G. Freund, and K. H. Sorenson, "Long-term results of Charnley total hip replacement: Review of 92 patients at 15 to 20 years," *J. Bone Jt. Surg. - Ser. B*, vol. 76, no. 2, pp. 245–251, 1994, doi: 10.1302/0301-620x.76b2.8113285.

[6] D. Fender, J. H. P. van der Meulen, and P. J. Gregg, "Relationship between outcome and annual surgical experience for the Charnley total hip replacement," *J. Bone Jt. Surg. - Ser. B*, vol. 85, no. 2, pp. 187–190, Mar. 2003, doi: 10.1302/0301-620X.85B2.12759.

[7] S. M. Kurtz, J. Dumbleton, R. S. Siskey, A. Wang, and M. Manley, "Trace concentrations of vitamin E protect radiation crosslinked UHMWPE from oxidative degradation," *J. Biomed. Mater. Res. - Part A*, vol. 90, no. 2, pp. 549–563, 2009, doi: 10.1002/jbm.a.32122.

[8] P. Kumar, R. Sen, S. Aggarwal, S. Agarwal, and R. K. Rajnish, "Reliability of Modified Harris Hip Score as a tool for outcome evaluation of Total Hip Replacements in Indian population," *J. Clin. Orthop. Trauma*, vol. 10, no. 1, pp. 128–130, Jan. 2019, doi: 10.1016/j.jcot.2017.11.019.

[9] L. Hongtao, G. Shirong, C. Shoufan, and W. Shibo, "Comparison of wear debris generated from ultra high molecular weight polyethylene in vivo and in artificial joint simulator," *Wear*, vol. 271, no. 5–6, pp. 647–652, 2011, doi: 10.1016/j.wear.2010.11.012.

[10] K. Elsharkawy, C. A. Higuera, A. K. Klika, and W. K. Barsoum, "Evolution of bearing surfaces in total hip arthroplasty: A review," *Curr. Orthop. Pract.*, vol. 21, no. 2, pp. 198–208, 2010, doi: 10.1097/BCO.0b013e3181c2bab8.

[11] H.-G. WILLERT, H. BERTRAM, and G. H. BUCHHORN, "Osteolysis in Alloarthroplasty of the Hip," *Clin. Orthop. Relat. Res.*, vol. 258, no. NA;, p. 108???121, 1990, doi: 10.1097/00003086-199009000-00014.

[12] S. A. Hanna, L. Somerville, R. W. Mccalden, D. D. Naudie, and S. J. Macdonald, "Highly cross-linked polyethylene decreases the rate of revision of total hip arthroplasty compared with conventional polyethylene at 13 years' follow-up," doi: 10.1302/0301-620X.98B1.

[13] T. von Schewelov, L. Sanzén, I. Önsten, Å. Carlsson, and J. Besjakov, "Total hip replacement with a zirconium oxide ceramic femoral head. A randomised roentgen stereophotogrammetric study," *J. Bone Jt. Surg. - Ser. B*, vol. 87, no. 12, pp. 1631–1635, 2005, doi: 10.1302/0301-620X.87B12.16873.

[14] A. H. De Aza, J. Chevalier, G. Fantozzi, M. Schehl, and R. Torrecillas, "Crack growth resistance of alumina, zirconia and zirconia toughened alumina ceramics for joint prostheses," 2002.

[15] G. K. Mckee and J. Watson-Farrar, "REPLACEMENT OF ARTHRITIC HIPS BY THE McKEE-FARRAR PROSTHESIS."

[16] J. H. Dumbleton and M. T. Manley, "Metal-on-metal total hip replacement: What does the literature say?," *J. Arthroplasty*, vol. 20, no. 2, pp. 174–188, 2005, doi: 10.1016/j.arth.2004.08.011.

[17] M. Silva, C. Heisel, and T. P. Schmalzried, "Metal-on-metal total hip replacement," in *Clinical Orthopaedics and Related Research*, 2005, vol. 430, pp. 53–61, doi: 10.1097/01.blo.0000149995.84350.d7.

[18] A. J. Smith, P. Dieppe, M. Porter, and A. W. Blom, "Risk of cancer in first seven years after metal-on-metal hip replacement compared with other bearings and general population: Linkage study between the National Joint Registry of England and Wales and hospital episode statistics," *BMJ*, vol. 344, Aug. 2012, doi: 10.1136/bmj.e2383.

[19] S. J. MacDonald, "Metal-on-metal total hip arthroplasty: The concerns," in *Clinical Orthopaedics and Related Research*, 2004, vol. 429, pp. 86–93, doi: 10.1097/01.blo.0000150309.48474.8b.

[20] P. R. Doom, P. A. Campbell, J. Worrall, P. D. Benya, H. A. McKellop, and H. C. Amstutz, "Metal wear particle characterization from metal on metalV total hip replacements: Transmission electron microscopy study of periprosthetic tissues and isolated particles," *J. Biomed. Mater. Res.*, vol. 42, no. 1, pp. 103–111, 1998, doi: 10.1002/(sici)1097-4636(199810)42:1<103::aid-jbm13>3.3.co;2-d.

[21] D. Hannouche, M. Hamadouche, R. Nizard, P. Bizot, A. Meunier, and L. Sedel, "Ceramics in total hip replacement," *Clin. Orthop. Relat. Res.*, no. 430, pp. 62–71, 2005, doi: 10.1097/01.blo.0000149996.91974.83.

[22] P. Boutin *et al.*, "The use of dense alumina–alumina ceramic combination in total hip replacement," *J. Biomed. Mater. Res.*, vol. 22, no. 12, pp. 1203–1232, 1988, doi: 10.1002/jbm.820221210.

[23] H. Miki *et al.*, "Phase transformation of a zirconia ceramic head after total hip arthroplasty," 2001.

[24] F. Traina, M. De Fine, A. Di Martino, and C. Faldini, "Fracture of ceramic bearing surfaces following total hip replacement: A systematic review," *BioMed Research International*, vol. 2013. 2013, doi: 10.1155/2013/157247.

[25] B. Habermann, W. Ewald, M. Rauschmann, L. Zichner, and A. A. Kurth, "Fracture of ceramic heads in total hip replacement," *Arch. Orthop. Trauma Surg.*, vol. 126, no. 7, pp. 464–470, Sep. 2006, doi: 10.1007/s00402-006-0173-y.

[26] J. C. Morrison and D. Ward, "Ceramic-on-Ceramic Bearings in Total," no. 405, pp. 158–163, 2002, doi: 10.1097/01.blo.0000038043.63743.9f.

[27] A. Wang, C. Stark, and J. H. Dumbleton, "Role of cyclic plastic deformation in the wear of UHMWPE acetabular cups," *J. Biomed. Mater. Res.*, vol. 29, no. 5, pp. 619–626, 1995, doi: 10.1002/jbm.820290509.

[28] N. D. L. Burger, P. L. de Vaal, and J. P. Meyer, "Failure analysis on retrieved ultra high molecular weight polyethylene (UHMWPE) acetabular cups," *Eng. Fail. Anal.*, vol. 14, no. 7, pp. 1329–1345, 2007, doi: 10.1016/j.engfailanal.2006.11.005.

[29] M. Wahyudi, Y. E. Putra, S. Arrohman, J. Jamari, and R. Ismail, "A comparison between mechanical properties of UHMWPE from ram extrusion process and UHMWPE from compression molding process for a hip joint liner," in *IOP Conference Series: Materials Science and Engineering*, Nov. 2018, vol. 432, no. 1, doi: 10.1088/1757-899X/432/1/012007.

[30] Merrill A. Ritter, "Direct Compression Molded Polyethylene for Total Hip and Knee Replacements," *J. Bone Jt. Surgery-American Vol.*, vol. 82, no. 12, p. 1806, 2000, doi: 10.2106/00004623-200012000-00020.

[31] E. Reay, J. Wu, J. Holland, and D. Deehan, "Premature failure of Kinemax Plus total knee replacements," *J. Bone Jt. Surg. - Ser. B*, vol. 91, no. 5, pp. 604–611, 2009, doi: 10.1302/0301-620X.91B5.21525.

[32] A. M. Kandahari, X. Yang, K. A. Laroche, A. S. Dighe, D. Pan, and Q. Cui, "A review of UHMWPE wear-induced osteolysis: The role for early detection of the immune response," *Bone Research*, vol. 4. Sichuan University, Jul. 12, 2016, doi: 10.1038/boneres.2016.14.

[33] E. Ingham and J. Fisher, "Biological reactions to wear debris in total joint replacement," *Proc. Inst. Mech. Eng. Part H J. Eng. Med.*, vol. 214, no. 1, pp. 21–37, 2000, doi: 10.1243/0954411001535219.

[34] O. K. Muratoglu, E. S. Greenbaum, C. R. Bragdon, M. Jasty, A. A. Freiberg, and W. H. Harris, "Surface Analysis of Early Retrieved Acetabular Polyethylene Liners: A Comparison of Conventional and Highly Crosslinked Polyethylenes," *J. Arthroplasty*, vol. 19, no. 1, pp. 68–77, 2004, doi: 10.1016/j.arth.2003.08.003.

[35] A. A. Edidin, C. M. Rimnac, V. M. Goldberg, and S. M. Kurtz, "Mechanical behavior, wear surface morphology, and clinical performance of UHMWPE acetabular components after 10 years of implantation," 2001.

[36] D. J. Lombardo, M. P. Siljander, C. K. Gehrke, D. D. Moore, M. S. Karadsheh, and E. A. Baker, "Fretting and Corrosion Damage of Retrieved Dual-Mobility Total Hip Arthroplasty Systems," *J. Arthroplasty*, vol. 34, no. 6, pp. 1273–1278, Jun. 2019, doi: 10.1016/j.arth.2019.02.008.

[37] D. R. Bijukumar *et al.*, "Wear particles induce a new macrophage phenotype with the potential to accelerate material corrosion within total hip replacement interfaces," *Acta Biomater.*, vol. 101, pp. 586–597, Jan. 2020, doi: 10.1016/j.actbio.2019.10.039.

[38] S. Affatato, W. Leardini, and M. Zavalloni, "Hip Joint Simulators: State of the Art," in *Bioceramics and Alternative Bearings in Joint Arthroplasty*, 2006, pp. 171–180.

[39] J. Fisher *et al.*, "Wear of surface engineered metal-on-metal hip prostheses," *Mater. Med.*, vol. 5, pp. 225–235, 2004.

[40] S. M. Kurtz, *UHMWPE Biomaterials Handbook: Ultra High Molecular Weight Polyethylene in Total Joint Replacement and Medical Devices: Third Edition*. 2015.

[41] S. Kurtz, K. Ong, E. Lau, F. Mowat, and M. Halpern, "Projections of Primary and Revision Hip and Knee Arthroplasty in the United States from 2005 to 2030," pp. 780–785, 2007, doi: 10.2106/JBJS.F.00222.

[42] A. D. Toms, D. Davidson, B. A. Masri, C. P. Duncan, and H. C. P. Duncan, "The management of peri-prosthetic infection in total joint arthroplasty," *J Bone Jt. Surg [Br]*, vol. 88, no. 2, pp. 149–55, 2006, doi: 10.1302/0301-620X.88B2.

[43] American Joint Replacement Registry, "ANNUAL REPORT 2018." 2018.

[44] A. Laska, V. M. Archodoulaki, and B. Duscher, "Failure analysis of retrieved PE-UHMW acetabular liners," *J. Mech. Behav. Biomed. Mater.*, vol. 61, pp. 70–78, 2016, doi: 10.1016/j.jmbbm.2016.01.007.

[45] A. J. Peacock, *Handbook of Polyethylene Structures: Properties, and Applications*, vol. 7, no. 1. 2015.

[46] M. B. Turell and A. Bellare, "A study of the nanostructure and tensile properties of ultra-high molecular weight polyethylene," *Biomaterials*, vol. 25, no. 17, pp. 3389–3398, 2004, doi: 10.1016/j.biomaterials.2003.10.027.

[47] T. H. Lee, F. Y. C. Boey, and K. A. Khor, "On the determination of polymer crystallinity for a thermoplastic PPS composite by thermal analysis," *Compos. Sci. Technol.*, vol. 53, no. 3, pp. 259–274, 1995, doi: 10.1016/0266-3538(94)00070-0.

[48] N. C. Parasnis and K. Ramani, "Analysis of the effect of pressure on compression moulding of UHMWPE," *J. Mater. Sci. Mater. Med.*, vol. 9, no. 3, pp. 165–172, 1998, doi: 10.1023/A:1008871720389.

[49] A. A. Edidin, C. W. Jewett, A. Kalinowski, K. Kwarteng, and S. M. Kurtz, "Degradation of mechanical behavior in UHMWPE after natural and accelerated aging," *Biomaterials*, vol. 21, no. 14, pp. 1451–1460, 2000, doi: 10.1016/S0142-9612(00)00021-1.

[50] K. S. Kanaga Karuppiah *et al.*, "Friction and wear behavior of ultra-high molecular weight polyethylene as a function of polymer crystallinity," *Acta Biomater.*, vol. 4, no. 5, pp. 1401–1410, 2008, doi: 10.1016/j.actbio.2008.02.022.

[51] A. V. Maksimkin *et al.*, "Multilayer porous UHMWPE scaffolds for bone defects replacement," *Mater. Sci. Eng. C*, vol. 73, pp. 366–372, 2017, doi: 10.1016/j.msec.2016.12.104.

[52] Y. Khalil, N. Hopkinson, A. Kowalski, and J. P. A. Fairclough, "Characterisation of UHMWPE polymer powder for laser sintering," *Materials (Basel).*, vol. 12, no. 21, 2019, doi: 10.3390/ma12213496.

[53] P. Dong *et al.*, "Pursuit of the correlation between yield strength and crystallinity in sintering-molded UHMWPE," *Polymer (Guildf).*, vol. 215, no. December 2020, p. 123352, 2021, doi: 10.1016/j.polymer.2020.123352.

[54] T. R. Green, J. Fisher, M. Stone, B. M. Wroblewski, and E. Ingham, "Polyethylene particles of a 'critical size' are necessary for the induction of cytokines by macrophages in vitro," *Biomaterials*, vol. 19, no. 24, pp. 2297–2302, 1998, doi: 10.1016/S0142-9612(98)00140-9.

[55] O. K. Muratoglu *et al.*, "Unified wear model for highly crosslinked ultra-high molecular weight polyethylenes (UHMWPE)," *Biomaterials*, vol. 20, pp. 1463–1470, 1999.

[56] P. S. R. Sreekanth and S. Kanagaraj, "Influence of multi walled carbon nanotubes reinforcement and gamma irradiation on the wear behaviour of UHMWPE," *Wear*, vol. 334–335, pp. 82–90, 2015, doi: 10.1016/j.wear.2014.12.014.

[57] E. Oral, S. D. Christensen, A. S. Malhi, K. K. Wannomae, and O. K. Muratoglu, "Wear Resistance and Mechanical Properties of Highly Cross-linked, Ultrahigh-Molecular Weight Polyethylene Doped With Vitamin E," *J. Arthroplasty*, vol. 21, no. 4, pp. 580–591, 2006, doi: 10.1016/j.arth.2005.07.009.

[58] E. Oral and O. K. Muratoglu, "Vitamin E diffused, highly crosslinked UHMWPE: A review," *Int. Orthop.*, vol. 35, no. 2, pp. 215–223, 2011, doi: 10.1007/s00264-010-1161-y.

[59] E. Oral, K. K. Wannomae, N. Hawkins, W. H. Harris, and O. K. Muratoglu, "α-Tocopherol-doped irradiated UHMWPE for high fatigue resistance and low wear," *Biomaterials*, vol. 25, no. 24. pp. 5515–5522, 2004, doi: 10.1016/j.biomaterials.2003.12.048.

[60] B. R. Micheli, K. K. Wannomae, A. J. Lozynsky, S. D. Christensen, and O. K. Muratoglu, "Knee Simulator Wear of Vitamin E Stabilized Irradiated Ultrahigh Molecular Weight Polyethylene," *J. Arthroplasty*, vol. 27, no. 1, pp. 95–104, 2012, doi: 10.1016/j.arth.2011.03.006.

[61] R. Lerf, D. Zurbrügg, and D. Delfosse, "Use of vitamin E to protect cross-linked UHMWPE from oxidation," *Biomaterials*, vol. 31, no. 13, pp. 3643–3648, 2010, doi: 10.1016/j.biomaterials.2010.01.076.

[62] E. Oral, B. W. Ghali, S. L. Rowell, B. R. Micheli, A. J. Lozynsky, and O. K. Muratoglu, "A surface crosslinked UHMWPE stabilized by vitamin E with low wear and high fatigue strength," *Biomaterials*, vol. 31, no. 27, pp. 7051–7060, 2010, doi: 10.1016/j.biomaterials.2010.05.041.

[63] J. Fu, B. N. Doshi, E. Oral, and O. K. Muratoglu, "High temperature melted, radiation cross-linked, vitamin e stabilized oxidation resistant UHMWPE with low wear and high impact strength," *Polymer (Guildf).*, vol. 54, no. 1, pp. 199–209, 2013, doi: 10.1016/j.polymer.2012.11.017.

[64] S. Teramura, H. Sakoda, T. Terao, M. M. Endo, K. Fujiwara, and N. Tomita, "Reduction of wear volume from ultrahigh molecular weight polyethylene knee components by the addition of vitamin E," *J. Orthop. Res.*, vol. 26, no. 4, pp. 460–464, 2008, doi: 10.1002/jor.20514.

[65] C. Wolf, K. Lederer, and U. Müller, "Tests of biocompatibility of α-tocopherol with respect to the use as a stabilizer in ultrahigh molecular weight polyethylene for articulating surfaces in joint endoprostheses," *J. Mater. Sci. Mater. Med.*, vol. 13, no. 7, pp. 701–705, 2002, doi: 10.1023/A:1015750112343.

[66] P. K. Chu, J. Y. Chen, L. P. Wang, and N. Huang, "Plasma-surface modification of biomaterials," *Mater. Sci. Eng. R Reports*, vol. 36, no. 5–6, pp. 143–206, 2002, doi: 10.1016/S0927-796X(02)00004-9.

[67] K. Balani *et al.*, "Plasma-sprayed carbon nanotube reinforced hydroxyapatite coatings and their interaction with human osteoblasts in vitro," *Biomaterials*, vol. 28, no. 4, pp. 618–624, 2007, doi: 10.1016/j.biomaterials.2006.09.013.

[68] D. Firouzi *et al.*, "A new technique to improve the mechanical and biological performance of ultra high molecular weight polyethylene using a nylon coating," *J. Mech. Behav. Biomed. Mater.*, vol. 32, pp. 198–209, 2014, doi: 10.1016/j.jmbbm.2014.01.001.

[69] S. Calderon V, A. Cavaleiro, and S. Carvalho, "Chemical and structural characterization of Zr-C-N-Ag coatings: XPS, XRD and Raman spectroscopy," *Appl. Surf. Sci.*, vol. 346, pp. 240–247, 2015, doi: 10.1016/j.apsusc.2015.03.161.

[70] J. A. Puértolas *et al.*, "Improved wear performance of ultra high molecular weight polyethylene coated with hydrogenated diamond like carbon," *Wear*, vol. 269, no. 5–6, pp. 458–465, 2010, doi: 10.1016/j.wear.2010.04.033.

[71] F. Ruan and L. Bao, "Mechanical enhancement of UHMWPE fibers by coating with carbon nanoparticles," *Fibers Polym.*, vol. 15, no. 4, pp. 723–728, 2014, doi: 10.1007/s12221-014-0723-9.

[72] H. Dong and T. Bell, "State-of-the-art overview: Ion beam surface modification of polymers towards improving tribological properties," *Surf. Coatings Technol.*, vol. 111, no. 1, pp. 29–40, 1999, doi: 10.1016/S0257-8972(98)00698-7.

[73] R. C. Powles, D. R. McKenzie, S. J. Meure, M. V. Swain, and N. L. James, "Nanoindentation response of PEEK modified by mesh-assisted plasma immersion ion implantation," *Surf. Coatings Technol.*, vol. 201, no. 18, pp. 7961–7969, 2007, doi: 10.1016/j.surfcoat.2007.03.030.

[74] W. Shi, X. Y. Li, and H. Dong, "Improved wear resistance of ultra-high molecular weight polyethylene by plasma immersion ion implantation," *Wear*, vol. 250–251, no. PART 1, pp. 544–552, 2001, doi: 10.1016/S0043-1648(01)00636-6.

[75] H. Ito, K. Kaneda, T. Yuhta, I. Nishimura, K. Yasuda, and T. Matsuno, "Reduction of polyethylene wear by concave dimples on the frictional surface in artificial hip joints," *J. Arthroplasty*, vol. 15, no. 3, pp. 332–338, 2000, doi: 10.1016/S0883-5403(00)90670-3.

[76] A. López-Cervantes, I. Domínguez-López, J. D. O. Barceinas-Sánchez, and A. L. García-García, "Effects of surface texturing on the performance of biocompatible UHMWPE as a bearing material during in vitro lubricated sliding/rolling motion," *J. Mech. Behav. Biomed. Mater.*, vol. 20, pp. 45–53, 2013, doi: 10.1016/j.jmbbm.2012.12.010.

[77] X. Wang, J. Wang, B. Zhang, and W. Huang, "Design principles for the area density of dimple patterns," *Proc. Inst. Mech. Eng. Part J J. Eng. Tribol.*, vol. 229, no. 4, pp. 538–546, 2015, doi: 10.1177/1350650114531939.

[78] A. Wang, R. Lin, C. Stark, and J. H. Dumbleton, "Suitability and limitations of carbon fiber reinforced PEEK composites as bearing surfaces for total joint replacements," *Wear*, vol. 225–229, no. PART II, pp. 724–727, 1999, doi: 10.1016/S0043-1648(99)00026-5.

[79] U. G. M. C. Galetz, T. Blab, H. Ruckdaschel, J. K. W. Sandler, V. Altstadt, "Carbon Nanofibre-Reinforced Ultrahigh Molecular Weight Polyethylene for Tribological Applications," *J. Appl. Polym. Sci.*, vol. 116, no. 5, pp. 2658–2667, 2010, doi: 10.1002/app.

[80] X. Dangsheng, "Friction and wear properties of UHMWPE composites reinforced with carbon fiber," *Mater. Lett.*, vol. 59, no. 2–3, pp. 175–179, 2005, doi: 10.1016/j.matlet.2004.09.011.

[81] G. Sui, W. H. Zhong, X. Ren, X. Q. Wang, and X. P. Yang, "Structure, mechanical properties and friction behavior of UHMWPE/HDPE/carbon nanofibers," *Mater. Chem. Phys.*, vol. 115, no. 1, pp. 404–412, 2009, doi: 10.1016/j.matchemphys.2008.12.016.

[82] A. Borruto, "A new material for hip prosthesis without considerable debris release," *Med. Eng. Phys.*, vol. 32, no. 8, pp. 908–913, 2010, doi: 10.1016/j.medengphy.2010.06.007.

[83] S. Utzschneider *et al.*, "Inflammatory response against different carbon fiber-reinforced PEEK wear particles compared with UHMWPE in vivo," *Acta Biomater.*, vol. 6, no. 11, pp. 4296–4304, 2010, doi: 10.1016/j.actbio.2010.06.002.

[84] W. J. Wood, R. G. Maguire, and W. H. Zhong, "Improved wear and mechanical properties of UHMWPE-carbon nanofiber composites through an optimized paraffin-assisted melt-mixing process," *Compos. Part B Eng.*, vol. 42, no. 3, pp. 584–591, 2011, doi: 10.1016/j.compositesb.2010.09.006.

[85] S. Xu *et al.*, "Wear and friction of carbon nanofiber-reinforced HDPE composites," *J. Tribol.*, vol. 134, no. 4, pp. 1–7, 2012, doi: 10.1115/1.4007016.

[86] S. V. Panin, L. A. Kornienko, V. O. Alexenko, D. G. Buslovich, S. A. Bochkareva, and B. A. Lyukshin, "Increasing wear resistance of UHMWPE by loading enforcing carbon fibers: Effect of irreversible and elastic deformation, friction heating, and filler size," *Materials (Basel).*, vol. 13, no. 2, Jan. 2020, doi: 10.3390/ma13020338.

[87] C. Lee, X. Wei, J. W. Kysar, and J. Hone, "of Monolayer Graphene," *Science (80-.).*, vol. 321, no. July, pp. 385–388, 2008.

[88] Y. Chen, Y. Qi, Z. Tai, X. Yan, F. Zhu, and Q. Xue, "Preparation, mechanical properties and biocompatibility of graphene oxide/ultrahigh molecular weight polyethylene composites," *Eur. Polym. J.*, vol. 48, no. 6, pp. 1026–1033, 2012, doi: 10.1016/j.eurpolymj.2012.03.011.

[89] D. Lahiri, F. Hec, M. Thiesse, A. Durygin, C. Zhang, and A. Agarwal, "Nanotribological behavior of graphene nanoplatelet reinforced ultra high molecular weight polyethylene composites," *Tribol. Int.*, vol. 70, pp. 165–169, 2014, doi: 10.1016/j.triboint.2013.10.012.

[90] P. G. Ren, Y. Y. Di, Q. Zhang, L. Li, H. Pang, and Z. M. Li, "Composites of ultrahigh-molecular-weight polyethylene with graphene sheets and/or MWCNTs with segregated network structure: Preparation and properties," *Macromol. Mater. Eng.*, vol. 297, no. 5, pp. 437–443, 2012, doi: 10.1002/mame.201100229.

[91] X. L. Xie, C. Y. Tang, K. Y. Y. Chan, X. C. Wu, C. P. Tsui, and C. Y. Cheung, "Wear performance of ultrahigh molecular weight polyethylene/quartz composites," *Biomaterials*, vol. 24, no. 11, pp. 1889–1896, 2003, doi: 10.1016/S0142-9612(02)00610-5.

[92] Q. Wang, D. Zhang, and S. Ge, "Biotribological behaviour of ultra-high molecular weight polyethylene composites containing Ti in a hip joint simulator," *Proc. Inst. Mech. Eng. Part J J. Eng. Tribol.*, vol. 221, no. 3, pp. 307–313, 2007, doi: 10.1243/13506501JET232.

[93] K. Plumlee and C. J. Schwartz, "Improved wear resistance of orthopaedic UHMWPE by reinforcement with zirconium particles," *Wear*, vol. 267, no. 5–8, pp. 710–717, 2009, doi: 10.1016/j.wear.2008.11.028.

[94] J. long LIU, Y. yuan ZHU, Q. liang WANG, and S. rong GE, "Biotribological behavior of ultra high molecular weight polyethylene composites containing bovine bone hydroxyapatite," *J. China Univ. Min. Technol.*, vol. 18, no. 4, pp. 606–612, 2008, doi: 10.1016/S1006-1266(08)60303-X.

[95] S. Ge, S. Wang, and X. Huang, "Increasing the wear resistance of UHMWPE acetabular cups by adding natural biocompatible particles," vol. 267, pp. 770–776, 2009, doi: 10.1016/j.wear.2009.01.057.

[96] S. L. Ruan, P. Gao, X. G. Yang, and T. X. Yu, "Toughening high performance ultrahigh molecular weight polyethylene using multiwalled carbon nanotubes," *Polymer (Guildf).*, vol. 44, no. 19, pp. 5643–5654, 2003, doi: 10.1016/S0032-3861(03)00628-1.

[97] Y. S. Zoo, J. W. An, D. P. Lim, and D. S. Lim, "Effect of carbon nanotube addition on tribological behavior of UHMWPE," *Tribol. Lett.*, vol. 16, no. 4, pp. 305–309, 2004, doi: 10.1023/B:TRIL.0000015206.21688.87.

[98] S. Kanagaraj, F. R. Varanda, T. V. Zhil'tsova, M. S. A. Oliveira, and J. A. O. Simões, "Mechanical properties of high density polyethylene/carbon nanotube composites," *Compos. Sci. Technol.*, vol. 67, no. 15–16, pp. 3071–3077, 2007, doi: 10.1016/j.compscitech.2007.04.024.

[99] S. Kanagaraj, M. T. Mathew, A. Fonseca, M. S. A. Oliveira, J. A. O. Simões, and L. A. Rocha, "Tribological characterisation of carbon nanotubes/ultrahigh molecular weight polyethylene composites: The effect of sliding distance," *Int. J. Surf. Sci. Eng.*, vol. 4, no. 4–6, pp. 305–321, 2010, doi: 10.1504/IJSURFSE.2010.035138.

[100] H. I. B. Meschi Amoli, S. A. Ahmad Ramazani, "Preparation of ultrahigh-molecular-weight polyethylene/carbon nanotube nanocomposites with a Ziegler–Natta catalytic system and investigation of their thermal and mechanical properties," *J. Appl. Polym. Sci.*, vol. 116, no. 5, pp. 2658–2667, 2012, doi: https://doi.org/10.1002/app.36368.

[101] Y. Liu and S. K. Sinha, "Wear performances and wear mechanism study of bulk UHMWPE composites with nacre and CNT fillers and PFPE overcoat," *Wear*, vol. 300, no. 1–2, pp. 44–54, 2013, doi: 10.1016/j.wear.2013.01.102.

[102] M. J. Martínez-Morlanes, P. Castell, P. J. Alonso, M. T. Martinez, and J. A. Puértolas, "Multi-walled carbon nanotubes acting as free radical scavengers in gamma-irradiated ultrahigh molecular weight polyethylene composites," *Carbon N. Y.*, vol. 50, no. 7, pp. 2442–2452, 2012, doi: 10.1016/j.carbon.2012.01.066.

[103] S. Ruan, P. Gao, and T. X. Yu, "Ultra-strong gel-spun UHMWPE fibers reinforced using multiwalled carbon nanotubes," *Polymer (Guildf).*, vol. 47, no. 5, pp. 1604–1611, 2006, doi: 10.1016/j.polymer.2006.01.020.

[104] A. Sobajima *et al.*, "Multiwall Carbon Nanotube Composites as Artificial Joint Materials," *ACS Biomater. Sci. Eng.*, vol. 6, no. 12, pp. 7032–7040, 2020, doi: 10.1021/acsbiomaterials.0c00916.

[105] S. Iijima, P. M. Ajayan, and T. Ichihashi, "Growth model for carbon nanotubes," *Phys. Rev. Lett.*, vol. 69, no. 21, pp. 3100–3103, 1992, doi: 10.1103/PhysRevLett.69.3100.

[106] M. Endo *et al.*, "Comparison study of semi-crystalline and highly crystalline multiwalled carbon nanotubes," *Appl. Phys. Lett.*, vol. 79, no. 10, pp. 1531–1533, 2001, doi: 10.1063/1.1400774.

[107] L. G. Zhou and S. Q. Shi, "Formation energy of Stone-Wales defects in carbon nanotubes," *Appl. Phys. Lett.*, vol. 83, no. 6, pp. 1222–1224, 2003, doi: https://doi.org/10.1063/1.1599961.

[108] N. Chakrapani, S. Curran, B. Wei, P. M. Ajayan, A. Carrillo, and R. S. Kane, "Spectral fingerprinting of structural defects in plasma-treated carbon nanotubes," *J. Mater. Res.*, vol. 18, no. 10, pp. 2515–2521, 2003, doi: 10.1557/JMR.2003.0350.

[109] B. Smith *et al.*, "Colloidal properties of aqueous suspensions of acid-treated, multi-walled carbon nanotubes," *Environ. Sci. Technol.*, vol. 43, no. 3, pp. 819–825, 2009, doi: 10.1021/es802011e.

[110] H. D. W. Carole A Coopera, Diana Ravicha, David Lipsb, Joerg Mayerb, "Distribution and alignment of carbon nanotubes and nanofibrils.PDF," *Compos. Sci. Technol.*, vol. 62, pp. 1105–1112, 2002.

[111] C. G. Hu, W. L. Wang, S. X. Wang, W. Zhu, and Y. Li, "Investigation on electrochemical properties of carbon nanotubes," *Diam. Relat. Mater.*, vol. 12, no. 8, pp. 1295–1299, 2003, doi: 10.1016/S0925-9635(03)00071-2.

[112] P. C. P. Watts, P. K. Fearon, W. K. Hsu, N. C. Billingham, H. W. Kroto, and D. R. M. Walton, "Carbon nanotubes as polymer antioxidants," *J. Mater. Chem.*, vol. 13, no. 3, pp. 491–495, 2003, doi: 10.1039/b211328g.

[113] A. V. Krasheninnikov and K. Nordlund, "Irradiation effects in carbon nanotubes," *Nucl. Instruments Methods Phys. Res. Sect. B Beam Interact. with Mater. Atoms*, vol. 216, no. 1–4, pp. 355–366, 2004, doi: 10.1016/j.nimb.2003.11.061.

[114] R. M. Lucente-schultz *et al.*, "Antioxidant Single-Walled Carbon Nanotubes," no. 9, pp. 3934–3941, 2009, doi: 10.1155/JBB/2006/31372.(32).

[115] J. Wallace, D. Chen, and L. Shao, "Irradiation-enhanced torsional buckling capacity of carbon nanotube bundles," *J. Appl. Phys.*, vol. 128, no. 19, 2020, doi: 10.1063/5.0013229.

[116] M. Sammalkorpi, A. Krasheninnikov, A. Kuronen, K. Nordlund, and K. Kaski, "Mechanical properties of carbon nanotubes with vacancies and related defects," *Phys. Rev. B - Condens. Matter Mater. Phys.*, vol. 70, no. 24, pp. 1–8, 2004, doi: 10.1103/PhysRevB.70.245416.

[117] U. Ritter *et al.*, "Radiation damage and Raman vibrational modes of single-walled carbon nanotubes," *Chem. Phys. Lett.*, vol. 447, no. 4–6, pp. 252–256, 2007, doi: 10.1016/j.cplett.2007.09.010.

[118] E. B. Zeynalov and J. F. Friedrich, "Antioxidative Activity of Carbon Nanotube and Nanofiber," *Open Mater. Sci. J.*, vol. 2, no. 1, pp. 28–34, 2008, doi: 10.2174/1874088x00802010028.

[119] A. Galano, "Carbon nanotubes: Promising agents against free radicals," *Nanoscale*, vol. 2, no. 3, pp. 373–380, 2010, doi: 10.1039/b9nr00364a.

[120] P. S. R. Sreekanth, N. N. Kumar, and S. Kanagaraj, "Effect of MWCNT on mechanical properties of γ-irradiated UHMWPE during shelf ageing process," *Adv. Mater. Res.*, vol. 410, pp. 160–163, 2012, doi: 10.4028/www.scientific.net/AMR.410.160.

[121] C. A. Poland *et al.*, "Carbon nanotubes introduced into the abdominal cavity of mice show asbestos-like pathogenicity in a pilot study," *Nat. Nanotechnol.*, vol. 3, no. 7, pp. 423–428, 2008, doi: 10.1038/nnano.2008.111.

[122] A. Bianco and M. Prato, "Can Carbon Nanotubes Be Considered Useful Tools for Biological Applications?," *Adv. Mater.*, vol. 15, no. 20, pp. 1765–1768, 2003, doi: 10.1002/adma.200301646.

[123] C. W. Lam, J. T. James, R. McCluskey, and R. L. Hunter, "Pulmonary toxicity of single-wall carbon nanotubes in mice 7 and 90 days after intractracheal instillation," *Toxicol. Sci.*, vol. 77, no. 1, pp. 126–134, 2004, doi: 10.1093/toxsci/kfg243.

[124] S. Koyama *et al.*, "Role of systemic T-cells and histopathological aspects after subcutaneous implantation of various carbon nanotubes in mice," *Carbon N. Y.*, vol. 44, no. 6, pp. 1079–1092, 2006, doi: 10.1016/j.carbon.2005.08.006.

[125] S. T. Yang *et al.*, "Long-term accumulation and low toxicity of single-walled carbon nanotubes in intravenously exposed mice," *Toxicol. Lett.*, vol. 181, no. 3, pp. 182–189, 2008, doi: 10.1016/j.toxlet.2008.07.020.

[126] P. Cherukuri *et al.*, "Mammalian pharmacokinetics of carbon nanotubes using intrinsic near-infrared fluorescence," *Proc. Natl. Acad. Sci. U. S. A.*, vol. 103, no. 50, pp. 18882–18886, 2006, doi: 10.1073/pnas.0609265103.

[127] Y. Sato *et al.*, "Influence of length on cytotoxicity of multi-walled carbon nanotubes against human acute monocytic leukemia cell line THP-1 in vitro and subcutaneous tissue of rats in vivo," *Mol. Biosyst.*, vol. 1, no. 2, pp. 176–182, 2005, doi: 10.1039/b502429c.

[128] A. Nel, T. Xia, L. Mädler, and N. Li, "Toxic potential of materials at the nanolevel," *Science (80-.).*, vol. 311, no. 5761, pp. 622–627, 2006, doi: 10.1126/science.1114397.

[129] J. Reis *et al.*, "In vitro studies of multiwalled carbon nanotube/ultrahigh molecular weight polyethylene nanocomposites with osteoblast-like MG63 cells," *Brazilian J. Med. Biol. Res.*, vol. 43, no. 5, pp. 476–482, 2010, doi: 10.1590/S0100-879X2010007500038.

[130] R. Ormsby, T. McNally, P. O'Hare, G. Burke, C. Mitchell, and N. Dunne, "Fatigue and biocompatibility properties of a poly(methyl methacrylate) bone cement with multi-walled carbon nanotubes," *Acta Biomater.*, vol. 8, no. 3, pp. 1201–1212, 2012, doi: 10.1016/j.actbio.2011.10.010.

[131] L. Lacerda, A. Bianco, M. Prato, and K. Kostarelos, "Carbon nanotubes as nanomedicines: From toxicology to pharmacology," *Adv. Drug Deliv. Rev.*, vol. 58, no. 14, pp. 1460–1470, 2006, doi: 10.1016/j.addr.2006.09.015.

[132] H. A. Mckellop and I. C. Clarke, "Degradation and Wear of Ultra-HighMolecular-Weight Polyethylene," *Corros. Degrad. Implant Mater.*, vol. Second Sym, pp. 351–368, 1985.

[133] V. Saikko, T. Eli, T. Eli, and T. Eli, "A simulator study of friction in total replacement hip joints," *Proc Instn Mech Engrs*, vol. 206, pp. 201–211, 1992.

[134] V. Saikko, "A three-axis hip joint simulator for wear and friction studies on total hip prostheses," *Proc Instn Mech Engrs*, vol. 210, 2015.

[135] U. T. O. C. Mejia, "A HIP WEAR SIMULATOR FOR THE EVALUATION OF BIOMATERIALS IN HIP ARTHROPLASTY COMPONENTS," *Biomed. Mater. Eng.*, vol. 4, no. 4, pp. 259–271, 1994.

[136] V. Saikko, "A 12-station anatomic hip joint simulator," *J. Eng. Med.*, vol. 219, pp. 437–448, 2015, doi: 10.1243/095441105X34419.

[137] A. Essner, K. Sutton, and A. Wang, "Hip simulator wear comparison of metal-on-metal , ceramic-on-ceramic and crosslinked UHMWPE bearings," *Wear*, vol. 259, pp. 992–995, 2018, doi: 10.1016/j.wear.2005.02.104.

[138] S. Affatato, M. Spinelli, S. Squarzoni, F. Traina, and A. Toni, "Mixing and matching in ceramic-on-metal hip arthroplasty : An in-vitro hip simulator study," *J. Biomech.*, vol. 42, no. 15, pp. 2439–2446, 2009, doi: 10.1016/j.jbiomech.2009.07.031.

[139] N. Shahemi, S. Liza, A. A. Abbas, and A. M. Merican, "Long-term wear failure analysis of uhmwpe acetabular cup in total hip replacement," *J. Mech. Behav. Biomed. Mater.*, vol. 87, no. July, pp. 1–9, 2018, doi: 10.1016/j.jmbbm.2018.07.017.

[140] V. Saikko and O. Calonius, "Slide track analysis of the relative motion between femoral head and acetabular cup in walking and in hip simulators," *J. Biomech.*, vol. 35, pp. 455–464, 2002.

[141] P. E. Paré, F. W. Chan, S. Bhattacharya, and V. K. Goel, "Surface slide track mapping of implants for total disc arthroplasty," *J. Biomech.*, vol. 42, no. 2, pp. 131–139, 2009, doi: 10.1016/j.jbiomech.2008.10.025.

[142] S. Affatato, F. Traina, and A. Toni, "Microseparation and stripe wear in alumina-on-alumina hip implants," *Int. J. Artif. Organs*, vol. 34, no. 6, pp. 506–512, 2011, doi: 10.5301/IJAO.2011.8457.

[143] I. C. Clarke, V. Good, L. Anissian, and A. Gustafson, "Charnley wear model for validation of hip simulatorsball diameter versus polytetrafluoroethylene and polyethylene wear," *Proc. Inst. Mech. Eng. Part H J. Eng. Med.*, vol. 211, no. 1, pp. 25–36, 1997, doi: 10.1243/0954411971534656.

[144] C. R. Bragdon, M. Jasty, O. K. Muratoglu, D. O. O. Connor, and W. H. Harris, "Third-Body Wear of Highly Cross-Linked Polyethylene in a Hip Simulator," *J. Arthroplasty*, vol. 18, no. 5, pp. 553–561, 2003, doi: 10.1016/S0883-5403(03)00146-3.

[145] V. Saikko, T. Ahlroos, O. Calonius, and J. Kera, "Wear simulation of total hip prostheses with polyethylene against CoCr , alumina and diamond-like carbon," *Biomaterials*, vol. 22, pp. 1507–1514, 2001.

[146] V. Saikko, "A 12-station anatomic hip joint simulator," *Proc. Inst. Mech. Eng. Part H J. Eng. Med.*, vol. 219, no. 6, pp. 437–448, 2005, doi: 10.1243/095441105X34419.

[147] S. L. Smith and A. Unsworth, "A ve-station hip joint simulator," vol. 215, pp. 61–64.

[148] N. I. Galanis and D. E. Manolakos, "Design of a hip joint simulator according to the ISO 14242," *Proc. World Congr. Eng. 2011, WCE 2011*, vol. 3, pp. 2088–2093, 2011.

[149] P. S. M. Barbour, M. H. Stone, and J. Fisher, "A hip joint simulator study using new and physiologically scratched femoral heads with ultra-high molecular weight polyethylene acetabular cups," *Proc. Inst. Mech. Eng. Part H J. Eng. Med.*, vol. 214, no. 6, pp. 569–576, 2000, doi: 10.1243/0954411001535598.

[150] J. B. Medley, J. J. Krygier, J. D. Bobyn, F. W. Chan, A. Lippincott, and M. Tanzer, "Kinematics of the MATCO™ hip simulator and issues related to wear testing of metal-metal implants," *Proc. Inst. Mech. Eng. Part H J. Eng. Med.*, vol. 211, no. 1, pp. 89–98, 1997, doi: 10.1243/0954411971534719.

[151] C. Kaddick and M. A. Wimmer, "Hip simulator wear testing according to the newly introduced standard ISO 14242," *J. Biomech.*, vol. 34, no. SUPPL. 1, pp. 429–442, 2001, doi: 10.1016/s0021-9290(04)00168-x.

[152] M. Alvarez-Vera, J. A. Ortega-Saenz, and M. A. L. Hernandez-Rodríguez, "A study of the wear performance in a hip simulator of a metal-metal Co-Cr alloy with different boron additions," *Wear*, vol. 301, no. 1–2, pp. 175–181, 2013, doi: 10.1016/j.wear.2013.01.085.

[153] "ISO/TR-9325. Implants for surgery—Partial and total hip joint prostheses. Recommendations for simulators for evaluation of hip joint prostheses." (accessed Jan. 08, 2020).

[154] "ASTM-F1714. Standard Guide for Gravimetric Wear Assessment of Prosthetic Hip-Designs in Simulator Devices." ASTM- (accessed Jan. 08, 2020).

[155] M. Viceconti, G. Cavallotti, A. O. Andrisano, and A. Toni, "Discussion on the design of a hip joint simulator," *Med. Eng. Phys.*, vol. 18, no. 3, pp. 234–240, 1996, doi: 10.1016/1350-4533(95)00026-7.

[156] I. C. Clarke, S. Johnson, W. Phipatanakul, and V. Good, "Effects of hip-loading input on simulated wear of Al2O3-PTFE materials," *Wear*, vol. 250–251, no. PART 1, pp. 159–166, 2001, doi: 10.1016/S0043-1648(01)00618-4.

[157] I. Standard, "INTERNATIONAL STANDARD," *ISO 14242-1* vol. 2002. 2002.

[158] I. Standard, "INTERNATIONAL STANDARD," *ISO 14242-3*, vol. 2009. 2009.

[159] S. S. Brown and I. C. Clarke, "A review of lubrication conditions for wear simulation in artificial hip replacements," *Tribol. Trans.*, vol. 49, no. 1, pp. 72–78, 2006, doi: 10.1080/05698190500519223.

[160] V. Saikko, "Effect of lubricant protein concentration on the wear of ultra-high molecular weight polyethylene sliding against a CoCr counterface," *J. Tribol.*, vol. 125, no. 3, pp. 638–642, 2003, doi: 10.1115/1.1537751.

[161] A. M. Smith, L. Fleming, U. Wudebwe, J. Bowen, and L. M. Grover, "Development of a synovial fluid analogue with bio-relevant rheology for wear testing of orthopaedic implants," *J. Mech. Behav. Biomed. Mater.*, vol. 32, pp. 177–184, 2014, doi: 10.1016/j.jmbbm.2013.12.009.

[162] S. Affatato, M. Spinelli, M. Zavalloni, C. Mazzega-Fabbro, and M. Viceconti, "Tribology and total hip joint replacement: Current concepts in mechanical simulation," *Med. Eng. Phys.*, vol. 30, no. 10, pp. 1305–1317, 2008, doi: 10.1016/j.medengphy.2008.07.006.

[163] M. Xie and H. Li, "Viscosity reduction and disentanglement in ultrahigh molecular weight polyethylene melt: Effect of blending with polypropylene and poly(ethylene glycol)," *Eur. Polym. J.*, vol. 43, no. 8, pp. 3480–3487, 2007, doi: 10.1016/j.eurpolymj.2007.05.016.

[164] Y. M. Li, Y. Wang, L. Bai, H. L. Z. Zhou, W. Yang, and M. B. Yang, "Dynamic rheological behavior of HDPE/UHMWPE blends," *J. Macromol. Sci. Part B Phys.*, vol. 50, no. 7, pp. 1249–1259, 2011, doi: 10.1080/00222348.2010.503167.

[165] A. E. Brink, K. J. Jordens, and J. S. Riffle, "Sintering high performance semicrystalline polymeric powders," *Polym. Eng. Sci.*, vol. 35, no. 24, pp. 1923–1930, 1995, doi: 10.1002/pen.760352403.

[166] ASTM standards, "D792 – 13: Standard Test Methods for Density and Specific Gravity (Relative Density) of Plastics by Displacement," *ASTM Int.*, vol. 15, no. 3, pp. 145–149, 2013, doi: 10.1520/D0792-13.2.

[167] ASTM E384 - 17, "Standard Test Method for Microindentation Hardness of Materials," *ASTM Int.*, pp. 1–40, 2017, doi: 10.1520/E0384-17.

[168] E. I. Materials, C. B. Manufacturing, D. Hardness, and C. Laboratories, "Standard Test Method for Rubber Property — Durometer Hardness 1 This standard is for EDUCATIONAL USE ONLY .," vol. 05, no. Reapproved, pp. 1–13, 2010, doi: 10.1520/D2240-05R10.2.

[169] P. Specimens, "Compressive Properties of Rigid Plastics 1," *Annu. B. ASTM Stand.*, vol. i, pp. 1–8, 2008, doi: 10.1520/D0695-15.2.

[170] E3-95, "Standard Practice for Preparation of Metallographic Specimens," *ASTM Int.*, vol. 82, no. C, pp. 1–15, 2016, doi: 10.1520/D0638-14.1.

[171] C. Boon Peng, M. A. Hazizan, and M. N. Ramdziah Bt, "The effect of zeolite on the crystallization behaviour and tribological properties of UHMWPE composite," *Adv. Mater. Res.*, vol. 812, no. May 2014, pp. 100–106, 2013, doi: 10.4028/www.scientific.net/AMR.812.100.

[172] A. E. Brink, K. J. Jordens, and J. S. Riffle, "Sintering high performance semicrystalline polymeric powders," *Polym. Eng. Sci.*, vol. 35, no. 24, pp. 1923–1930, 1995, doi: 10.1002/pen.760352403.

[173] Y. C. Chang, T. H. Hung, H. M. Chen, J. C. Huang, T. G. Nieh, and C. J. Lee, "Viscous flow behavior and thermal properties of bulk amorphous Mg58Cu31Y11 alloy," *Intermetallics*, vol. 15, no. 10, pp. 1303–1308, 2007, doi: 10.1016/j.intermet.2007.03.012.

[174] S. Hambir and J. P. Jog, "Sintering of ultra high molecular weight polyethylene," *Bull. Mater. Sci.*, vol. 23, no. 3, pp. 221–226, 2000, doi: 10.1007/BF02719914.

[175] R. M. Gul and F. J. Mcgarry, "Processing of ultra-high molecular weight polyethylene by hot isostatic pressing, and the effect of processing parameters on its microstructure," *Polym. Eng. Sci.*, vol. 44, no. 10, pp. 1848–1857, 2004, doi: 10.1002/pen.20186.

[176] E. S. Greenbaum, B. B. Burroughs, W. H. Harris, and O. K. Muratoglu, "Effect of lipid absorption on wear and compressive properties of unirradiated and highly crosslinked UHMWPE: An in vitro experimental model," *Biomaterials*, vol. 25, no. 18, pp. 4479–4484, 2004, doi: 10.1016/j.biomaterials.2003.11.049.

[177] Esumi K, Ishigami M, Nakajima A, Sawada K, and Honda H, "Chemical treatment of carbon nanotubes," *Carbon N. Y.*, vol. 34, pp. 279–281, 1996.

[178] Y. Kong and J. N. Hay, "The measurement of the crystallinity of polymers by DSC," *Polymer (Guildf).*, vol. 43, no. 14, pp. 3873–3878, 2002, doi: 10.1016/S0032-3861(02)00235-5.

[179] S. Naskar, A. K. Panda, A. Jana, S. Kanagaraj, and B. Basu, "UHMWPE-MWCNT-nHA based hybrid trilayer nanobiocomposite: Processing approach, physical properties, stem/bone cell functionality, and blood compatibility," *J. Biomed. Mater. Res. - Part B Appl. Biomater.*, vol. 108, no. 5, pp. 2320–2343, 2020, doi: 10.1002/jbm.b.34567.

[180] S. Kanagaraj, F. R. Varanda, T. V. Zhil'tsova, M. S. A. Oliveira, and J. A. O. Simões, "Mechanical properties of high density polyethylene/carbon nanotube composites," *Compos. Sci. Technol.*, vol. 67, no. 15–16, pp. 3071–3077, Dec. 2007, doi: 10.1016/j.compscitech.2007.04.024.

[181] S. Jana, Ashirbad; Senthilvelan, Selvaraj, Kanagaraj, "A novel technique for the development of acetabular cup by cold isostatic compaction and sintering of UHMWPE powder with optimized processing parameters," *J. Pol. Engg. Sci.*, no. August, pp. 1–21, 2021, doi: 10.1002/pen.25779.

[182] U. S. Patent, I. J. Schryver, and D. M. Ryan, "United States Patent (19)," no. 19, 1992.

[183] V. M. Litvinov, J. Xu, C. Melian, D. E. Demco, M. Möller, and J. Simmelink, "Morphology, chain dynamics, and domain sizes in highly drawn gel-spun ultrahigh molecular weight polyethylene fibers at the final stages of drawing by SAXS, WAXS, and 1H Solid-State NMR," *Macromolecules*, vol. 44, no. 23, pp. 9254–9266, 2011, doi: 10.1021/ma201888f.

[184] A. P. D. Elfick, R. M. Hall, L. M. Pinder, and A. Unsworth, "The influence of femoral head surface roughness on the wear of ultrahigh molecular weight polyethylene sockets in cementless total hip replacement," *J. Biomed. Mater. Res.*, vol. 48, no. 5, pp. 712–718, 1999, doi: 10.1002/(SICI)1097-4636(1999)48:5<712::AID-JBM17>3.0.CO;2-R.

[185] Y. S. Kang, C. H. Hager, and R. D. Evans, "Effects of skewed surface textures on lubricant film thickness and traction," *Tribol. Trans.*, vol. 58, no. 3, pp. 397–406, 2015, doi: 10.1080/10402004.2014.980592.

[186] P. Damm, A. Bender, V. Waldheim, T. Winkler, and G. N. Duda, "Surgical cup placement affects the heating up of total joint hip replacements," *Sci. Rep.*, vol. 11, no. 1, pp. 1–11, 2021, doi: 10.1038/s41598-021-95387-8.

[187] T. B. Goudoulas, E. G. Kastrinakis, S. G. Nychas, L. G. Papazoglou, G. M. Kazakos, and P. V. Kosmas, "Rheological study of synovial fluid obtained from dogs: Healthy, pathological, and post-surgery, after spontaneous rupture of cranial cruciate ligament," *Ann. Biomed. Eng.*, vol. 38, no. 1, pp. 57–65, 2010, doi: 10.1007/s10439-009-9832-9.

[188] A. Wang, V. K. Polineni, C. Stark, and J. H. Dumbleton, "Effect of femoral head surface roughness on the wear of ultrahigh molecular weight polyethylene acetabular cups," *J. Arthroplasty*, vol. 13, no. 6, pp. 615–620, 1998, doi: 10.1016/S0883-5403(98)80002-8.

[189] J. M. Brandt, K. D. J. Charron, S. J. MacDonald, and J. B. Medley, "Mass gain behaviour of tibial polyethylene inserts during soak testing," *Proc. Inst. Mech. Eng. Part H J. Eng. Med.*, vol. 225, no. 3, pp. 324–331, 2011, doi: 10.1177/2041303310392629.

[190] ISO 14242-2, "International Standard International Standard," *61010-1 © Iec2001*, vol. 2003, p. 13, 2003.

[191] ASTM, "F732-00(2006) Standard test method for wear testing of polymeric materials used in total joint prostheses," *Astm*, vol. i, pp. 1–10, 2006, doi: 10.1520/F0732-17.ization.

[192] B. Sahoo, D. Narsimhachary, and J. Paul, "Surface mechanical and self-lubricating properties of MWCNT impregnated aluminium surfaces," *Surf. Eng.*, vol. 35, no. 11, pp. 970–981, 2019, doi: 10.1080/02670844.2019.1584959.

[193] L. Reinert, M. Varenberg, F. Mücklich, and S. Suárez, "Dry friction and wear of self-lubricating carbon-nanotube-containing surfaces," *Wear*, vol. 406–407, no. March, pp. 33–42, 2018, doi: 10.1016/j.wear.2018.03.021.

[194] N. Viswanath and D. G. Bellow, "Development of an equation for the wear of polymers," *Wear*, vol. 181–183, pp. 42–49, 1995, doi: 10.1016/0043-1648(95)90006-3.

[195] D. Xiong and S. Ge, "Friction and wear properties of UHMWPE/Al2O3 ceramic under different lubricating conditions," *Wear*, vol. 250–251, no. PART 1, pp. 242–245, 2001, doi: 10.1016/S0043-1648(01)00647-0.

[196] C. R. Bragdon, D. O. Connor, J. D. Lowenstein, M. Jasty, and W. D. Syniuta, "The importance of multidirectional motion on the wear of polyethylene," *Proc Iostn Mcch Engrs*, vol. 210, pp. 156–165, 1996.

[197] M. Jasty *et al.*, "Wear of polyethylene acetabular components in total hip arthroplasty," *J. Bone Jt. Surg.*, vol. 79-A, no. 3, pp. 349–358, 1997.

[198] G. W. Hastings, "In vivo wear properties of ultra-high molecular weight polyethylene used in a total knee prosthesis," *Wear*, vol. 55, no. 1, pp. 1–9, 1979, doi: 10.1016/0043-1648(79)90175-3.

[199] K. K. Kakulite and B. Kandasubramanian, "Rudiment of 'galling: Tribological phenomenon' for engineering components in aggregate with the advancement in functioning of the anti-galling coatings," *Surfaces and Interfaces*, vol. 17, no. November 2018, p. 100383, 2019, doi: 10.1016/j.surfin.2019.100383.

[200] D. Zhang, H. Liu, J. Wang, C. Sheng, and Z. Li, "Wear Mechanism of Artificial Joint Failure Using Wear Debris Analysis," *J. Nanosci. Nanotechnol.*, vol. 18, no. 10, pp. 6805–6814, 2018, doi: 10.1166/jnn.2018.15513.

[201] J. L. Tipper *et al.*, "Characterisation of wear debris from UHMWPE on zirconia ceramic, metal-on-metal and alumina ceramic-on-ceramic hip prostheses generated in a physiological anatomical hip joint simulator," *Wear*, vol. 250–251, no. 1–12, pp. 120–128, 2001, doi: 10.1016/S0043-1648(01)00653-6.

[202] M. Semlitsch and H. G. Willert, "Clinical wear behaviour of ultra-high molecular weight polyethylene cups paired with metal and ceramic ball heads in comparison to metal-on-metal pairings of hip joint replacements," *Proc. Inst. Mech. Eng. Part H J. Eng. Med.*, vol. 211, no. 1, pp. 73–88, 1997, doi: 10.1243/0954411971534700.

[203] L. Hongtao, G. Shirong, C. Shoufan, and W. Shibo, "Comparison of wear debris generated from ultra high molecular weight polyethylene in vivo and in artificial joint simulator," *Wear*, vol. 271, no. 5–6, pp. 647–652, Jun. 2011, doi: 10.1016/j.wear.2010.11.012.

[204] A. S. Shanbhag, J. J. Jacobs, T. T. Glant, J. L. Gilbert, J. Black, and J. O. Galante, "Composition and morphology of wear debris in failed uncemented total hip replacement," *J. Bone Jt. Surg. - Ser. B*, vol. 76, no. 1, pp. 60–67, 1994, doi: 10.1302/0301-620x.76b1.8300684.

[205] V. Saikko and T. Ahlroos, "Type of motion and lubricant in wear simulation of polyethylene acetabular cup," *Proc. Inst. Mech. Eng. Part H J. Eng. Med.*, vol. 213, no. 4, pp. 301–310, 1999, doi: 10.1243/0954411991535130.

[206] K. D. Moore, P. R. Beck, D. W. Petersen, J. M. Cuckler, J. E. Lemons, and A. W. Eberhardt, "Early failure of a cross-linked polyethylene acetabular liner: A case report," *J. Bone Jt. Surg.*, vol. 90, no. 11, pp. 2499–2504, 2008, doi: 10.2106/JBJS.G.01304.

[207] L. Vitos, P. A. Korzhavyi, and B. Johansson, "Elastic Property Maps of Austenitic Stainless Steels," *Phys. Rev. Lett.*, vol. 88, no. 15, p. 4, 2002, doi: 10.1103/PhysRevLett.88.155501.

[208] Ashirbad Jana, Anirban Basumataray, S. Senthilvelan, and Subramani Kanagaraj. "Importance of in vitro assessment of total hip arthroplasty using hip simulator and preliminary results." *Tribocorrosion* (2021): 173-197. https://doi.org/10.1016/B978-0-12-818916-0.00006-7

Outcome from the Thesis Work

Patents

1. Ashirbad Jana, S. Senthilvelan, S. Kanagaraj. A novel processing technique for the development of Acetabular cup from Ultra high molecular weight polyethylene powder to be used in Total Hip Replacement surgeries. Indian Patent No. 379704, *Official Journal of the Indian patent office*. 21st October 2021

2. Ashirbad Jana, S. Senthilvelan, S. Kanagaraj. Design of an Orbital Bearing Machine Hip Wear Simulator as per ISO 14242-3 incorporating necessary modifications to a Pin-On-Disc device. Indian Patent Application No. 202031010845A, *Official Journal of the Indian patent office*. 19th March 2021 [FER under review]

Published research works

1. Ashirbad Jana, Senthilvelan Selvaraj, and Kanagaraj Subramani. "A novel technique for the development of acetabular cup by cold isostatic compaction and sintering of UHMWPE powder with optimized processing parameters." *Polymer Engineering & Science* 61, no. 10 (2021): 2536-2556. https://doi.org/10.1002/pen.25779

2. Naskar Sharmistha, Asish K. Panda, Ashirbad Jana, Subramani Kanagaraj, and Bikramjit Basu. "UHMWPE-MWCNT-nHA based hybrid trilayer nanobiocomposite: Processing approach, physical properties, stem/bone cell functionality, and blood compatibility." *Journal of Biomedical Materials Research Part B: Applied Biomaterials* 108, no. 5 (2020): 2320-2343. https://doi.org/10.1002/jbm.b.34567

Submitted research work

1. Ashirbad Jana, Senthilvelan Selvaraj, and Kanagaraj Subramani. "Design of a Novel Mechanism Attachable to a Pin-on-Disc device for *in vitro* Evaluation of Total Hip Joint Arthroplasty as per ISO 14242-3". [Submitted to the Journal of *Scientific Reports: Nature Portfolio* on 06/12/2021]

Book Chapter

1. Ashirbad Jana, Anirban Basumataray, S. Senthilvelan, and Subramani Kanagaraj. "Importance of in vitro assessment of total hip arthroplasty using hip simulator and preliminary results." *Tribocorrosion* (2021): 173-197. https://doi.org/10.1016/B978-0-12-818916-0.00006-7

Paper work under progress

1. Ashirbad Jana, Senthilvelan Selvaraj, and Kanagaraj Subramani. "*In vitro* Evaluation of UHMWPE-MWCNT Nanocomposite based Acetabular Cups meant for Total Hip Replacement using 'Ball-on-Cup' Tribometer as per ISO 14242-3 with a Synovial fluid Analogue" [Under preparation]

Papers presented at International Conferences

1. Ashirbad Jana, S Senthilvelan and S Kanagaraj. "Hip Joint Simulator: A New Design According to the ISO 14242". International Conference on Materials, Design and Manufacturing Process (ICMDM 2016), 17-19 February **2016**, Anna University, Chennai, India

2. Ashirbad Jana, S Senthilvelan and S Kanagaraj. "A novel manufacturing technique to develop an acetabular cup made of UHMWPE". The 6th Asian Biomaterials Congress (ABMC 6), 25-27 October **2017**, Thiruvananthapuram, India

3. Ashirbad Jana, Anirban Basumataray, S Senthilvelan and S Kanagaraj. "A novel acetabular cup for total hip joint arthroplasty (THA)". The 6th International Conference on Advanced Nanomaterials and Nanotechnology (ICANN 2019), 18-21 December **2019**, IIT Guwahati, Assam, India

4. Ashirbad Jana, S Senthilvelan and S Kanagaraj. "Influence of isostatic and uniaxial compaction during processing of medical grade Ultra-high molecular weight polyethylene powder for bio-medical implants". **30th** Annual SBAOI Meeting & International Conference on Biomedical Materials Innovation-2020 (ICBMI-2020), 6-9 December **2020**, Coimbatore, India

5. Ashirbad Jana, S Senthilvelan and S Kanagaraj. "A Next Generation Acetabular Cup for Total Hip Arthroplasty (THA)". India International Science Festival 2021(IISF 2021), 10-13 December **2021**, Goa, India

SYNOPSIS

Since my joining IIT Guwahati as a research scholar, I have been working in Biomedical Devices and Biomaterials Laboratory in the department of Mechanical Engineering under the mentorship of Prof. S. Kanagaraj. I have been associated with projects for the development of various biomedical devices and implants funded by Govt. Of India. During the last six years at IIT Guwahati, I have been exposed to different aspects in design and development of biomedical devices like market research, CAD design, Numerical simulation, Manufacturing challenges, patent filing and patient trials.

During my thesis work I have developed an ingenious manufacturing technique for a machining-free UHMWPE acetabular cup reinforced with MWCNT, meant for a total hip arthroplasty with average bearing surface roughness of less than 100 nanometers for which a patent is granted in 2021.

I have filed another patent application for a novel design of a modular mechanism which can be attached to a simple pin-on-disc tribometer to transform it into an OBM hip simulator for evaluating total hip arthroplasties under bio-lubricant before their clinical use and developed the same at the central workshop at IIT Guwahati.

CONTACT

ADDRESS:
Town Shankararah, P.O.- Tamluk
Dist.- Purba Medinipur
West Bengal- 721636

PHONE:
+91-7896889268

EMAIL:
ashirbadjaana@gmail.com
j.ashirbad@iitg.ac.in

ASHIRBAD JANA

S/O- Mr. **Asit Ranjan Jana** and Mrs. **Sarbani Jana**

Research Scholar

Department of Mechanical Engineering, IIT Guwahati

EDUCATION

Ph.D.- Mechanical Engineering
Pursuing Ph.D. at IIT Guwahati, Govt. of India
Title of Thesis- Development of Ingenious Total Hip Prosthetic liners made of UHMWPE and its composites using a novel Ball-On-Cup tribometer
Synopsis on thesis presented and submitted on 10th March 2022
Thesis Submitted on 31st August 2022

B.Tech. – Mechanical Engineering
NIT Durgapur, Govt. of India
First-class with Distinction (CGPA 8.14) Year: 2010

Higher Secondary Examination (Class XII)
Ramakrishna Mission Residential College Narendrapur
First Class with Distinction (Percentage 80%)

Madhyamik Pariksha (Class X)
Ramakrishna Mission Vidyalaya Narendrapur
First Class with Distinction (Percentage 88%)

WORK EXPERIENCE

Assistant Project Engineer at IIT Guwahati
November 2021–Present, Sponsor- DST, Govt. Of India
Role- Development of new generation Acetabular Socket Linear and Femoral Head Prototypes with unique 3D microstructures and better fracture resistance for Osteoporosis and Osteoarthritis treatment

Junior Research Fellow at IIT Kharagpur
November 2011-April 2013
Role- Numerical analysis of Solid Oxide Fuel Cell (SOFC) developed at CGCRI-CSIR Lab. Kolkata using COMSOL Multiphysics platform

Assistant Manager at Hindusthan National Glass & Industries Ltd.
June 2010-November 2011
Research and Development, CAD Modelling, Mould Manufacturing and Inspection

Assistant Manager at Hindusthan National Glass & Industries Ltd.
June 2010-November 2011
Research and Development, CAD Modelling, Mould Manufacturing and Inspection

AWARDS AND HONORS

- **Best Presentation Award** in *India International Science Festival (IISF) 2021*
- **Project** titled '*Development of a next generation acetabular cup for total hip arthroplasty* (₹ 2.5 Lakh), sponsored by NewGen IEDC- DST Govt. of India
- **Best Model Award** in *Research Conclave 2017*, IIT Guwahati